Seismic imaging of crust beneath the western Tibet-Pamir and western Himalaya using ambient noise and earthquake waveform data

A thesis

Submitted in partial fulfillment of the requirements

Of the degree of

Doctor of Philosophy

By

Vivek Kumar

Roll No. 20153398

IISER PUNE

INDIAN INSTITUTE OF SCIENCE EDUCATION AND RESEARCH PUNE

2021

DECLARATION

I declare that this written submission represents my ideas in my own words and where others' ideas have been included, I have adequately cited and referenced the original sources. I also declare that I have adhered to all principles of academic honesty and integrity and have not misrepresented or fabricated or falsified any idea/data/fact/source in my submission. I understand that violation of the above will be cause for disciplinary action by the Institute and can also evoke penal action from the sources which have thus not been properly cited or from whom proper permission has not been taken when needed.

(Vivek Kumar)

Roll No. 20153398

Date: October 28, 2021

CERTIFICATE

Certified that the work incorporated in the thesis entitled "**Seismic imaging of crust beneath the western Tibet-Pamir and western Himalaya using ambient noise and earthquake waveform data**" Submitted by **Vivek Kumar** was carried out by the candidate, under my supervision. The work presented here or any part of it has not been included in any other thesis submitted previously for the award of any degree or diploma from any other University or institution.

Date: October 28, 2021

(Prof. Shyam S. Rai)
Supervisor
DAE-Raja Raman Fellow and
Professor Emeritus,
Department of Earth and Climate Science
Indian Institute of Science Education and
Research (IISER) Pune
Dr. Homi Bhabha Road, Pashan,
Pune-411008, India

ACKNOWLEDGEMENTS

(Vivek Kumar)

PUBLICATIONS

1 **Kumar V**., Rai S. S., Hawkins, R., and Bodin T., 2021, Seismic imaging of crust beneath the western Tibet-Pamir and western Himalaya using ambient noise and earthquake waveform data. *Journal of Geophysical Research: Solid Earth* (Revision submitted).

2 **Kumar V**., Rai S. S., Hawkins, R., and Bodin T., 2021, Crustal variability in northwest Himalaya and Ladakh-Kohistan arc. *Geophysical Research Letters* (In Preparation).

3 **Kumar V**. and Rai S. S., 2021, Complex seismic image of the Main Himalayan Thrust in Garhwal and implication to earthquake hazard. *Journal of Earth System Science* (in press).

x

CONTENTS

SYNOPSIS

Kinematics and dynamics of the evolution of continental collisions and mountain building processes have been a primary area of research to understand the deformation mechanism of continental interiors. The Himalaya-Tibet-Pamir mountain belts, which have an evolutionary history beginning about 50 million years ago with the closure of the Tethys Ocean followed by the collision of the Eurasian and Indian landmass, is a natural laboratory for studying the ongoing large-scale geodynamic processes. Since the early versions of isostasy, proposed by Airy (1855), and Pratt (1859) inferring that a deficit of mass must underlie the Himalayas and Tibet, several models are proposed to explain its large-scale crustal shortening and consequent thickening, and uplift. End member models include thrusting of the Indian continental lithosphere beneath Asia, first proposed by Argand (1924), and/or diffused deformation within Asia that led to crustal thickening and uplift of the orogen. Much of our knowledge about these models are based on geological and geophysical investigations from the central and eastern parts of the Tibet-Himalaya system. These studies have further revealed evidence for the underplating and subsequent eclogitization of the Indian lower crust beneath the Tibetan plateau and the partially molten state of the middle crust of the Tibetan plateau. However, continuity of these features to the western segment of the Himalaya-Tibet system comprising western Himalaya, Ladakh-Kohistan arc, western Tibet and Karakoram, and Pamir Hindu Kush regions, remain speculative due to the absence of experiments on a similar scale as in the central and eastern Tibet.

In this thesis, we present a 3-D crustal architecture, including vertical extent and stratification, and the nature of boundaries separating distinct units laterally and vertically with a lateral resolution of $30-50$ km up to a depth of 100 km below sea level beneath the western Himalaya-Ladakh-Pamir-Tibet region, to understand the geological evolution of the region with a focus on defining the geometry of the underthrusting Indian crust and its northern edge, understanding crustal deformation and disparity of evidence for channel flow and mapping the depth reach of the Karakoram fault. The velocity image is produced using ambient noise cross-correlations from about 530 seismological stations along with surface wave observations from 1,261 earthquakes recorded over the seismological network. The velocity image is reconstructed following a two-step procedure. Firstly, we compute Rayleigh wave group velocity maps for the region at $0.5° \times 0.5°$ grid interval from period 5 to 60 seconds using earthquake and ambient noise waveform by the Bayesian Trans-dimensional tree tomography.

The dispersion data at each grid node is then converted to shear wave velocity variation with depth by a trans-dimensional, hierarchical Bayesian inversion.

We present the first-order crustal structure in terms of lateral distribution and connectivity of the mid-crustal low-velocity zones (LVZs) and the nature of the Indian lower crust that underplates the Tibetan Plateau. Moho beneath the Himalayas and south Tibet correlates with a velocity of 4.4−4.6 km/s and a reduced velocity of 4.0−4.2 km/s in northern Tibet and Pamir. We used the Moho depth and nature of high-velocity lower crust (Vs > 4.0 km/s) to map the northern limit of the Indian crust that extends beyond the Qiangtang block in western Tibet (77−82°E) from its previously assumed boundary in the Lhasa block and till central Pamir further west. The velocity image reveals discontinuous low-velocity zones (LVZs) (Vs < 3.4 km/s) in the upper and middle crust in western Tibet and Pamir that rarely connect to the high Himalayas as expected for a ductile channel flow. The LVZs in Pamir correlate with the surface distribution of gneiss domes. The lowest velocities (Vs < 3.2 km/s) are observed over Ladakh-Karakoram batholiths and the Nanga Parbat region. The study suggests a continuation of LVZs across the Karakorum Fault at a depth beyond 20 km, indicating the fault's very shallow (upper crustal) depth extent.

The detailed analysis of the velocity image reveals an unreported nearly arc perpendicular crustal-scale transverse structure along ~77°E that segments western Himalaya longitudinally. East of this transverse structure, the Main Himalaya Thrust (MHT) has a gentle northward dip of 10−16° and reaching a depth of 40−45 km near the Indus Suture Zone (ISZ). In contrast, to the west, the MHT is nearly flat at 15−20 km depth between the Main Frontal Thrust (MFT) and the ISZ with no evidence of a north dipping ramp. The transverse structure is a broad zone with low velocity (Vs < 3.4 km/s) in the mid to lower crust. The eastern limit of this transverse structure coincides with the northward extension of the Simla/Ropar Manali lineament, a pre-Himalayan basement fault in the Indian lithosphere. We propose that the reactivation of this lineament in the down-going Indian plate and subsequent strain propagation onto the surface through the weak mid/lower crust is possibly responsible for the segmentation in the western Himalayan arc.

The velocity image of the region provides a unique opportunity to understand the nature of the Kohistan-Ladakh complex formed as an island arc within the Tethys Ocean in Mesozoic times, thrust southward onto the Indian margin to become ultimately squeezed between the converging Indian and Asian plates. Based on the modeling of seismological data, we present

the first evidence for the high-velocity (high-density) lower crustal root under the Kohistan arc that is conspicuously absent in Ladakh. In the upper and middle crust, the Kohistan arc shows a uniform Vs ~ 3.5 km/s underlain by a thick (~25 km) high velocity lower crust (Vs > 4.0 km/s). In contrast, the Ladakh arc crust is largely characterized by a Vs < 3.4 km/s between 15 to 40 km depth, and an absence of the thick mafic basal layer at greater depths.

Finally, we use seismic waveform recorded on 26 closely spaced (~10 km) broadband seismographs across the strike of Garhwal Himalaya to produce a high-resolution image of the MHT geometry from ambient noise tomography. Our model suggests two distinct ramps on the MHT -a gentle dipping (~ 9°) at shallow depth (~ 7−12 km) located 40 km north of the Main Boundary Thrust, and other a steeply dipping (~ 30° to 35°) at ~15−25 km depth beneath the Higher Himalayan front. The inferred double ramp geometry in this study highlights the complex segmentation of MHT in the Garhwal Himalaya, which provides an important constraint in simulating earthquake hazard potential and modeling the growth of Himalayan topography.

CHAPTER 1

Introduction

Tibet has remained a focal point for the development of models of large-scale continental geodynamics, for more than a century. The history could be traced to the proposition of the theory of Isostasy (Airy, 1855; Pratt, 1859) and inference of a mass deficit beneath the Himalayas and Tibet. Later, the concept was expanded by Dewey and Burke (1973) to explain older belts of intracontinental deformation globally. Chang and Cheng (1973), had by then, proposed that Tibet comprised of a set of belts that had accreted to Eurasia from late Paleozoic to late Mesozoic time. Molnar and Tapponnier (1975, 1978) used global seismological observations and Landsat imagery to provide the first evidence of extensive normal faulting over Tibet that is superimposed over older folding with the west-east axis. Major transformation to our understanding of Himalaya–Tibet geodynamics emerged from the INDEPTH program (Zhao et al., 1993) that showed that intact Indian continental lithosphere underthrusts the Himalaya. Since then Himalaya-Tibet (and recently Pamir-Hindukush) has been explored through numerous geological-geophysical experiments. Molnar (1988), Yin and Harrison (2000), Klemperer (2006), Searle (2015), Avouac (2015), and Kapp and DeCelles (2019) provide an excellent review on the subject.

Despite a large number of experiments over the last 40 years, the most fundamental question relating to the origin of the Tibetan Plateau remains unresolved: Does the intact Indian lithosphere slide horizontally beneath the plateau? Proposed first by Argand (1924), the hypothesis was adopted with minor modifications by many others (Barazangi & Ni, 1982; Zhao et al., 1993; Nábělek et al., 2009; Zhao et al., 2010; Guo et al., 2017). Beyond wholesale underthrusting of India, other possibilities include intracontinental subduction (Mattauer, 1986; Roecker, 1982; Burtman & Molnar, 1993; Huang et al., 2011) or its variants, distributed thickening of the Asian lithosphere by indentation of stronger Indian lithosphere (Dewey and Burke, 1973; Molnar & Tapponnier,1975; Kufner et al., 2016; Chen et al., 2017).

In this chapter, we briefly present (i) geological background and previous studies of the India-Asia convergence zone with a focus on the western Tibet-Himalaya, Pamir-Hindu Kush, and Ladakh-Kohistan arc, (ii) kinematic models for the evolution of Himalaya and

the pervasive east-west extension of the Tibet-Himalaya orogeny. This is followed by the aim and structure of the thesis.

1.1 Geological context

1.1.1 India-Asia convergence

India was part of Gondwana land, a supercontinent of the southern hemisphere that existed ~300 Ma ago, comprising present-day South America, Africa, Arabia, Madagascar, Sri Lanka, India, Antarctica, and Australia (Yin & Harrison, 2000). In the Late Carboniferous and early Permian (~ 300 Ma), a major rifting event (Panjal basalt explosion) led to separation of the northern portion of Gondwana and opening a new oceanic basin. It is believed that the rifted part is the present-day Qiangtang block of the Tibet plateau. Subsequent major rifting events in the Late Triassic (~200 Ma) formed the present-day Lhasa block (Figure 1.1). When India separated from the rest of the Gondwana land at around 140 Ma, the Lhasa and the Qiangtang blocks had already collided and accreted with Eurasia (Yin & Harrison, 2000).

The motion of the Indian plate relative to the Eurasian plate is derived from a series of Euler rotations obtained from multiple sources with different errors and uncertainty (White et al., 2012). Figure 1.2 provides a compilation of the motion of the Indian plate relative to the Eurasian plate. Two distinct motions of the Indian plate can be identified, i) anomalously fast convergence of India-Eurasia between 80 to 65 Ma, ii) drop in convergence rate after 65 Ma. The relatively fast velocity of India-Eurasia has been explained by mantle plume erupting around 67 Ma and forming the Deccan traps (Cande et al., 2011, Van Hinsbergen et al., 2011) and/or double subduction of oceanic plates between India and Eurasia (Jagoutz et al., 2015). On the other hand, the significant drop in convergence rate from 160 mm/yr to 50 mm/yr after 70-50 Ma has been suggested to occur because of many factors such as a) increase in resistance between plate and asthenosphere (Kumar et al., 2007), b) increased distance of the plate from the mantle plume and decrease in plume flux after initial eruption (Cande et al., 2010; Van Hinsbergen, et al., 2012), c) multiple accretion events (e.g., collision with Ladakh-Kohistan around 65 Ma) before India-Asia collision (Khan et al., 2009). Conventionally, this deceleration of India-Eurasia has been interpreted to indicate the continued collision of India with Asia (Patriat & Achache, 1984; Molnar & Stock, 2009).
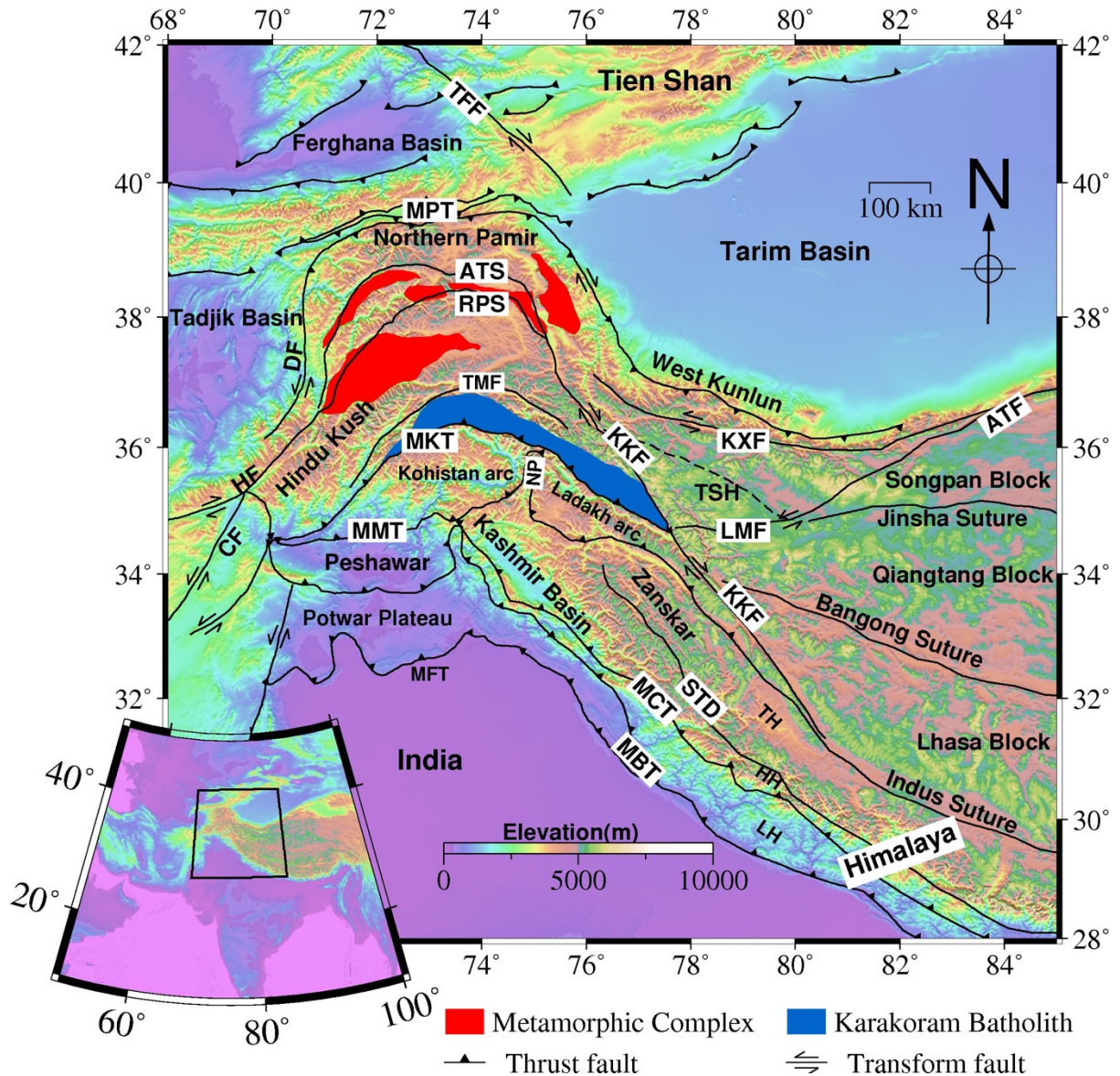
Figure 1.1. *Topographic map of the study region that includes Western Tibet-Himalaya, Ladakh-Kohistan arc, and Pamir-Hindu Kush. Major tectonic blocks and faults are marked as black lines (Searle & Hacker, 2019; Yin & Harrison, 2000). The red shaded areas denote metamorphic complexes (gneiss domes) of Pamir. The blue shaded area is the Karakoram batholith. The black polygon in the inset image at the bottom left indicates the study region. MFT-Main Frontal Thrust, MBT-Main Boundary Thrust, MCT-Main Central Thrust, STD-Southern Tibetan Detachment, MMT-Main Mantle Thrust, LMF-Longmucuo Fault, TSH-Tianshuihai block, ATF- Altyn Tagh Fault, KXF -Karakax Fault, KKF-Karakoram Fault, MKT-Main Karakoram Thrust, NP-Nanga Parbat, TTF-Talas Ferghana Fault, RPS-Rushan Pshart Suture, ATS-Akbaytal Tanymas Suture, MPT-Main Pamir Thrust, CF- Chaman Fault, HF-Herat Fault, DF- Darvaz Fault, TMF-Tirich Mir Fault, TH-Tethys Himalaya, HH-High Himalaya, LH-Lesser Himalaya.*
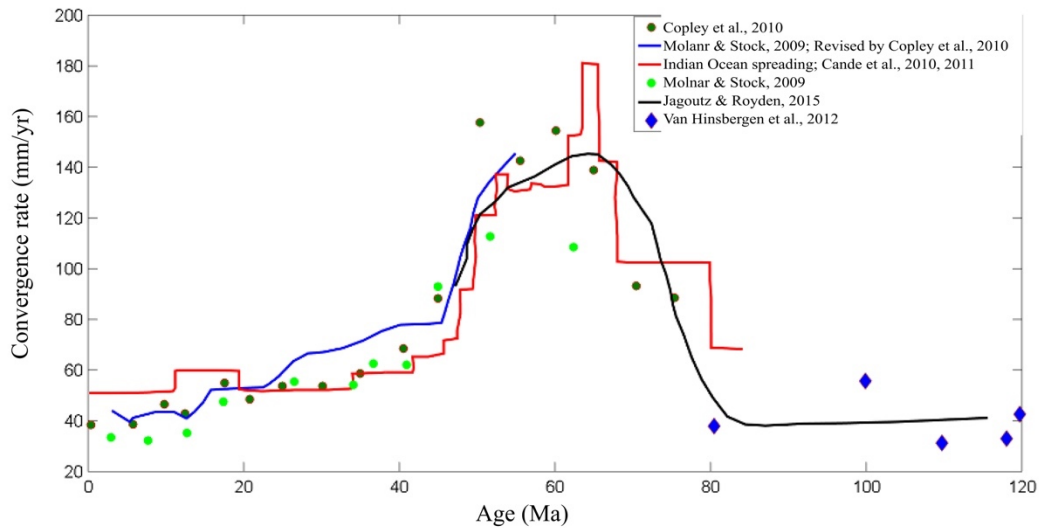
Figure 1.2. *Convergence rate of India-Asia after Copley et al. (2010), Molnar and Stock (2009), and Van Hinsbergen et al. (2012). The convergence rate from numerical modeling of Jagoutz et al. (2015) is shown by a black line. Indian Ocean's spreading rate is shown in a red line after Cande et al. (2010, 2011).*

The continued convergence between India and Asia along the Indus Zangbo Suture (IZS) created the highest mountain system comprising Himalaya, Tibet, and Pamir-Hindu Kush. The Eurasian plate is an amalgamation of several crustal blocks. The prominent ones are - the Tian Shan and further north, considered as Precambrian to Paleozoic microcontinents; the Tarim and Tadjik rigid blocks south of the Tien Shan; and Tibet-Pamir-Hindu Kush with Gondwana affinity. The southernmost part of Asia is an Andean-type margin with a 2500 km long Trans-Himalayan (Kohistan-Ladakh-Gangdese) granitoid batholith. Subsequently, the deformation spread southward across Tibet from the Tethys zone to the High Himalaya and further south. Major geological terrains, suture zones, and fault systems are shown in Figure 1.1. Sengör and Natal'in (1996), Burtman and Molnar (1993), Kapp and DeCelles (2019), and Yin and Harrison (2000) provide excellent reviews of the geological evolution of these terrains.

1.1.2 Tibetan plateau

The Tibetan plateau is a collage of continental blocks that include from north to south, Songpan-Ganzi block, Qiangtang block (QB), and Lhasa block (LB) separated by Jinsha Suture (JS) and Bangong-Nujiang Suture (BNS). The BNS was formed in the Late Jurassic–Early Cretaceous when the Lhasa terrane collided with Asia's southern margin (Qiangtang terrane) to the north, followed by its northward subduction. The Tibetan plateau

is joined to the Tarim Basin in the north by the Altyn Tagh fault (ATF) and south to the Himalaya through the IZS. The northeast part of Tibet joins the Qaidam Basin along the Kunlun fault (KF). Most of these Asian terranes are separated by narrow suture zones. The northern limit of the plateau consists of low-altitude sedimentary basins underlain by stable Precambrian cratons - the Tarim Basin in the northwest and the Qaidam Basin in the north (Zhu & Helmberger 1998; Yin & Harrison, 2000; Unsworth et al., 2004). The plateau's western limit corresponds to the trace of the Altyn Tagh Fault (ATF) and the Karakoram Fault (KKF) (Westaway, 1995; Yin & Harrison, 2000).

1.1.3 Pamir and Hindu Kush

Pamir and Hindu Kush, situated north of the western Himalayan syntaxis, define accretion of Gondwana derived microcontinents, Andean-type arc magmatism, and subduction-accretion system of Paleozoic and early Mesozoic age (Burtman & Molnar, 1993). After the collision of India with Asia around 50 Ma, intense crustal shortening, ultra-high pressure metamorphism, shallow to deep focused seismicity, and lateral extrusion of crustal material mark the Cenozoic evolution of the Pamir and Hindu-Kush. Bending of east-west trending tectonic blocks of the Tibet-Himalaya system in the Pamir and Hindu-Kush area gives ~300 km of northward displacement of northern Pamir with respect to the rest of Eurasia in Cenozoic time (Burtman & Molnar, 1993). The Pamir and Hindu Kush area experienced the same Cenozoic shortening as Tibet but in a relatively narrow region. At present, GPS measurements suggest ~30 mm/yr of northward movement of the Pamir and the surrounding region with respect to the stable Pakistan and Eurasia (Ischuk et al., 2013). This convergence is partitioned into 10-15 mm/yr shortening along the Main Pamir Thrust (MPT), which bounds the Northern Pamir, ~ 11 mm/yr right-lateral strike-slip motion along the Darwaz-Karakul fault, which flanks the western margin of the Pamir-Hindu Kush, and ~ 9 mm/yr of east-west extension of the Pamir (Ischuk et al., 2013; Mohadjer et al., 2010).

The classical tectonic division of the Pamir contains three parts: north, central and south Pamir. The northern Pamir is a Carboniferous-Triassic Karakul-Mazar subduction-accretion belt between the central Pamir in the south and the Tien-Shan in the north, which is further correlated with the Songpan-Garze-Hoh Xi system of Tibet between the north-facing Kunlun suture and the south-facing Jinsha suture. The Jinsha suture is correlated with the Akbaytal Tanymas Suture (ATS) in southern Pamir (Schwab et al., 2004). In addition, the Allai valley along the northern margin of the Pamir represents the last remnant

of the former Tadjik-Yarkand Basin that once connected the Tadjik Basin in the west to the Tarim Basin in the east (Burtman & Molnar, 1993). The central Pamir zone lies between the ATS in the north and the Rushan-Pshart Suture (RPS) in the south. Amphibolite facies sedimentary and igneous rocks of central Pamir were buried to a depth of 25-35 km during 35-20 Ma and then exhumed on the surface during 20-12 Ma (Rutte et al., 2017). Central Pamir gneiss domes (Muskal & Satput) mark the Cenozoic metamorphic complex. The regional structure and metamorphic rocks of central Pamir gneiss domes are correlated with the Qiangtang block of Tibet (Schwab et al., 2014). The RPS, correlated with the BNS, separates the southern Pamir from the central Pamir. The Shakhadra Alichur gneiss dome of southern Pamir is a major metamorphic core complex that records 37-22 Ma prograde metamorphism and burial of crustal rocks to a depth of more than 50 km. The exhumation started at 21-20 Ma and progressed till 2 Ma. The southern Pamir shares a similar metamorphic history as the Hunza and Baltoro complex in the Karakoram, suggesting continuity of Cenozoic metamorphism from the north Karakoram to the north Pamir. Therefore, it is correlated with the Lhasa block in Tibet (Schwab et al., 2004). Gneiss domes of the Pamir are bounded by normal sense shear zones, representing lateral extension and crustal thinning during the retrograde motion of metamorphic rocks. The Dunkeldik valley in the southeastern Pamir exposes the crustal origin xenoliths of ultra-high pressure mineral assemblages, which records eruption of material from 90-100 km depth at ~11 Ma (Hacker et al., 2005).

The occurrence of intermediate-depth earthquakes makes The Pamir-Hindu Kush one of Earth's most seismically active zones. Shallow events (< 50 km) are located in the entire Pamir and Hindu Kush area with the most clustering of the seismicity in the northern margin of the Pamir defined the Main Pamir Thrust (MPT) fault. The intermediate-depth seismicity displays two distinct zones: a) Hindu Kush: East-west striking and steeply north dipping zone to a depth more than 300 km, b) Pamir: north-south striking and eastward dipping at the eastern end of the Hindu Kush and east-west striking and south-dipping along the Main Pamir Thrust to a depth of 300 km, which makes an arc shape (Burtman & Molnar, 1993, Sippl et al., 2013). Several models have been proposed explaining the geometry of the seismicity of the Pamir and Hindu Kush, which can be broadly characterized into two end-member groups: a) the Pamir and Hindu Kush forms a single contorted Benioff zone (Billington et al., 1977; Pelgar & Das,1998; Pavlis & Das, 2000) or two distinct zones (Chatelain et al., 1980, Burtman & Molnar, 1993; Sippl et al., 2013, Schurr et al., 2014), b) intermediate-depth earthquakes are associated with a remnant oceanic slab (Chatelain et

al., 1980; Pelgar & Das, 1998; Pavlis & Das, 2000) or deep continental subduction (Roecker et al., 1982, Burtman & Molnar, 1993; Sippl et al., 2013, Schurr et al., 2014).

1.1.4 Kohistan-Ladakh arc

Most of the modern continental crusts are formed in convergent margins (Rudnick, 1995). The Kohistan-Ladakh arc (KLA) sandwiched between the Karakoram and the western Himalayan syntaxis is recognized as an island arc setting based on 1) absence of pre 50 Ma old continental basement (Bard, 1983; Tahirkheli, 1979), and 2) paleomagnetic data showing the formation of the KLA near the equator in the oceanic basin during Mesozoic (Khan et al., 2009; Schettino & Scotese, 2005). This makes the KLA an ideal laboratory to study how a juvenile continental crust is formed from island arcs.

The Kohistan arc displays a complete exposure of an island arc crust compared to less complete exposure of the Ladakh arc, and tectonic processes might have varied eastward from the Kohistan (Burg, 2006). The gross geology of the Kohistan arc is divided into three parts (Jagoutz & Schmidt, 2012) from north to south as 1) Gilgit complex: dominantly calc-alkaline batholith with inclusions of volcanic and sedimentary rocks which exposes mid and upper arc crust and records a magmatic history from 120-50 Ma, 2) Chilas complex: mafic to ultramafic intrusions representing mid-crustal arc rocks created by the arc rifting at around 85 Ma, and 3) Southern Plutonic complex: southernmost part of Kohistan, which exposes mafic to ultramafic lower arc crust rocks formed during 120-85 Ma (Figure 1.3).

The exact timing of the collision of India with Kohistan and Asia is controversial, with some authors suggesting KLA collided first with India (Reuber, 1986; Yin & Harrison, 2000; Bard, 1983; Builhol et al., 2013) and others suggesting KLA collided first with Asia (Treloar et al., 1989; Clift et al., 2002). Burg (2006) suggested that island arcs which were formed east of KLA were thin and negatively buoyant that got subducted during Neo-Tethys subduction under the southern Tibet.

1.1.5 Himalaya

The Himalayas spanning ~ 3000 km from north Pakistan in the west to southeastern Tibet and northeast India, has been traditionally divided into orogen parallel tectonostratigraphic zones (Figure 1.3) bounded by major faults (Gansser, 1964; Le Fort, 1975; Hodges, 2000). From north to south, tectonic divisions are: i) Tethyan Himalaya Sequence (THS): Late Precambrian to Eocene age (~650-40 Ma) marine and fossiliferous

sedimentary rocks locally interbedded with volcanic flows, bounded by the Indus Suture (ISZ) in the north and a normal sense South Tibetan Detachment fault (STD) in the south, ii) Greater Himalayan Sequence (GHS): high-grade metamorphic rocks (800-480 Ma) dominantly kyanite-sillimanite gneisses and migmatites, bounded by the STD in the north and the Main Central Thrust (MCT) in the south, iii) Lesser Himalaya Sequence (LHS): Proterozoic metasedimentary sequence (1870-800 Ma) of low-grade metamorphism, is emplaced over unmetamorphosed Siwalik sediments by the Main Boundary Thrust (MFT) fault. These thrust faults converge to a major detachment called the Main Himalayan Thrust (MHT), which separates the top of the underthrusting Indian plate from the overlying Himalayan wedge (Schelling & Arita, 1991). Three along-strike divisions of the Himalayan arc, after Yin (2006), include i) western Himalaya (66-81°E) comprising the Salt range of northern Pakistan, Kashmir, Zanskar, Chamba, Lahul and Spiti, Garhwal and Kumaun; ii) central Himalaya (81-89°E), which includes Nepal, Sikkim and south-central Tibet; iii) eastern Himalaya (89-98°E), which includes Bhutan, Arunachal Pradesh, and southeastern Tibet.

The MCT marks a ductile, synmetamorphic 2-10 km thick shear zone in the central Himalaya where the grade of metamorphism increases from biotite to sillimanite northward from the base of the shear zone producing inverted metamorphism. Arita (1983) defined this base as MCT-I, which coincides with the Munsiari Thrust (MT) in Kumaun and Garhwal (Valdiya, 1980), whereas the top of the zone where kyanite first becomes dominant is called MCT-II, which coincides with the Vaikrita Thrust (VT) in Kumaun and Garhwal (Valdiya, 1980). The geometry of the MCT zone is flat-ramp (Lyon-Caen and Molnar, 1985; Schelling and Arita, 1991; Yin, 2006; Bilham et al., 2017), with the ramp showing stress concentration due to intense micro-seismicity and low electrical conductivity (Pandey et al., 1999; Bilham et al., 2017). The flat portion of the MCT zone is folded in the south producing Lesser Himalaya Crystalline Nappes (LHCN) like Almora nappes in Garhwal and Kumaun, and Kathmandu nappes in Nepal. Across the STD, the metamorphic grade drastically decreases in the THS. Rocks in the THS form a folded and imbricated anticlinorium exposing GHS rocks at their crest, commonly known as North Himalayan gneiss domes.

The activity on the MCT zone indicates a protracted history (Yin, 2006), with MCT-II being active at 23-20 Ma. Further southward, the deformation age becomes relatively

CHAPTER 1

younger to about 5-3 Ma. At the southernmost part of the MCT root zone, the activity ranges from 21 to 14 Ma. The STD shares a coeval motion with the MCT (Yin, 2006). The estimate of the total crustal shortening across the central Himalaya fold and thrust belt is about 600 km (Murphy & Yin, 2003; Yin, 2006).
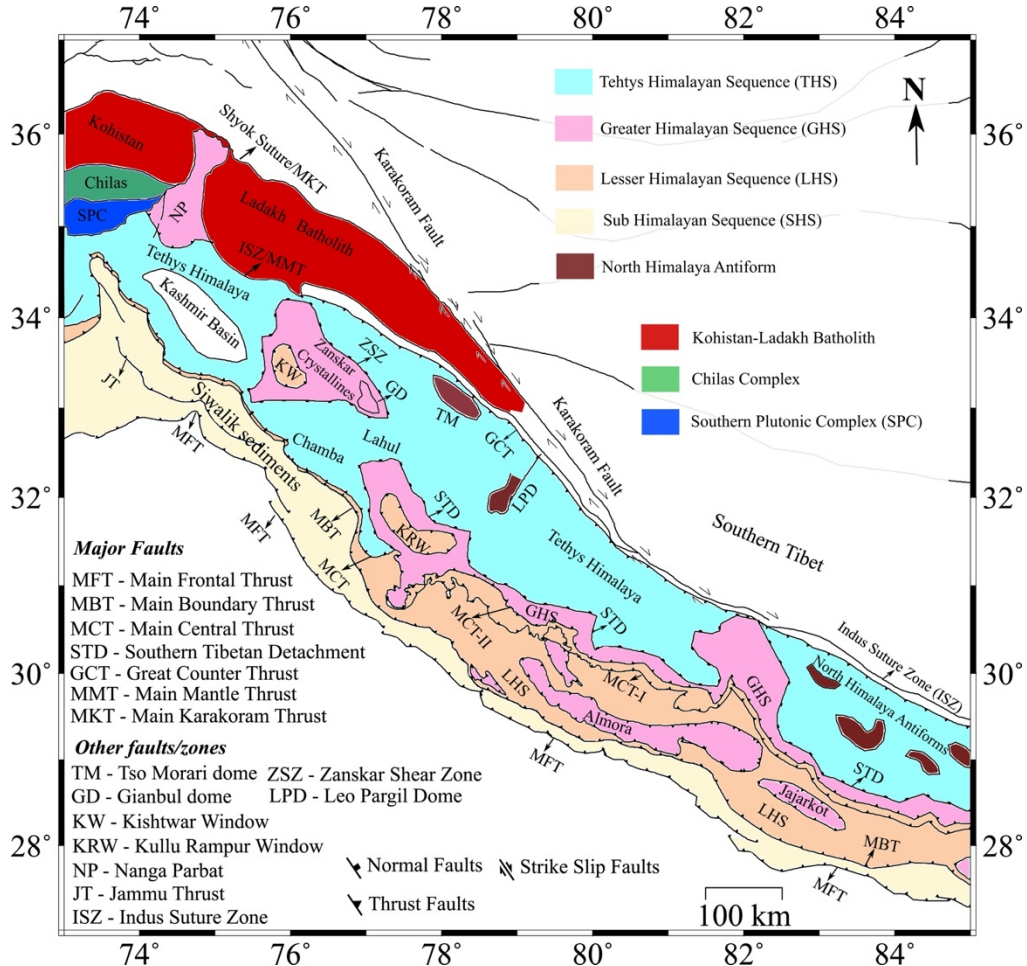
Figure 1.3. *Simplified geological map of western and central Himalaya, and Ladakh-Kohistan arc after Yin (2006), DiPietro and Pogue (2004), and Jagoutz and Schmidt (2012).*

1.1.6 Extension of traditional Himalayan subdivisions to western Himalaya

Classical subdivisions of Himalayas, as discussed above, become less applicable in western Himalayan west of ~ 77°E, where the MCT comes close to the MBT, and both extend as a parallel fault pair with a narrow but continuous (< 8 km wide) Lesser Himalayan sedimentary zone further west (DiPietro & Pogue, 2004; Yin, 2006). In contrast to the central Himalaya, where the high-grade metamorphic rocks (kyanite and sillimanite) are present in the hanging wall of the MCT, the fault juxtaposes low-grade rocks of the THS

and the LHS in the western Himalaya. Equivalents of the GHS are present in the more internal part far north of the MCT in the Zanskar region (Figure 1.3), where they are referred to as Zanskar crystallines. In Chamba-Lahul and Kashmir Himalaya, the high-grade rocks between the MCT and the THS are missing. The continuity of the STD is broken in Lahul, and the Zanskar shear zone, bounding the northern limit of Zanskar crystallines, is considered the STD equivalent. The high-grade rocks of the GHS of the central Himalaya are laterally exhumed as a slab due to the motion along the MCT and STD. In contrast, Zanskar crystalline rocks are exposed as large-scale dome structures such as the Gianbul dome (Robyr et al., 2006). Within the GHS of the western Himalaya, two significant windows expose the low-grade LHS rocks. These are the Kishtwar Window (KW) in the Zanskar region and the Kulu-Rampur Window (KRW) in Himanchal Himalaya east of the Chamba region, representing the folding of the MCT zone.

The northern portion of the western Himalaya exposes eclogite bearing Ultra High Pressure (UHP) rocks such as Kaghan valley in northern Pakistan and Tso Morari dome in NW India. Their protoliths belong to the Indian Precambrian basement. The peak metamorphism of Kaghan valley records a temperature of about 600°C and pressure > 23-24 Kbar, with its exhumation occurring at 46-40 Ma. The UHP metamorphism of Tso Morari rocks is dated ~ 55 Ma with its exhumation ~ 47 Ma (Yin, 2006). These UHP rocks indicate subduction of the Indian continental margin to a depth > 80 km followed by a rapid exhumation at 1 cm/yr to > 3 cm/yr (Treloar et al., 2003). This high uplift rate is attributed to the slab decoupling between the oceanic crust and the Indian continent during the middle Eocene (O'Brien, 2019).

1.1.7 Kinematic models for Himalayan evolution

Kinematic models for the overall evolution of the Himalayas have primarily focused on how the high-grade GHS was emplaced between the low-grade LHS below and the THS above. Earlier, the motion on the MCT was believed to have played an essential role in GHS emplacement (Heim & Gansser 1939). With the discovery of the STD (Burg et al., 1984) and its coeval motion with the MCT, many workers thought that the GHS was extruded as a ductile wedge (Grujic et al., 1996) or a rigid wedge (Burchfiel & Royden, 1985) with its protolith belonging to the Indian crust. These models require the MCT and STD to have hanging and footwall ramps and merge downdip. Other models assume lateral extrusion of partially molten middle/lower crust beneath Tibet to the Himalayan front via channel flow possibly due to pressure gradient between the eroding Himalayan front and

the partial melt or gravitational collapse of the thickened crust (Nelson et al., 1996; Beaumont et al., 2001). The channel flow model requires i) rapid extrusion of GHS between the MCT and STD, with the STD having a unidirectional (i.e., top-to-south) normal sense shear history, ii) large-scale laterally continuous presence of mid/lower crustal partial melts beneath Himalaya and Tibet with a weak upper crust (i.e., Tethys sediments or THS).

These kinematic models discussed above are essentially two-dimensional in nature, making specific predictions about the exhumation geometry of GHS mainly derived from studies performed in the central Himalaya (DiPietro & Pogue, 2004; Yin, 2006). They are inadequate to explain the large-scale lateral variation of the Himalayan geology as discussed in earlier sections. A major limitation of these extrusion-based models is that the STD and MCT merge in the up-dip direction in western and eastern Himalaya and the STD has acted as a back thrust rather than a normal fault with early top-to-south shearing (Yin, 2006). The continuity of partial melts from the mid/lower crustal depth beneath Tibet to the high Himalayan front required for the channel flow is questioned by the presence of restricted to localized zones of partial melts beneath north-trending rifts in southern Tibet (Yin, 2000, 2006; Yin and Harrison, 2000).

Yin (2006) provided a possible kinematic model which explains the along-strike variation of the Himalayan geology. The model considers the early top-to-south shearing of the STD and its up-dip merger with the MCT and is popularly known as the tectonic wedging model (He et al. (2016). The Himalayan evolution is then described in five time zones i) late Paleocene to early Eocene (60-50 Ma): subduction of the Indian continent beneath Asia to a depth of > 100 km and UHP metamorphism followed by its return to mid-crustal depth (15-20 km), ii) Eocene to early Oligocene (45-24 Ma): development of the Tethyan fold and thrust belt and crustal thickening, and prograde metamorphism of Indian northern margin with the STD as a basal thrust, iii) late Oligocene to early Miocene (24-20 Ma): initiation of the MCT and reactivation of the STD as top-to-north sense shear zone, iv) early to middle Miocene (20-15 Ma): continued convergence of India-Asia collision zone results development of thrust duplexes causing north Himalayan antiforms and exposure of the MCT to the surface, v) late Miocene to Pliocene (7-4 Ma): reactivation of lower MCT zone and continued motion on the MBT results into the folding of the MCT and STD forming the Lesser Himalayan Crystalline Nappes (LHCN). The continued motion among major fault boundaries and subsequent development of thrust duplexes are basic structures of the tectonic wedge model.
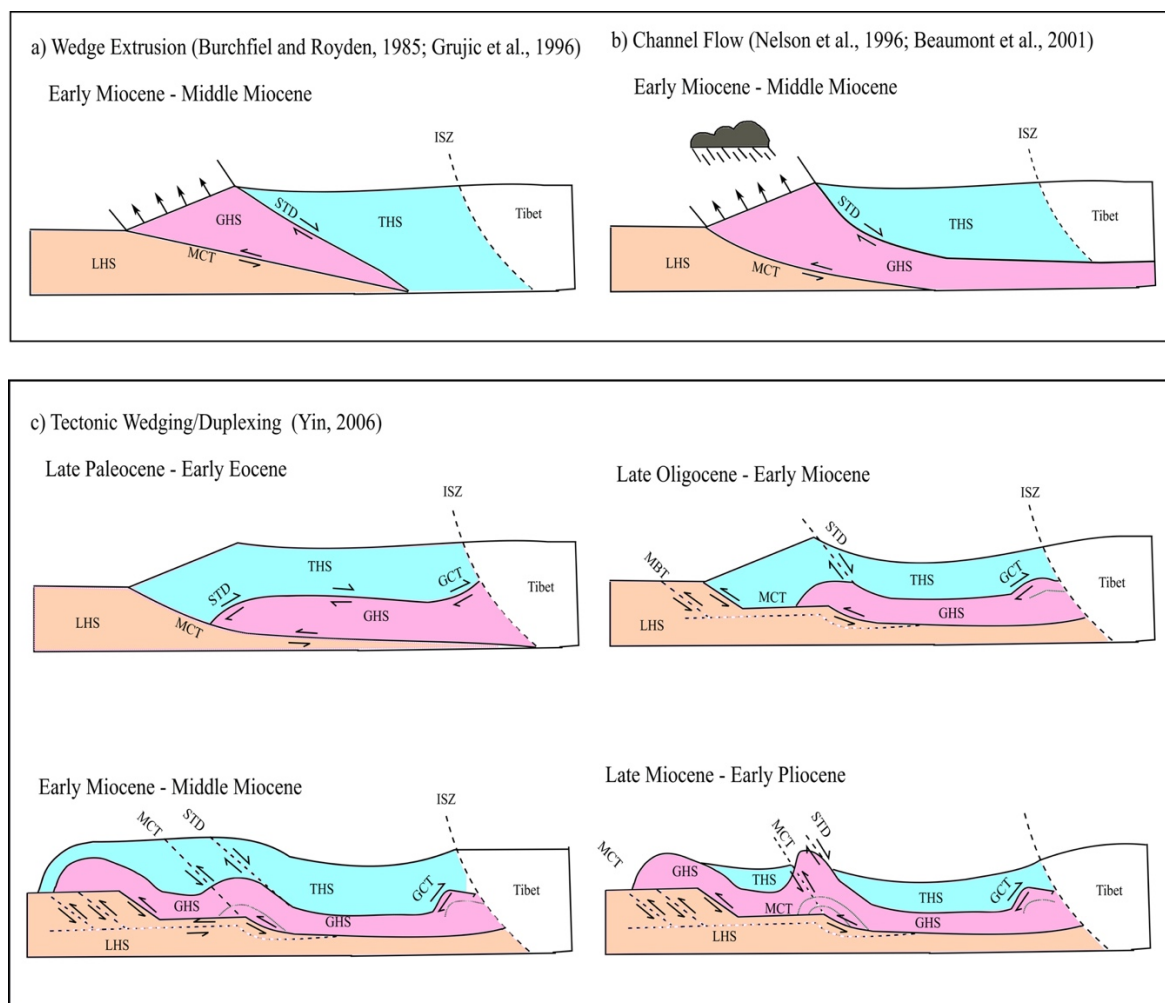
Figure 1.4. *Kinematic models of the evolution of the Himalayas modified after He et al. (2016) and Yin (2006).*

These kinematic models can be grouped into two end-member models that is i) extrusion models (e.g., wedge extrusion, channel flow) and ii) duplexing models (e.g., tectonic wedging) (Figure 1.4). Extrusion-based models require rapid exhumation of GHC by the coeval motion of the MCT and STD with significant out-of-sequence deformation. In contrast, duplexing models involve accretion of forward-moving sole thrusts or basal shear zones and subsequent crustal-scale thrust duplexing leading to transfer of materials from the subducting plate to the overriding wedge. It is important to note that these models are not mutually exclusive (He et al., 2016) because materials from the down-going plate can be accreted due to duplexing and extruded later by the channel flow. Finding the dominant mode of deformation, that is either lateral extrusion or duplexing, is critical to understand the present deformation mechanism in the Himalayas. Studies showing evidence for an up-dip merger of the MCT-STD in central Himalaya (He et al., 2016, 2015)

and the dominant role of crustal-scale doming in Zanskar Himalaya and Himanchal Himalaya (Yu et al., 2015; Robyr et al., 2006) support duplexing models.

1.2 Crustal structure

1.2.1 Western Tibet, Pamir-Hindu Kush

During the last three decades, in addition to controlled source seismic experiments, several broadband seismological investigations have been performed to study the crust and mantle velocity structure of the Himalaya-Tibet region using earthquake waveform, ambient noise, and receiver function (Nelson et al. 1996; Owens & Zandt 1997; Wittlinger et al., 2004; Galvé et al., 2006; Rai et al., 2006; Nábělek et al., 2009; Acton et al., 2010; Chen et al., 2010; Yang et al., 2010, 2012; Zhao et al., 2011; Bao et al., 2015; Shen et al., 2016). These investigations show the progressive deepening of Moho from 40 km in India to 50−60 km beneath the Himalayas, to 70 km beneath Ladakh, and ~90 km beneath the western Qiangtang-Kunlun. Earthquakes also accompany the unusually deep Moho beneath Kunlun to a depth of 90 km (Huang et al., 2011). Further north, Moho has been mapped at 44−60 km in the Tarim Basin and 55−60 km beneath the Tian Shan. The sedimentary cover in the Tarim basin ranges from Proterozoic to Neogene age, with variable thickness from a maximum of up to 15 km in the depression center to 5 km in the central uplift area (Jia et al., 1997).

Seismic data from western Tibet reveal significant segmentation of the crustal structure beneath mapped tectonic boundaries (Zhang et al., 2014), questioning the idea of laterally flowing mobile lower crust. This view is contradicted by Gilligan et al. (2015), who investigated the crustal structure of western Tibet (76−85°E), modeling receiver function and surface wave data jointly. In the middle/lower crust (20−40 km), shear wave velocity in Tibet is anomalously low and interpreted to indicate the presence of partial melts (Owens & Zandt, 1997, Makovsky & Klemperer, 1999, Yang et al., 2012). Continuity of partial melts of the Tibetan crust to the west of the Karakoram and the vertical extent of Karakoram fault is a subject of debate (Leech, 2008; Caldwell et al., 2009; Searle, 2015).

Between 2008 and 2018, several seismological experiments were made to study earthquake patterns and lithospheric structure of the Hindu Kush-Pamir region (Mechie et al., 2012; Sippl et al., 2013; Schurr et al., 2014; Feld et al., 2015; Kufner et al., 2016, Li et al., 2018). These studies reveal distinct low Vp (4.2-5.2 km/s) and high Vp/Vs ratio in the upper crust of Tadjik Basin compared to the high Vp and low Vp/Vs ratio in the Pamir-Tian

Shan, and Hindu Kush area. With a roughly 40 km thick crust, the Tadjik Basin has a sedimentary thickness of 6 km in the north and 15 km in the eastern and southern parts. The basement of Tadjik Basin seems to underthrust the Hindu Kush crustal rocks in the south. Li et al. (2018) imaged a large-scale low-velocity anomaly in the crust at 20–50 km depth in the Pamir overlain by a high-velocity anomaly. The high-velocity zone collocates with the exposed gneiss domes, suggesting linkage among the crustal deformation, partial melting, and exhumation.

1.2.2 Ladakh-Kohistan arc

As discussed earlier in section 1.1.4, Kohistan and Ladakh arcs provide building blocks of the evolution of the continental crust. Seismic structures of active island arcs are reviewed in Calvert (2011). The crustal thickness of island arcs shows a significant variation (10-35 km) due to different amounts of extensions during arc rifting. The crust-mantle transition zone can be broad (up to 4-10 km). In contrast, continental crusts, except active orogens or rifts, show sharp Moho transition (< 2 km) (Christensen & Mooney, 1995). At upper crustal depths (< 10 km), the seismic velocity of island arcs broadly follows continental crust values (Vp ~5-6 km/s), whereas, beyond 10 km depth, island arcs exhibit high seismic velocities than continental crusts representing a predominant mafic rock (Calvert, 2011).

The crustal structure of Kohistan and Ladakh arcs is mainly derived from thermodynamic modeling and laboratory measurements of exposed rocks in Kohistan (Jagoutz & Klemen, 2015; Jagoutz & Behn, 2013; Clift et al., 2002; Almqvist et al., 2013) and a few geophysical experiments primarily conducted across the eastern Ladakh (Rai et al., 2006, 2009; Caldwell et al., 2009; Priestley et al., 2019). These studies indicate an absence of a sharp Moho under Kohistan. The crustal thickness from receiver function modeling ranges from 60 to 70 km (reviewed in Priestley et al., 2019). The lower crust (beyond 40 km depth) under the Kohistan arc has unusually high density above a relatively low-density upper mantle (Jagoutz & Klemen, 2015; Jagoutz & Behn, 2013). This has been interpreted to represent a density-unstable lower crust that undergoes subsequent modification via foundering, resulting in a typical continental crust of thickness ~ 40 km (Jagoutz & Behn, 2013).

Despite similarities with the Kohistan arc, the Ladakh shows differences in tectonic processes (Burg, 2006) indicated by a volumetrically large volcanic and sedimentary unit with increasing continental signature (Rolland et al., 2000; Burg, 2011). Low seismic

velocities at mid-crustal depths (Caldwell et al., 2009) and high seismic attenuation (Rai et al., 2009) indicate a melt-dominated crust of thickness reaching up to ~ 75 km (Rai et al., 2006).

1.2.3 Northwest Himalaya

The tectonic process responsible for the development of Himalayan topography include the transfer of Indian crustal material to Himalayan wedge by laterally extruding melt channel (Nelson et al., 1996; Beaumont et al., 2001, 2004) and/or crustal-scale thrust duplexing (Yin, 2006; Gao et al., 2016; Guo et al., 2017), and loss of downgoing Indian crust by subduction (Capitanio et al., 2010) or eclogitization of mafic Indian crust and subsequent underplating beneath Tibet (Monsalve et al., 2008; Le Pichon et al., 1992; Sapin & Hirn, 1997; Nábělek et al., 2009). South of the Himalayan front (MFT), the Indian crust has a uniform internal structure with a crustal thickness of ~ 42 km and ~ 48 km near the southern and northern boundary of the Foreland basin, respectively (Gilligan & Priestley, 2018; Rai et al., 2006). Within the Himalayan range, the crustal thickness increases from ~ 50 km beneath the Lesser Himalaya to 60-65 km beneath the Tethys Himalaya (Nábělek et al., 2009; Rai et al., 2006). The seismic structure of the overlying wedge is defined by a low Vp/Vs ratio (~ 1.65) compared to the high Vp/Vs ratio of the underthrusting crystalline crust (> 1.73) (Monsalve et al., 2008). Beneath the Tethys Himalaya and ISZ, the Indian crust exhibits mantle velocities (Vs > 4.4 km/s, Vp ~ 8.4 km/s) commonly attributed to eclogite grade metamorphism (Monsalve et al., 2008; Sapin & Hirn, 1997; Nábělek et al., 2009).

The current understanding of the crustal structure of the Himalayas as discussed above is largely based on the geophysical studies from Nepal and surrounding areas (e.g., Hi-Climb, INDEPTH, and HIMNT experiments). Along strike variation in crustal structures and applicability of Himalayan kinematic models in the western Himalaya are poorly understood due to lack of similar scale studies. In the last decade, seismic experiments in the western Himalaya have shade light on the gross geometry of Moho discontinuity and the MHT (Caldwell et al., 2013; Hazarika et al., 2017; Rai et al., 2006; Mir et al., 2017; review of Priestley et al., 2019; Kanna & Gupta, 2020, 2021). The surface wave dispersion analysis in northwest Himalaya indicates a continuous low shear wave velocities (with 7-17 % velocity reduction) at mid-crustal depth (~ 30 km) from Tethyan Himalaya to Tibet plateau (Caldwell et al., 2009). Coupled with high conductivity zones (Arora et al., 2007). This ductile zone is believed to represent an active channel flow. Recent shear wave velocity variation data derived from teleseismic modeling show high velocity (Vs ~ 3.9 – 4.4 km/s)

eclogite bearing Indian lower crust underthrusting Tibet plateau (Kanna & Gupta, 2020, 2021).

1.2.4 E-W extension

A review of geodetic data sets and fault plane solutions in the Himalaya-Tibet region reveals the pattern of ongoing active deformation. The crustal shortening is limited to the areas bounding the Tibetan plateau, essentially the sedimentary basins (e.g., Tarim, Qaidam, Sichuan) in the north and the Himalayan front in the south (Molnar & Lyon-Caen, 1989; Bai et al., 2017; Styron et al., 2011). This shortening is reflected by northward underthrusting of Indian crust and southward underthrusting of Asian crust, where earthquakes are distributed throughout the crust with reverse faulting. Within the interior of the Tibetan plateau, the seismicity is restricted to the upper crust only, and the deformation exhibits a dominant eastward extension, which is accommodated by north-south trending rift zones, and northeast and northwest striking strike-slip faults (Armijo et al., 1986; Taylor & Yin, 2009).
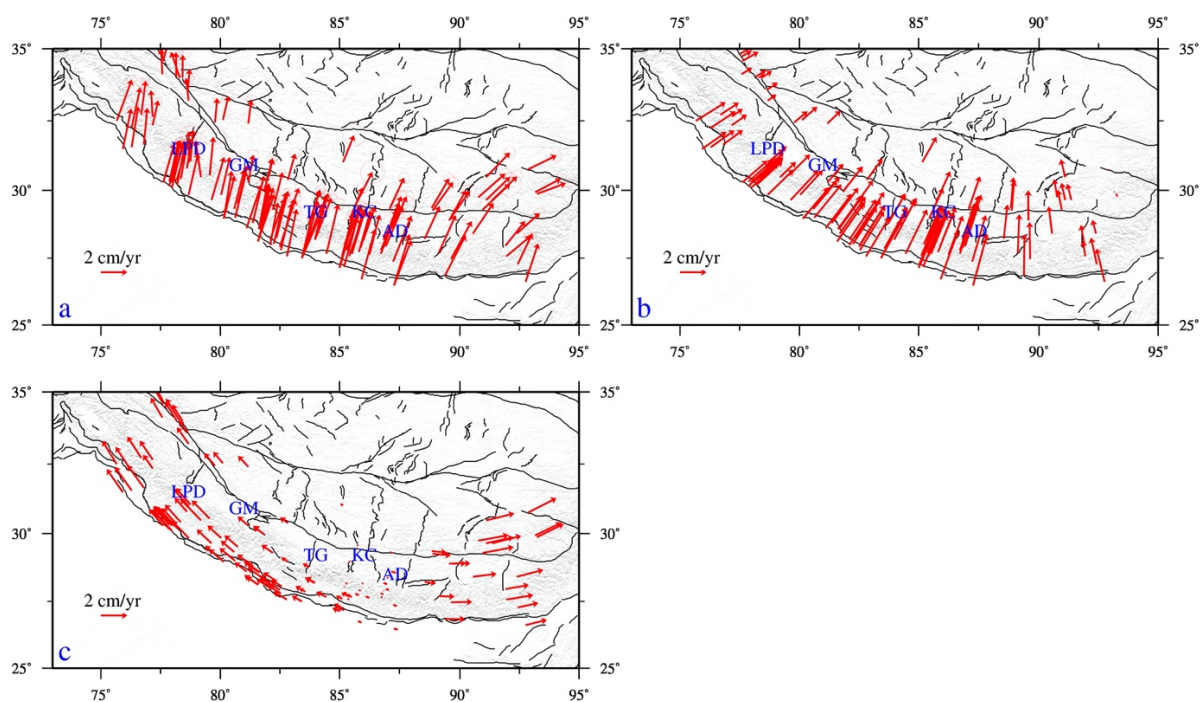
Figure 1.5. *Himalaya-Tibet convergence from GPS velocities after Styron et al. (2011). (a) GPS velocities of the Indian plate relative to stable Eurasia. (b) Arc-normal component of GPS velocities. (c) Arc parallel component of GPS velocities. LPD-Leo Pargil dome; GM-Gurla Mandhata; TG-Thakkhola graben; KC-Kung Co rift; AD-Ama Drime massif.*
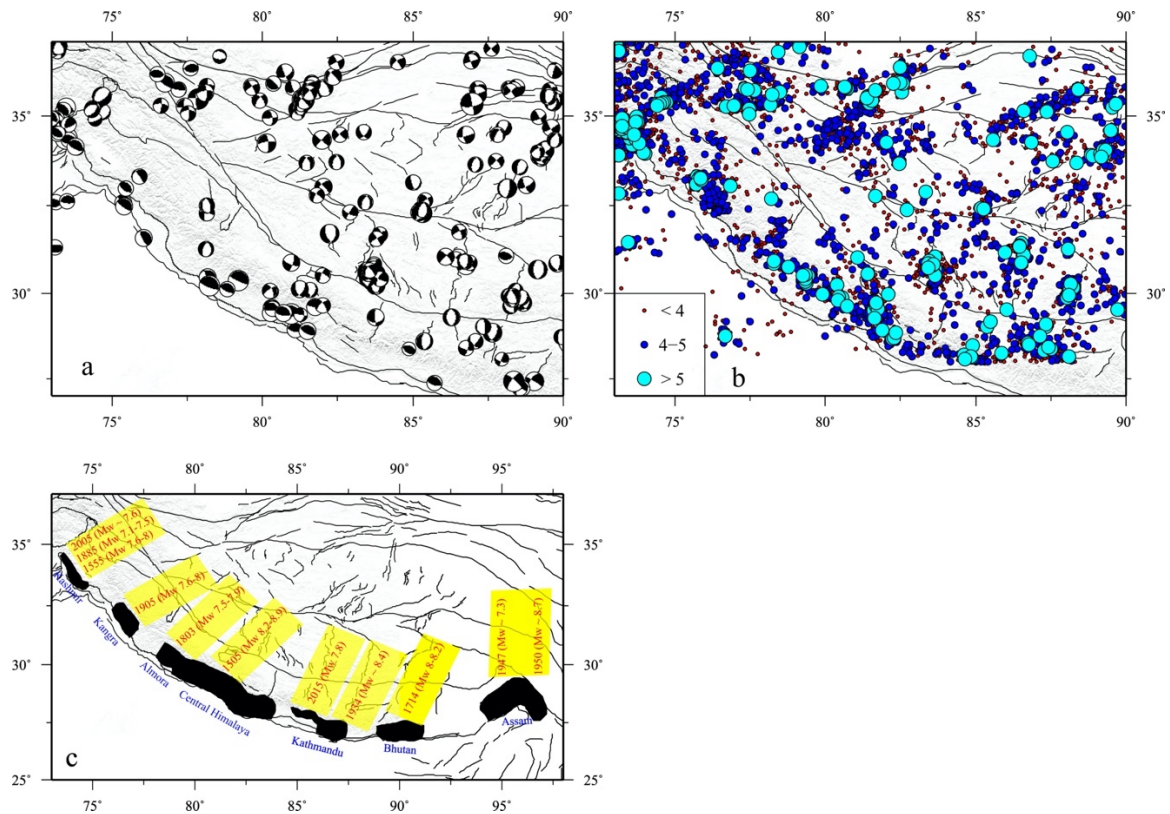
Figure 1.6 *(a) Fault plane solutions obtained from the Global CMT Catalog. (b) Seismicity (ISC reviewed catalog, Mw > 3.2; https://doi.org/10.31905/D808B830). (c) Historical seismicity after Bilham (2019).*

The large-scale extension of the Himalaya-Tibet orogen is not just limited to the plateau's interior. GPS measurements of the Himalayan arc show that the plate motion is purely arc normal in eastern Nepal (Figure 1.5a), and the convergence becomes more oblique towards the western and eastern Himalaya (Styron et al., 2011; Murphy et al., 2010). This obliquity of the Indo-Himalayan convergence provides evidence of arc-parallel extension in the Himalayan arc. Although the arc-normal convergence is consistent throughout the Himalayan arc, the arc-parallel extension increases westward and eastward from central Nepal (Styron et al., 2011) (Figure 1.5a,b). This extension is accommodated by several arc-perpendicular normal faults documented in the vicinity of major domes and grabens such as Tso Morari (TM) and Leo Pargil dome (LPD) in northwest Himalaya, Gurla Mandhata (GM) complex at the eastern termination of the Karakoram Fault (KKF), Thakkhola Graben (TG) in central Himalaya, and Kung Co rift (KC) and Amma Drime (AM) complex further east (Murphy & Copeland; 2005; Thiede et al., 2006). In northwest Himalaya, Hintersberger et al. (2010) documented pervasive E-W extension by mapping several N-S-striking normal faults in the hanging wall of the north dipping STD. Apart from

the thrust dominated earthquakes following the high Himalayan front, a narrow swath (77.5-79E) of shallow (< 20 km) earthquakes with normal faulting (Figure 1.6a, b) between the Tso Morari dome in the north to the STD in the south provide additional evidence of a large-scale extension in the northwest Himalaya (Hintersberger et al., 2010, 2011; Molnar & Lyon-Caen, 1989). The timing of the extension in the Himalayas, as well as the Tibet plateau, ranges from 22-10 Ma (middle Miocene), which is coeval with the motion of the MCT and STD (Styron et al., 2011).

1.2.5 Geometry of the MHT

A long-standing view is that the MHT contains a kink or steep ramp, and the mountain grows as rocks are forced upward over this ramp. Earlier seismological studies show clustering of the moderate-sized earthquakes along the front of the Higher Himalaya at a depth of 10−20 km below sea level. These earthquakes are believed to occur because of the mid-crustal ramp in the MHT, where stress builds up around an asperity during the inter-seismic period (Ni & Barazangi, 1984). Large earthquakes (such as the 1897 Mw 8.2, and the 1950 Mw ~8.5-8.7 Assam earthquakes, the 1905 Mw 7.9 Kangra earthquake, the 1934 Mw 8.4 Bihar-Nepal earthquake, and the 2015 Mw 7.8 Gorkha earthquake) (Figure 1.6c) are proposed to nucleate close to the ramp and release energy several kilometers southward below the surface of the Himalaya. Therefore, accurate mapping of the MHT and the ramps are critical to model the Himalayan growth, predict earthquake nucleation, and build appropriate earthquake hazard scenarios (Bilham et al., 2017; Stevens & Avouac, 2015).

The MHT forms a shallow flat detachment at 5−10 km depth beneath the Lesser Himalaya, joining the mid-crustal ramp at about 10−20 km depth near the contact of the Lesser and Higher Himalaya. Further north beneath the Tethys Himalaya and Southern Tibet, the MHT is nearly flat. The shallower flat portion of the MHT is fully locked (no-slip zone) due to friction, while the deeper flat part of MHT is fully unlocked (aseismic creep). The ramp is the transition zone of inter-seismic decoupling (Bilham et al., 2017), whose width (and dip of the ramp) controls the capacity of the MHT to store elastic strain energy and release it in the form of possible large earthquakes.

Seismologists mapped MHT exploiting the impedance contrast because of the distinct geophysical properties of the underthrusted Indian crystalline crust and the overlying crushed rocks forming the Himalayan wedge (Caldwell et al., 2013). The other diagnostic features are low velocity (Nábělek et al., 2009; Acton et al., 2011; Kanna &

Gupta, 2020, 2021) and a high electrical conductive zone (Rawat et al., 2014) due to water released from underthrusting sediments on top of the Indian crust. Analysis of results from seismic experiments suggests significant variation in geometry and property of the MHT along and across the strike of the Himalaya (reviewed in Priestley et al., 2019). In central Himalaya, the MHT is mapped as a north dipping structure beneath Higher Himalaya (Nábělek et al., 2009; Schulte-Pelkhum et al., 2005; Acton et al., 2011), which continues to 30-40 km depth beneath Tethys Himalaya (Makovsky et al., 1996; Hauck et al., 1998) and ~ 60 km depth further north (Guo et al., 2017). In Garhwal Himalaya, Caldwell et al. (2013) imaged the MHT with the negative impedance contrast (dip 2° at ~ 10 km depth) below the lesser Himalaya while its deeper flat part has positive impedance contrast (dip 4° at ~ 20 km depth) below the Higher Himalaya. They mapped a gentle mid-crustal ramp with a dip of 10−25° between 10−20 km depth beneath the MCT zone. Further west in northwest Himalaya, there is weak evidence for the MHT ramp (Priestley et al., 2019). A gently north dipping structure at a depth of 8-10 km in Siwalik sediments to 14-16 km in Kashmir valley (Mir et al., 2017) to ~ 27 km in the Zanskar Tethys Himalaya (Hazarika et al., 2017), and a broad interseismic coupling width (~160 km, Figure 1.7) marks the gross geometry of the MHT in the northwest Himalaya.
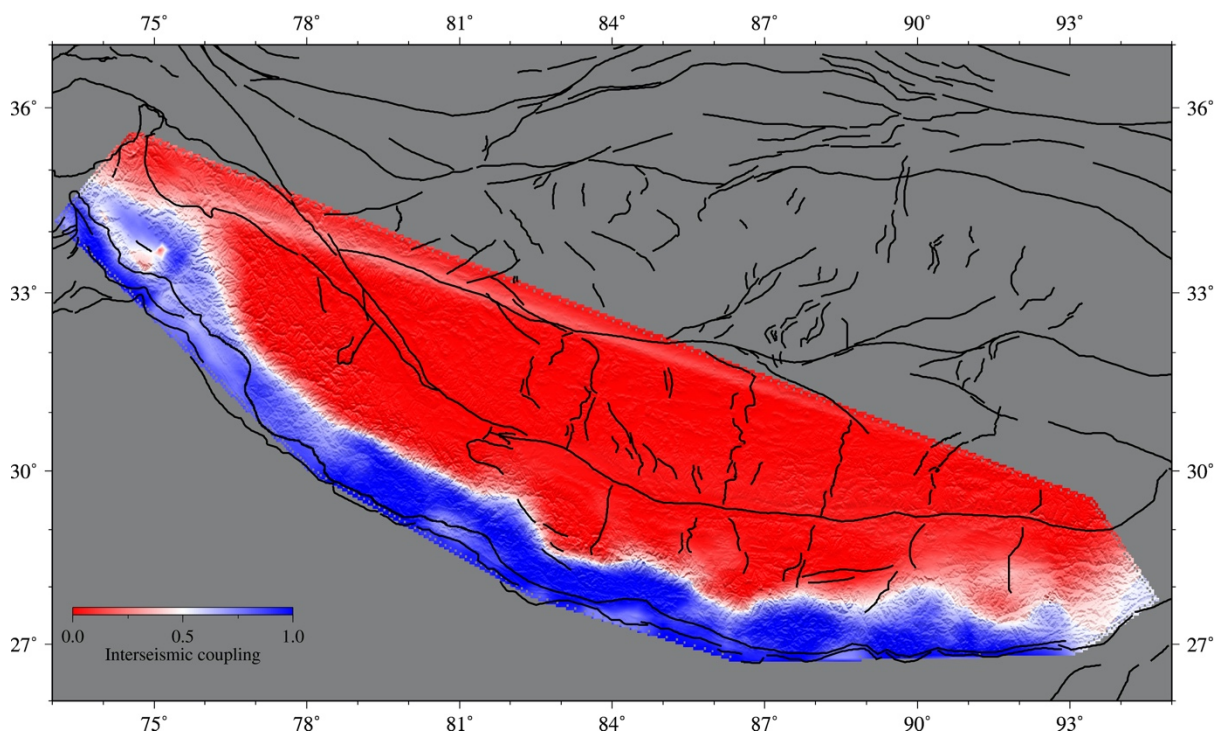
Figure 1.7. *Interseismic coupling map of the Main Himalayan Thrust (MHT) after Stevens and Avouac (2015).*

1.3 Aims of the Thesis

The detailed geological and geophysical background presented above shows the presence of large-scale lateral variations in the crustal structure as well as surface geological features of the India-Asia convergence zone. Continuity and applicability of geodynamic and kinematic models proposed so far to the western part of the orogen comprising western Himalaya-Tibet, Ladakh-Kohistan arc, Pamir-Hindu Kush, and Karakoram regions remain sketchy. These models are primarily derived from experiments conducted in the central and eastern part of the India-Asia orogen, and there is a lack of similar scale studies are in the western part of the orogen. Although there have been several recent attempts to image the crustal structure in western Tibet-Himalaya (Gilligan et al., 2015; Gilligan & Priestley, 2018; Kumar et al., 2019), and Pamir-Hindu Kush (Li et al., 2018; Schneider et al., 2013, 2019), coherent knowledge of the deep crustal structures connecting western Tibet with Pamir-Hindu Kush, Ladakh-Kohistan arc, and the Karakoram is still unknown. Similarly, the nature of the Himalayan wedge and the underthrusting northern Indian margin under the western Himalaya are least explored.

In this thesis, we provide a crustal shear wave velocity model (up to 100 km depth) of the western segment of the convergence zone with improved lateral resolution (~30-50 km) using fundamental mode Rayleigh wave group velocity dispersion data obtained from ambient noise and earthquake waveform analysis between period 5 to 60 s. We have used cutting-edge imaging tools based on Bayesian inversion resulting in a data-driven velocity model. This thesis sheds light on some of the important issues, which are:

1. Distribution and connectivity of mid-crustal low-velocity zones and their implication in the large-scale deformation of the crust.

2. Nature and northern extent of the underthrusting Indian lower crust beneath the Tibetan plateau.

3. Depth extent of major transform faults e.g., the Karakoram Fault, and their role in accommodating total crustal shortening.

4. Nature and geometry of the Main Himalayan Thrust (MHT). Study of the possible segmentation of the MHT geometry in western Himalaya.

5. Crustal structure beneath the Ladakh-Kohistan arc, and its relation to the rest of the Tibetan plateau.

1.4 Structure of the Thesis

The thesis is structured in a way that it provides sequential discussions on the methodology and data used for the dispersion analysis with a detailed description of the estimation of the uncertainties, and sensitivity of various parameters associated with the final shear wave velocity model. The key issues raised in the previous section are further addressed with an elaborate discussion on their broad implications in the ongoing deformation of the India-Asia convergence zone. Subsequent chapters of this thesis are outlined as follows:

Chapter 2 provides detailed background on the basic theory and methodology behind tools used in data processing and inversion. We start with a discussion on the theoretical development of Green's function and its retrieval using ambient noise analysis. Furthermore, we discuss in depth the algorithm used to measure group/phase velocity dispersion. The method of inversion, which is used to create continuous dispersion maps by the tomographic method followed by the estimation of shear velocity-depth model, is discussed with a comparison between the least square-based regularized inversion and the probabilistic method of the Bayesian inversion. We end with a description of the broadband seismic data used in this study and its preliminary analysis.

Chapter 3 presents first-order group velocity maps between periods 5 to 60 s with a lateral resolution of 30-50 km using the Bayesian Trans-Dimensional Tree tomography. Group velocities at each grid-nodes are further inverted using the Hierarchical Bayesian inversion and subsequently interpolated to produce the 3-D shear velocity model at a grid interval of $0.5\times0.5°$. In addition, we discuss the robustness of inverted models using several synthetic experiments which include tests for the prior sensitivity, ability of the data to image mid-crustal low-velocity layers, and the crustal-mantle velocity trade-offs. With the help of the shear wave velocity model, we map the lateral distribution of the wide-spread mid-crustal low-velocity zones (LVZs) and discuss their relationship with surface geology. Furthermore, we discuss the northern extent of the underthrusting Indian lower crust by mapping high-velocity features (Vs > 4 km/s) above the Moho. The depth extent of the Karakoram Fault is estimated by examining the continuity of the LVZs across the fault.

CHAPTER 1

Chapter 4 focuses on the crustal structure of the western Himalaya and Ladakh-Kohistan arc. For this purpose, we recalculate group velocity maps from period 5 to 60 s at a grid-interval of 0.25×0.25°. The 1-D inversion of individual grid-point group velocities covering grid-nodes of western Himalaya and Ladakh-Kohistan arc is further interpolated to provide the 3-D shear wave velocity model at the grid-interval of 0.25×0.25°. The velocity model efficiently captures the large-scale lateral variation of the crustal structure along the western Himalayan arc and the Ladakh-Kohistan arc. We present in-depth discussions on the nature of the crustal structure in terms of the geometry of the MHT, structure of the down-going Indian plate, and the Himalayan wedge. The crustal structure beneath the Ladakh-Kohistan arc is further discussed and compared with southern Tibet.

Chapter 5 presents a high-resolution shear wave velocity profile across the Garhwal Himalaya. We use a linear array of 26 broadband seismographs with an average inter-station distance of ~10 km between the Main Frontal Thrust (MFT) and the South Tibetan Detachment (STD) and perform ambient noise analysis to measure phase velocity dispersion from 3 to 23 seconds. Using a regularized inversion scheme, we perform the phase velocity tomography followed by the 1-D inversion to create the crustal shear wave velocity profile along the array length. The inferred velocity structure provides new insights on the geometry of the MHT in the Garhwal Himalaya.

Finally, in Chapter 6, we conclude important findings of this thesis.

CHAPTER 2

Seismic Imaging Methodology and Preliminary Data Analysis

This chapter discusses (1) the basic theory for retrieval of Green's function from ambient noise records at seismographs, (2) methodology for the extraction of surface wave dispersion from ambient noise and earthquake waveforms, (3) travel-time inversion schemes (linearized subspace inversion (e.g., FMST of Rawlinson & Sambridge, 2003) and the Trans-dimensional Tree (TDT, Hawkins & Sambridge, 2015)) of source-receiver /receiver- receiver Rayleigh wave group velocity dispersion measurements to generate 2-D velocity maps at different periods, and finally (4) Bayesian Trans-dimensional inversion approach for shear velocity-depth imaging (Bodin et al., 2012b) at grid nodes of 2-D maps in the study region. The second part of the chapter presents a detailed description of broadband seismic data and its preliminary analysis as followed in this study.

2.1 Elastodynamic Green's Function

A displacement field due to a unit impulse source is the elastodynamic Green's function, denoted by G_{in} (x, t; ξ, τ) when the unit impulse is applied in the *n*-direction at x $= \xi$, and $t = \tau$. The Green's function satisfies the equation of motion (equation A2.8)

$$\rho \frac{\partial^2}{\partial t^2} G_{in} = \delta_{in}\delta(x - \xi)\delta(t - \tau) + \frac{d}{dx_j}\left(C_{ijkl} \frac{d}{dx_l} G_{kn}\right). \qquad 2.1$$

Using initial conditions (i.e. G and $\dot{G}$ are zero for $t \leq \tau$ and x $\neq \xi$), the function G can be uniquely determined by imposing different boundary conditions on a surface S. For a time-independent boundary condition (e.g., rigid surface S), the time origin in the equation 2.1 can be shifted indicating a time reciprocity of the Green's function (G)

$$G_{in} \text{ (x}, t; \xi, \tau) = G_{in} \text{ (x}, t - \tau; \xi, 0) = G_{in} \text{ (x}, -\tau; \xi, -t).$$

For a traction-free boundary condition on S (i.e., homogenous boundary condition), we can use the Betti's theorem (equation A4.9) to prove spatial reciprocity of the Green's function. Consider two systems with a unit impulse f applied in *m*-direction (at x $= \xi_1$, and $t = \tau_1$) and another unit impulse g applied in *n*-direction (at x $= \xi_2$, and $t = \tau_2$) such that

$$f_i(\text{x}, t) = \delta_{im}\delta(x - \xi_1)\delta(t - \tau_1) \text{ and } u_i(\text{x}, t) = G_{im} \text{ (x}, t; \xi_1, \tau_1),$$

$$g_i(\text{x}, t) = \delta_{in}\delta(x - \xi_2)\delta(t + \tau_2) \text{ and } v_i(\text{x}, t) = G_{in}(\text{x}, t; \xi_2, -\tau_2).$$

Substituting above expressions in the Betti's theorem with causality (equation A4.9), we get

$$\int_{-\infty}^{\infty} dt \iiint_v (G_{im}(\text{x}, t; \xi_1, \tau_1) \cdot \delta_{in}\delta(x - \xi_2)\delta(\tau - t + \tau_2))dV$$

$$= \int_{-\infty}^{\infty} dt \iiint_v (G_{in}(\text{x}, \tau - t; \xi_2, -\tau_2) \cdot \delta_{im}\delta(x - \xi_1)\delta(t - \tau_1))dV,$$

which implies

$$G_{nm}(\xi_2, \tau + \tau_2; \xi_1, \tau_1) = G_{mn}(\xi_1, \tau - \tau_1; \xi_2, -\tau_1).$$

With $\tau_1 = \tau_2 = 0$, we get a pure spatial reciprocity

$$G_{nm}(\xi_2, \tau; \xi_1, 0) = G_{mn}(\xi_1, \tau; \xi_2, 0),$$

and with $\tau = 0$, we have a space-time reciprocity

$$G_{nm}(\xi_2, \tau_2; \xi_1, \tau_1) = G_{mn}(\xi_1, -\tau_1; \xi_2, -\tau_2).$$

The Green's function provides a way to represent a displacement field due to a complex seismic source in terms of a simple unidirectional impulse localized in space and time. Using the Bett's theorem (equation A4.9 or equation 2.2) with a Green's function for one of the displacement fields, a representation theorem for the other displacement field can be obtained.

$$\int_{-\infty}^{\infty} dt \iiint_v (u_i g_i - v_i f_i)dV = \int_{-\infty}^{\infty} dt \iint_S v_i T_i^u - u_i T_i^v) \, dS. \qquad 2.2$$

Considering $g_i(\text{x}, t) = \delta_{in}\delta(x - \xi)\delta(t), v_i(\text{x}, t) = G_{in}(\text{x}, t; \xi, 0)$, and $T_i^v = C_{ijkl}G_{kn,l}n_j$, equation (2.2) can be written as:

$$\int_{-\infty}^{\infty} dt \iiint_v (u_i(x, t)\delta_{in}\delta(x - \xi)\delta(\tau - t) - G_{in}(\text{x}, \tau - t; \xi, 0)f_i(x, t))dV$$

$$=$$

$$\int_{-\infty}^{\infty} dt \iint_{S} (G_{in} \ (\mathrm{x}, \tau - t; \ \xi, 0) \ T_i^u(x,t) - u_i(x,t) C_{ijkl} G_{kn,l}(x, \tau$$

$$- t; \xi, 0)n_j) \ dS \ .$$

Because $\int_{-\infty}^{\infty} dt \ \iiint_{v} (u_i(x,t)\delta_{in}\delta(x - \xi)\delta(\tau - t))dV = u_n(\xi, \tau)$, we get the following relation after applying change of variables $(x \longrightarrow \xi, t \longrightarrow \tau, \xi \longrightarrow x, \tau \longrightarrow t)$

$$u_n(x,t) = \int_{-\infty}^{\infty} dt \ \iiint_{v} (G_{in} \ (\xi, t - \tau; \ \mathrm{x}, 0) \ f_i(\xi, \tau))dV(\xi)$$

$$+ \int_{-\infty}^{\infty} dt \ \iint_{S} [(G_{in} \ (\xi, t - \tau; \ \mathrm{x}, 0) \ T_i^u(\xi, \tau))$$

$$- u_i(\xi, \tau) C_{ijkl} G_{kn,l}(\xi, t - \tau; \ \mathrm{x}, 0)n_j] \ dS(\xi). \qquad 2.3$$

Use of different types of reciprocity of the Green's function as discussed earlier, the equation 2.3 results into different forms of the representation theorems. For example, using spatial reciprocity $(G_{in} \ (\xi, t - \tau; \ \mathrm{x}, 0) = \ G_{ni} \ (x, t - \tau; \ \xi, 0)$, we get

$$u_n(x,t) = \int_{-\infty}^{\infty} dt \ \iiint_{v} (G_{ni} \ (x, t - \tau; \ \xi, 0) \ f_i(\xi, \tau))dV(\xi)$$

$$+ \int_{-\infty}^{\infty} dt \ \iint_{S} [(G_{ni} \ (\mathrm{x}, t - \tau; \ \xi, 0) \ T_i^u(\xi, \tau))$$

$$- u_i(\xi, \tau) C_{ijkl} G_{kn,l}(x, t - \tau; \ \xi, 0)n_j] \ dS(\xi).$$

2.2 Green's Function for the Wave Equation

The elastic wave equation with known impulse source (equation 2.1) transforms to the 3D Helmholtz equation in the frequency domain

$$\nabla^2 G + k^2 G = \ \delta(x - \xi),$$

where $k = \ \omega/c$ (k is the wavenumber with the angular frequency ω and the elastic wave velocity c). In spherical coordinates, the above equation is written as

$$\frac{1}{r^2} \frac{d}{dr} \left(r^2 \frac{dG(r,\omega)}{dr} \right) + k^2 G(r, \omega) = \ \delta(r),$$

$$\frac{d^2 G(r,\omega)}{dr^2} + \frac{2}{r} \frac{dG(r)}{dr} + k^2 G(r, \omega) = \ \delta(r),$$

$$\frac{d^2}{dr^2} \{rG(r, \omega)\} + k^2 \{rG(r, \omega)\} = \ \delta(r),$$

where r is the distance between the source and the receiver. For $r \neq 0$, we get

$$\frac{d^2}{dr^2}\{rG(r,\omega)\} + k^2\{rG(r,\omega)\} = 0,$$

with a generalized solution as

$$G(r,\omega) = \frac{A}{r}e^{\pm ikr}.$$

The above equation can be further expressed in time domain as

$$G(r,t) = \frac{1}{2\pi}\int_{-\infty}^{\infty} G(r,\omega)\,e^{-i\omega t}\,d\omega,$$

$$= \frac{1}{2\pi}\int_{-\infty}^{\infty} \frac{A}{r}e^{\pm ikr}\,e^{-i\omega t}\,d\omega,$$

$$= \frac{A}{r}\left[\frac{1}{2\pi}\int_{-\infty}^{\infty} e^{-i[\omega t \mp kr]}\,d\omega\right], \qquad 2.4$$

$$= \frac{A}{r}\left[\frac{1}{2\pi}\int_{-\infty}^{\infty} e^{i\omega\left[-t\pm\frac{r}{c}\right]}\,d\omega\right],$$

$$= \frac{A}{r}\delta\left(-t\pm\frac{r}{c}\right).$$

Taking $t = \tau - t$ and $r = x - \xi$, in the last part of the above equation, the Green's function for the wave equation is obtained

$$G(x,t;\ \xi,\tau) = \frac{A}{|x-\xi|}\delta\left(\{t-\tau\}\pm\frac{|x-\xi|}{c}\right). \qquad 2.5$$

The equation 2.5 is valid only for a non-attenuating medium. By substituting $c = c_o + ic_i$ in the equation 2.4, the Green's function for an attenuating medium becomes

$$G(x,t;\ \xi,\tau) = \frac{A}{|x-\xi|}\left[\frac{1}{2\pi}\int_{-\infty}^{\infty} exp\left(i\omega\left\{(t-\tau)\pm \qquad 2.6\right.\right.\right.$$

$$\left.\left.\left.\frac{|x-\xi|}{c}\right\}\right) exp\left(\pm\omega c_i \frac{|x-\xi|}{c_o^2}\right)d\omega\right].$$

2.3 Cross-Correlations of diffuse (random) wavefield

A random field where all modes are equally excited is called a diffuse wavefield. For an elastic body, a diffuse wavefield $\emptyset(x, t)$ at a position x and time t can be represented as (Lobkis & Weaver, 2001)

$$\emptyset(x,t) = \sum_{n=1}^{\infty} a_n\,u_n(x)e^{i\omega_n t}, \qquad 2.7$$

where a_n are complex modal amplitudes, ω_n and $u_n(x)$ are eigenfrequencies and eigenfunctions of real Earth, respectively. For a diffuse field, modal amplitudes are uncorrelated random variables such that

$$\langle a_n a_n^*\rangle = \delta_{nm}F(\omega_n),$$

where the left-hand side represents an average over all possible realizations, and the function $F(\omega_n)$ is related to the spectral energy density. The cross-correlation of the diffuse wavefield at two positions, x and y, is then expressed as

$$\langle \emptyset(x,t)\emptyset(y,t+\tau)\rangle = \sum_{n=1}^{\infty} F(\omega_n)\, u_n(x)u_n(y)e^{-i\omega_n\tau}.$$

2.8

If F is a constant (Lobkis & Weaver, 2001), equation 2.8 differs from an actual Green's function between x and y only by an amplitude factor F. This expression resembles the fluctuation-dissipation theorem (Kubo, 1996), which states that the two-point correlation of a diffuse wavefield over a long time is related to the Green's function between them (Van Tiggelen, 2003; Callen & Welton, 1951). For the case of arbitrary noise fields, Cox (1973) estimated the spatial correlation in equation 2.8 in terms of normalized cross-spectral density $C(r, \omega)$ between two points at distance r as:

$$C(r,\omega) \propto \frac{\sin\left(\frac{\omega r}{c}\right)}{\frac{\omega r}{c}}.$$

In time domain, this correlation function is

$$C(r,\tau) \propto \frac{1}{2\pi}\int_{-\infty}^{\infty} C(r,\omega)\, e^{-i\omega\tau} d\omega$$

$$C(r,\tau) \propto \frac{1}{2\pi}\int_{-\infty}^{\infty} \frac{\sin\left(\frac{\omega r}{c}\right)}{\frac{\omega r}{c}}\, e^{-i\omega\tau} d\omega$$

$$C(r,\tau) \propto \frac{1}{4\pi}\int_{-\infty}^{\infty} \frac{exp\left(i\omega(r/c - \tau)\right)}{i\omega r/c} d\omega$$

$$-\frac{1}{4\pi}\int_{-\infty}^{\infty} \frac{exp\left(i\omega(-r/c - \tau)\right)}{i\omega r/c} d\omega.$$

The time derivative of the last part of the above equation results

$$\frac{d}{d\tau} C(r,\tau) \propto \frac{1}{4\pi r/c}[\delta(r/c - \tau) - \delta(-r/c - \tau)].$$

2.9

Because a delta function is an even function, the equation 2.9 can be expressed as

$$\frac{d}{d\tau} C(r,\tau) \propto \frac{1}{4\pi r/c}[\delta(\tau - r/c) - \delta((\tau + r/c))],$$

2.10

$$\frac{d}{d\tau} C(r,\tau) \propto [G^-(r,-\tau) - G^+(r,\tau)] \text{ (from equation 2.5)},$$

where G^- and G^+ correspond to the ant-causal and causal Green's function.

Equation 2.10 is the time derivative of the cross-correlation function between two points in a diffuse field that corresponds to the Green's function between them. This

theorem is a manifestation of the fluctuation-dissipation theorem (Van Tiggelen, 2003; Callen & Welton, 1951) and has been successfully applied to extract the Green's function in ultrasonics (Weaver & Lobkis, 2001; Lobkis & Weaver, 2001), helioseismology (Rickett & Claerbout, 2000; Duvall et al., 1993), marine acoustics (Roux et al., 2003; Godin, 2007), and seismic coda (Campillo & Paul, 2003; Hennino et al., 2001).

2.4 Application of diffuse cross-correlation to ambient seismic noise

Random fluctuations recorded on a seismograph during a seismically quiet period (i.e., no earthquakes) are known as seismic ambient noise. The frequency range of the ambient noise field ranges from 10^{-3} Hz to 100 Hz. Below 1 Hz, oceanic gravity waves are the dominant source of this field (Yang & Ritzwoller, 2008; Hasselmann, 1963). Based on frequency ranges, they are further categorized into i) seismic hum ($10^{-3} - 0.02$ Hz), ii) primary microseism ($0.02-0.1$ Hz), and iii) secondary microseism ($0.1-1$ Hz) (Figure 2.1). The primary microseism is believed to be generated due to a direct interaction between ocean swells and shallow seafloor, whereas the secondary microseism is generated by a nonlinear interaction between two primary microseisms of the same frequency traveling in the opposite direction (Hasselmann, 1963; Longuet-Higgins, 1950). For the long-period ambient noise (seismic hum), the Earth's continuous background free oscillations are dominant sources (Nawa et al., 1998). However, long period interactions of ocean and atmosphere may also generate seismic hum signals (Rhie & Romanowicz, 2004). In the microseism band, two strong peaks of high-frequency noise are observed, one about 0.15 Hz (7 s) in the secondary microseism and another about 0.07 Hz (14 s) in the primary microseism. The long period seismic hum peaks at about ~ 0.01 Hz (100 s). Above 1 Hz, seismic ambient noise wavefields are primarily generated by human activities (Bonnefoy-Claudet et al., 2006).

The distribution of seismic ambient noise sources on the Earth at a given time may not satisfy the randomness criteria for Green's function retrieval, as discussed earlier. However, it has been demonstrated that ambient noise sources randomize when taken over a long time (Shapiro et al., 2005; Sabra et al., 2005). Consequently, ambient noise analysis has been successfully applied to image crust and upper mantle structures in Europe (Yang et al., 2007), Australia (Saygin & Kennett, 2010), Tibet (Shen et al., 2016), India (Saha et al., 2020), and United States (Ritzwoller et al., 2011). Froment et al. (2010) studied the effect of the non-isotropic distribution of ambient noise sources on time-domain cross-

correlations. They found the relative error on measured travel-time in the order of 1 %, which may affect seismic monitoring studies but not seismic tomography (Yao & Van Der Hilst, 2009). The application of ambient noise wavefield in seismic imaging has advantages over traditional earthquake tomography. Seismic images derived from earthquakes have limited resolution due to inhomogeneous azimuthal distribution of events and insufficient source information. In contrast, the ambient noise analysis is independent of sources and has been used to obtain high-resolution short-period tomography (Shapiro et al., 2005).

Early works of Shapiro et al. (2005) and Sabra et al. (2005) were mainly performed in microseism bands. Subsequent studies laid out ambient noise data processing workflow (Figure 2.2) to extract broadband signals (Bensen et al., 2007; Schimmel et al., 2011). The preprocessing of single-station data before performing ambient noise cross-correlation is one of the critical steps followed. This includes removing mean, trend, and instrument response followed by bandpass filtering, time-domain normalization, and spectral whitening. Time-domain normalization reduces the effect of earthquakes on cross-correlations, performed commonly by 1-bit normalization or running-absolute-mean normalization (Bensen et al., 2007). Ambient noise signals are broadened in bandwidth using spectral normalization. Preprocessed signals from two seismic stations are further cross-correlated and stacked to estimate the Green's function.
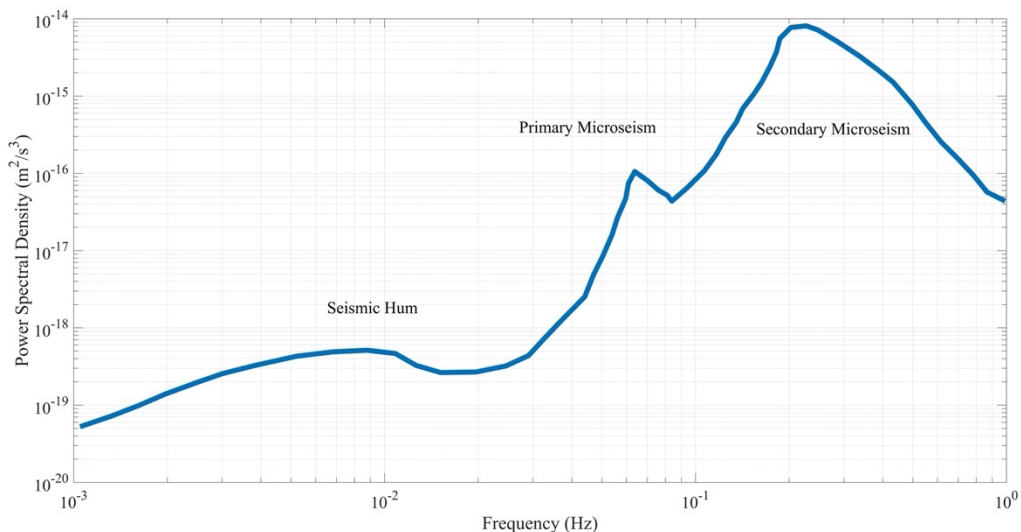
Figure 2.1 *Power spectrum of the seismic ambient noise wavefield.*

Raw Data

Remove mean, trend, instrument response
and apply band pass filter

Time-domain normalization
and Spectral whitening

Cross-correlation and Stacking

Dispersion measurement, Error analysis
and Quality control
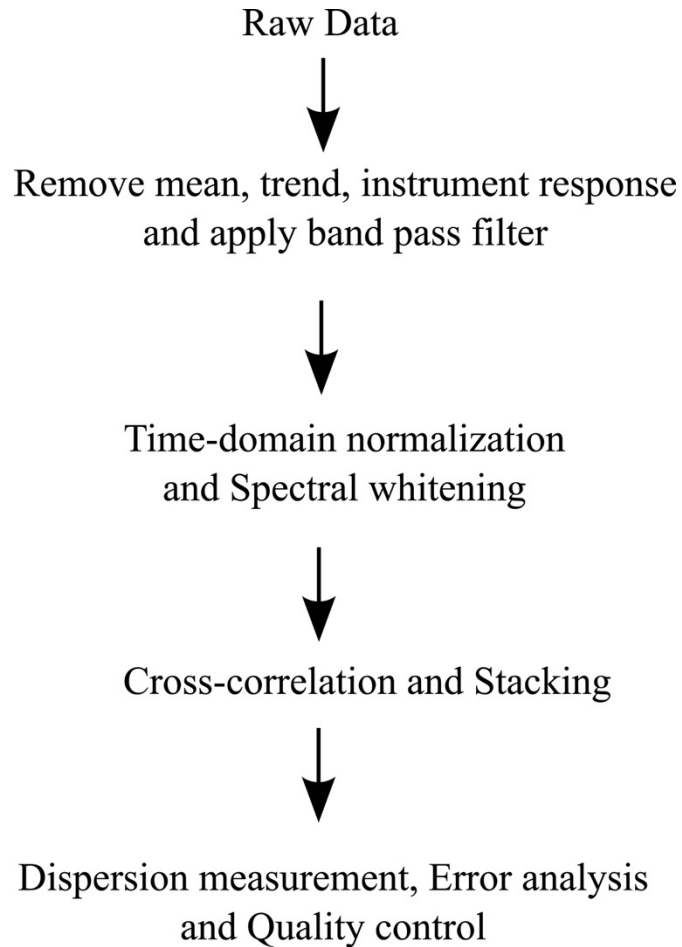
Figure 2.2 *Representation of data processing adopted in ambient noise analysis after Bensen et al. (2007).*

2.4.1 Cross-correlation and Stacking

Cross-correlation of ambient noise signals, $u_1(t)$ and $u_2(t)$, at two receivers can be classically expressed as

$$C_{cc}(\tau) = \sum_{t=t_o}^{t_o+T} u_1(t+\tau)u_2(t),$$

2.11

where cc stands for cross-correlation and τ is the lag-time. Sometimes a geometrically normalized cross-correlation (CCGN) is used to minimize the effect of amplitude variation within signals (equation 2.12).

$$C_{ccgn}(\tau) = \frac{\sum_{t=t_o}^{t_o+T} u_1(t+\tau)u_2(t)}{\sqrt{\sum_{t=t_o}^{t_o+T} u_1(t+\tau)^2 \sum_{t=t_o}^{t_o+T} u_2(t)^2}}. \qquad 2.12$$

These cross-correlation schemes (CC and CCGN) represent the sum of cross-multiplication of amplitudes, which is strongly influenced by the presence of large amplitude (e.g., earthquakes) wavelets. Hence, similar wavelets with different amplitudes have different cross-correlation values. In order to reduce this amplitude sensitivity, time-domain normalization and spectral whitening are performed before ambient noise signals are cross-correlated. Schimmel (1999) introduced Phase Cross-correlation (PCC), an alternative tool based on analytic signal theory, which uses phase coherence to detect weak coherent signals and discriminates between closely similar wavelets. Because the PCC uses phase coherence, it is amplitude unbiased. It does not require explicit preprocessing (such as time-domain normalization and spectral whitening) and has been shown to improve the signal-to-noise ratio of retrieved Green's functions (Ventosa et al., 2019; Hable et al., 2019; Acevedo et al., 2021). Schimmel (1999) and Schimmel et al. (2011) provide detailed explanations of the PCC scheme. A brief discussion of the basic theory of the PCC is given below.

For a seismic trace $s(t)$, the analytic signal $S(t)$ can be obtained using the Hilbert transform of the original trace $s(t)$ as

$$S(t) = s(t) + iH[s(t)] = A(t)e^{i\emptyset(t)} \qquad 2.13$$

where H denotes the Hilbert transform. $A(t)$ and $\emptyset(t)$ are the envelope and instantaneous phase, respectively. Using equation 2.13, an amplitude-unbiased measure of phase coherence, also called phase stack, is obtained by the sum of N analytic traces:

$$C_{ps}(t) = \frac{1}{N}\sum_{j=1}^{N} e^{i\emptyset(t)}. \qquad 2.14$$

The complex summation in the above equation involves constructive and destructive interference. For perfectly phase-coherent waves, the amplitude ($C_{ps}(t)$) is one and reduces to zero for perfectly uncorrelated phases. Schimmel (1999) use this property of the phase stack to find similarity between two signals $u_1(t)$ and $u_2(t)$ by the following summation

$$C(\tau) = \frac{1}{2N} \sum_{t=t_o}^{t_o+T} \left| e^{i\emptyset(t+\tau)} + e^{i\psi(t)} \right|, \qquad 2.15$$

where amplitude normalized analytic signals of seismic traces $u_1(t)$ and $u_2(t)$ are indicated by $e^{i\emptyset(t)}$ and $e^{i\psi(t)}$, respectively. When these two signals are correlated after one of the signals is shifted in time, the value of $C(\tau)$ is nonzero. In order to ensure that anticorrelated signals give -1, equation 2.15 is modified as following

$$C_{pcc}(\tau) = \frac{1}{2N} \sum_{j=1}^{N} \left| e^{i\emptyset(t+\tau)} + e^{i\psi(t)} \right|^{v} - \left| e^{i\emptyset(t+\tau)} - e^{i\psi(t)} \right|^{v}, \qquad 2.16$$

where the normalization $1/2N$ ensures that $C_{pcc}(\tau)$ is always between -1 and 1, with $C_{pcc} = 1$ indicating perfect correlation, $C_{pcc} = 0$ means no correlation and $C_{pcc} = -1$ is anticorrelation. The exponent v indicates the sensitivity of the PCC method where $v > 1$ improves the signal-to-noise ratio (Schimmel et al., 2011).

The cross-correlation between two points needs to be repeated over a longer time to satisfy the randomness criteria of noise distribution (Shapiro & Campillo, 2004). Hence, individual cross-correlograms are further staked to improve the SNR. Coherent signals are added constructively, while random perturbations are removed destructively after stacking. However, sometimes large amplitude signal generated noise, though they stack less coherently, may produce ambiguous phases in stacked traces. Consequently, nonlinear stacking techniques are often preferred over classical linear stacking in seismology. Schimmel and Paulssen (1997) used the concept of phase stack (equation 2.15) to obtain a set of phase coherence values of N traces at each time sample and then weighted each sample of the linear stack by that amplitude unbiased phase coherence. This nonlinear stacking further enhances SNR because phase coherence of weak coherent signals is large compared to incoherent random perturbations. Schimmel and Gallart (2007) used S-transform to obtain the analytic signal used in equation 2.15. The time-frequency decomposition following S-transform of a real signal $s(t)$ is expressed as

$$S(\tau, f) = \int_{-\infty}^{\infty} s(t)w(\tau - t, f)e^{-i2\pi ft}dt, \qquad 2.17$$

$$w(\tau - t, f) = \frac{|f|}{k\sqrt{2\pi}} e^{\frac{-f^2(\tau-t)^2}{2k^2}},$$

where $w(\tau - t, f)$ is a Gaussian window function centered at time τ with a width proportional to $|1/f|$, and the variable k ($k > 0$) controls the resolution. It has been shown that $S(\tau, f)e^{i2\pi f\tau}$ is an analytic signal for any real signal at a fixed frequency f. Hence, analogous to equation 2.15, time-frequency phase stack (tf-PS) can be written as

$$C_{tf-PS}(\tau, f) = \left| \frac{1}{N} \sum_{j=1}^{N} \frac{S_j(\tau, f)e^{i2\pi f\tau}}{S_j(\tau, f)} \right|^v . \qquad 2.18$$

Samples of a Linear stack of N traces can now be weighted by C_{tf-PS} resulting in Time-Frequency-Phase weighted stack (tf-PWS)

$$2.19$$
$$S_{\text{tf-PWS}}(\tau, f) = C_{\text{tf-PS}}(\tau, f)S_{\text{ls}}(\tau, f),$$

where $S_{\text{ls}}(\tau, f)$ is the S-transform of the linear stack. Using inverse S-transform, $S_{\text{tf-PWS}}(\tau, f)$ is converted to a time-domain stack (Schimmel & Gallart, 2007). In the last decade, several studies have shown the efficient application of the tf-PWS method improving SNR of weak coherent signals (Li et al., 2016; Zeng et al., 2017; Acevedo et al., 2021).

2.5 Dispersion measurements and quality control

2.5.1 Group and Phase velocity

For an event at a distance r and azimuth θ with respect to a seismic station, the Fourier transform of the recorded wave-train $f(t)$ $[f(t) = 0 \; for \; t < 0]$ at the station is

$$f(\omega) = \int_0^{\infty} f(t)e^{-i\omega t}dt . \qquad 2.20$$

The complex spectrum $f(\omega)$ can also be expressed in terms of its amplitude and phase

$$f(\omega) = A(r, \theta, \omega)e^{i\emptyset(r,\theta,\omega)} . \qquad 2.21$$

CHAPTER 2

The amplitude $A(r, \theta, \omega)$ depends on source characteristics (e.g., event depth, fault plane solutions), medium properties, and instrument response of the recording station. The phase function $\emptyset(r, \theta, \omega)$ is

$$\emptyset(r, \theta, \omega) = k(\omega) \cdot r + \emptyset_o(\theta, \omega) + \emptyset_i(\theta, \omega), \qquad 2.22$$

where $k(\omega)$ is the wavenumber, $\emptyset_o(\theta, \omega)$ is the source phase, and $\emptyset_i(\theta, \omega)$ is the instrument phase. Assuming zero source and instrument phase shift, inverse transform of equation 2.20 becomes

$$f(t) = \int_0^\infty A(r, \theta, \omega) \ e^{i[\omega t - k(\omega)r]} d\omega . \qquad 2.23$$

For a monochromatic wave of frequency ω_o, we have

$$\omega_o t - k(\omega_o)r = constant , \qquad 2.24$$

for all r (provided k does not depend on r). Taking differential of equation 2.24 with respect to r, we get

$$\omega_o(dt/dr) - k(\omega_o) = 0 . \qquad 2.25$$

From equation 2.25, phase velocity $C(\omega_o)$ is defined as

$$C(\omega_o) = \frac{\omega_o}{k(\omega_o)} = \frac{dr}{dt}. \qquad 2.26$$

For the definition of group velocity, we evaluate equation 2.24 in the vicinity of a frequency ω_o:

$$f(t) = \int_{\omega_o - \epsilon}^{\omega_o + \epsilon} A(r, \theta, \omega) \ e^{i[\omega t - k(\omega)r]} d\omega . \qquad 2.27$$

Group velocity corresponds to the propagation of maximum energy, and hence, the function $f(t)$ takes its maximum value when all waves in the frequency range are in phase, i.e.

$$\frac{d}{d\omega}(\omega t - k(\omega)r)_{\omega = \omega_o} = 0, \qquad 2.28$$

$$t_{\omega_o} = \left\{ \frac{dk(\omega)}{d\omega} \right\}_{\omega = \omega_o} \cdot r , \qquad 2.29$$

$$u(\omega)_{\omega=\omega_o} = \left\{ \frac{d\omega}{dk(\omega)} \right\}_{\omega=\omega_o}, \qquad\qquad 2.30$$

where $u(\omega)$ is the group velocity. A signal is dispersive if $u(\omega)$ or $C(\omega)$ changes with changing values of ω. Using equations 2.26 and 2.30, we can establish a relationship between phase velocity $C(\omega)$ and group velocity $u(\omega)$. Starting with equation 2.30, we can write

$$u(\omega) = \frac{d\omega}{dk(\omega)},$$

$$= \frac{d[C(\omega)\cdot k(\omega)]}{dk(\omega)},$$

$$u(\omega) = C(\omega) + k(\omega)\frac{dC(\omega)}{dk(\omega)}. \qquad\qquad 2.31$$

2.5.2 Group Velocity measurements

The group travel time (for a frequency band , see equation 2.27) correspond to the time at which the amplitude is maximum and is calculated using bandpass filtration, described in detail by Dziewonski et al. (1969) and Levshin et al. (1972). The method uses a filtered trace to calculate instantaneous amplitude, which further constrains the group arrival time by mapping the maxima of the amplitude. Here, we briefly describe the algorithm of group velocity measurement.

The instantaneous amplitude $a(t)$ and phase $\emptyset(t)$ can be derived by constructing an analytic signal (using equation 2.13)

$$a(t) \cdot e^{i\emptyset(t)} = f(t) + iq(t), \qquad\qquad 2.32$$

$$a(t) = [f^2(t) + q^2(t)]^{1/2}, \qquad\qquad 2.33$$

$$\emptyset(t) = tan^{-1}[q(t)/f(t)]. \qquad\qquad 2.34$$

where $q(t)$ is Hilbert transform of $f(t)$. The bandpass filtered trace is then expressed as

$$h_n(t) = \frac{1}{2\pi}\int_0^\infty f(\omega) \cdot H(\omega_n, \omega) \cdot e^{i\omega t} d\omega, \qquad\qquad 2.35$$

where $h_n(t)$ is the filtered output of the signal $f(t)$ by n^{th} spectral window. $H(\omega_n, \omega)$ is a Gaussian filter

$$H(\omega_n, \omega) = e^{-\alpha[(\omega-\omega_n)/\omega_n]^2}, \qquad\qquad 2.36$$

where α is a parameter that controls the resolving power of the filter which are determined depending upon the source-receiver distance (Levshin et al., 1972).

Substituting equation 2.36 in equation 2.35 and using equations 2.30 and 2.31, we can expand the filtered trace as

$$h_n(t) = \frac{1}{2\pi}\int_0^\infty A(\omega)\cdot cos[k(\omega)r + \emptyset_o(\omega) + \emptyset_i(\omega) - \omega t]\cdot e^{-\alpha[(\omega-\omega_n)/\omega_n]^2}d\omega \quad 2.37$$

.

$A(\omega)$ and $k(\omega)$ can be expanded in the vicinity of ω_n by Taylor series with first-order approximation:

$$k(\omega) = k(\omega_n) + (dk/d\omega)_{\omega_n}\cdot(\omega-\omega_n) = k_n + k_n'\cdot(\omega-\omega_n),$$
$$A(\omega) = A(\omega_n) + (dA/d\omega)_{\omega_n}\cdot(\omega-\omega_n) = A_n + A_n'\cdot(\omega-\omega_n). \quad 2.38$$

Assuming $\emptyset_o(\omega) = \emptyset_i(\omega) = 0$, and substituting above expressions in equation 2.37, we get

$$h_n(t) = \omega_n\cdot(\pi/\alpha)^{1/2}\{A_n cos(k_n r - \omega_n t) - [A_n'\omega_n(k_n'r - t)/2\alpha] \quad 2.39$$
$$\cdot sin(k_n r - \omega_n t)\}e^{[-\omega_n^2(k_n'r-t)^2/4\alpha]}$$

$$h_n(t) = g(\omega_n, t)\cdot cos[k_n r - \omega_n t + \epsilon_n(t)]\cdot e^{[-\omega_n^2(k_n'r-t)^2/4\alpha]}, \quad 2.40$$

where

$$g(\omega_n, t) = (\pi/2)^{1/2}\cdot\omega_n\{A_n{}^2 + [A_n'\omega_n(k_n'r - t)^2/4\alpha^2\}^{1/2},$$

and

$$\epsilon_n(t) = tan^{-1}[A_n'\omega_n(k_n'r - t)/2\alpha A_n].$$

Using equation 2.33 and 2.34, we can now write expressions for instantaneous amplitude $a(t)$ and phase $\emptyset(t)$ as

$$a(t) = g(\omega_n, t)\cdot e^{[-\omega_n^2(k_n'r-t)^2/4\alpha]} \quad 2.41$$
$$\emptyset(t) = k_n r - \omega_n t + \epsilon_n(t). \quad 2.42$$

Equation 2.41 can now be used to derive a matrix of instantaneous amplitude for a given range of group velocity and central frequencies. The algorithm can be summarized as follows:

1) Take the Fourier transform of the signal $f(t)$ and perform instrument correction
2) Make a selection of central frequencies
3) Apply narrow bandpass filter having a central frequency
4) Take inverse Fourier transform to get filtered trace in the time domain
5) Calculate the instantaneous amplitude as in equation 2.41 for a given range of group velocity values
6) Repeat steps 1 to 5 for all central frequencies and prepare a matrix of the instantaneous amplitudes
7) Map the contour of maximum amplitude to derive fundamental mode group velocities.

The method described above is obtained after the first-order approximation of the Taylor series in equation 2.38. The inclusion of higher-order terms may not guarantee the group travel time corresponding to the envelope's maximum. Phase velocity measurements can also be made by following the above algorithm using equation 2.42 by constructing a 2-D envelope function ($|\emptyset(t)|$) corresponding to a range of frequencies and phase trave-times. In addition, for earthquake and ambient noise analysis, the phase term (equation 2.42) contains inherent 2π ambiguity ($\emptyset_a = 2\pi N$, where $N = 0, \pm 1, . .$). A reference phase velocity at longer periods is often used to predict the value of N to resolve this ambiguity. This algorithm is commonly called Frequency-Time-Analysis (FTAN), which has been modified to work as an automated tool for analyzing a large number of stacked ambient noise cross-correlations and earthquakes (Levshin et al., 1972; Bensen et al., 2007).

In ambient noise analysis, the number of inter-station paths is proportional to the square of the number of seismic stations used. Therefore, efficient data quality measures are required to reject bad dispersion measurements. Constraints on the signal-to-noise ratio (SNR) and maximum period that can be reliably measured during dispersion analysis are commonly used to accept or reject measured group velocity or phase velocity at a given period (Bensen et al., 2007). It is customary to accept dispersion measurements with inter-station distance (Δ in km) of at least three times of wavelengths (λ) (Bensen et al., 2007). However, several studies have shown that this distance cut-off criteria may be relaxed (Luo

et al., 2015; Salomón et al., 2021). In order to assign uncertainties to the measured dispersion, standard deviation derived from stacking individual cross-correlogram for different seasons (Yang et al., 2007; Bensen et al., 2007) or random stacking in a bootstrapping scheme (Acevedo et al., 2019) are often used.

2.6 Travel-time prediction and Fast Marching Method

Inter-station dispersion measurements from ambient noise analysis or event dispersion obtained by methods described above are further used to obtain continuous group or phase speed maps by tomographic inversion (discussed in subsequent sections). One of the critical steps in the tomography is predicting group or phase travel-time given a source-receiver pair on a velocity field. Travel-time prediction is commonly made by solving the Eikonal equation using ray-based methods and grid-based methods. In ray-based methods, the Eikonal equation is solved as an initial value problem (also known as the "shooting method") where a ray is traced given an initial trajectory of a path. The boundary value problem of locating receiver and source is then treated as an inverse problem where the initial guess of ray trajectory is iteratively updated. Another form of a ray-based method, called the "bending method", tries to perturb an arbitrary initial ray trajectory between source and receiver until it satisfies Fermat's principle. The main challenge of ray-based methods is the nonlinearity of the ray trajectory problem, increasing with model complexity. Grid-based methods provide an alternative approach where instead of computing ray trajectory between the source and receiver, a global travel-time field at all grid points is calculated. The ray path between source and receiver is then calculated retrospectively by mapping the travel-time gradient from each receiver back to the source. Key advantages of grid-based methods include their stability in strongly heterogeneous media and computational speed. A popular grid-based method, called the Fast marching method (FMM), uses finite difference approximation to the Eikonal equation. Rawlinson et al. (2010) and Rawlinson and Sambridge (2004) provide detailed design and application of the FMM. In the following paragraphs, we first introduce the Eikonal equation and then briefly explain the FMM algorithm.

CHAPTER 2

2.6.1 Eikonal equation

The elastic wave equation in an isotropic medium is (from equation A4.4)

$$\rho\frac{\partial^2 u}{\partial^2 t} = \nabla\lambda(\nabla \cdot u) + \nabla\mu \cdot [\nabla u + (\nabla u)^T] + (\lambda + 2\mu)\nabla(\nabla \cdot u) - \mu\nabla \times \nabla \times u \,, \quad 2.43$$

where u is displacement and ρ is density, λ and μ are Lame's constants. Two terms at the beginning of the right-hand side (RHS) of equation 2.43 represent the gradient of Lame's parameter, which disappears when the variations in the scale length of λ and μ are small compared to seismic wave frequency. This approximation makes the basis of ray theory, and the wave equation is now reduced to

$$\rho\frac{\partial^2 u}{\partial^2 t} = (\lambda + 2\mu)\nabla(\nabla \cdot u) - \mu\nabla \times \nabla \times u \,. \quad\quad 2.44$$

The displacement filed u can be expressed in terms of a scalar potential $\emptyset(x, t)$ and vector potential $\psi(x, t)$ using Helmholtz theorem as

$$u = \nabla\emptyset + \nabla \times \psi \,, \quad\quad 2.45$$

where the first and second terms in RHS represent compressional waves and shear waves, respectively. Substituting equations 2.45 in 2.44 and using

$$\nabla \cdot u = \nabla \cdot \nabla\emptyset + \nabla \cdot \nabla \times \psi = \nabla^2\emptyset$$
$$\nabla \times u = \nabla \times \nabla\emptyset + \nabla \times \nabla \times \psi = \nabla^2\psi$$
$$\nabla \times \nabla \times (\nabla \times \psi) = \nabla^2(\nabla \times \psi) \,,$$

the wave equation 2.44 can be reduced to

$$\frac{\partial^2\emptyset}{\partial^2 t} = \frac{\lambda + 2\mu}{\rho}\,\nabla^2\emptyset \,,$$

$$\frac{\partial^2\psi}{\partial^2 t} = \frac{\mu}{\rho}\,\nabla^2\psi,$$

which has a general form of vector wave equation as

$$\frac{\partial^2 f}{\partial^2 t} = \frac{1}{c^2}\,\nabla^2 f \,, \quad\quad 2.46$$

where C is wave velocity. Using a harmonic solution of the form $f = A(x)e^{-i\omega[T(x)+t]}$ (where $A(x)$ and $T(x)$ represent amplitude and phase of the wave, respectively), the gradient terms in equation 2.46 can be written as

$$\nabla f = \nabla A e^{-i\omega(T+t)} - i\omega A \nabla T e^{-i\omega(T+t)} ,$$

$$\nabla^2 f = \nabla^2 A e^{-i\omega(T+t)} - i\omega \nabla T \cdot \nabla A e^{-i\omega(T+t)} - i\omega \nabla A \cdot \nabla T e^{-i\omega(T+t)}$$

$$- i\omega A \nabla^2 T e^{-i\omega(T+t)} - \omega^2 A \nabla T \cdot \nabla T e^{-i\omega(T+t)} , \qquad 2.47$$

$$\frac{\partial^2 f}{\partial^2 t} = -\omega^2 A e^{-i\omega(T+t)} .$$

Substituting 2.47 in equation 2.46, we get

$$\nabla^2 A - i\omega \nabla T \cdot \nabla A - i\omega \nabla A \cdot \nabla T - i\omega A \nabla^2 T - \omega^2 A \nabla T \cdot \nabla T + \frac{A\omega^2}{C^2} = 0 ,$$

which can be further reduced to

$$\nabla^2 A - \omega^2 A |\nabla T|^2 - i[2\omega \nabla A \cdot \nabla T + \omega A \nabla^2 T] = \frac{-A\omega^2}{C^2} .$$

The real part of the above equation is

$$\nabla^2 A - \omega^2 A |\nabla T|^2 = \frac{-A\omega^2}{C^2}, \qquad 2.48$$

which upon division by $A\omega^2$ and assuming high-frequency gives the Eikonal equation

$$|\nabla T|^2 = \frac{1}{C^2} , \qquad 2.49a$$

and the imaginary part after diving by ω gives

$$2\nabla A \cdot \nabla T + A\nabla^2 T = 0, \qquad 2.49b$$

which is known as the transport equation. As shown in equation 2.49a, the Eikonal equation states that the wavefront gradient (defined as travel-time) equals the local slowness. The direction of wave propagation becomes the direction of maximum change of the wavefront. For a defined local velocity field (C), it is possible to construct rays from a source to a receiver. The transport equation describes the amplitude of the propagating wave. Ray theory results from a high-frequency approximation where the distance over which C changes needs to be larger than the seismic wavelength.

2.6.2 Fast Marching Method

FMM algorithm developed by Sethian (1996) uses finite-difference solution to the Eikonal equation (2.49), which can also be expressed as

$$|\nabla T| = S, \qquad\qquad\qquad 2.50$$

where S is the slowness and ∇T is the gradient of travel-time. One of the key challenges to finite-difference solvers is that the gradient ∇T needs to be continuous at all grid points to ensure that the travel-time of first arrivals can be calculated. The gradient becomes discontinuous when the media involves multipathing where wavefronts intersect, and first arrivals are not guaranteed (Figure 2.3a). An alternative approach to avoid intersecting wavefronts is to use a "viscosity solution" given as

$$|\nabla T| = S + \epsilon \nabla T^2, \qquad\qquad\qquad 2.51$$

where ϵ is the smoothness parameter which produces a smooth solution as $\epsilon \to 0$. The "viscosity solution" smoothens out the shallow tail (Figure 2.3a) but preserves the discontinuity (Figure 2.3b).
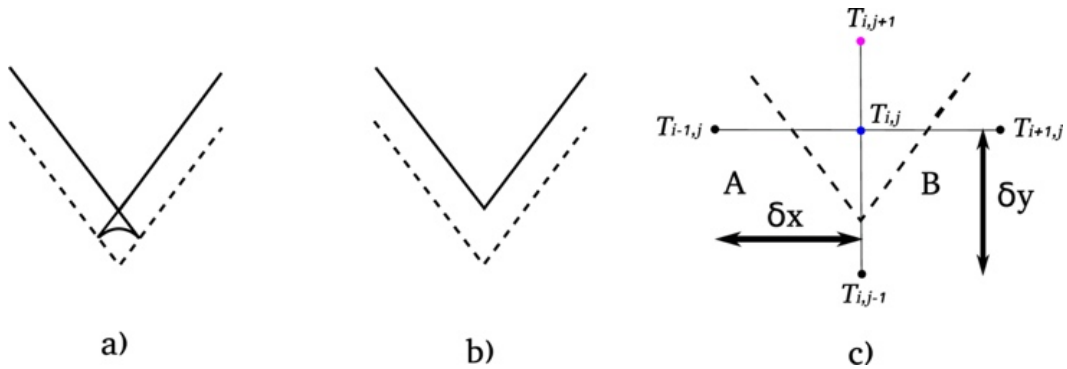
Figure 2.3 *Representation of the entropy satisfying upwind scheme. (a) wavefront propagating with a gradient discontinuity resulting in a tail. (b) first arrival wavefront after viscous-limit solution. (c) entropy-satisfying upwind scheme. Black dots indicate known travel times, whereas blue and pink dots have unknown travel times.*

Sethian and Popovici (1999) used an entropy satisfying viscosity solution where a wavefront can cross a grid point only once, ensuring the stability of the FMM scheme. The entropy condition is implemented using an upwind gradient scheme where the travel time

at a grid point is updated only using a set of grids that lie upwind (Figure 2.4). The upwind scheme of Sethian and Popovici (1999) approximates the Eikonal equation as

$$\left[max\ (\mathcal{D}_a^{-x}T\ , -\ \mathcal{D}_b^{-x}T, 0)^2\ +\ max(\mathcal{D}_c^{-y}T\ , -\ \mathcal{D}_d^{-y}T, 0)^2 \right]_{ij}^{\frac{1}{2}} = S_{ij}, \qquad 2.52$$

where T is the travel time, i, j are grid index values in x, y space. $\mathcal{D}$ represent the upwind gradient operator with $a, b, c,$ and d as the order of accuracy of the upwind finite-difference scheme. The first order upwind operator derived from Taylor series summation is given as

$$\mathcal{D}_1^{-x}T_i = \frac{T_i - T_{i-1}}{\delta x}\ . \qquad 2.53$$

For a simple example given in Figure 2.3c, substituting equation 2.53 in equation 2.52 gives the first-order upwind approximation to the Eikonal equation in quadrant A, which is written as

$$\left(\frac{T_{i,j} - T_{i-1,j}}{\delta x}\right)^2 + \left(\frac{T_{i,j} - T_{i,j-1}}{\delta y}\right)^2 = S_{ij}^{\ 2}\ , \qquad 2.54$$

and in the case of quadrant B, we get

$$\left(\frac{T_{i+1,j} - T_{i,j}}{\delta x}\right)^2 + \left(\frac{T_{i,j} - T_{i,j-1}}{\delta y}\right)^2 = S_{ij}^{\ 2}. \qquad 2.55$$

$T_{i,j}$ is calculated in each quadrant by solving the above quadratic equation. Of the two possible solutions of $T_{i,j}$ in quadrant A, the maximum value corresponds to wavefront in quadrant A. Similarly, the maximum value of $T_{i,j}$ is taken for quadrant B. Out of two values of $T_{i,j}$ from both the quadrants, the minimum is taken as the final value of the travel time. In this way, the entropy satisfying upwind scheme considers the information from both sides of the gradient discontinuity (Figure 2.3c) to provide a robust and stable travel time field.

The algorithm of the FMM scheme is summarized as follows

1. For a given velocity field defined at discrete grid points, three different sets of grid points are defined as: *known, neighbours,* and *far*. The set of grid points whose values are set and not updated during iterations make up the *known* set. While, the other set of grid points next to the known sets are *neighbours*. Rest grid points constitute the *far* set (Figure 2.4).

2. The FMM scheme starts with a given starting point (i, j) on the grid (for example, at a source location) and assigns $T_{i,j} = 0$. This starting point becomes the *known* set, and points next to it are made the *neighbours*.

3. Travel time $(T_{i,j})$ of all points in the *neighbours* are calculated using the entropy satisfying upwind scheme described earlier. The grid point in the neighbours corresponding to minimum time is then included in the *known* set.

4. This process is repeated until all grid points become part of the *known* set. This way, the FMM scheme calculates the travel time field at all grid points.

5. For a given receiver, the trajectory from the source is then calculated retrospectively by tracing the wavefront from the receiver back to the source.
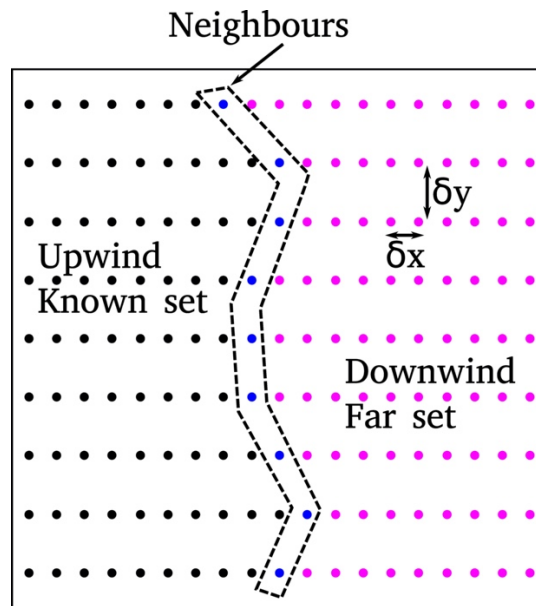
Figure 2.4 *Demonstration of different sets of grid points used in the Fast marching method.*

2.7 Seismic Imaging

Dispersion measurement by analysis of surface wave data (section 2.5) from a large number of raypaths using ambient noise and/or earthquake is used to obtain maps of corresponding group/phase velocities at different frequencies following tomographic inversion approach. At each grid point, 1-D inversion of dispersion data is then performed to compute depth-dependent shear wave velocity. Subsequently, interpolation of individual 1-D velocity model produces a 3D continuous seismic velocity model.

Classical inversion techniques (e.g., subspace inversion, discussed below) employ optimization schemes to minimize an objective function, consisting of data residuals, using

error norms (e.g., L_2 norm), and provide a single optimal model that fits data. In most cases, a fixed parametrization of Earth models (e.g., number of cells in 2-D inversion and number of layers in 1-D inversion) is used, which is a compromise between model uncertainty and model resolution. For example, if a relatively large cell size is used, the final model estimated by independent information is least biased by data noise. In contrast, for smaller cells, the data noise maps into large error in the final model, leading to a non-unique solution. Analysts often use regularization (damping and smoothing) to obtain a single solution and avoid overfitting the data. The choice of regularization parameters is subjective, often done by L-curve tests (Hansen, 1992). In addition, the model complexity (i.e., level of detail present in the recovered model) depends on an efficient quantification of the level of noise present in the data. In seismic tomography, prior knowledge of the data noise is difficult (Scales & Snieder, 1998). Furthermore, this limited knowledge of data noise creates a problem when multiple data sets with different noise variances sample the Earth at different scales. Because regularization procedures are global, the solution model does not account for the unevenness of data's spatial distribution.

Another class of inversion, based on Bayesian inferences, attempts to overcome the above-discussed limitations of regularized solution models by generating an ensemble of solution models using a trans-dimensional sampler, known as reversible jump Monte Carlo Markov Chain (rj-McMC) algorithm (Bodin & Sambridge, 2009; Green, 1995) with a hierarchical estimation of data noise (Bodin et al., 2012a). Statistical inferences from the ensemble of models are made to represent a single solution model in terms of ensemble mean, median or mode, etc. In the trans-dimensional framework, model parametrization is made irregular. For example, the number of cells in 2-D inversion or number of layers in 1-D inversion is taken as unknown to be separately inverted for. Therefore, the dimension of the model space changes during inversion. The hierarchical Bayes treats the data noise as an unknown and produces a joint inference on model complexity as well as data uncertainty (Bodin et al., 2012a). This method provides a flexible approach resulting in a "parsimonious" solution, where model complexity is derived completely by data only without any need for explicit regularization. Bodin and Sambridge (2009) used Voronoi cells for the model parametrization whose geometry and number change during trans-dimensional steps. Later, Hawkins and Sambridge (2015) introduced a multiresolution wavelet tree parametrization that reduces computational time and allows more flexibility in seismic imaging. For details on the trans-dimensional inversion, the reader is referred to

Bodin and Sambridge (2009), Bodin et al. (2012a, 2012b), and Hawkins and Sambridge (2015). Here in the following, a brief introduction of tomographic inversion by the subspace inversion and the Bayesian Trans-dimensional inversion is presented with a test example. Then, a summary of 1-D inversion of surface wave data to obtain shear wave velocity-depth variation with a synthetic example is provided.

2.7.1 Subspace inversion

A regularized inversion minimizes an objective function to match model prediction to observed data. The objective function $\emptyset(\theta)$ can be given by

$$\emptyset(\theta) = (g(\theta) - d)C_e^{-1}(g(\theta) - d) + \epsilon(\theta - \theta_o)^T C_m^{-1}(\theta - \theta_o) + \eta(\theta^T D^T D\theta),$$ 2.56

where d is the data (i.e observed group or phase travel time), θ is the vector of unknown model parameters (i.e group or phase velocity), D is flatness matrix, g(θ) is predicted group travel times for the model (θ), θ_o is reference velocity model, C_e and C_m are data and model covariance matrices, respectively. Regularization parameters are given by ϵ (damping) and η (smoothing). The prediction of travel-time is done by the grid-based Eikonal solver (FMM) discussed earlier. Assuming invariant and uncorrelated Gaussian random data noise, $C_e = \sigma_d^2 I$, where σ_d is the standard deviation of data noise and I is the identity matrix. The damping and smoothing parameters are constrained by the L-curve test, which gives an optimum value that minimizes the tradeoff of data residual with model perturbation and model roughness. All three terms in the right-hand side of equation 2.56 correspond to different minimization schemes that collectively constrain model parameters by reducing the solution's non-uniqueness. The first term minimizes the difference between observed and predicted data given the model (θ), and the second term avoids the solution model (θ) going far away from the reference model (θ_o), while the third term ensures that the solution model contains minimum structural variation.

Gradient-based methods aim to explore local behaviour of $\emptyset(\theta)$ to get the desired minimum. If $\emptyset(\theta)$ is a smooth function of model parameters, a Taylor series expansion of $\emptyset(\theta)$ about a current model θ_o gives

$$\emptyset(\theta_o + \delta\theta) \approx \emptyset(\theta_o) + \hat{\gamma}\delta\theta + \frac{1}{2}\delta\theta^T \hat{H}\delta\theta,$$ 2.57a

where $\delta\theta$ is model perturbation, $\hat{\gamma} = \delta\emptyset/\delta\theta$ and $\hat{H} = \delta^2\emptyset/\delta\theta^2$ represent the gradient and Hessian matrix, respectively. For equation 2.56, these partial derivates are

$$\hat{\gamma} = G^T C_e^{-1}(g(\theta) - d) + \epsilon C_m^{-1}(\theta - \theta_o) + \eta D^T D\theta,$$

$$\hat{H} = G^T C_e^{-1} G + \nabla_\theta G^T C_e^{-1}(g(\theta) - d) + \epsilon C_m^{-1} + \eta D^T D,$$

2.57b

where $G = \delta g/\delta\theta$, is the Fréchet matrix. Because of the non-linearity of $g(\theta)$, an iterative approach is adopted to update a current model until an optimum termination criteria for the minimization of the function $\emptyset$ is reached. A suitable termination criteria is provided by normalized χ^2 misfit function expressed as

$$\chi^2 = \frac{1}{N} \sum_{i=1}^{N} \left(\frac{d_\theta^i - d_{obs}^i}{\sigma_d^i} \right)^2,$$

2.58

where $d_\theta^i = g(\theta)$, and d_{obs}^i is the observed data with uncertainties given by σ_d^i. A termination criterion is achieved when $\chi^2 = 1$.

Inversion schemes such as the steepest descent and conjugate gradient attempt to perform minimization in a single model space (i.e., line minimization) at each iteration. In the majority of geophysical problems, model parameters consist of varying physical dimensions (e.g., seismic velocity, density). While such a suit of model parameters has limited implications for small-scale linear inverse problems, appropriate scaling of different parameters types is required for sufficiently large non-linear iterative inversion. A popular class of inversion called "subspace inversion" performs the iterative inversion along p-dimensional search directions (Kennett et al, 1988; Rawlinson & Sambridge, 2003, 2005). The method restricts the minimization of $\emptyset(\theta)$ to a p-dimensional model space such that the model perturbation $(\delta\theta)$ is obtained in terms of a basis vector $\{a^j\}$:

$$\delta\theta = \sum_{j=1}^{p} \mu_j a^j = A\mu$$

2.59

where $A (= a^j)$ is the projection matrix. The coefficient μ, which controls the length of the vector a^j, can be found by substituting equation 2.59 to equation 2.57a, which gives the following form

$$\emptyset(\theta_o + \delta\theta) = \emptyset(\theta_o) + \sum_{j=1}^{p} \mu_j \hat{\gamma}^T a^j + \frac{1}{2} \sum_{j=1}^{p} \sum_{k=1}^{p} \mu_j \mu_k [a^k]^T \hat{H}[a^j].$$ 2.60

The minimum of $\emptyset$ with respect to μ gives

$$\frac{\partial\emptyset}{\partial\mu_q} = \hat{\gamma}^T a^q + \sum_{k=1}^{p} \mu_k [a^k]^T \hat{H}[a^j] = 0,$$ 2.61

for $q = 1, \dots p$. Rearrangement of the above equation and substitution from equations 2.57b and 2.59 gives the following for the model perturbation ($\delta\theta$)

$$\mu = -[A^T \hat{H} A]^{-1} A^T \hat{\gamma},$$
$$\delta\theta = -A[A^T (G^T C_e^{-1} G + \epsilon C_m^{-1} + \eta D^T D)A]^{-1} A^T \hat{\gamma},$$ 2.62

where the model perturbation $\delta\theta$ is used to update a current model. The advantage of the subspace inversion is that only a relatively small p x p matrix is inverted at each iteration.

2.7.2 Bayesian Trans-Dimensional Tree inversion

The Trans-Dimensional Tree (TDT) scheme (Hawkins & Sambridge, 2015) uses a multi-resolution wavelet tree structure to represent a velocity field with a single-pixel mean (at the root of the tree) and a hierarchy of local deviations (i.e., wavelet coefficients) from coarse to fine-scale. The method predicts group travel-time using the Fast Marching Method (FMM) and subsequently adopts a Bayesian inversion using a reversible-jump Markov chain Monte Carlo algorithm (rj-McMC; Green, 1995) to construct an ensemble of solution models. These solution models collectively define *a posteriori* probability distribution $p(\theta|d)$ which gives the probability of model parameters θ given observed data d using Bayes theorem (Bayes, 1763)

$$p(\theta|d) \propto p(d|\theta) \times p(\theta),$$ 2.63

where $p(\theta)$ is prior probability distribution or *a priori* which is a probability on the plausible range of model parameters, before observing the data. $p(d|\theta)$, known as the likelihood, represents the probability of observing d, given a set of model parameters. Assuming data errors are distributed as a Gaussian distribution, the likelihood writes

$$p(d|\theta) = \frac{1}{\sqrt{(2\pi)^n |C_e|}} \ exp\left\{-\frac{(G(\theta)-d)^T C_e^{-1} (G(\theta)-d)}{2}\right\},\qquad\qquad 2.64$$

where the operator G represents data predictions from the model θ and, C_e is data error covariance matrix ($C_e = \sigma_d^2 I$, where σ_d is the standard deviation of data noise). The level of σ_d controls how well the predicted data should fit the actual observations, which further affects the complexity of the recovered models. For example, in the case of large data errors, a smooth and simple model will be enough to explain observations. Quantification of the data noise before the tomographic inversion is difficult, so a hierarchical Bayesian framework is often used (Bodin et al., 2012a; Malinverno & Briggs, 2004), where the data noise is treated as an unknown parameter to be inverted for. In the TDT approach, a scaling term (λ, also called the hierarchical error scale) is used to scale the standard deviation of data noise (σ_d) to get an estimate of true data noise, $\sigma_t = \lambda\sigma_d$, where λ is an unknown to be inverted for.

In the trans-dimensional framework (or rj-MCMC), the parametrization of the model (θ) and its size can change during inversion steps using the Birth/Death scheme (Geyer & Moller, 1994; Green, 1995). The rj-McMC sampler, using an iterative approach, generates a candidate model (θ') from a current model (θ) using a proposal distribution, $q(\theta'|\theta)$. The new candidate model (θ') is accepted or rejected based on generalized Metropolis-Hasting-Green (Green, 1995) acceptance criteria

$$\alpha(\theta',\theta) = min\left\{1, \frac{p(\theta')}{p(\theta)}\ \frac{p(d|\theta')}{p(d|\theta)}\ \frac{q(\theta|\theta')}{q(\theta'|\theta)}\ |J|\right\},\qquad\qquad 2.65$$

where $|J|$ is the Jacobian determinant that maintains detailed balance when the model dimension changes.

The prior $p(\theta)$ in this case is a probability of available information about the plausible range of group or phase velocity values. The prior mean (or the reference velocity) is given by the average of the inter-station group or phase velocity measurements. Since the TDT approach uses wavelet tree structures to represent the velocity field, the prior on velocity is provided in terms of wavelet coefficients using a Laplacian prior. The width of the Laplacian prior can be chosen following Hawkins et al. (2018) by performing a number of tests with different prior widths and sampling the prior to examine the resultant "a priori" distribution for group or phase velocities (Figure 2.5). For example, a suitable width of the

Laplacian prior on wavelet coefficients may be chosen such that, for a mean group velocity of 3 km/s, the prior on group velocity ranges from 2.4 to 3.6 km/s.
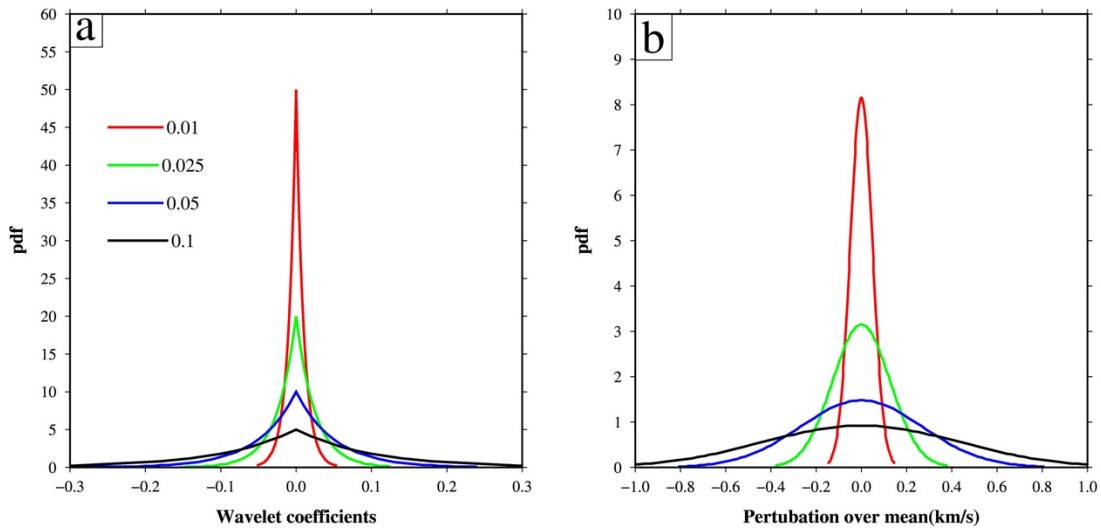
Figure 2.5 *Sampling the prior. The plot demonstrates the expected range of group velocities given a Laplacian prior. (a) Laplacian priors with zero mean and different widths (or standard deviations) are indicated by colorful lines. (b)Histogram of group velocities relative to a mean (e.g., 3 km/s used for this plot). The group velocity perturbations follow a Gaussian distribution centered around zero. The prior width equal to 0.05 (blue line in (a)) is used in this study.*

Independent Markov chains are assumed to converge when negative log-likelihood reaches an equilibrium state. Although the TDT approach does not depend on the choice of the starting model (Rosalia et al., 2020), the use of reasonable starting models in Bayesian tomography helps in an early convergence of model parameters and significantly reduces computational time. One can use velocity maps obtained from the subspace FMM inversion as the starting model. The TDT method has been successfully applied in several geophysical studies (Hawkins et al., 2018; Pilia et al., 2020; Rosalia et al., 2020).

In Figure 2.6, a synthetic tomography is presented. For an input checkerboard image with a maximum group velocity perturbation of 14% (at the top left), group travel times are calculated using the FMM scheme. Then, tomographic inversions are performed using the subspace method by the Fast Marching Surface Tomography (FMST) software (Rawlinson & Sambridge, 2003) as well as the Trans-dimensional Tree (TDT) inversion to illustrate and compare the potential of recovering the input image. In order to show the effect of the regularization on the recovered model, several subspace inversions with different values of

damping and smoothing parameters are performed. It can be seen that the structural variation as well the velocity amplitude are distorted when damping and smoothing parameters are larger. In contrast, small-scale spurious features are observed in the case of underdamped and under smooth case. When regularization parameters are optimized, recovery of the input image is relatively improved. In the case of the TDT method, robust recovery of input structures and amplitude is achieved without the need for regularization. In addition, the Bayesian inversion provides an efficient way to represent the model uncertainty using the posterior standard deviation.
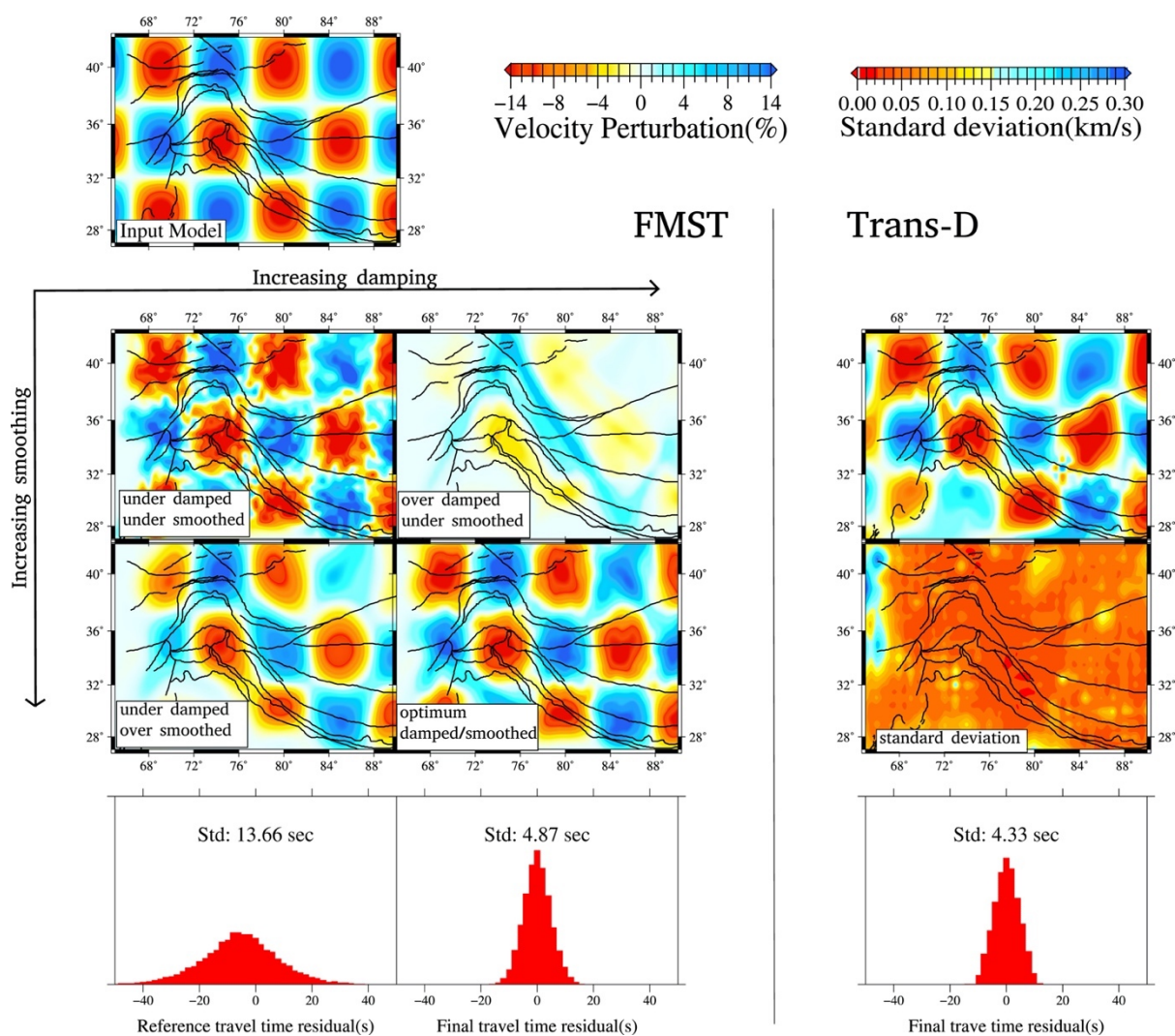
Figure 2.6 *Synthetic test showing recovery potential for the linearized subspace inversion (FMST) and the Trans-dimensional Tree (TDT) inversion. The top left image shows the input checkerboard image. Histograms in the bottom part are travel time residuals.*

2.7.3 Bayesian Trans-dimensional inversion of surface wave

Group velocities at each grid-points in 2-D tomography maps are used to derive shear wave velocity (Vs) variation with depth using a 1-D inversion scheme based on a hierarchical, trans-dimensional Bayesian inversion (Bodin et al., 2012b). One then interpolates the 1-D shear velocity model obtained at each grid-point to produce a 3-D shear wave velocity model. The basic framework of the Bayesian inversion with the trans-dimensional sampling is the same as discussed in the earlier section. The model parametrization is made dynamic by considering the number of layers, position, and shear velocity as unknowns during the inversion. Like the 2-D tomographic inversion, the data noise level (σ_d) can be taken as an unknown parameter to be inverted here (although the standard deviations obtained from the 2-D inversion could also be used as the data noise). Broad uniform priors on various parameters such as the number of layers, data noise level and, shear wave velocities are used. The lower and upper bounds of the prior on shear wave velocity are defined as $m_0(1 \pm w)$, where m_0 is a reference model (or mean of the prior on shear velocities), and w is the width of perturbation. For the forward calculation of the group velocities given a 1-D model, the subroutine DISPERSE80 (Saito,1988) is used.

To illustrate the inversion methodology, a synthetic test using a 3-layer earth model is presented in Figure 2.7. Synthetic group velocities from 5 to 60 seconds were computed, and random Gaussian noise (1 % of the synthetic value) was added (Figure 2.7b). Uniform prior bounds on the number of layers (2−45) and data noise level (0−2) are assigned. The inversion was performed with a half-space reference velocity model (m_0) having a maximum allowed perturbation of 40% (i.e., w = 0.40). Computed mean and maximum aposteriori (MAP) from the resultant posterior distribution are compared to the input model (Figure 2.7c,d), showing that both amplitudes and patterns are well resolved. The posterior distribution on the location of discontinuities, level of data noise, and the number of layers (Figure 2.7e-g) also peak at actual values.
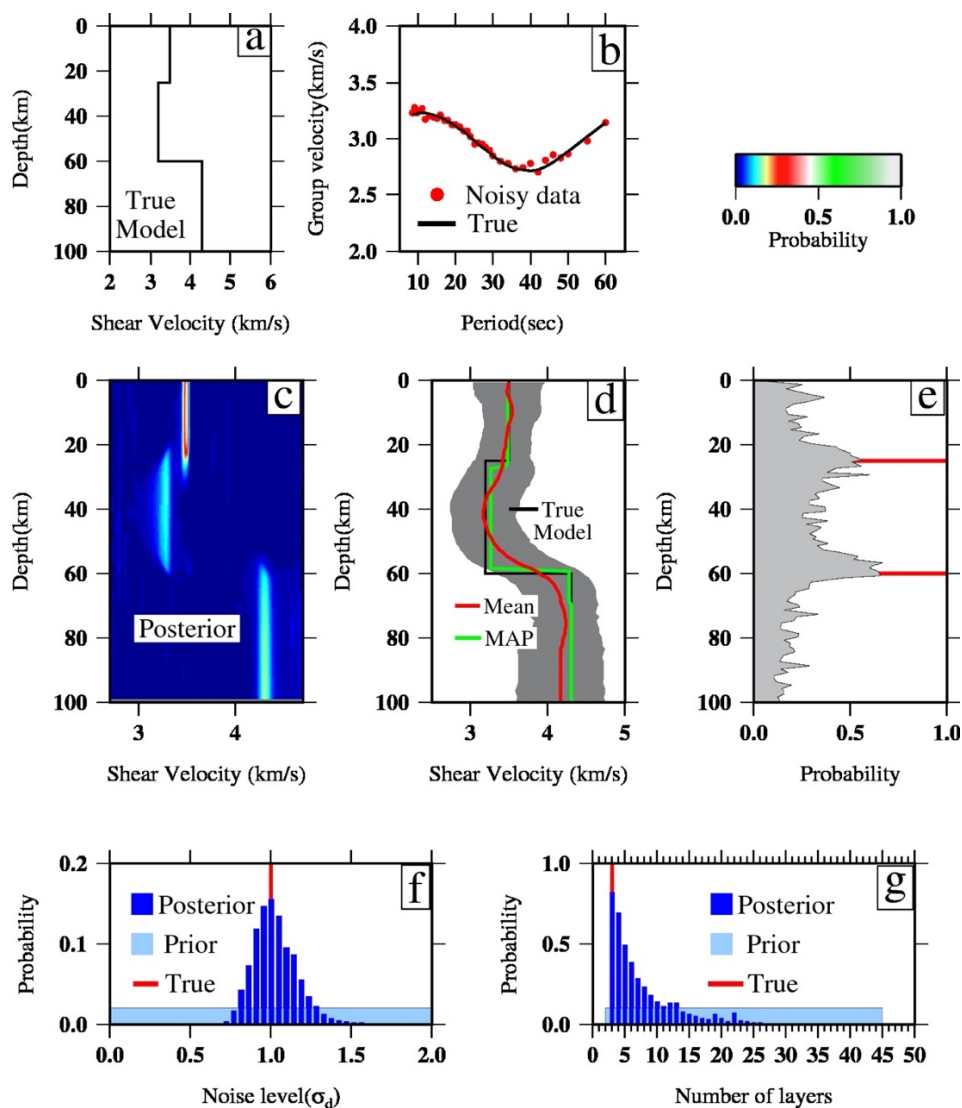
Figure 2.7 Demonstration of Trans-dimensional hierarchical inversion. (a) An example 3 layered shear velocity model (black line). (b) Synthetic dispersion data (with added noise). (c) The posterior probability after inversion is shown in color data. (d) Output velocity model in terms of posterior mean (red) and Maximum aposteriori (MAP) (green) compared with the true model (black). The grey shaded area represents one standard deviation bounds. Posterior probability on the position of discontinuities as a function of depth (e), data noise level (f), and the number of layers (g) are shown with the red line indicating true values. A half-space model with shear wave velocity at 4 km/s was used as the reference model.

CHAPTER 2

2.8 Data and preliminary analysis

2.8.1 Data

We use broadband seismological data from about 530 seismic stations operated between 1991 and 2016 (Figure 2.8a) during different time intervals. The seismic network includes stations from the PASSCAL experiments, the Global Seismograph Network (GSN), and various seismological experiments in Kyrgyzstan, Kazakhstan, Tajikistan, China, Nepal, and Western Tibet. We also used data from the French deployments in western Kunlun and Kazakhstan and Indian deployments in the western Himalayas. Table 2.1 provides details of the network and stations used. We analyzed the vertical component of the seismic records to extract the fundamental mode Rayleigh wave dispersion using the ambient noise cross-correlation method and earthquake waveforms analysis as discussed below.

NETWORK	Year	Remark
PASSCAL	XW (1997-2001)	Tien-Shan Continental Dynamics
	XP(2005-2007)	MANAS (Tien-Shan)
	XR(1994,1997-1999)	INDEPTH II,III (Tibet)
	XG(1995-1996)	Nanga Parbat Pakistan
	XF(2002-2005)	Nepal-Himalaya-Tibet Seismic Transect
	YL(2001-2002)	Himalayan Nepal Tibet Experiment
KYRGYZSTAN	KR (2007-2016)	Kyrgyz Digital Network
	KN (1991-2016)	Kyrgyz Seismic Telemetry Network
	7B (2008-2010)	TIPAGE Network, Tadjikistan/Kirgistan
	KC (2010-2017)	Central Asian Seismic Network of CAIAG (Kyrgyzstan)
KAZAKHSTAN	KZ (1997-2016)	Kazakhstan Network
GLOBAL SEISMOGRAPH NETWORK (GSN)	II-NIL (1998-2013)	Global Seismograph Networks (GSN), Pakistan
	IU-KBL (2007-2013)	Global Seismograph Networks (Afghanistan)
CHINA	IC-LSA,WMQ (1995-2013)	New China Digital Seismograph Network
	CB-KSH (2009-2016)	China National Seismic Network
TAJAKISTAN	TJ (2005-2016)	Tajikistan National Seismic Network
NEPAL	XQ (2015-2016)	Nepal Mw 7.9 earthquake of April 25, 2015
	NQ (2015-2016)	NetQuakes (Nepal)
WESTERN TIBET	Y2 (2007-2011)	Western Tibet

GEOSPCOPE	G-WUS (1991-2016)	Kazakhstan Network
WESTERN KUNLUN	YT (2001)	Western Kunlun (Tibet)
CSIR-NGRI	UT (2005-2008,2011-2012)	Uttaranchal, India
	NG (2002-2003)	North-West Himalaya
Wadia Institute of Himalayan Geology (WIHG)	WADIA (2007-2009)	Uttaranchal Himalaya
CSIR- CMMACS	CM (2013)	Western Himalaya

Table 2.1 *List of seismic networks along with their operational period used in this study.*

2.8.2 Ambient noise analysis

Seismic ambient noise has been used to construct crust and mantle velocity structures with an improved vertical and lateral resolution for almost two decades (Ritzwoller et al., 2011; Saha et al., 2020; Shapiro et al., 2005; Shen et al., 2016; Yang et al., 2010). As discussed earlier, cross-correlation of ambient noise records between two stations is an estimate of Green's function (Shapiro & Campillo, 2004; Wapenaar, 2004). We follow Bensen et al. (2007) and Schimmel et al. (2011) to process the ambient noise data. The pre-processing involves continuous waveform data from the vertical seismograph cut to one-day length followed by removal of mean and trend, decimation to one sample per second, correction for instrument response, and bandpass filtering from 0.01 Hz to 0.25 Hz range (4 to 100 sec period range). Next, we compute inter-station Green's functions from ambient noise time series using the phase cross-correlations (PCC) technique (Schimmel, 1999; Schimmel et al., 2011). Finally, the daily cross-correlations are stacked by the time-frequency phase weighted stack (tf-PWS) approach (Schimmel et al., 2011; Schimmel & Gallart, 2007). We separate negative (acausal) and positive (causal) components and stack them to obtain symmetric cross-correlations (Figure 2.8b).
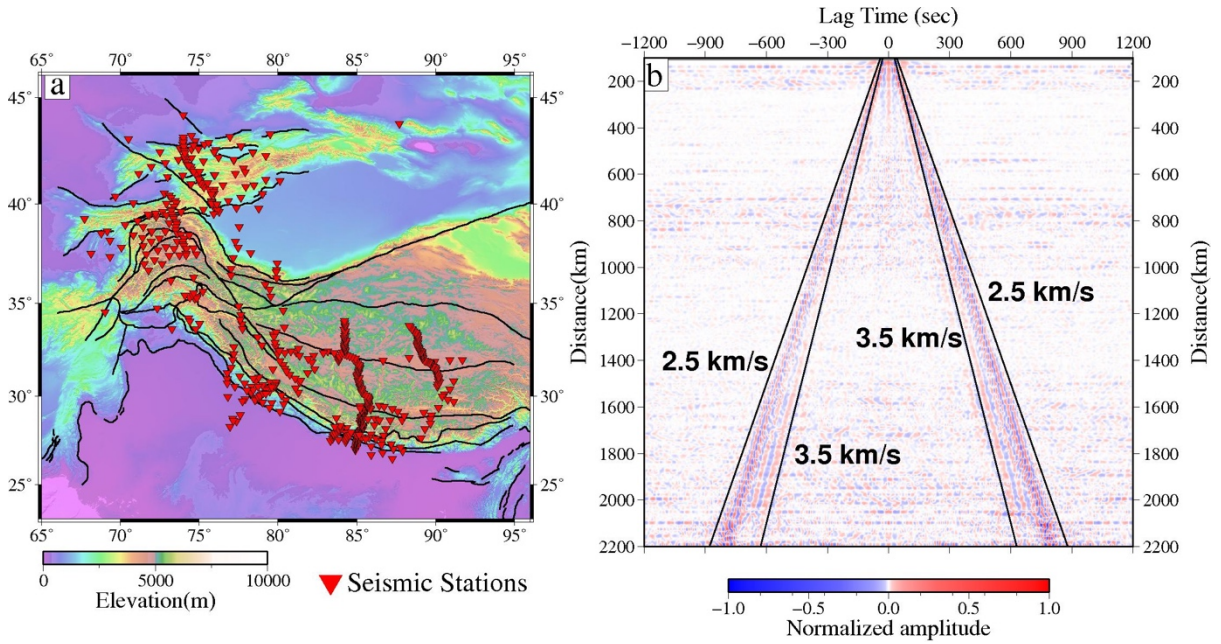
Figure 2.8 *Ambient noise data used in this study. (a) Locations of seismic stations (red inverted triangles). (b) Symmetric component of stacked ambient noise cross-correlations plotted with increasing interstation distance. Black lines indicate the signal window of the estimated Green's function with velocity from 2.5 km/s to 3.5 km/s.*

The final stacked cross-correlations are used to compute group velocity dispersion using the Frequency-Time-Analysis (FTAN) method (Levshin & Ritzwoller, 2001). The uncertainty in group velocity measurement is computed by generating 20 different combinations of 75% of daily cross-correlations selected randomly to obtain 20 stacks through bootstrapping and estimating their standard deviations (Acevedo et al., 2019). We retain dispersion data which has interstation distance $\geq 3\lambda$ (λ is wavelength), and has at least ten random stacks with SNR ≥ 10. For a typical station pair GARM-GUGE, the group velocity dispersion computed from the bootstrapping and the corresponding SNR are presented in Figure 2.9 (a-c). To validate group velocity measurement from ambient noise, we also compared it with the group velocity dispersion computed from an earthquake of magnitude 5 in the proximity of GARM recorded at GUGE (Figure 2.9d). Both the dispersion curves show an excellent match. After applying the selection criteria mentioned earlier, we selected 9,794 (out of 22,958 inter-station pairs) inter-station dispersion measurements with Rayleigh wave group velocity data from period 5 to 60 seconds for further analysis.
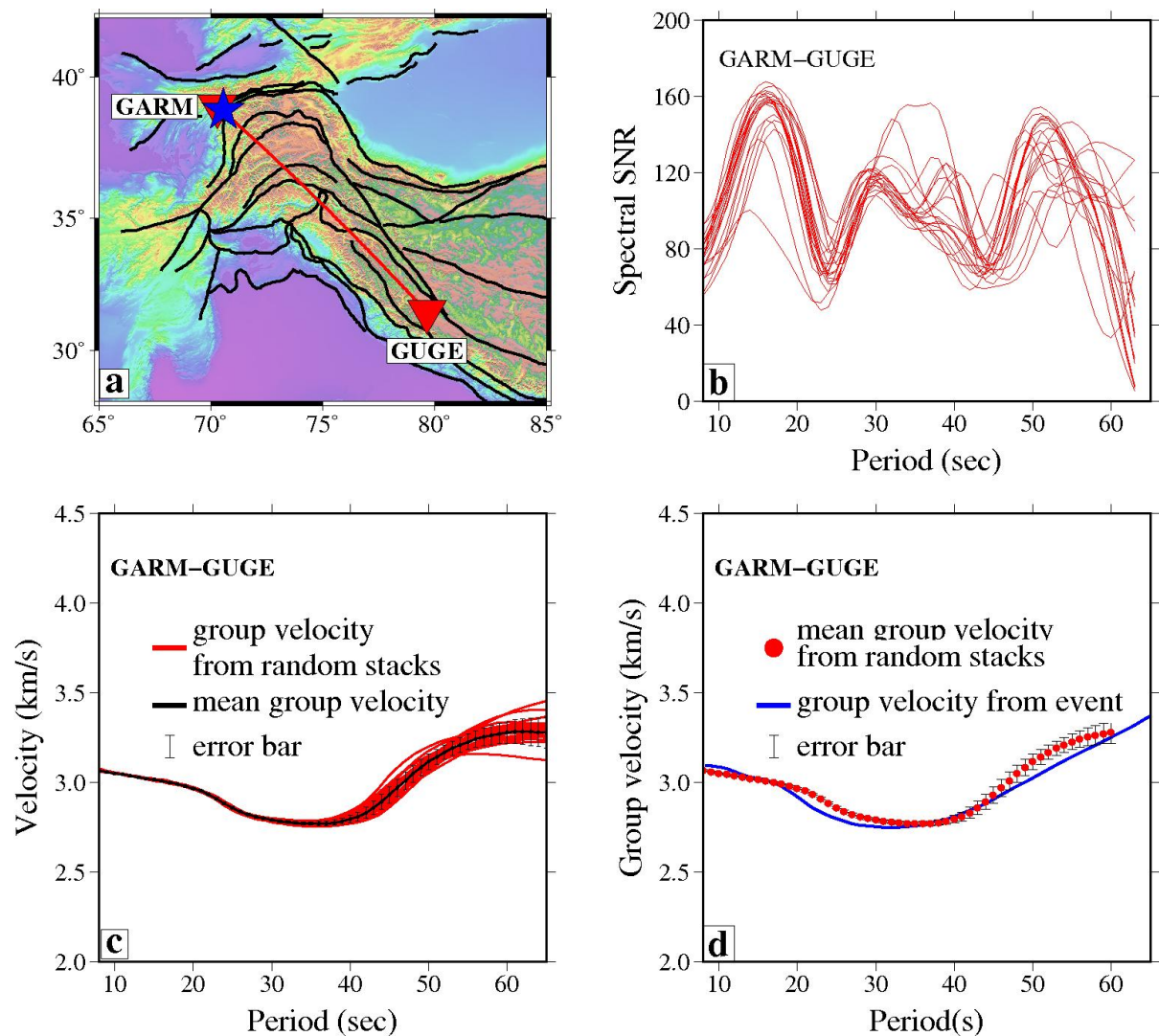
Figure 2.9 *Example dispersion with bootstrapping and comparison of ambient noise dispersion with event dispersion. (a) Location of two stations (red inverted triangles) GARM and GUGE used for computing noise cross-correlation and group velocity dispersion. An earthquake near GARM (blue star) recorded at GUGE. (b) Spectral SNR of 20 random stacks obtained through bootstrapping for the ray-path GARM-GUGE. (c) Group velocity dispersion plot with uncertainties obtained from bootstrapping. (d) Comparison of the dispersion data from ambient noise analysis with the earthquake waveform for station pair GARM-GUGE.*

2.8.3 Earthquake data analysis

To improve the ray path coverage, we also used dispersion measurements from local and regional earthquakes located within our study region. Around 1,261 earthquakes of a magnitude more than 4.5 and depth less than 30 km were selected from reviewed ISC

catalog between 1991 and 2016 (Figure 2.10). Like the ambient noise analysis, dispersion measurements were made using the FTAN method, resulting in additional dispersion data along 12,932 ray paths. Thus, the combined noise and earthquake ray paths of 22,726 provide dispersion measurements for the period range of 5 to 60 seconds. Figure 2.10d provides detail of the number of ray paths derived from ambient noise and earthquake data at different periods.
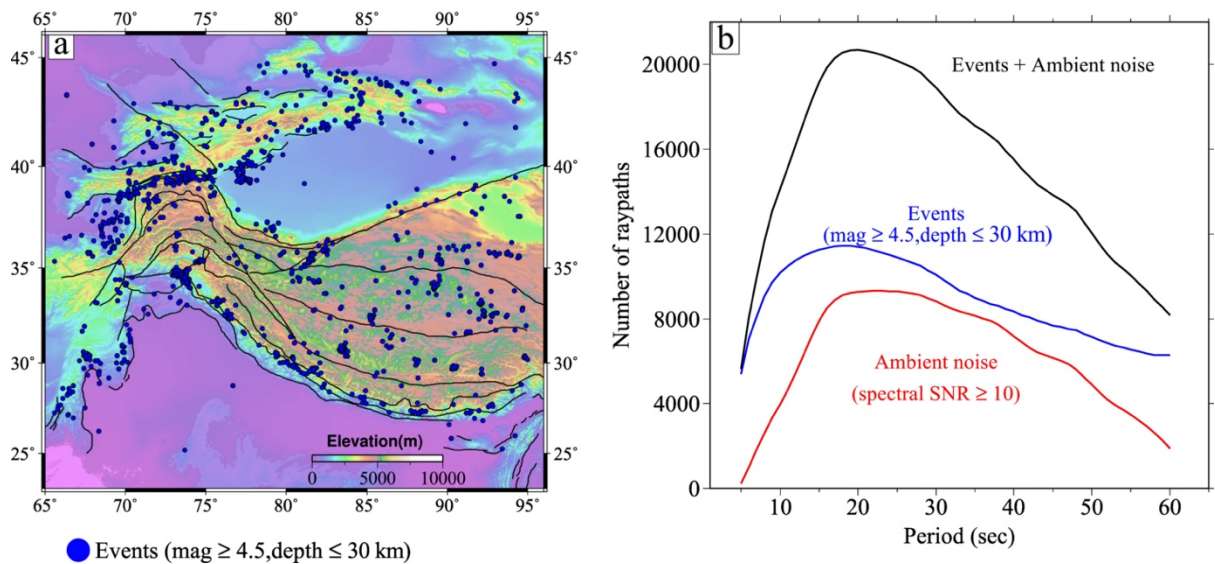
Figure 2.10 *Event data used in this study. (a) Map showing the location of earthquakes marked as blue dots (mag ≥ 4.5, depth ≤ 30 km) used for dispersion measurement. (b) Number of ray paths along which Rayleigh wave group velocity measurements are available using ambient noise (red line), earthquake waveform (blue line) and a combination of both at different periods (black line).*

CHAPTER 2

3-D Shear velocity image of western Tibet-Himalaya, Pamir-Hindu Kush, Karakoram, and Ladakh-Kohistan

This chapter presents a regional crustal shear wave velocity model of geological domain encompassing western Tibet-Himalaya, Karakoram, Ladakh-Kohistan arc, and Pamir-Hindu Kush regions using the data and methodology described in Chapter 2. Group velocity maps are computed from the analysis of inter-station ambient noise and earthquake waveforms recorded over seismological stations. These maps between 5 s to 60 s period with a horizontal resolution of 0.5° form the base of data. The group velocity dispersion at each grid node is then inverted in terms of shear velocity variation with depth up to 100 km. We discuss in detail several experiments to assess the reliability and robustness of the inversion scheme and velocity images. The interpolated velocity maps are used to investigate 3-D crustal architecture, including vertical extent and stratification and the nature of boundaries separating distinct units laterally and vertically. We discuss in detail the significance of these images in resolving a few important geological questions, such as the Northern limit of Indian lower crust beneath the Tibet-Karakoram-Pamir, Lateral variability and possible continuity of mid-crustal low velocity, and depth extent of the Karakoram Fault.

3.1 Group velocity tomography

The inter-station Rayleigh wave group velocities obtained from the ambient noise and earthquake data are used to perform group velocity tomography at each period. The velocity tomography is computed in two stages: the initial inversion using the Fast Marching Method (FMM) (Rawlinson & Sambridge, 2005), followed by the Bayesian Trans-dimensional inversion (Hawkins & Sambridge, 2015).

3.1.1 Tomography image resolution tests

We first performed several linearized subspace inversions with the FMM to assess the quality of image reconstruction through a series of synthetic discrete spike tests. Following Rawlinson and Spakman (2016), we used three different-sized (1° x 1°, 0.5° x 0.5° and 0.3° x 0.3°) positive and negative anomalies with 10 % perturbation from an average of 3 km/s. These velocities anomalies are separated by one degree. Using the same

ray path distribution observed in the experiment, we computed synthetic dispersion data for each of the above models and inverted them. The results of the sensitivity tests at five representative periods (5, 10, 20, 40, and 60 s) are presented in Figure 3.1. The recovered checkerboard patterns corresponding to 1° x 1° and 0.5° x 0.5° input models show excellent recovery of negative and positive anomalies at all periods without lateral smearing within the study region.
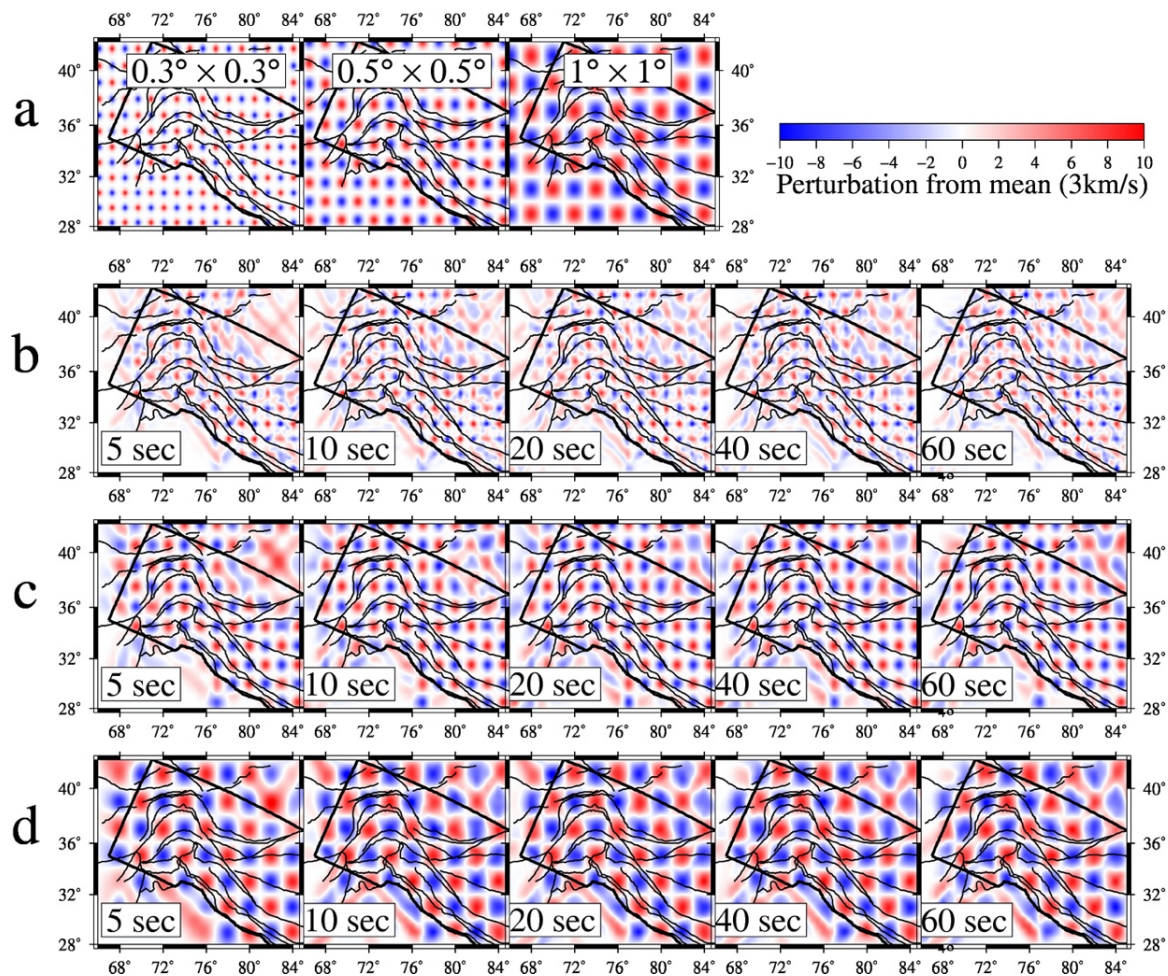
Figure 3.1 Synthetic checkerboard test of three different sized input anomalies of alternating negative and positive perturbation (10 % of 3 km/s) with 1° spacing between them. (a) Input model with anomaly size of 0.3° x 0.3° in the left panel, 0.5° x 0.5° in the middle panel, and 1° x 1° in the right panel. (b) The output model after tomographic inversion at periods 5, 10, 20, 40, and 60 s corresponding to the input model with an anomaly size of 0.3° x 0.3°. (c) same as (b) for the input model with an anomaly size of 0.5° x 0.5°. (d) same as (b) for the input model with an anomaly size of 1° x 1°. The thick black

polygon indicates the region of interest in this study. Thin black lines mark tectonic boundaries such as sutures and faults.

The well-resolved velocity tomography regions include Pamir, Kohistan-Ladakh, western Tibet, and a large part of central and west Himalayas segments. Model recovery for 0.3° x 0.3° input model shows small-scale lateral smearing near Peshawar Basin, Hindu-Kush, Tadjik Basin, and Tarim Basin. The velocity image degrades with a further decrease in block size. We preferred 0.5° x 0.5° block dimension as the optimal lateral resolution for this regional study. We then run the subspace inversion from period 5 to 60 seconds to obtain reasonable starting models. We discarded ray paths having large travel-time residuals in the FMM inversion from data for further analysis and modeling. Regularized parameters are obtained using the L-cure test discussed in Appendix A.6 (Figure A6).

In the next stage, we employed the Bayesian Trans-dimensional Tree (TDT) tomography with wavelet parametrization (Hawkins & Sambridge, 2015), using the velocity image from final subspace inversion as the starting model. Although the TDT approach does not depend on the choice of the starting model (Rosalia et al., 2020), the use of reasonable starting models in Bayesian tomography helps in an early convergence of model parameters and significantly reduces computational time. We ran a total of 24 parallel Markov chains, each with 500,000 samples. The first 400,000 samples were discarded as burn-in steps, and subsequently, every 100th sample was retained to obtain the final ensemble models. The mean and standard deviation of the final ensemble model was used to derive group velocity map and associated uncertainties. In a Bayesian inversion, the choice on the prior distribution does affect the form of the posterior distribution. To investigate this, we generated a set of group velocity maps through Bayesian inversion with larger prior widths (Figure 3.2 and Figure A7). The mean group velocity maps obtained with different priors show consistency in recovered structures without significant differences.

Figure 3.3 depicts the convergence of various parameters (e.g., number of coefficients, negative log-likelihood, and hierarchical error scale) with 500,000 iterations. Due to the robust initial model, the negative log-likelihood reaches equilibrium in the early stage of iterations. A test inversion with a larger number of iterations shows no change in output models (Figure 3.4).
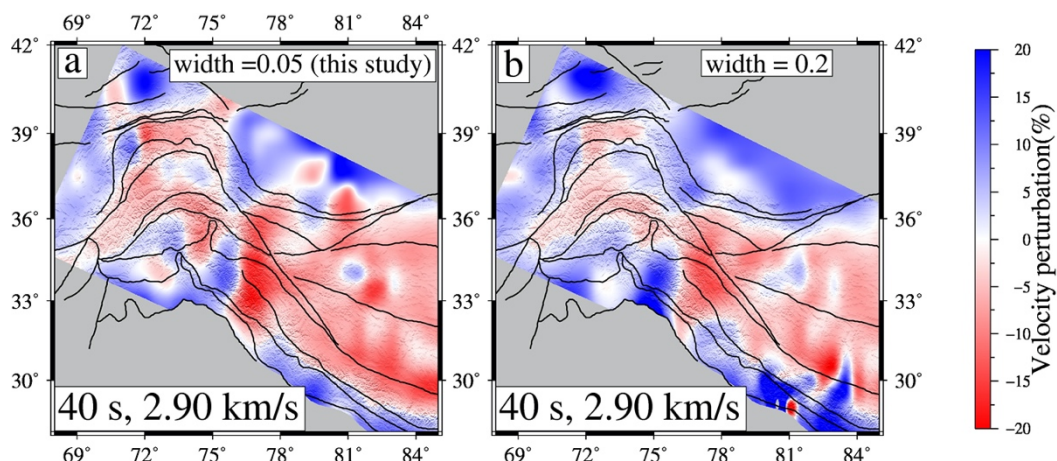
Figure 3.2 *Effect of prior widths on recovered models. The tomographic results are presented for period 40 s in terms of velocity perturbations from the regional mean. (a) Output map at prior width of 0.05 (used in the study). (b) Output map at prior widths of 0.2.*
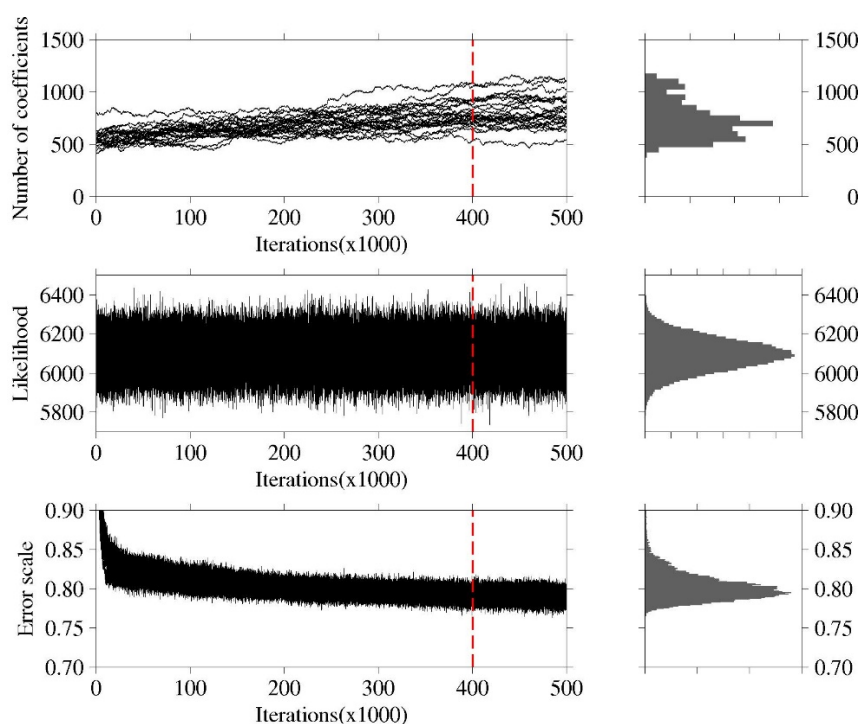
Figure 3.3 *History of the number of coefficients (top panel), negative log-likelihood (middle panel), and hierarchical error scale (lower panel) after inversion at 40 s. The corresponding histogram is shown on the right, where the red dashed line indicates the 400,000^{th} iteration position. Earlier samples are termed as "burn-in". The samples after the "burn-in" steps are used to obtain the final ensemble of models.*
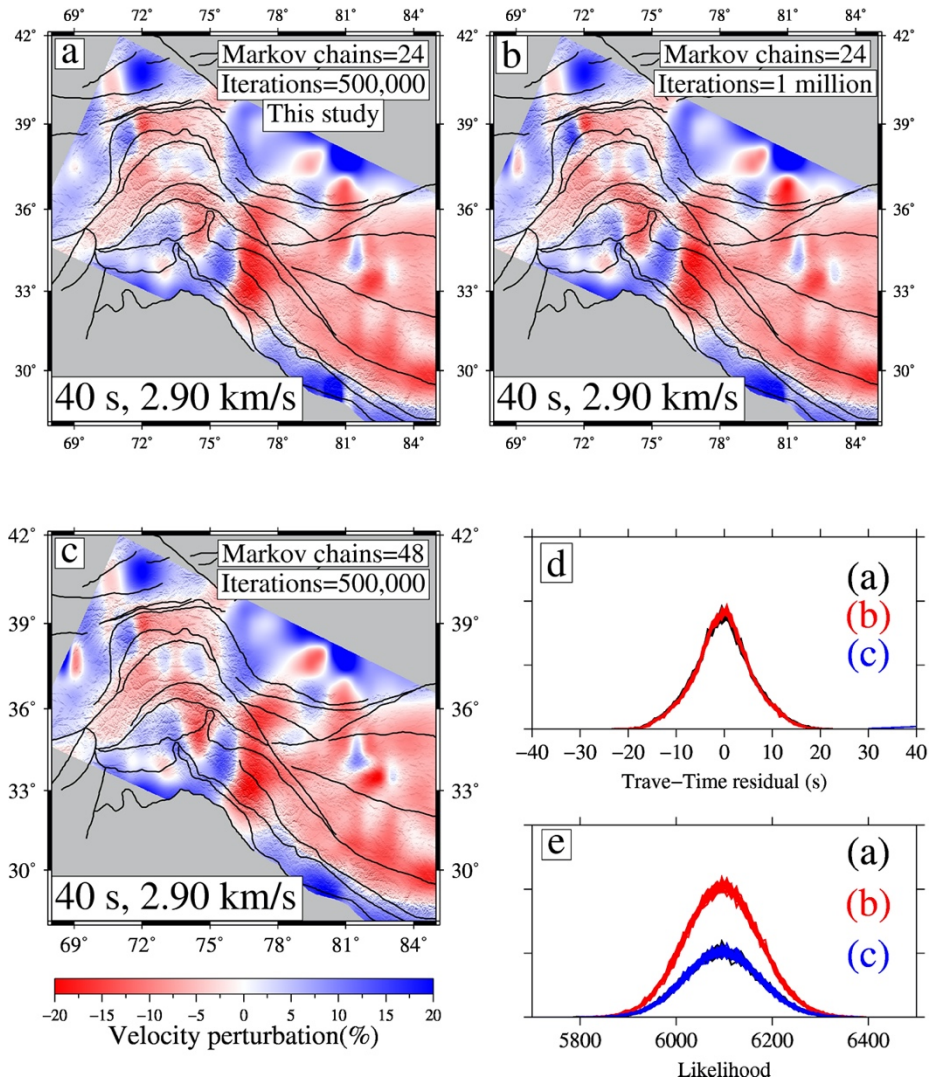
Figure 3.4 *Test with a large number of iterations at 40 s period. Group velocity maps are generated with 24 Markov chains and (a) 500,000 samples used in this study, (b) one million samples, and (c) 48 Markov chains with 500,000 samples. The color data is the group velocity in terms of velocity perturbations from the regional mean. Comparison of resultant trave-time residuals and likelihood for case (a) in black, (b) in red, and (c) in blue is shown in (d) and (e), respectively.*

3.1.2 Comparison of velocity image from ambient noise and earthquake data

To ensure that the two independent data sets, ambient noise, and earthquake, produce consistent velocity images, we generated three group velocity maps at 40 s using ambient noise data only, earthquake data only, and the combination of both (Figure 3.5). While the velocity images are similar, combining the two data sets increases the total ray paths, improving resolution.
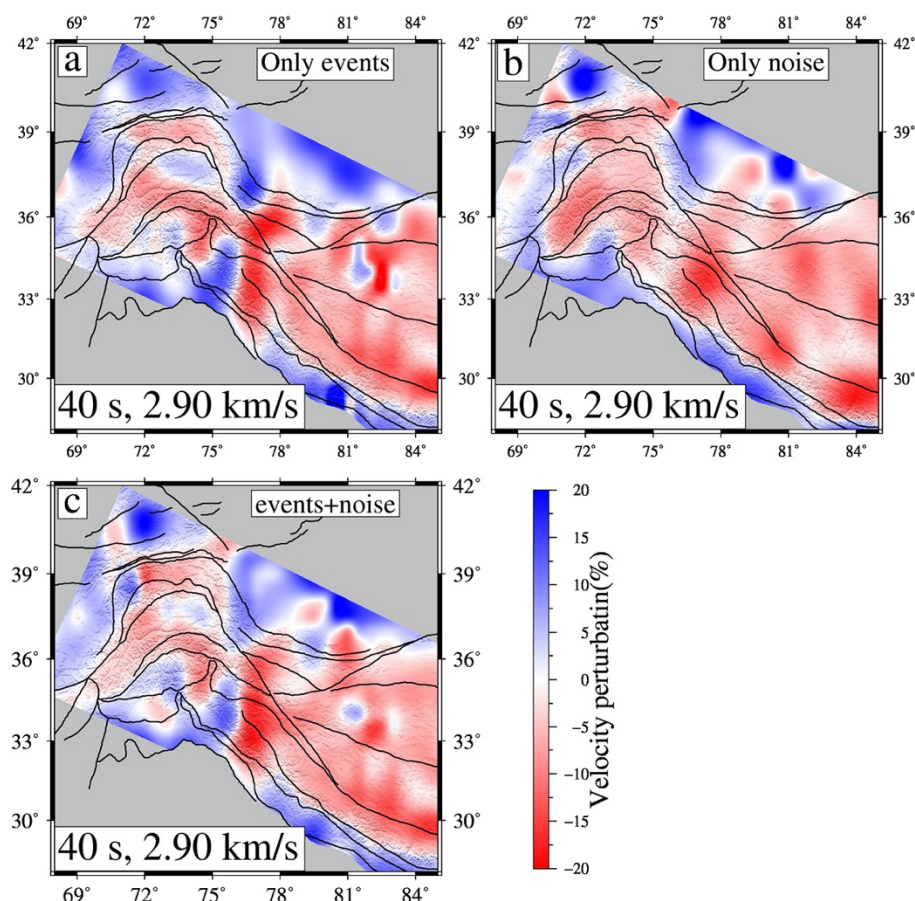
Figure 3.5*. Comparison of tomographic results at 40 s period with (a) only earthquake, (b) only ambient noise, and (c) combined earthquake and ambient noise. The color data is the group velocity in terms of velocity perturbations from the regional mean.*

3.2 Lateral variation of Rayleigh wave dispersion

Following the above approach, group velocity maps are constructed from period 5 to 60 s at every 1 s interval on a 0.5° x 0.5° grid interval (Figure 3.6a-g). The general consistency of structural features is observed across all periods. The sensitivity kernel shows the relation between the group velocity at a period and the corresponding depth of investigation (Figure 3.6h). The group velocity at 10−15s with a peak sensitivity at ~8−10 km below the Earth surface represents the upper crust, sedimentary basins, fold belts (Pasyanos, 2005). At shorter periods (10−20 s), the sedimentary basins (Tarim, Tadjik, Ferghana) and the Himalayan arc are characterized by low group velocities due to 5−15 km thick sediments. In contrast, the interior of both Pamir and Tibet have higher group velocities. Higher group velocities beneath the sedimentary basins and the Himalayan arc are observed for a higher period (30-40s) with peak sensitivity at 30-45 km depth. In

contrast, Pamir and Tibet have lower group velocities, albeit as discrete blocks separated by higher velocity N-S linear feature. These low-velocity features continue at 50−60s (with peak sensitivity depth ~ 50-80 km), possibly due to increased crustal thickness (up to 90 km) and widely reported mid/lower crustal low shear velocity of ~3.3 km/s under Tibet and Pamir.

The uncertainties in group velocities, ray hit counts, and the travel-time residuals are presented in Figures 3.7-3.9. Large standard deviations associated with the group velocity maps correspond to the areas with poor ray-path coverage, such as the northern Indian Peninsula and north-eastern Tarim Basin. At higher periods ($\geq$ 40 s), Western Syntaxis and central Himalaya show relatively higher uncertainties. Our group velocity maps significantly improve ray-path coverage and lateral resolution compared with previous experiments in the study region (Shen et al., 2016, Gilligan & Priestley, 2018; Kumar et al., 2019, Yang et al., 2012, Khan et a., 2017). We invert the dispersion curve at a given geographical location to constrain a 1D shear wave velocity model.
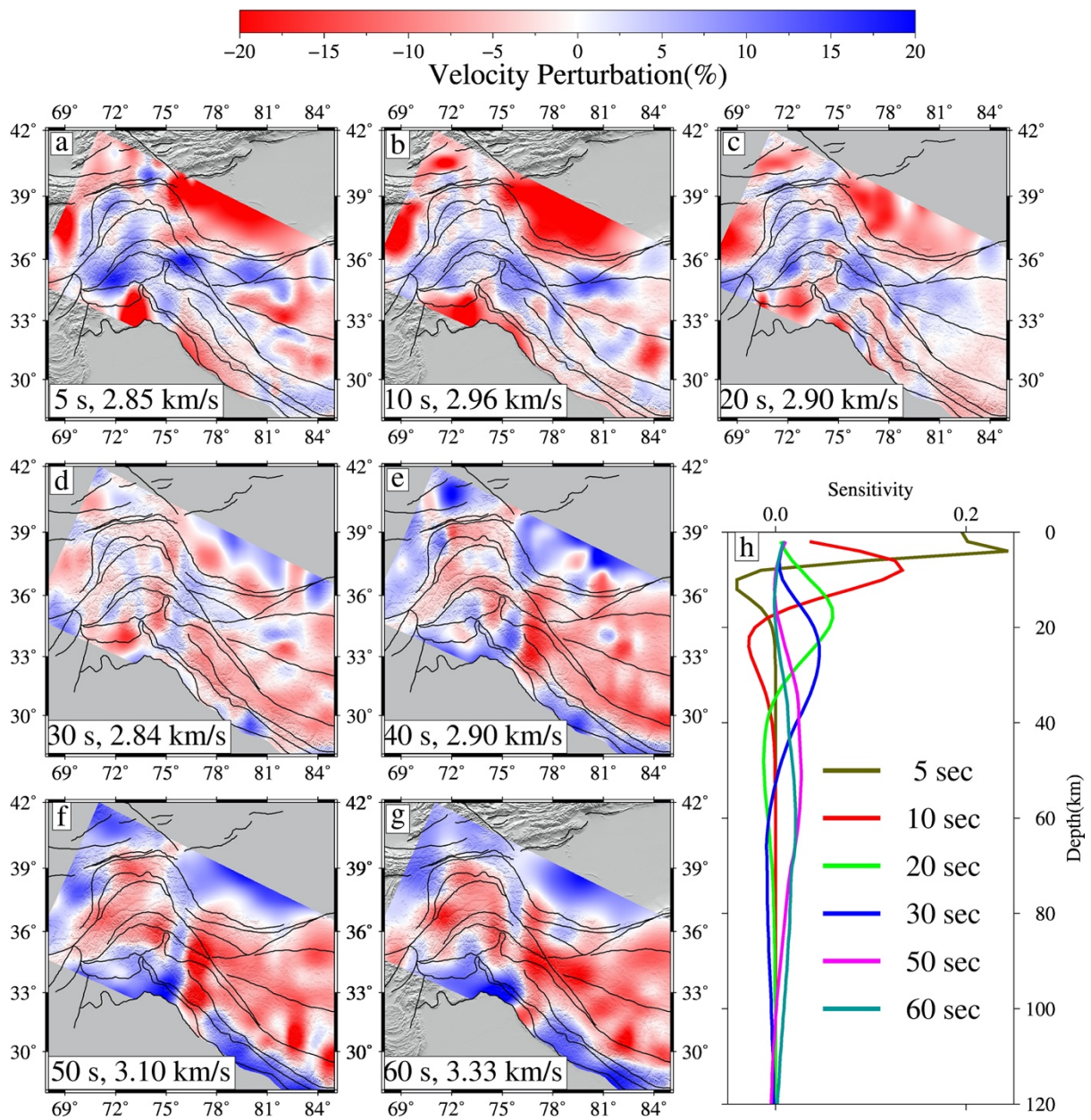
Figure 3.6 *Rayleigh wave group velocity maps. (a) to (g) Group velocity maps from period 5 to 60 s plotted as percentage deviations from the regional mean. The period and regional mean are marked at the bottom of each map. (h) Sensitivity kernels for Rayleigh wave group velocities at periods 5−60 s.*
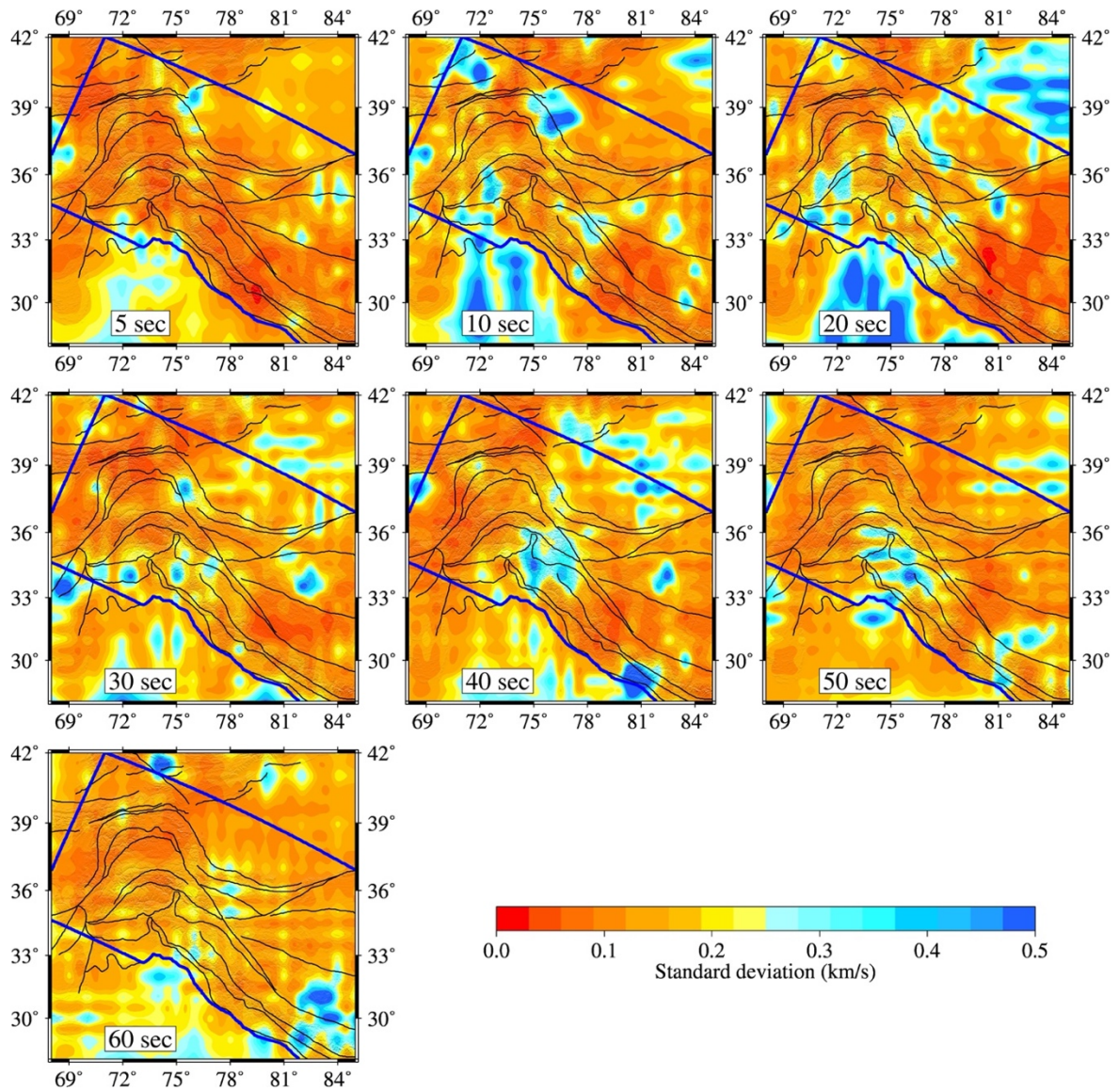
Figure 3.7 *Standard deviations of the posterior distributions for group velocity tomography at periods 5s, 10s, 20s, 40s, and 60s. The thick blue polygon indicates the region of interest in the study.*
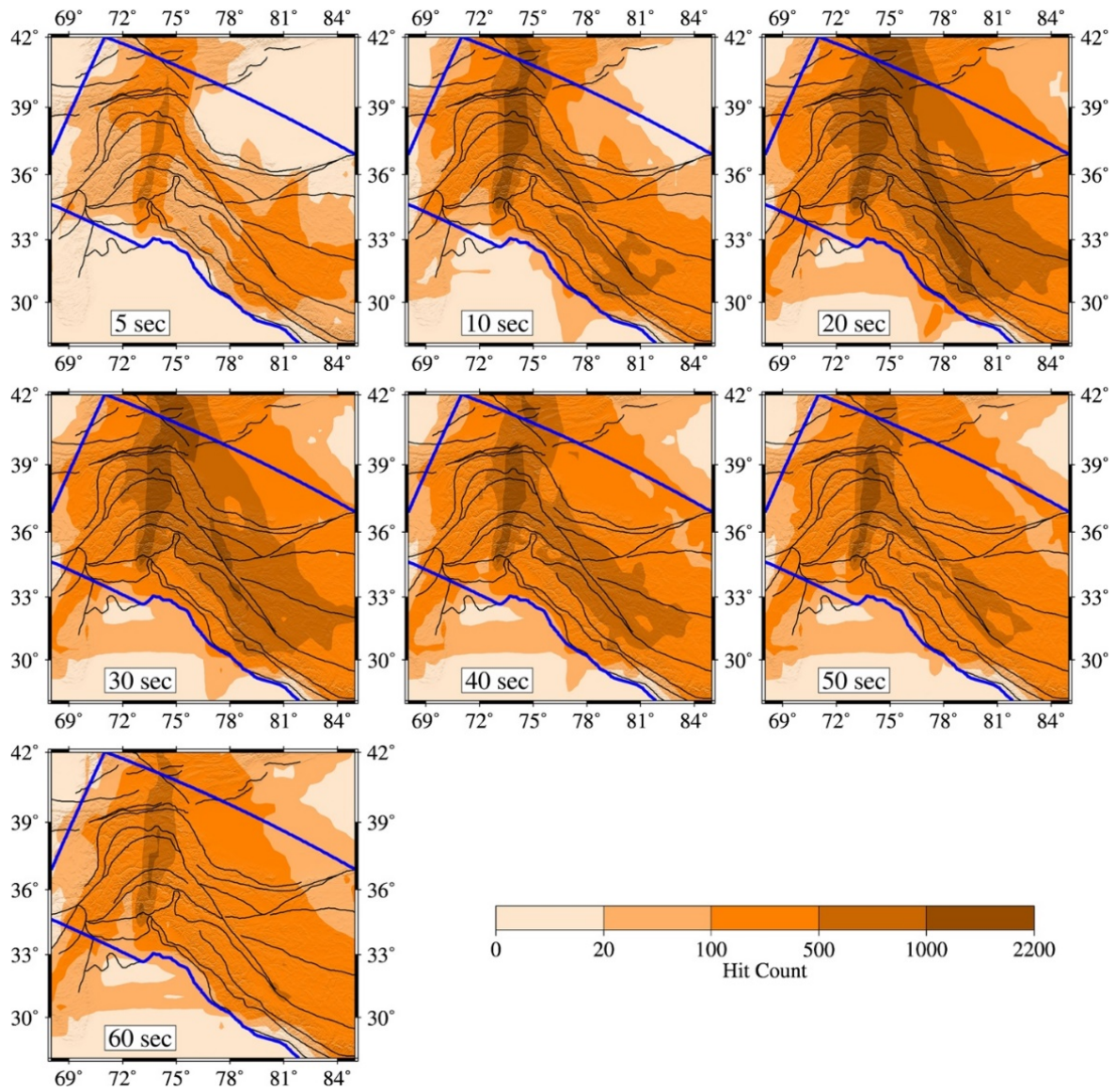
Figure 3.8 *Ray path density in 0.5° x 0.5° grid cells at different periods from 5 to 60 s.*
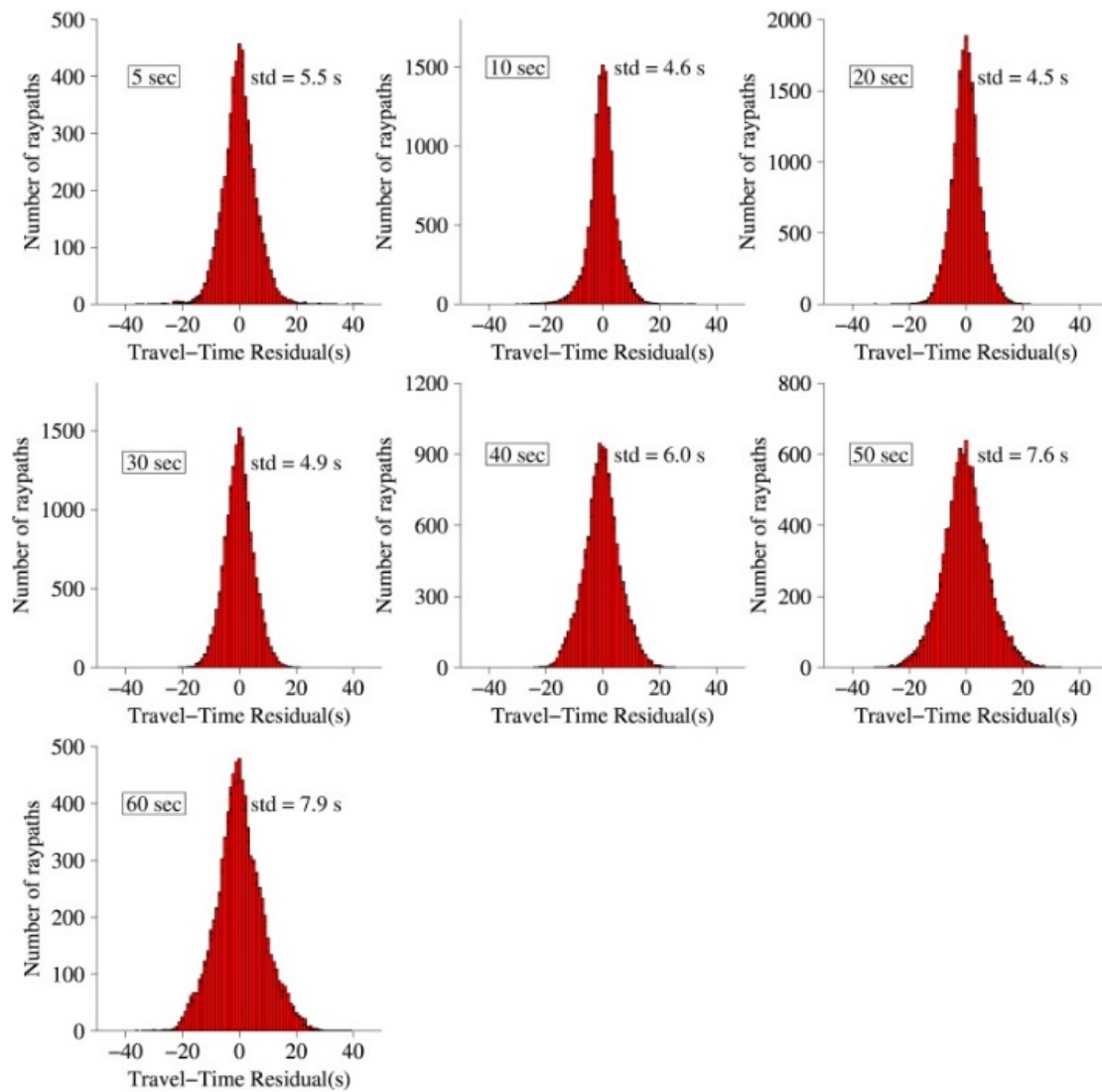
Figure 3.9 *Travel-time residuals after tomographic inversion at various periods from 5 to 60 s. The corresponding standard deviations are presented in each panel.*

3.3 1-D Velocity-depth models and their reliability

The velocity-depth variation from continuous group velocity maps is created following 1-D hierarchical Bayesian Inversion (Bodin et al., 2012b). First, we discuss various synthetic tests to analyze the sensitivity of prior on final models and resolving power of the inversion as discussed below.

CHAPTER 3

3.3.1 Effect of the prior distribution

We demonstrate the influence of the prior information on the inversion result using an input candidate model from Shen et al. (2016) (Figure 3.10a). A random Gaussian noise (2% of synthetic value) was added to the synthetic group velocity dispersion data (Figure 3.10b) from 5 to 60 s. Following Yuan and Bodin (2018), we selected three different reference models (m_0): i) ref-1: a simple homogenous half-space with 4 km/s velocity, ii) ref-2: a layered velocity model obtained from a regularized least square method using *surf96* (Herrmann 2013), iii) ref-3: a smoothly layered average model of Tibet obtained from averaging the 1-D models of Shen et al. (2016). We allow the velocity to vary up to 40 % from the reference models (i.e., w = 0.40) at all depths and invert the group velocity curve (Figure 3.10b) separately using the three prior distributions (prior 1-3; Figure 3.10c, 3.10f, and 3.10i).

The posterior distributions with computed mean and maximum are compared with the input model in Figure 3.10 (middle and right panels). For the half-space model (ref-1), the posterior is broad (Figure 3.10d). The mean and maximum of the posterior (MAP) do not follow each other, and a significant velocity mismatch happens between the input and output MAP models (Figure 3.10e). For the other two reference models (ref-2 and ref-3), both mean and maximum follow each other with a narrow posterior, which shows an improvement over the homogeneous half-space model (Figure 3.10g and 3.10j). The output means with the reference model from the least square method (Ref-2) slightly underestimates the input structure at higher depths than the output MAP model (Figure 3.10h). In contrast, inversion using Tibet's average model (Ref- 3) can recover the velocity amplitude up to 75 km (Moho depth in the input model) in both the mean and MAP model (Figure 3.10k). Note here that the model uncertainty (derived from the posterior standard deviation) increases with depth. Beyond 75 km depth, we observe a significant departure from the actual model, possibly due to the poor sensitivity of surface wave data in the current period range (5-60 s) to greater depths. This test demonstrates that the choice of the reference model does not influence the mean of the posterior, and the crustal structures can be reliably recovered within the period range considered in this study. However, other statistical measures such as median and mode can also be used apart from the posterior mean. For this study, we use the average model of Tibet (ref-3) as the reference model to invert for the final shear wave velocity model.
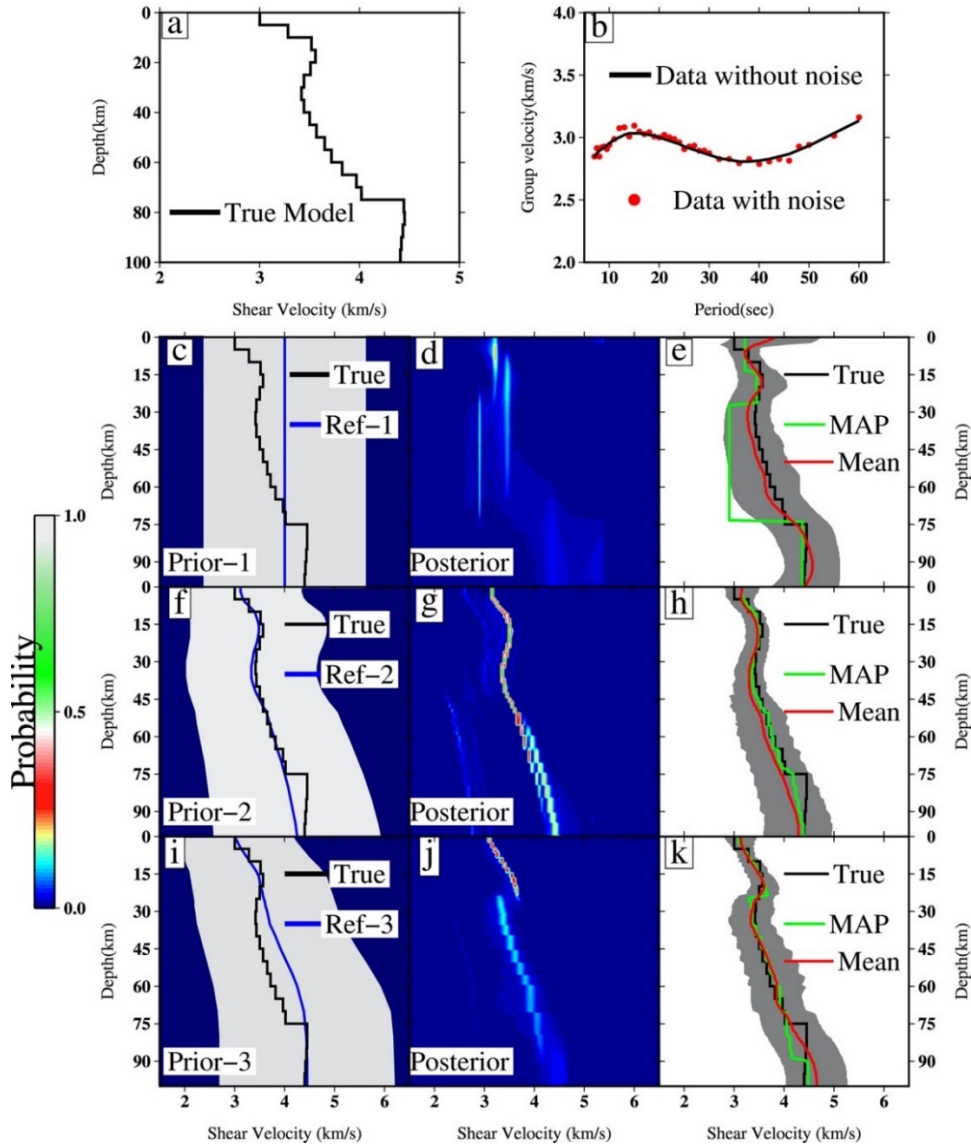
Figure 3.10 *Sensitivity test for prior distribution. (a) A synthetic input model at 32° N, 82°*
E is taken from Shen et al. (2016). (b) Synthetic dispersion with and without added Gaussian
noise. Three different priors (Prior-1, 2, 3) are shown in c, f, and i, with corresponding
reference models shown in the blue line. Ref-1= homogenous half-space model, Ref-2=
smoothly layered model from the regularized least square method, Ref-3= smoothly layered
average model of Tibet from Shen et al. (2016). White shaded area indicates 40 % velocity
perturbation from these reference models with probability 1 and blue colour with
probability 0. The true input model is also shown in the black line. Output posterior
distributions for the three priors are shown towards their right in d, g, and j. c, h, and k
show a comparison of the mean (red) and maximum (green) of the posterior distributions
with the actual input model (black). The grey shaded area represents one standard deviation
bounds.
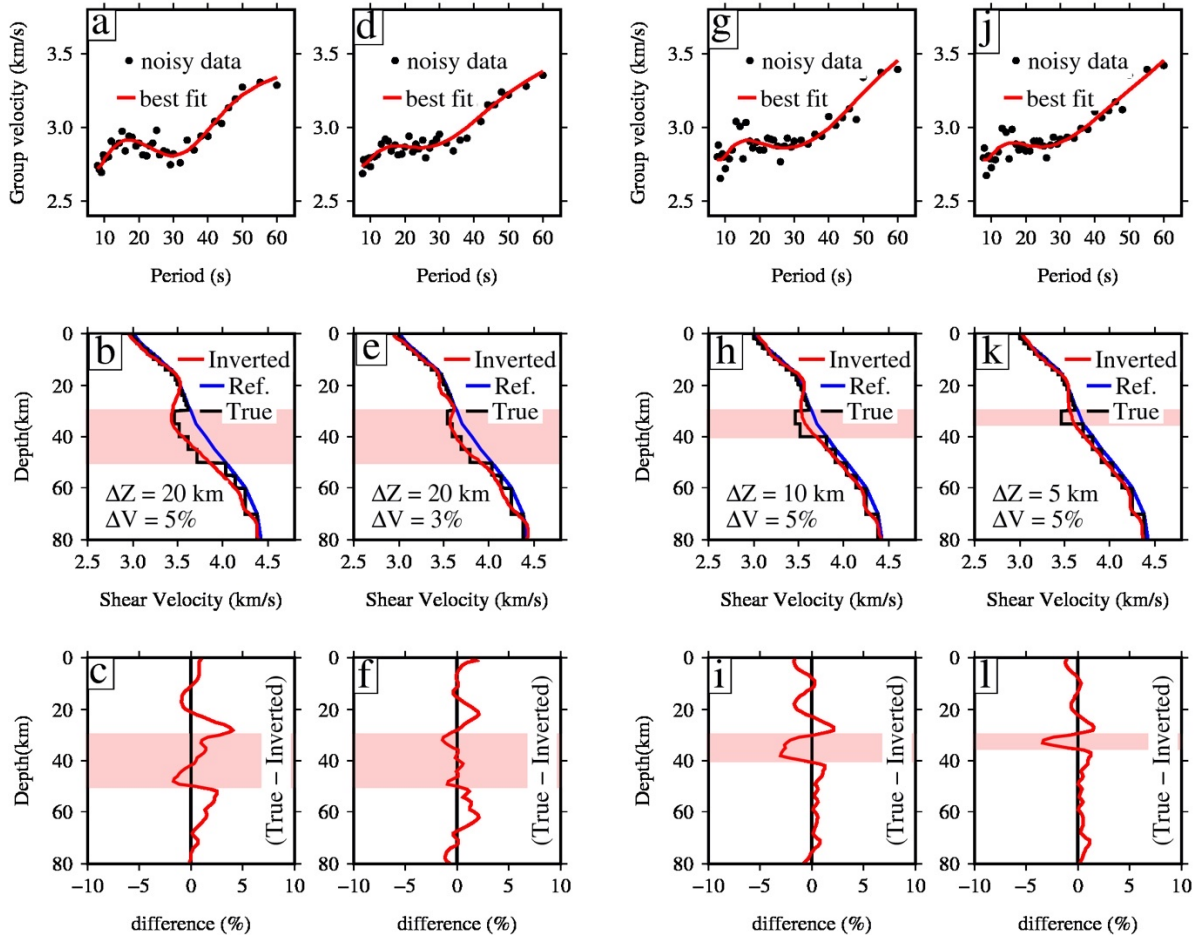
Figure 3.11 Synthetic test for resolving a low-velocity layer in the crust. The blue lines show the reference model. The black lines show the input model with a low-velocity layer created by perturbing the reference model between 30 to 50 km. The pink shaded areas denote the low-velocity layers with different thicknesses (ΔZ). (a-c) test with a 20 km thick low-velocity layer created by perturbing the reference velocity (shown in blue) by 5%. The synthetic data with added noise and the best fit after the inversion are shown in (a). The inverted model (red) is compared with the actual model (black) in (b). Red line in (c) shows the percent difference between the True and the inverted model. (d-f) same as (a) to (c) with the low-velocity layer created by perturbing the reference velocity by 3%. (g-i) same as (a) to (c), but the low-velocity layer has a thickness of 10 km with the low-velocity amplitude perturbed by 5 % from the reference. (j-l)): same as (a) to (c), but the low-velocity layer has a thickness of 5 km with the low-velocity amplitude perturbed by 5 % from the reference.

CHAPTER 3

3.3.2 Resolving a mid-crustal low-velocity layer

The mid-crustal low velocity between 20 to 50 km depth is widely observed over Tibet. Thus, it is critical to investigate the resolving power of the period range and inversion scheme considered in this study in mapping the low-velocity layer. We use the average model of Tibet (Ref-3 in the previous section) and perturbed it by 5% and 3% to create input models with a low-velocity layer (LVL, black lines in Figure 3.11) of varying thickness in the depth range of 30−50 km. In the first case (Figure 3.11a-f), we kept a constant layer thickness (20 km) and varied the amplitude of LVL by 5% and 3%. In the second case (Figure 3.11g-l), we altered the thickness of the LVL while keeping a constant velocity perturbation of 5%. Similar to the previous test, we generated synthetic group velocities from 5 to 60 seconds with added random Gaussian noise (2 % of the theoretical value) for all combinations of the LVL (Figure 3.11, top panels). The inversion results (Figure 3.11b and 3.11e) in the first case of constant 20 km LVL recover both the amplitude and low-velocity pattern. As the layer thickness decreases in the second case, the recovered models (Figure 3.11h and 3.11k) underestimate the amplitude of the LVL while the pattern is well resolved. Also, note that the inversion always underestimates the low-velocity amplitude by less than 5 % of the true value (Figure 3.11, bottom panels). Based on this experiment, we believe that an LVL with a minimum thickness of 5 km can be resolved within the considered period range in this study.

After various synthetic tests investigating the resolving power of the dispersion data in crustal imaging, we performed the final 1-D inversion using 480 parallel Markov chains with maximum iterations of 100,000. The first 50,000 samples were discarded as "burn-in" samples, and every 10th sample of the remaining 50,000 samples constitute the final ensemble of solution models. The final ensemble model's mean and standard deviations were used as average shear velocity and associated uncertainty. We used uniform priors on the number of layers (2−100) and the data noise level (0−10 %) by allowing the shear wave velocity to perturb up to 40 % from the reference model (ref-3) within a maximum depth of 100 km. A 3-D shear velocity with 0.5° × 0.5° grid intervals was constructed by interpolating each 1-D model. To strengthen the reliability of the inversion result, we compare our velocity model with several previous studies at different locations such as IZS, Western Syntaxis, and Hindu Kush (Figure 3.12). Also, we generated a velocity depth section along with the profile of Gilligan et al. (2015) in western Himalayas and contiguous Tibet (Figure 3.12). We observe a general similarity in the present work and earlier velocity

models, albeit with local variations due to different data, methodology, and spatial resolution.
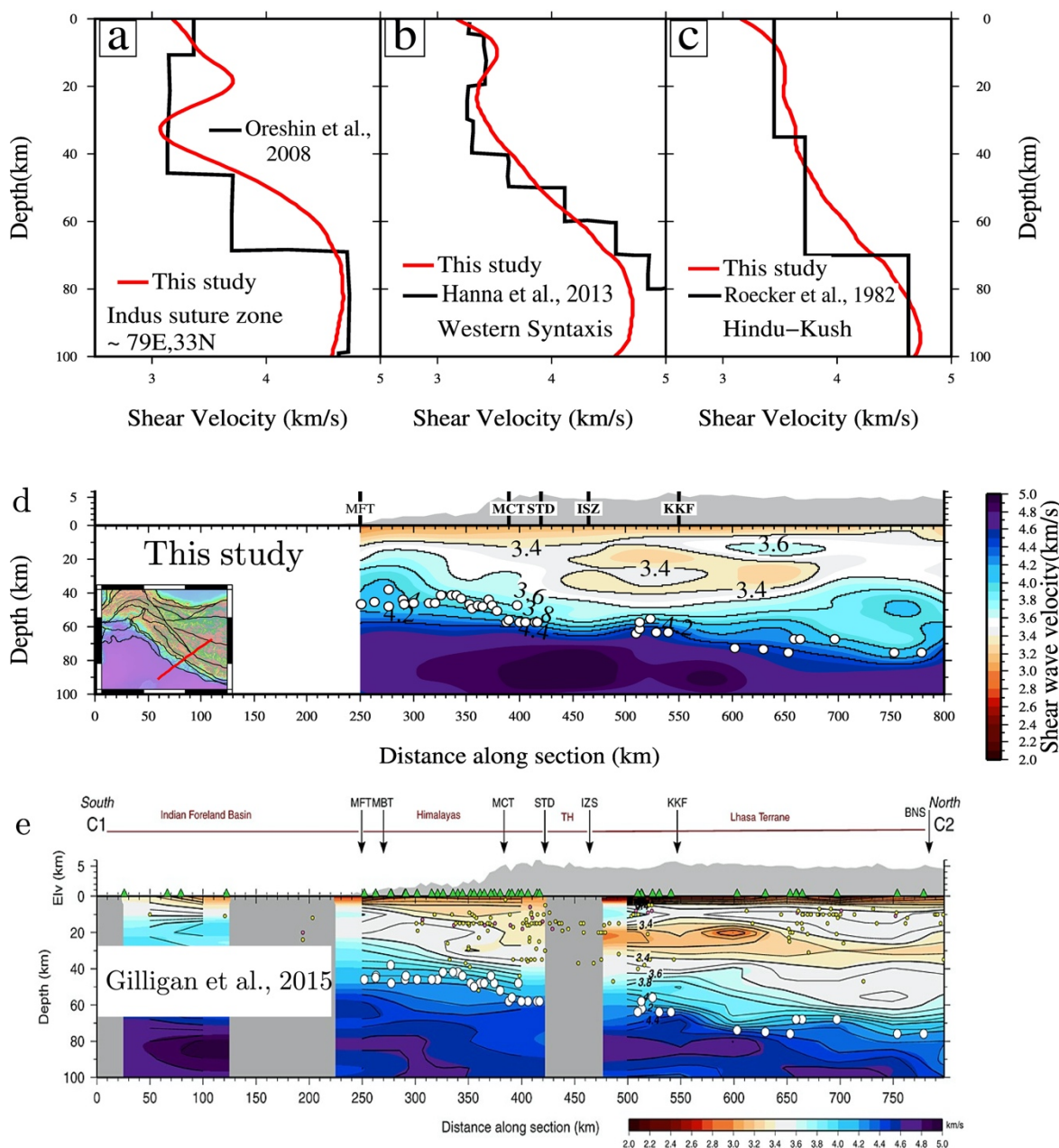
Figure 3.12 *Comparison of shear velocity model of this study with previous studies. Comparison of the 1-D model of this study with (a) Oreshin et al. (2008), (b) Hanna et al. (2013), and (c) Roecker et al. (1982). In Figure d and e ,we compare our velocity depth section (d) across Garhwal Himalaya - western Tibet with Gilligan et al. (2015) . Location of the profile is shown in Figure d inset. The surface topography with major faults and boundaries is shown on top of the profiles. The black lines are Vs contours, and white dots are Moho depths.*

3.4. Shear wave velocity structure and regional variability

3.4.1 3-D Shear wave velocity maps

We discuss general features of the computed shear velocity model over the study region. Figure 3.13 shows the map of shear wave velocities at depths 10, 30, 50, and 70 km relative to the regional average. At shallower depths (~ 10 km), parts of the Tarim, Tadjik, and Ferghana sedimentary basins show prominent low-velocity zones (LVZ) due to thick sediments. The Himalayan arc has a distinct velocity contrast with noticeable low velocities in its western and northwestern segment (west of 78°E) compared to marginally higher velocity in the central Himalaya (east of 78°E). Such a velocity divide could be due to several basins (e.g., Kangra, Kashmir, and Peshawar) in the western Himalayas, which are absent in the central Himalayas. The interior of Pamir, Hindu-Kush, and west Tibet mostly contain high shear wave velocities.

 At 30 km depth, three prominent regions of LVZ corresponding to western Tibet (L1), Zanskar Ḥimalaya-Ladakh-Karakorum (L2), and Pamir-Hindu Kush (L3) are observed. Low velocities in western Tibet are well documented and are possibly due to partial melts or aqueous fluid (Gilligan et al., 2015; Yang et al., 2012). Beneath Ladakh and Karakoram, low velocities indicate the presence of young granites (Searle et al., 2010). In Zanskar Himalaya, the low-velocity zones collocate with large-scale migmatites and granites. Low velocities from eastern Kohistan through Ladakh continue to southern Tibet. Beneath Pamir, the low velocities correlate with the surface exposure of gneissic domes formed due to melting at a 30−50 km depth and transported upward.

The LVZs become more widespread at 50 km depth (Figure 3.13c). Its continuity can be observed from western Tibet to the Pamir-Hindu Kush region through Ladakh and Karakoram. An interesting feature of the velocity map is a well-defined N-S trending low-velocity region extending from Zanskar Himalaya in the south to Ladakh-Karakoram and up to western Kunlun (76-78°E). Generally, depth ranges of crustal LVZs have a progressive northward deepening starting from ~ 20 km in the western Himalaya to ~ 30 km in the Indus suture zone, southwestern Tibet, Karakoram, Hindu Kush, and southern Pamir. Further north, we observe LVZ in northwestern Tibet, central and south Pamir, and northern Hindu-Kush at depths of ~ 40−50 km. At a progressively deeper depth of 70 km, most parts of the Himalayas and Ladakh are characterized by higher velocities representing

the uppermost mantle. At the same time, western Tibet-Kunlun and Pamir-Hindu Kush regions have lower velocities (correlating with deep seismicity), possibly due to the thicker crust and higher mantle temperature (Rai et al., 2006; Zhang et al., 2014; Schneider et al., 2019).
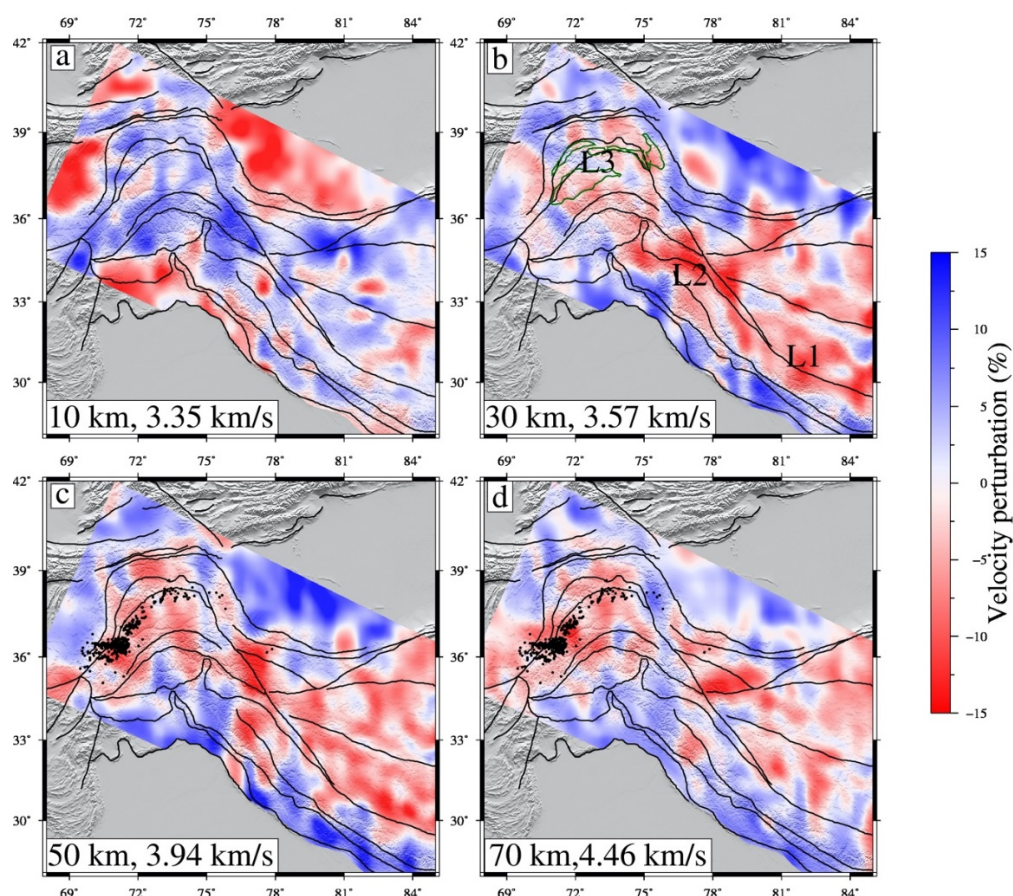
Figure 3.13 Shear velocity maps at depths of (a) 10, (b) 30, (c) 50, and (d) 70 km are plotted as perturbations from the regional mean velocity. The mean velocity is calculated by the area average of 3d velocity model at different depths. The black dots in (c) and (d) represent earthquakes at a depth > 50 km. The green polygon in b shows gneiss domes of Pamir. L1, L2, and L3 are the low-velocity zones at 30 km depth.

3.4.2 Uncertainty in velocity models

Uncertainty in the velocity model is analyzed in terms of posterior standard deviations presented in Figure 3.14. The velocity uncertainty increase with depth, also seen in the synthetic tests performed in sections earlier. At greater depths, the increased uncertainty could be the combined effect of the trade-off between the crust and upper mantle velocities

and poor data sensitivity to structure beyond 80 km. Although the posterior gets wider with depth given broad priors and flexible model parametrizations used in this study, the uncertainties clearly show the inherent non-uniqueness of inverse problems.
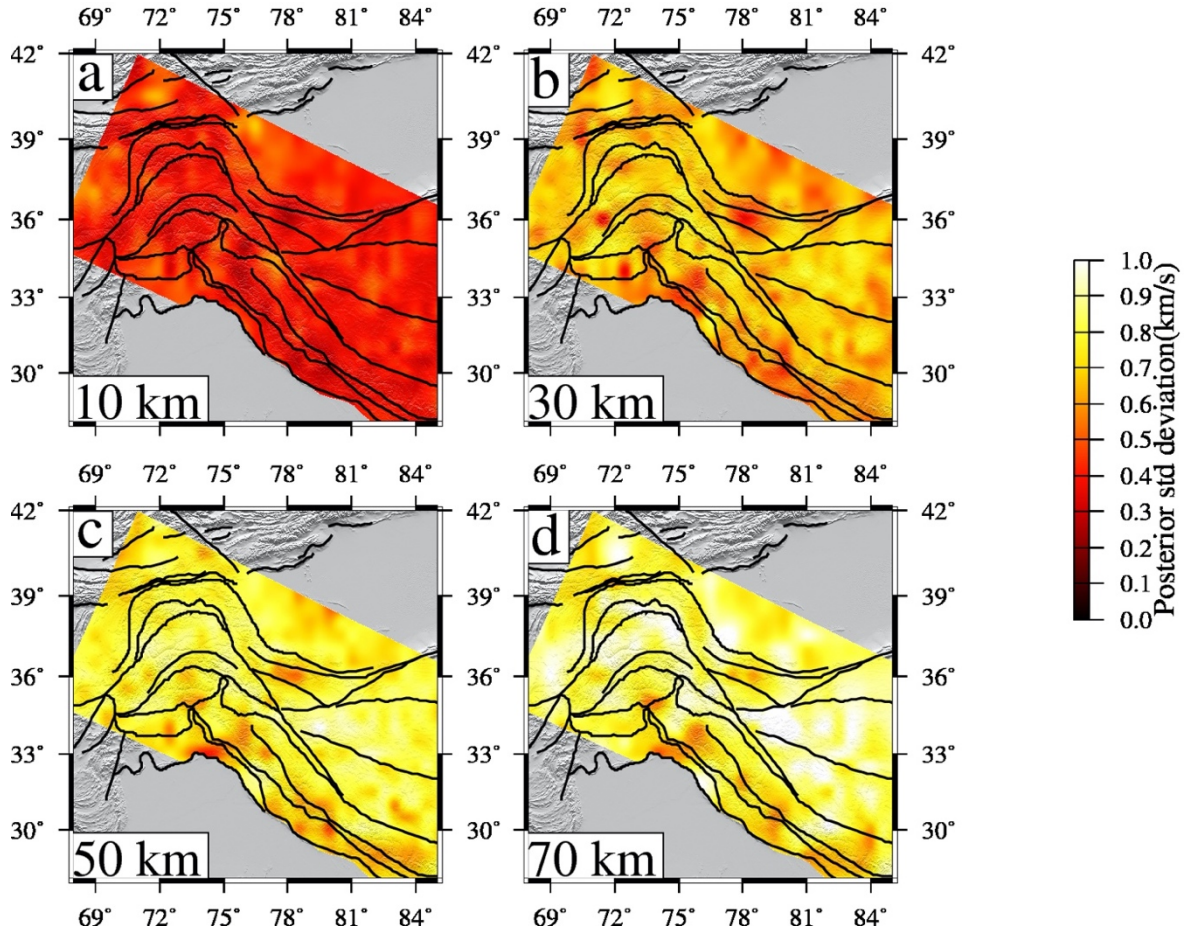
Figure 3.14 *Maps of posterior standard deviations for shear wave velocity models at depths 10, 30, 50, and 70 km.*

3.4.3 Influence of Moho depth and mantle velocity on crustal velocity

A synthetic test considering different Moho depths and mantle velocities shows that the velocity trade-off has minimal effect on the crustal structures (Figure 3.15), thereby enhancing the reliability of the velocity model presented here.
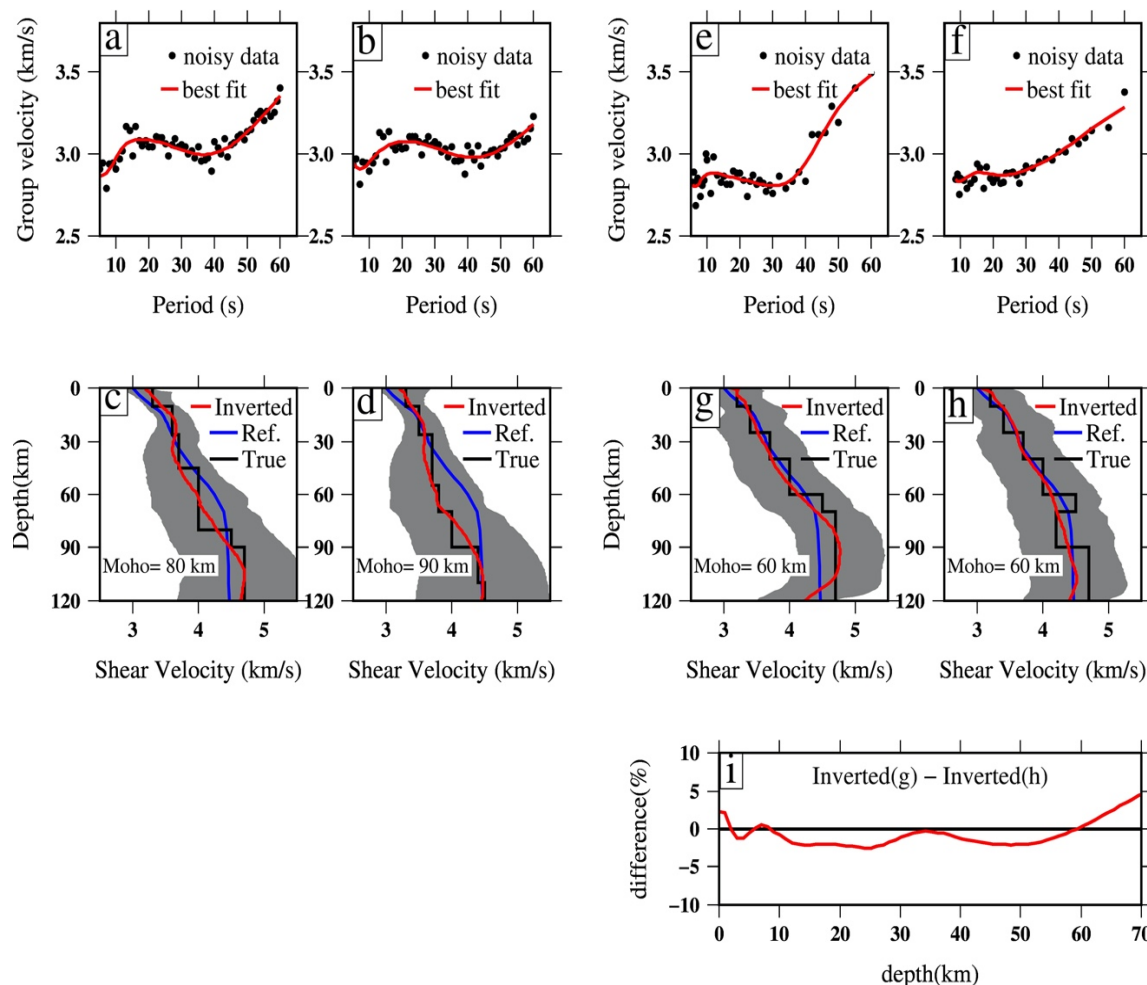
Figure 3.15 *Test for depth sensitivity and the trade-off between crust and mantle velocity.*
(a) Test with a Moho at 80 km. The synthetic dispersion data with noise (black dots) and
best fit obtained after inversion (red line) are presented. (b) same as (a) with a Moho at 90
km. (c) shows the comparison of the recovered model after inversion (red) with the actual
model (black) for data in (a). (d) same as (c) for data in (b). Dark shaded areas show one
standard deviation. (e-h) same as (a) to (d), but show the test for crust-mantle velocity
trade-off with a Moho depth of 60 km and an upper-mantle low-velocity anomaly in (h). (i)
difference of the output models with and without mantle anomaly in (g) and (h) shown in
percentage. For each experiment, the reference velocity is shown as the blue line.

3.4.4 The crustal velocity-depth sections and regional variability

To investigate the detailed crustal structure and correlation with surface geology and possible earth processes, we present six velocity-depth sections from the Himalayas in the south to Pamir/Tarim in the north (Figure 3.16). We did not compute Moho depth due to a

substantial trade-off between Moho depth and the crust-mantle velocity structure in the inversion of surface data (Lebedev et al., 2013). Instead, we marked the Moho depth on the velocity section obtained from earlier studies primarily using receiver function (RF) data (top right panel in Figure 3.16). We used a broad constraint on Moho depth based on Sn velocity tomography result that suggests an average value of 4.55 km/s for the Himalaya-Tibet, which reduces by 3−4 % over the northern Tibet (Pei et al., 2011).

The continental crust is divided into the upper, middle, and lower crust with a characteristic shear wave velocity Vs < 3.6 km/s, 3.6−3.8 km/s and, > 3.8 km/s, respectively. The shear wave velocities higher than 4.0 km/s are due to rocks of mafic composition (garnet granulite) and are widely referred to as 7x layer (Vp > 7 km/s) (Christensen & Mooney 1995; Rudnick & Fountain, 1995). A high-velocity lower crust can form by various mechanisms such as magmatic additions to the crust in the form of mafic magma or through magmatic differentiation processes. Mechanical addition of high-velocity materials to a crustal column is possible during collisional or accretionary tectonic events (Schulte-Pelkum et al., 2017). A Vs > 4 km/s layer in the lowermost crust may also represent an eclogite as proposed in the Himalayan collision zone (Sapin & Hirn, 1997; Nábělek et al., 2009). The shear wave velocity lower than 3.4 km/s is attributed to the presence of sediments and (or) fluids (Yang et al., 2012).

Figure 3.16 (profiles A-A′ to C-C′) represents three velocity-depth sections from High Himalaya to western Tibet-Tarim along 84°, 82°, and 79°E. The 84°E profile almost follows the Hi-CLIMB seismic line (Nábělek et al., 2009) re-investigated by Nowack et al. (2010) and Xu et al. (2013). The Moho between 28−34°N and 34−37°N is taken from Nábělek et al. (2009) and Shen et al. (2016), respectively. The result of the MT experiment provides an additional constraint on crustal structure around the BNS (Solon et al., 2005). Our velocity image has several notable features. Moho depth computed using RF correlates with the shear wave velocity (Vs) of 4.4−4.6 km/s in the Himalaya and southern Tibet, and a reduced velocity of 4.0−4.2 Km/s in Northern Tibet as expected due to significant deformation and higher mantle temperature in northern Tibet (Molnar et al., 1993). The Moho depth increases from ~50 km (Vs ~ 4.4 km/s) beneath the STD to about 75−80 km (Vs ~ 4.6 km/s) till 31°N in the Lhasa block. Further north, it is identified with Vs ~ 4.4 km/s at a depth of 70 km, continuing till 33.5°N in the Quiangtang block and at 60 km (Vs ~ 4.0−4.2 km/s) beneath the Songpan block. We observe a structural break in Moho and the upper mantle at 31°N, also correlated with the weak Moho converted phase in the

receiver function (Nábělek et al., 2009). A continuous 20 km thick underplated 7x layer (Vs > 4 km/s) is observed from the Tethys Himalaya to about 33°N, beyond which it significantly thins. Nábělek et al. (2009) interpreted the continuation of underplated Indian lower crust only till 31°N based on their CCP modeling. The complexity of Moho between 31−33°N has been inferred earlier by Xu et al. (2013). It is feasible that the Indian crust decoupled from the underlying subducting lithosphere at 31°N and moved further north with the overlying crust. In the middle crust at a depth of 20−50 km, we observe two prominent low-velocity pockets, one about 150 km long stretch of north dipping low velocity (Vs ∼ 3.4 km/s) across southern Lhasa block (Gangdese batholith) and the other beneath the north Qiangtang block at a depth of 10−25 km.

The velocity image along 82°E (Figure 3.16, profile B-B′) aligned with the ANTELOPE profile (Murodov et al., 2018) shows a complex crustal structure. The Moho with Vs of 4.4−4.6 km/s dips northward from 50 km below the High Himalaya to 80 km below the BNS at 32.5°N. Further north beneath the Qiangtang block (32.5−34.5°N), we observe complex velocity structures in the depth range of 70−100 km. In this region, Murodov et al. (2018) reported a 15 km upward offset in Moho below northern Lhasa (at 32°N) and a depressed Moho up to 90 km below central Qiangtang (at 33.5°N). In the Songpan block, the Moho is at a depth of 70 km (Vs ∼4.4 km/s) and then abruptly shallows to 48 km (Vs ∼ 4.2 km/s) beneath the Tarim Basin. Maceira and Ammon (2009) observed Moho depth of 53 km and uppermost mantle velocity of 4.3 km/s beneath the western Tarim. The lower crust high-velocity layer (7x) is about 20 km thick from the Tethys Himalaya (29°N) to the BNS (33°N) and thins to 10 km beneath the Songpan block. Our observation of the highly gradational Moho beneath the Tarim basin from 30 km (Vs ∼ 4.0 km/s) to 60 km (Vs ∼ 4.4 km/s) is also observed by Maceira and Ammon (2009). The uppermost mantle velocity and Moho complexity between 33°N and 34.5°N representing the Qiangtang block may indicate the domain of interaction between the subducting Indian and Asian plates. Similar to the profile A-A′, we observe a thick low-velocity zone (3.2−3.4 km/s) in the middle crust progressively deepening from about 20 km beneath the STD to 45 km at 32°N in the northern Lhasa. Two additional discrete and localized low-velocity zones are also present beneath the Qiangtang (central Tibet) and Songpan block. However, we could not find any spatial continuity of the mid-crustal low-velocity packets between the southern Tibet and northern Tibet in profiles along 84°E and 82°E (Figure 3.16, profile A-A′ and B-B′).
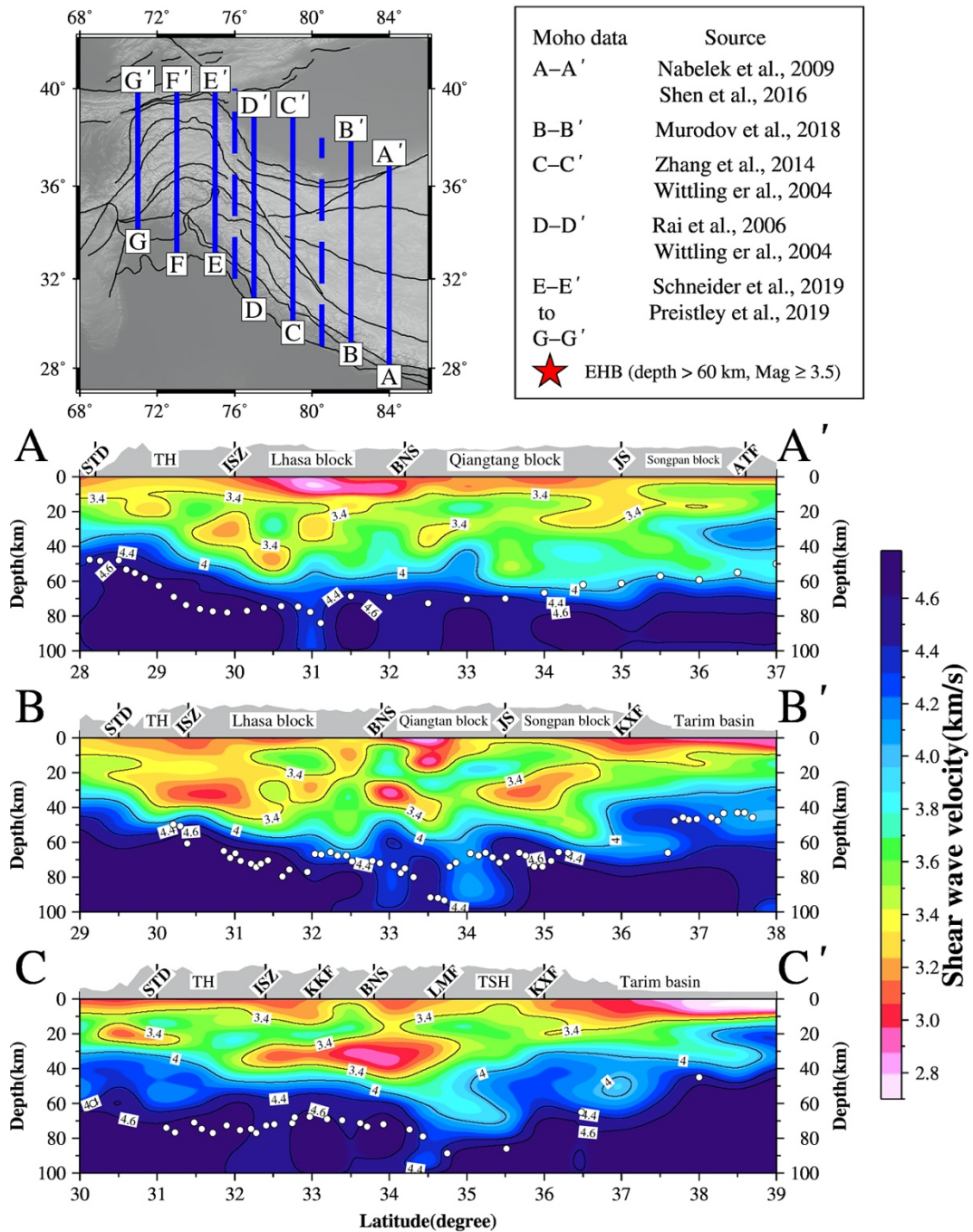
Figure 3.16 *North-south velocity-depth sections along varying latitudes. The Location of profiles (thick blue line) is shown at the top left corner. Sources providing Moho data (white dots in each profile) are presented in the top right corner. Surface topography with positions of major tectonic blocks and faults are presented at the top of each profile. The color data indicate absolute shear wave velocities below sea level from depth 0 to 100 km. The black lines in each velocity profiles indicate Vs contours at 3.4, 4.0, 4.4, and 4.6 km/s. Two additional profiles (dashed blue lines at the top right corner), between B and C and between D and E, are also presented in Figure 3.18.*

The velocity section along 79°E (Figure 3.16, profile C-C′) has been investigated by several researchers in individual segments from the Ganga basin to STD (Mahesh et al., 2013; Caldwell et al., 2013), Indus Suture to LMF (Zhang et al., 2014), and LMF to ATF (or KXF) with horizontal offsets (Wittlinger et al., 2004). We used Moho depths inferred from these experiments to constrain the nature of the lower crust. Two distinct low-velocity layers (Vs < 3.4 km/s) are present in the middle crust. The southern one at 20 km depth is between STD and MCT in Garhwal Himalaya with a thickness of 10 km, while the other is nearly horizontal from the ISZ to LMF with a varying thickness of 10−20 km. The high velocity (7x) lowermost crust is ~ 25 km thick (from 35 km to Moho at 60 km) beneath the high Himalaya, progressively decreasing to about 15 km between LMF and KXF, where Moho is 80 km deep. In the vicinity of the KXF and further north, we observe a sharp decrease in Moho depth. It reaches 60 km at the KXF and 45 km in the Tarim Basin at 38°N. Between 35°N and 37°N (approximately between LMF and KXF), the high-velocity lower crust is significantly thick. We identify continuity of the high-velocity Indian lower crust till 35.5°N (about 80 km north of LMF). The Moho corresponds to the shear velocity contour of 4.4 km/s in the TSH and Tarim Basin and 4.6 km/s in the Tethys Himalaya, Lhasa, and Qiangtang blocks.

Figure 3.17 represents velocity-depth sections in the western and northwestern Himalaya extending to western Tibet and Pamir-Hindukush. The velocity profile along 77°E (Figure 3.17, D-D′) is widely considered the contact of the western and central Himalaya and western Tibet and Pamir. It also represents changes like the production of granites and the subduction behavior of the India plate. The profile presents a complete section of India-Ladakh-Asia convergence with a well-preserved deformation history of the Indian plate in the strongly deformed Tethyan passive margin platform and the shelf sedimentary rocks in Zanskar (Corfield & Searle, 2000). Along the profile, the Indian crust is ~ 50 km thick with the high velocity lower crust (7x layer) of 15km. It flexes northward at MCT to the Zanskar shear Zone (STD equivalent). Note that 77°E marks a significant boundary in the western Himalayas. East of 77°E, the hanging wall of the MCT has high-grade metamorphic rocks of Greater Himalayan Crystalline (GHC), whereas, west of the 77°E, the MCT juxtaposes low-grade metasedimentary rocks of Tethys and Lesser Himalaya. The large offset in 4.0 km/s velocity contour at 32.5°E probably indicates this lateral variation in the Himalayan geology. The lowermost crust, identified by 4.0 km/s velocity contour, is nearly flat at a depth of 60 km northward from the Zanskar to Ladakh

and the Karakoram. The Moho deepens from 50 km beneath the MCT to about 70 km in the Tethys Himalaya and Ladakh and 80 km beneath the KXF. Farther north, it thins to 60 km with a large vertical offset in the Tarim Basin with about 20 km of the higher velocity lower crust. Along with this profile, we observe two prominent and discrete low-velocity layers between 20 to 50 km depth: a north-dipping layer (Vs ~ 3.4 km/s) beneath the Zanskar and the other (Vs 3.0−3.4 km/s) beneath the Ladakh and Karakoram. Across the Karakorum fault, all structures are continuous, suggesting the shallow nature of the fault. The northern edge of the Indian crust could be traced to the KXF, which marks the zone of deep seismicity and large vertical offsets in crustal structures.

The velocity sections along 75°E, 73°E, and 71°E (Figure 3.17, profile E-E′, F-F′, G-G′) represent the convergence of the western India-Kohistan plate with the Asian plate (Karakorum-Pamir-Hindukush). The Pamir-Hindukush is a complex interplay of eastward subduction of Asia in its southwestern part and southward subduction in the northern region. Along 75°E (E-E'), the Moho depth with Vs of 4.4 km/s, vary from 50 km beneath the Lower Himalaya to 70 km beneath the southern Pamir at 37°N. Further north, it progressively decreases to 50 km beneath the Main Pamir Thrust. The high velocity lower crust (7x layer) continues uninterrupted from the MCT in the south to Main Pamir thrust in the north, except a localized 40 km wide flexing at 37°N, where deep earthquakes are observed. This flexing combined with deep Moho and deep seismicity probably suggests an Indian and Asian crust intersection. The high velocity lower crust is interpreted as a seismic response of gradual eclogitization of subducting crustal materials, a view supported by the presence of eclogite and other high metamorphic rocks in the crustal xenoliths (Hacker et al., 2005), receiver function (Schneider et al., 2019), and tomographic studies (Sippl et al., 2013; Kufner et al., 2017). Two prominent low-velocity layers in the depth of 20−40 km are mapped along the profile: the first one from 34°N to 37°N between Indus suture/Main mantle thrust to Tirich Mir fault covering Kohistan arc-Karakorum batholith and its northward extension; and the second below the surface exposure of the gneissic dome in the central Pamir between RPS and ATS.

The velocity structure along 73°E (F-F′) from the Pakistan Himalaya to North Pamir crosses two major geologic terrains– the Kohistan arc and the Shakhadra dome. The Moho depth increases from 50 km below the lower Himalaya to about 80 km at the MKT represented by Vs of 4.4 km/s. Below Kohistan arc, the 7x layer is significantly thick (25 km) in the depth of 35−60 km, suggestive of an unstable lowermost crust that could detach

in the future, leading to the evolution of a more felsic continental crust (Jagoutz and Kelemen, 2015). In Pamir, the Moho is at an average depth of 60 km and characterized by reduced Vs of 4.0−4.2 km/s, suggesting higher mantle temperature. Schneider et al. (2019) inferred Moho doublet and large flexure of the 7x layer in central Pamir at ~ 38.5° N. The region is also characterized by deep seismicity. They interpreted this complex feature as a result of subducting Asian lower crust detached beneath the central Pamir (represented as dashed red lines in profile F-F′). Similar to the velocity profile along 75°E, we observe that interaction of the Indian and Asian crust may produce thick 7x layers with crustal thickness reaching 80 to 90 km depths at 38.5°N. A mid-crustal (20−40 km depth) low-velocity domain is mapped in south Pamir beneath the Shakhadra dome. The presence of low velocity in the depth of 20−40 km beneath the high-grade gneiss domes is also supported by local earthquake and surface wave studies (Sippl et al., 2013; Li et al., 2018). These high-grade gneiss domes were formed by large-scale crustal extension with exhumation from 30–50-km depth (Hacker et al., 2017), and have a geothermal gradient of ~40°C/km that would lead to melting temperatures > 700°C below ~20 km for most of the crustal rocks observed here as low-velocity zones. Peshawar basin (33-35°N), at the southern extremity of the profile, in the western Himalaya is characterized by low-velocity to a depth of ~20 km.

The westernmost velocity section along 71°E from the Main mantle thrust/ISZ in Pakistan to the Hindukush and western end of Pamir Plateau shows two important features. First, a low-velocity layer is mapped from 36-38°N beneath the gneiss domes in the west part of southern and central Pamir. Secondly, south verging high-velocity lowermost crust at 37°N correlates with the trend of (i) increasing Moho depth from 60 km at the northern Pamir to over 90 km beneath the western segment of ATS, (ii) south-dipping earthquake pattern, and (iii) previously identified double reflection at ~72 km and 95 km (Schneider et al., 2019) that correlates with our 4.0 and 4.4 km/s velocity contours.
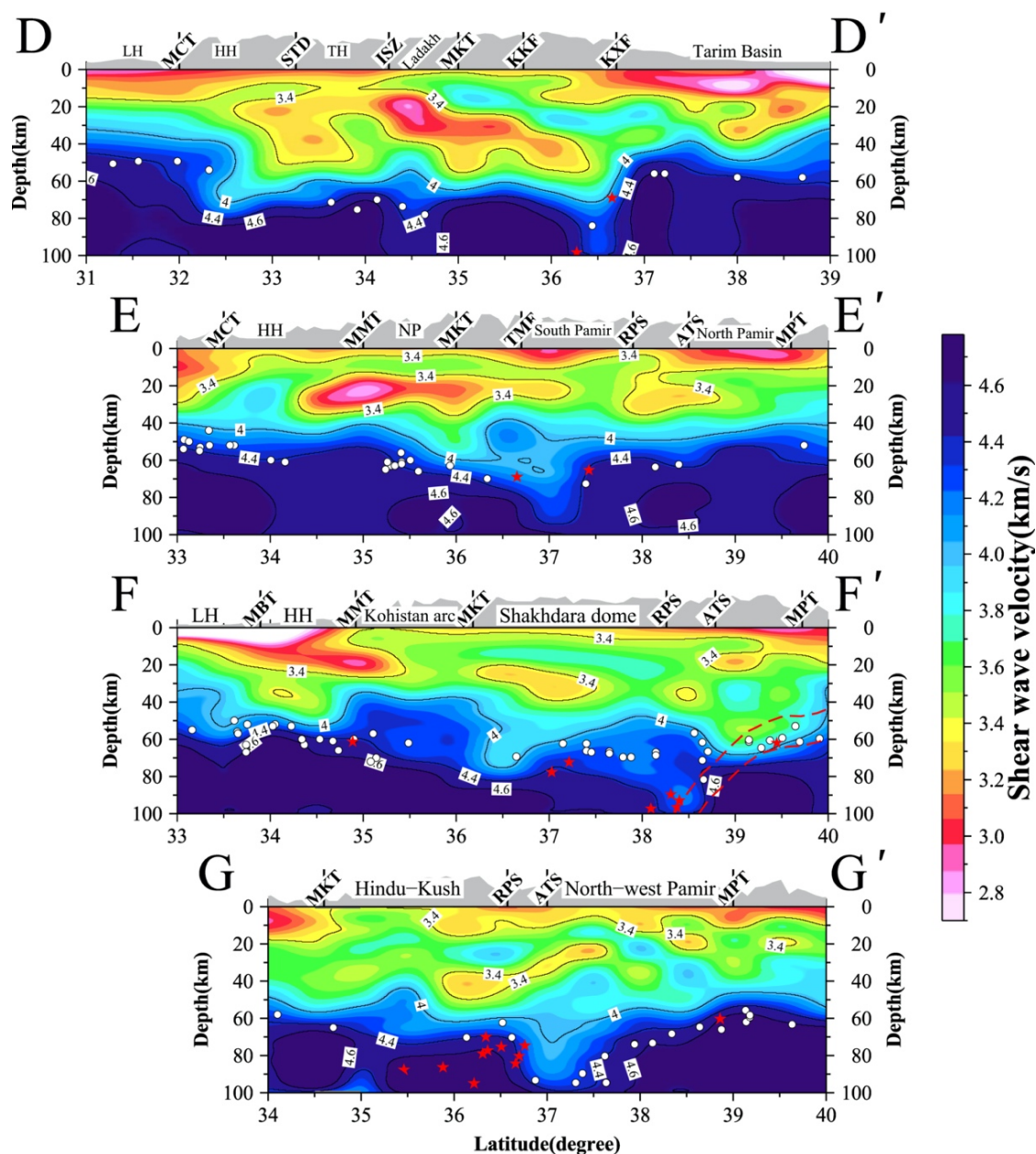
Figure 3.17 *Same as Figure 3.16. The red stars indicate locations of earthquakes below 60 km obtained from the EHB catalogue. The dashed red lines in profile F-F˝ represent subducting lower crust of Pamir (Schneider et al., 2019).*
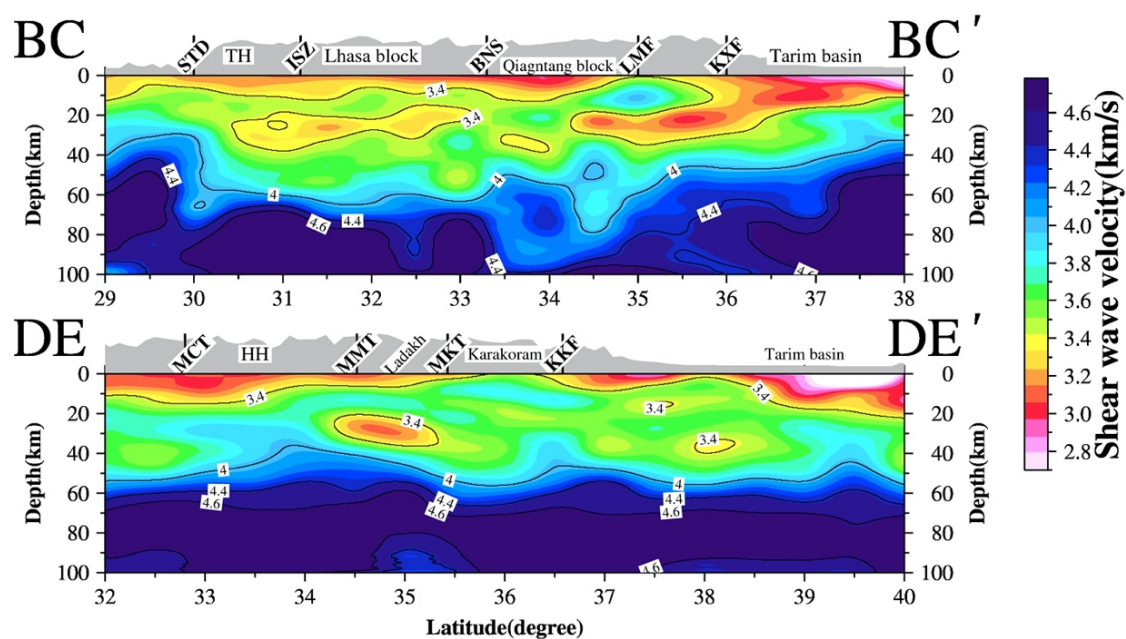
Figure 3.18 *Velocity depth section at two north-south profiles. The top profile lies between B-B′ and C-C′ of Figure 3.16. The bottom profile lies between D-D′ and E-E′ of Figure 3.17.*

3.5 Discussion

3.5.1 Northern limit of Indian lower crust beneath the Tibet-Karakoram-Pamir

Evidence for the Indian plate crust underplating Tibet and Pamir typically comes from the findings of faster lower-crustal material (Wittlinger et al., 2009), well-developed shear zones beneath the Himalaya (Schulte-Pelkum et al., 2017), and deep crustal earthquakes (Priestley et al., 2008). In eastern Tibet, deep earthquakes and fast seismic wave velocities at the bottom of the Tibetan crust signify the eclogitization of the lower crust of India (Monsalve et al., 2008; Huang et al., 2009). In southern parts of central and western Tibet, using seismic evidence for multiple impedance contrasts in the crust (or observing intra-crustal layers), Nábělek et al. (2009) and Xu et al. (2017) reported the presence of eclogitized Indian crust underthrusting at least the northern Lhasa block. Wittlinger et al. (2004) observed large offsets in Moho and crustal structures near the KXF and interpreted the southward underthrusting of the Tarim lithosphere under the northwestern Tibet-Kunlun. The deep seismicity, high-velocity intra-crustal layering, and Moho doublets have been used to delineate the geometry of subducting Asian lower crust under the Pamir and the Hindukush (Sippl et al., 2013; Li et al., 2018; Schneider et al., 2019).

CHAPTER 3

These studies provide evidence for northward underthrusting of Indian crust under Tibet and southward subduction of the Asian crust under Pamir and western Kunlun. While the geometry of the subducting Asian crust has become more evident in recent years (Li et al., 2018; Schneider et al., 2019), the fate of the underthrusting Indian crustal front beneath western Tibet-Karakoram and Pamir remain poorly understood. Priestley et al. (2008) combined the results from the previous studies with depths of moderate-size earthquakes at the northwestern edge of the plateau to argue for the presence of the cold, dry granulite-rich crust of India beneath most of western Tibet. However, more recent seismic velocity studies in west Tibet (Griffin et al., 2011; Razi et al., 2014) failed to detect high seismic velocity in the lower crust. By mapping deep seismic discontinuities under Tibet, Zhao et al. (2010) observed low-angle underthrusting of the Indian plate beneath the entire western Tibet, in contrast to the eastern Tibet.

The transformation of the mafic lower-crustal rocks into eclogite or garnet granulite creates a high-velocity lower crust under the Himalayas and Tibet. This process requires the Indian crust to underthrust the plateau. We use the continuity of high-velocity lowermost crust (7x layer) combined with observation of Moho doublets, large structural offsets across major fault boundaries, and deep seismicity to define the northern limit of the Indian crust under the western Tibet-Karakoram and Pamir region. Figure 3.19 depicts the extent of high velocity lower crust from the Himalaya in the south to various latitudes in west Tibet and Pamir.

As discussed earlier, the velocity profiles from A-A´ to D-D´ (Figures 3.16 and 3.17) constitute western Himalaya-western Tibet-Kunlun and Ladakh regions. Along profile A-A´ (84E), continuity of ~20 km thick fast velocity lower crust from Tethys Himalaya to southern Qiangtang block (33°N) has been used to represent the Indian crustal front. Farther north, the thickness of the 7x layer is insignificant. The crustal velocity profiles from B-B´ to D-D´ (between 82-77°E) show significant changes in the crustal structures in the vicinity of Karakax Fault (KXF) at the western end of the ATF. The thickness of the underplated lower crust varies from 25-30 km in the Himalaya to 10-15 km in northern Tibet. The most prominent characteristic is the depth offset of 4 km/s velocity contour in the proximity of the Karakax Fault. Also, we observe about 20 km shallowing of Moho across the KXF. The fault also marks the zone of deep earthquakes (Figure 3.17, profile D-D´).
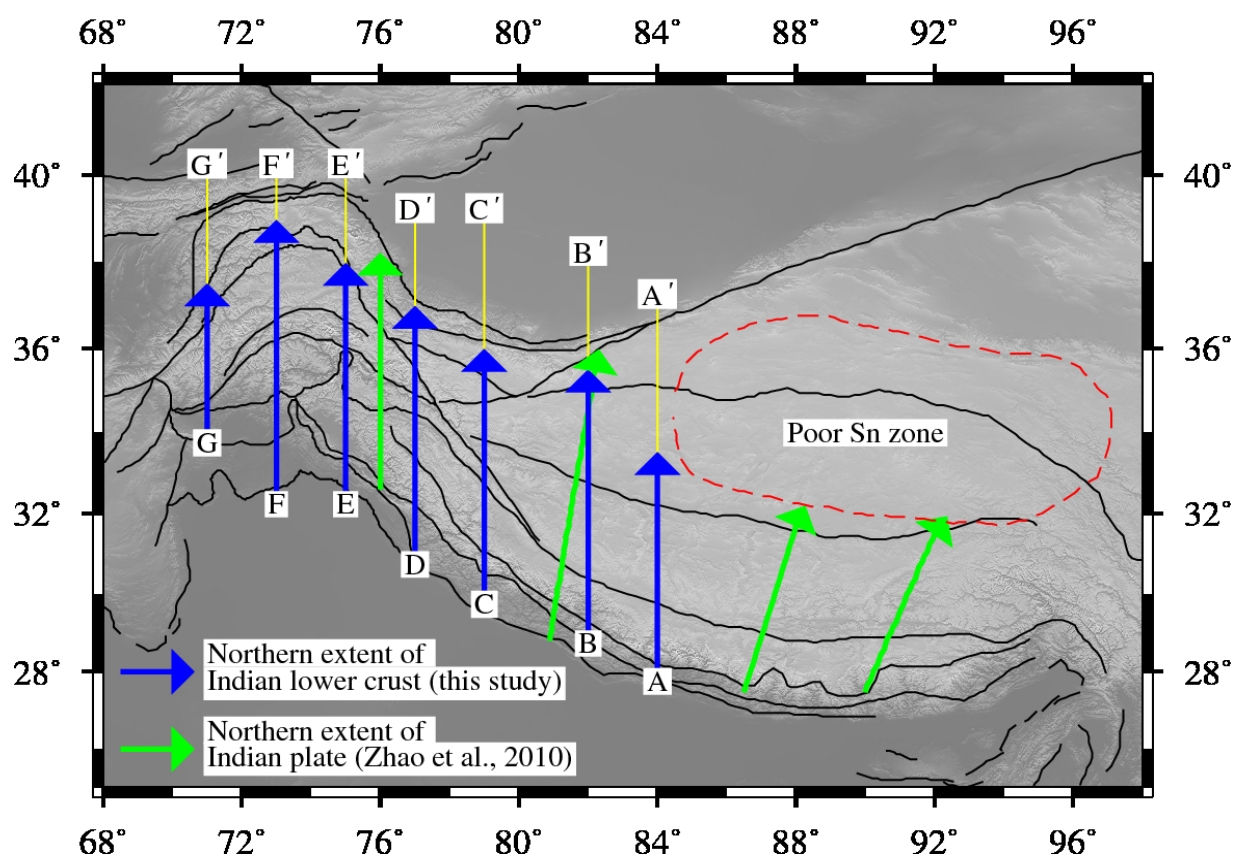
Figure 3.19 *Map showing the possible northern limit of the Indian crust along six-velocity profiles based on the nature of velocity of lowermost crust (7x layer) represented by the shear velocity of 4.0−4.4 km/s. The blue lines represent results from this study, and the green lines are from Zhao et al. (2010). The arrowhead indicates the northern limit. The red dashed polygon shows the zone of the low-velocity upper mantle in north Tibet (Zhao et al., 2010).*

Based on the above structural changes in the crust, we believe the KXF marks the boundary in northwestern Tibet where the Indian crust and Asian crust meet and jointly deform, producing deep-seated earthquakes consistent with previous studies (Priestley et al., 2008; Zhao et al., 2010). In Pamir-Hindukush-Karakoram regions, flexure of the high velocity (7x layer) resulted in the thicker lower crust, Moho doublets, and deep seismicity beneath the south-eastern Pamir (at 37°N in velocity profile E-E′). Similar features are inferred in central to west-central Pamir (between RPS and ATS in profiles F-F′ and G-G′) and define the zone of interaction between the northward underplating Indian lower crust and the southward subducting Asian crust. Our result of the Indian crustal front in western Tibet and Pamir combined with Zhao et al. (2010) shows that Indian lower crust

underthrusts from eastern Tibet to Pamir in the west up to varying latitudes (Figure 3.19). In the east part of the Tibet plateau, Indian crust is inferred to underthrust only till southern Tibet. However, it reaches up to northern Qiangtang and Tianshuhai blocks in central and western Tibet. In the Pamir-Hindu Kush, the northern limit of the Indian crustal front lies in Central Pamir.

3.5.2 Mid-crustal low velocity and its lateral variation

Since the early geophysical observations of significant P wave velocity decrease in the upper/middle crust of the Tibetan Plateau (Brown et al., 1996; Nelson et al., 1996), numerous geophysical studies followed to examine its plateau-wide distribution, depth control, geological explanation, and its role in making of the plateau (Klemperer, 2006; Caldwell et al., 2009; Rippe & Unsworth, 2010; Heteyni et al., 2011; Searle et al., 2011; Yang et al., 2012; Agius & Lebedev, 2014; Gilligan & Priestley, 2018; Li et al., 2018). Corresponding high conductivity zones at a mid-crustal level have also been reported in southern Tibet (Unsworth et al., 2005; Bai et al., 2010), northwest Tibet and Himalaya (Arora et al., 2007), and in Pamir (Sass et al., 2014) which further support fluid rich, weak middle crust throughout the orogenic belt. These studies suggest that the underthrusted Indian crust below about 20 km depth is partially molten, forming present-day Tibetan middle crust. Therefore, it is susceptible to southward flow in response to the gravitational potential energy gradient between Tibet's weak middle crust and eroding Himalayan front (summaries in Klemperer, 2006; Hodges, 2006). The above observations led to the suggestion of ductile flow in Greater Himalayan Sequence (GHS) rocks, continuity in the subsurface beneath the northern Himalayan thrust belt and molten middle crust of Tibet, and the evolution of the controversial concept of channel flow in the Himalayan-Tibetan orogenic system (Grujic et al., 1996, 2002; Law et al., 2004; Jones et al., 2006). The channel flow concept was introduced to explain the apparent partially molten Tibet's middle crust that is extruded southward by buoyancy forces acting on the elevated Tibetan crust. This process, which has been active at least since the early Miocene, has a surface manifestation in the early to mid-Miocene rocks produced from mid-crustal melts and now found at the surface between the MCT and the STD as leucogranites. Geologic and geophysical evidence exists for partial melting in the Himalaya between 15 to 20 km depths at 650−750°C temperature during decompression at 4−9 kbar pressure (Scaillet et al., 1996; Searle et al., 2010).

The early controlled source seismic data have been supplemented by networks of broadband seismographs as linear arrays or spread over the region and a few MT investigations providing evidence for conducting middle crust coinciding with low-velocity layer (LVL). The surface wave tomographic images of Yang et al. (2012) and Gilligan and Priestley (2018) suggest the continuous presence of low velocity (Vs ~ 3.2-3.4 km/s) in the middle crust of Tibet at a depth range of 20−40 km. Both the studies have limited spatial resolution. Yang et al. (2012) study is confined to the east of 80°E with a 150-200 km radius horizontal resolution. Gilligan and Priestley (2018) could resolve features of 3° × 3° or more for periods more than 10 s. Using high-density receiver function data, Hetenyi et al. (2011) proposed the existence of discontinuous low-velocity channels of the horizontal length of about 50 km. Due to the non-continuity of low-velocity layers and average mean, Vp/Vs ratio, Hetenyi et al. (2011) questioned the widespread existence of partial melt in southern Tibet and, hence, the channel flow model. The regional presence of low-velocity zones and conductors in the crust may be due to graphite, mica, fluids, partial melts, aqueous fluids, or a combination and are easily capable of producing an observed wave velocity decrease of 7−17 % (Takaei, 2000). The LVL may also represent strong radial anisotropy in the middle crust (Shapiro et al., 2004). Existing seismological images are inadequate to establish continuity of low-velocity zones within Tibet extending southward to the Greater Himalayan Sequence in the Garhwal Himalaya or the western Himalaya. Availability of newer data helps us develop better-resolved velocity images and examine the existence of such an LVL in the hitherto poorly explored region of west Tibet-Himalaya and Ladakh-Pamir-Hindukush. We can resolve the target of 50 km × 50 km that is at least three times better than the existing seismic velocity images.

At first, we quantify the amplitude of low velocity at mid-crustal depths for an undeformed crust. A solid, dry metamorphic rock at room temperature at ~1000 MPa (~ 30 km) has an average shear wave velocity of ~ 3.65 km/s (Christensen, 1996). Under the influence of temperature, the rock will begin to melt at a temperature > 900°C (Litvinovsky et al., 2000), leading to a reduced velocity of 3.4 km/s considering a 0.2 m/s/°C decrease in velocity (Kern et al., 2001). The velocity reduces further in presence of water and hydrous minerals. Wang et al. (2016) presented evidence for 8−22 % partial melts from central and northern Tibet constrained by estimates of Rb/Sr in the source from Nd and Sr isotopes and REE contents of the Pliocene-Quaternary lavas. While such estimate of 8−22 % is

consistent with the MT data in Tibet (Unsworth et al., 2005), they are higher than the melt fractions (1−7 %) suggested by many seismic studies (Caldwell et al., 2009).

Like Yang et al. (2012), we also use a reference velocity of Vs < 3.4 km/s as indicative of low-velocity zones. We focus on examining how widespread the distribution of mid-crustal low velocity in the region is by investigating its spatial distribution. Earlier, we have shown that low-velocity layer anomaly of up to 3−5 % and thickness 5 km could be best recovered (Figure 3.11). The S-velocity map at different depths (Figure 3.13, 3.16, and 3.17) suggests the presence of low velocity primarily confined to 20−40 km depth. The anomaly may be laterally averaged and smoothed during velocity contouring. To investigate the distribution of the low-velocity layers, we examine their depth distribution along the N-S velocity profiles of Figure 3.16 and 3.17 and a few more shown in Figure 3.18.

The distribution of mid-crustal low-velocity domains (between 20 to 50 km depth) along with their maximum depths (the approximate bottom of the layer) is presented in Figure 3.20. The low velocities could be broadly classified in regions with Vs ~ 3.0 to < 3.2 km/s and 3.2−3.4 km/s. The low-velocity zones are discontinuous and exist in patches with no specific distribution of coherent depth and velocity amplitude from the south to the north Tibet as required for continuous flow channels (Clark & Royden, 2000). In the Pamir region, the low-velocity zones in 20−40 km depth correlate well with surface distribution gneiss domes, a region with large-scale extension at 30−50 km depth (Shurr et al., 2014; Hacker et al., 2017). A Similar low-velocity layer is mapped at a depth of 30−50 km in the Great Himalayan Sequence beneath the western Himalaya (77°E, Figure 3.17, profile D−D′), continuing further north to the Ladakh and Karakoram batholith. We also observe a relatively continuous low-velocity middle crust extending from southern Tibet to the STD, suggesting that E-W extension in Tibet is transferred southward to the central and western Himalaya (Hintersberge et al., 2011). While the discrete mid-crustal LVZs in southeast Tibet partially correlate with surface grabens (Hetenyi et al., 2011), no correlation is found in western Tibet.

Though the low velocities due to crustal melts are widely present in the study region encompassing western Himalaya, Western Tibet, and Pamir, their generic linkage to a common source remains an open question. The absence of a coherent 3-D low-velocity zone suggests the complexity of this region as a consequence of mechanical deformation along with magmatic activities (Tseng et al., 2009). It could be correlated with geological processes/ features like broad extensional regime within Tibet (Gan et al., 2007), the

localized collision-parallel extension in the southernmost Tibet and northern Himalaya (Styron et al., 2011), presence of the localized low-velocity horizon in the western Himalaya (Caldwell et al., 2009) or decompressive melting beneath the gneiss domes in Pamir, western Himalaya, Karakorum, and Garhwal Himalaya. The observed disconnected low-velocity zones agree with the results of Hetenyi et al. (2011), question the validity of the channel flow model. It has been argued that heating related to crustal thickening drives crustal melting, reduces the strength of the crust, and causes orogenic collapse. Several tectonic and surficial processes may lead to near-isothermal decompression of the deep crust. Other mechanisms that could generate partial melt include extension, decompression via removal of the upper crust, crustal thinning, and diapirism.
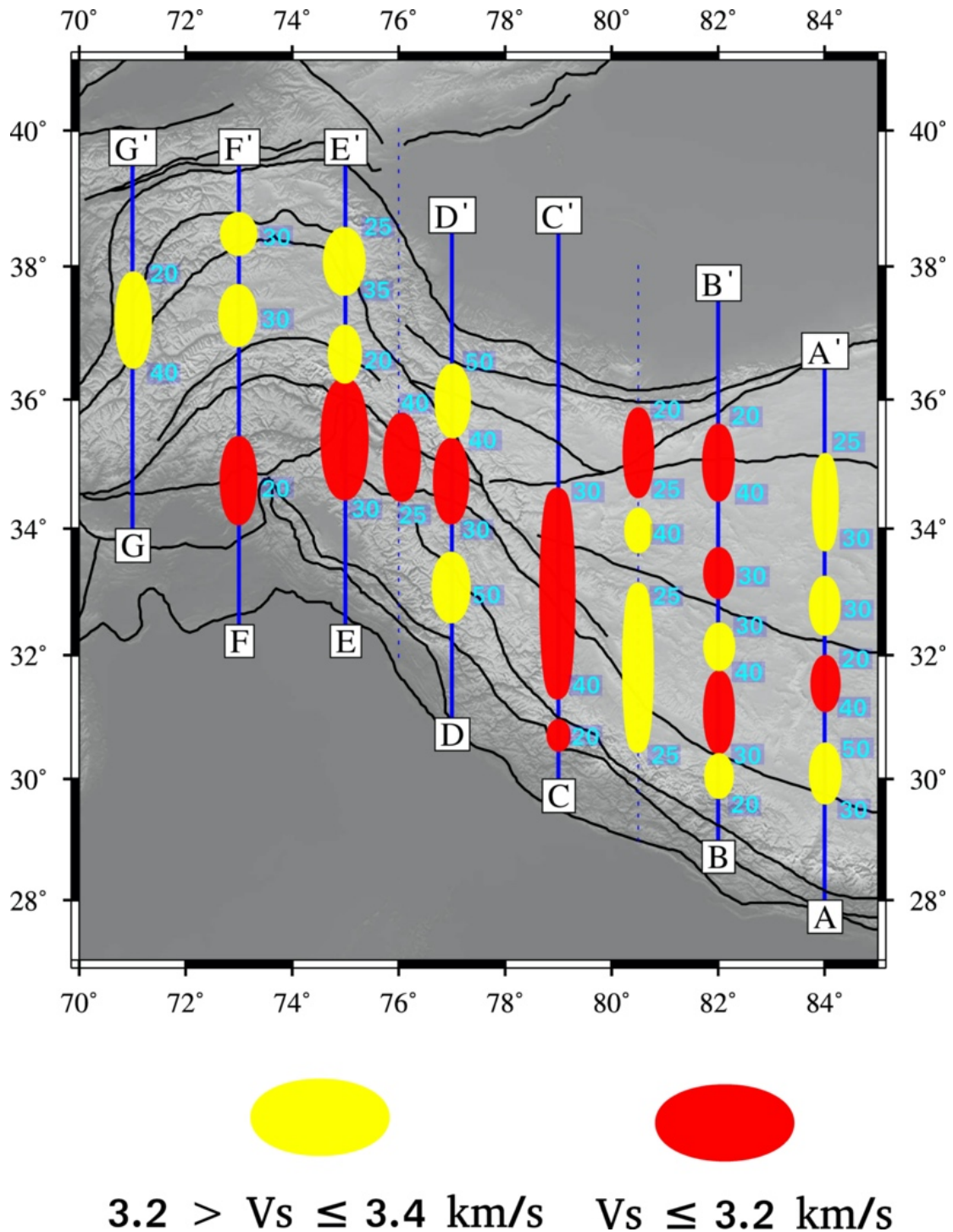
Figure 3.20 *Map showing the spatial distribution of low-velocity anomalies in the middle crust between 20 to 50 km depth. The position and size of each anomaly (shown as red and yellow ellipses) are determined by examining the Vs ~ 3.4 km/s contour of each north-south velocity profile of Figure 3.16 and Figure 3.17. The depth (in km) of the base of the low-velocity layer is shown beside the anomaly location. The velocity profiles corresponding to the dashed blue lines are presented in Figure 3.18.*

3.5.3 Depth extent of the Karakoram Fault- Does it interrupt the mid-crustal LVZ?

The NW-SE trending right-lateral Karakoram fault running from north-eastern Pamir to the Kailas region of southern Tibet marks the western flank of Tibet. Molnar and Tapponier (1975) first proposed the eastward extrusion of thickened Tibetan crust due to the northward indenting Indian crust. They suggested that the extruding crust is bound by the Altyn Tagh fault (ATF) in the north and the Karakorum fault (KKF) along the south-western margin of Tibet. The extrusion process requires these faults to be a lithospheric-scale structure with significant horizontal motion (~500–1000 km) (Molnar & Tapponier, 1975). While the ATF is at least a crustal-scale fault (Searle et al., 2011), the depth extent of KKF is still debated.
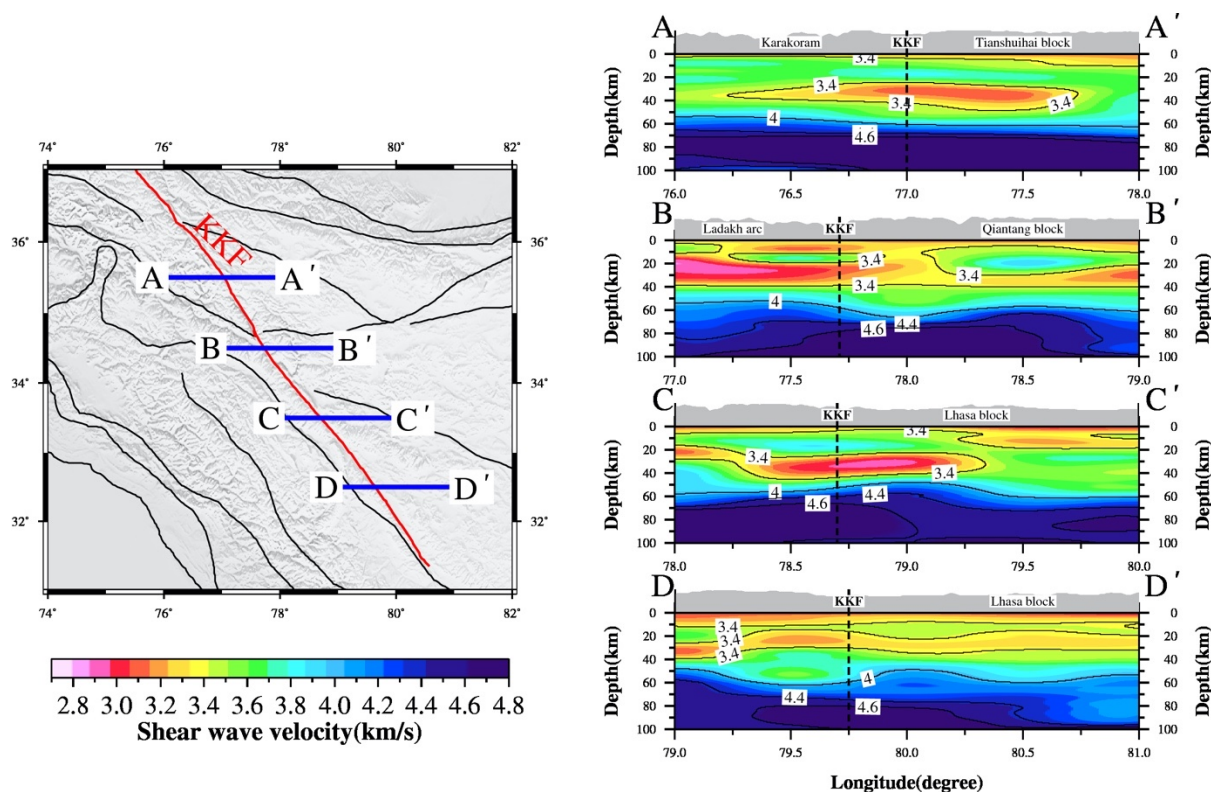
Figure 3.21 *E-W trending velocity-depth profiles across the Karakoram faults. The blue lines indicate the location of the profiles, and the red line shows the fault in a geological map at the left panel. The right panel show four velocity sections across the Karakorum fault showing the continuation of velocity signature and the depth extent of fault (< 20 km). The grey shaded area in velocity profiles shows surface topography. The dashed back line in each profile shows the approximate position of the KKF. The black lines are velocity contours.*

CHAPTER 3

Based on relatively less abundance and age of old leucogranites (> 18 Ma) west of eastern termination of the KKF, results of seismic and MT studies crossing it, and presence of high helium isotopic value indicating mantle fluid along the KKF, Leech (2008) and Klemperer et al. (2013) argue that the KKF penetrates deep into the crust and stops northward underthrusting of the Indian crust, thereby serving as a barrier to the crustal flow entering to the west in Himalaya and Ladakh. This conclusion would be correct even if the fault reached only halfway through the crust (Searle et al., 2011, 2015). Murphy and Copeland (2005) infer the mid-crustal reach of the KKF from the burial depths of rocks exposed by the associated normal fault. The depth extent of the KKF is vital to understand the possible mechanisms of crustal deformation and material transfer. A mid-crustal flow necessary for the plateau-wide outward expansion will preclude any surface faults from reaching deep into the crust. Limited seismological and MT studies show low shear wave velocity and high conductivity under Ladakh-Karakoram and western Himalaya, suggesting the continuity of mid-crustal LVZ south of KKF (Caldwell et al., 2009; Rai et al., 2009). Gilligan et al. (2015) could not see any significant offset of mid-crustal LVZ along the fault and suggested that KKF does not cut through the entire crust. Due to inhospitable terrain on the international boundary, no geophysical experiment has been performed across the fault, and the above hypotheses on the depth extent of the KKF are yet to be resolved conclusively. Initial results suggested a high late Quarternary slip rate (30-35mm/yr) on Karakorum fault (Avouac & Tapponnier, 1993), in contrast with recent GPS geodetic measurements suggesting a much lower rate of 3–5 mm/yr (Brown et al., 2002; Jade et al., 2004).

With a focus on resolving whether the KKF interrupts the mid-crustal flow from entering to western Himalaya and Ladakh, we generate several velocity-depth sections across the fault from its southern to the northern edge to examine the seismic velocity continuity (Figure 3.21). The seismic response of the KKF would be visible in terms of significant vertical offset in mid-crustal LVZ or underplated lowermost crust if it cuts deep into the crust. The four E-W trending velocity sections (Figure 3.21) across the fault show continuity of mid-crustal low-velocity zones in the depth of 20-40 km without vertical offsets. No significant variation in the underplated lower crustal layers across the fault is observed. Therefore, the fault is mainly an upper crustal feature and may not play a significant role in crustal shortening. This observation counters the idea of plate-like deformation (Molnar & Tapponier, 1975) and supports diffuse deformation in Tibet-Karakoram (England & McKenzie, 1982).

CHAPTER 3

3.6. Conclusions

We investigate the crustal structure of the western Tibet-Pamir and the adjoining Himalaya-Ladakh region using a high-resolution shear wave image to a depth of 100 km. The velocity image with a horizontal resolution of 50 km has brought out several interesting features summarised in Figures 3.19-3.21 and are discussed below:

(1) Moho beneath Himalaya and south Tibet correlates with a shear velocity of 4.4−4.6 km/s and a reduced velocity of 4.0−4.2 km/s in northern Tibet and Pamir. The Moho depth increases from 50 km in the Himalaya to 80 km below the BNS. There are marked E-W variations in lower crust complexity in western Tibet between 31−33°N. Beneath Pamir, the Moho is at 70−80 km with the extreme of 90 km in the western part at 37°N.

(2) Using Moho depth and the nature of high velocity lower crust (Vs > 4.0 km/s), we map the northern limit of the Indian crust extending beyond the Qiangtang block in the western Tibet (77−82°E) than the previously thought boundary in the southern Lhasa, and till central Pamir further west.

(3) We observe laterally discontinuos low-velocity zones (Vs < 3.4 km/s) in the upper and middle crust in Western Tibet. These LVZs generally do not connect to the high Himalaya as expected for a ductile channel flow. In Pamir, the LVZs correlate with the surface distribution of gneiss domes. The study suggest that the mid- crustal Channel flow model proposed for the central and eastern Tibet does not fit the seismological constarints in the western Tibet and Pamir.

(4) The study suggests that the Karakorum fault is an upper crustal feature due to the presence of uninterrupted LVZs beneath the fault at a depth beyond 20 km.

CHAPTER 4

Crustal variability in northwest Himalaya and Ladakh-Kohistan arc

4.1 Introduction

The Himalayan arc is broadly divided into three segments – western, central, and eastern. West of 76.5°E is western Himalaya that includes Kashmir, the Salt range in northern Pakistan, Zanskar, Ladakh, Lahul–Spiti, and Himachal Pradesh (Figure 4.1). Between 76.5°E and 87.5° is central Himalaya covering Panjab Himalaya, Garhwal–Kumaun, and Nepal. East of 87.5 is the eastern Himalaya (Hodges, 2000; Yin, 2006). The tectonic framework of western Himalaya differs from that of the central Himalaya with respect to the position of the Main Central Thrust and Higher Himalayan Crystalline, and the Lesser and Sub Himalayan structures (Thakur et al., 2019). The two segments of Himalaya are proposed to be separated by the Ropar–Manali lineament fault zone that continues further north into the Zanskar and Karakorum (Virdi 1979, Sharma and Virdi 1982). We discuss some of the other parameters differentiating these two Himalayan segments. The average convergence rate within the Himalaya decreases from ca. 18 mm/yr in the central segment to ca. 14 mm/yr in the NW segments. Inverse modeling of GPS-derived surface deformation rates for the data from 1995-2019 indicates that the arc-normal rates in the Northwest Himalaya have a complex deformation pattern involving both convergence and extension, and rigorous seismotectonic models in the Himalaya are necessary to account for this pattern (Jade et al., 2014, 2020). Paleoseismic evidence recorded on the Himalayan front suggests Mw > 8 earthquakes in the central Himalaya, and its absence in the NW Himalaya. The length of the interseismic locked zone that is ca. 100 km in the central Himalaya (Jouanne et al., 2004; Bettinelli et al. 2006) to ca 170 km in NW Himalaya (Schiffman et al. 2013). The above observations suggest remarkable diversity between the Western and Central Himalaya in terms of litho-stratigraphy, instrumental and paleoseismicity, nature of crustal shortening, etc., possibly leading to variability in the crustal architecture and the material property beneath these domains.

This chapter aims to image crustal structure and its variability along the strike of western-central Himalaya and further north into the Ladakh- Kohistan arc. Having achieved high lateral resolution (~30 km) of group velocity maps (see details in Chapter 3), we performed group velocity tomography at 0.25° ×0.25° resolution to generate a 3-D shear wave velocity model following the approach discussed in Chapters 2 and 3.
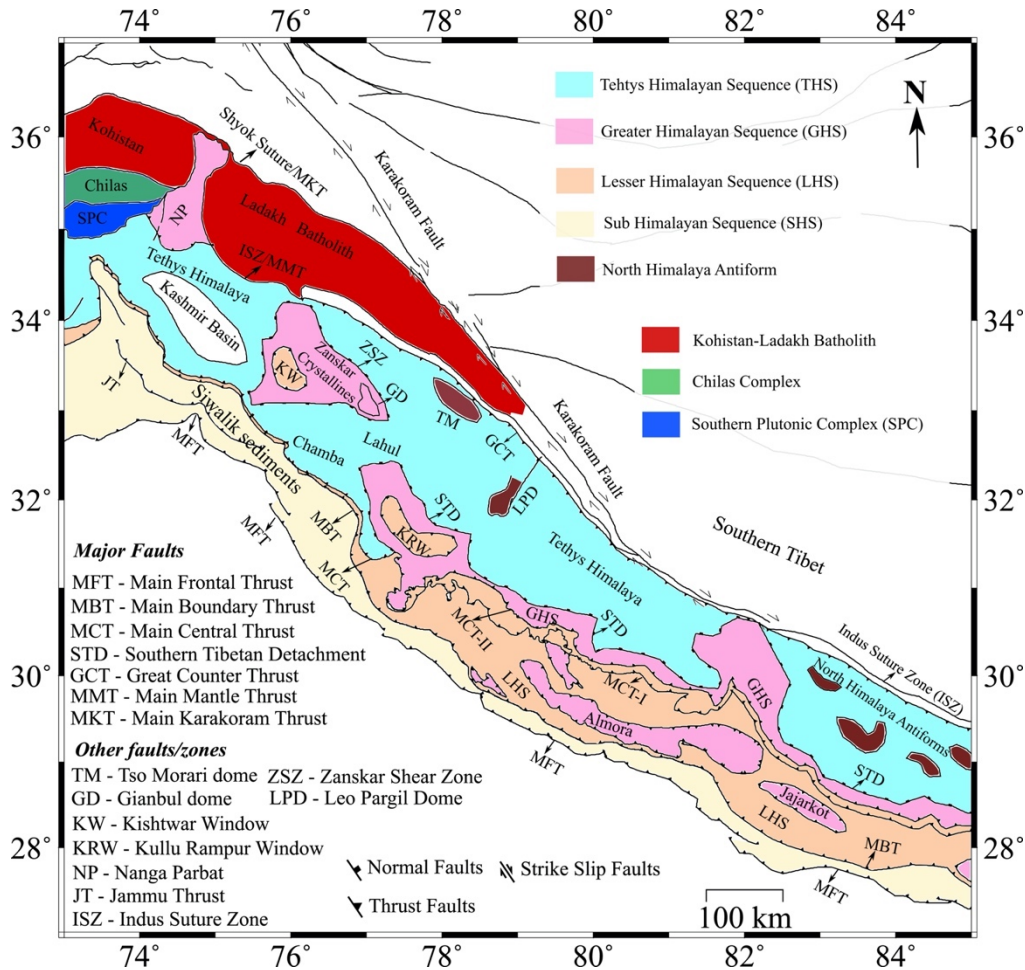
Figure 4.1 *Simplified geological map of western and central Himalaya, and Ladakh-Kohistan arc after Yin (2006), DiPietro and Pogue (2004), and Jagoutz and Schmidt (2012). This Figure is also presented in Chapter 1 as Figure 1.3.*

4.2 Lateral variation in group velocity

Group velocity dispersion maps at representative periods from 5 to 60 sec are shown in Figure 4.2. At a short period range (< 20 s), the dispersion is most sensitive to the shallow crustal velocity (< 20 km). Prominent low group velocities characterize the Sub Himalaya sedimentary sequence compared to other parts. With increasing periods (20-30 s), the group velocity is most sensitive to the mid-crustal velocity structure. In this period, we observe low-velocity anomalies appearing within the Himalayan interior Nanga Parbat, and Ladakh arc. Group velocity dispersion is primarily sensitive to crustal thickness at longer periods (> 40 S). While most of the Himalayan arc shows high group velocities indicating shallow Moho, western Tibet, Ladakh, and Nanga Parbat zones are characterized by low group velocities due to their increased crustal thickness. The most exciting feature at a longer

period is a low-velocity anomaly extending from Zanskar Himalaya in the north and Lahul-Chamba Himalaya further south.
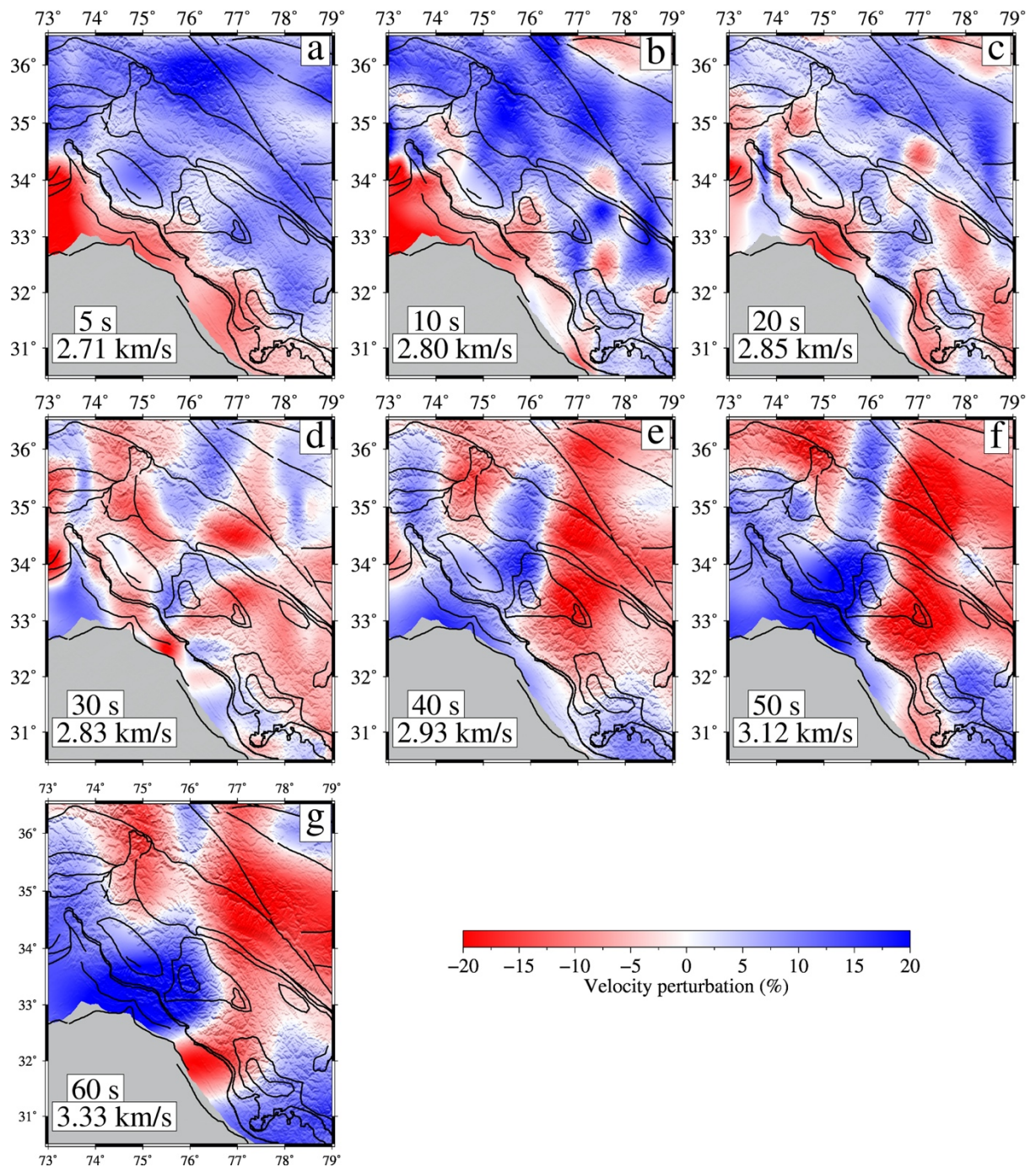
Figure 4.2 *Rayleigh wave group velocity maps from (a) to (g) are plotted as percentage deviations from the regional mean. The period and the regional mean are marked at the bottom of each map.*

4.3 Lateral variability of shear wave velocity

As discussed in the previous chapters, group velocities maps are inverted to obtain shear wave velocity structure at each depth. We present here velocity-depth sections from 10 to 60 km (Figure 4.3). In the upper crustal level (~ 10 km), the primary velocity structure is prominent low-velocity zones (LVZs, Vs < 3.2 km/s) in the Siwalik sedimentary basins. Note the emergence of wider sedimentary fold and thrust belt of western Sub Himalaya (west of 77°E). The width of the Siwalik sediment belt is narrow (~ 10 km) in central Himalaya (e.g., the Subathu basin, east of 77°E) increasing to ~90 km in the Kangra-Jammu basin (75−77°E), and Neoshera basin of the Potwar Plateau (west of 75°E) (Prasad et al., 2011). Small pockets of LVZs north of the Kullu-Rampur window and Zanskar shear zone may indicate unconsolidated sediments of the Tethys Himalaya. Further north, the Ladakh-Kohistan arc, Karakoram metamorphic zone, and western Tibet have higher shear wave velocities.

At 20-30 km depth representing the middle crust, shear wave velocities are higher beneath the sedimentary basins. Three prominent mid-crustal LVZs (L1, L2, and L3) are marked in Figure 4.3. The LVZ L1 generally maps the surface trace of Nanga Parbat and Ladakh-Karakoram batholith, also previously documented as low resistivity zones associated with the presence of granitic melts (Arora et al., 2007; Caldwell et al., 2009; Hanna et al., 2013; Searle et al., 2010). The southern limit of this LVZ is the Indus Suture Zone (ISZ). The Kohistan arc lacks such a mid-crustal LVZ, especially in the southern half, which includes the Chilas and Southern Plutonic Complex, exposing the lower crustal rocks (Jagoutz & Schmidt, 2012).

The LVZ marked as L2 is present in the Tso Morari and Leo Pargil dome within the Tethys Himalaya. However, this LVZ does not continue beyond 20 km depth, probably represent deformed sediments of the Himalaya wedge or aqueous fluid above the MHT (Caldwell et al., 2013). Alternately, this LVZ could be associated with the large-scale arc-parallel extension in the western Himalaya, which is characterized by shallow (< 20 km) earthquakes with normal faulting (Hintersberger et al., 2010, 2011; Molnar & Lyon-Caen, 1989).

At 30 km depth, a distinct LVZ marked as L3 lay directly below the large-scale migmatitic Gianbul dome, indicating the low-viscosity and high-temperature migmatites exhumed during 26-20 Ma and formed the Higher Himalayan Complex (HHC) of Zanskar (Robyr et al., 2006).
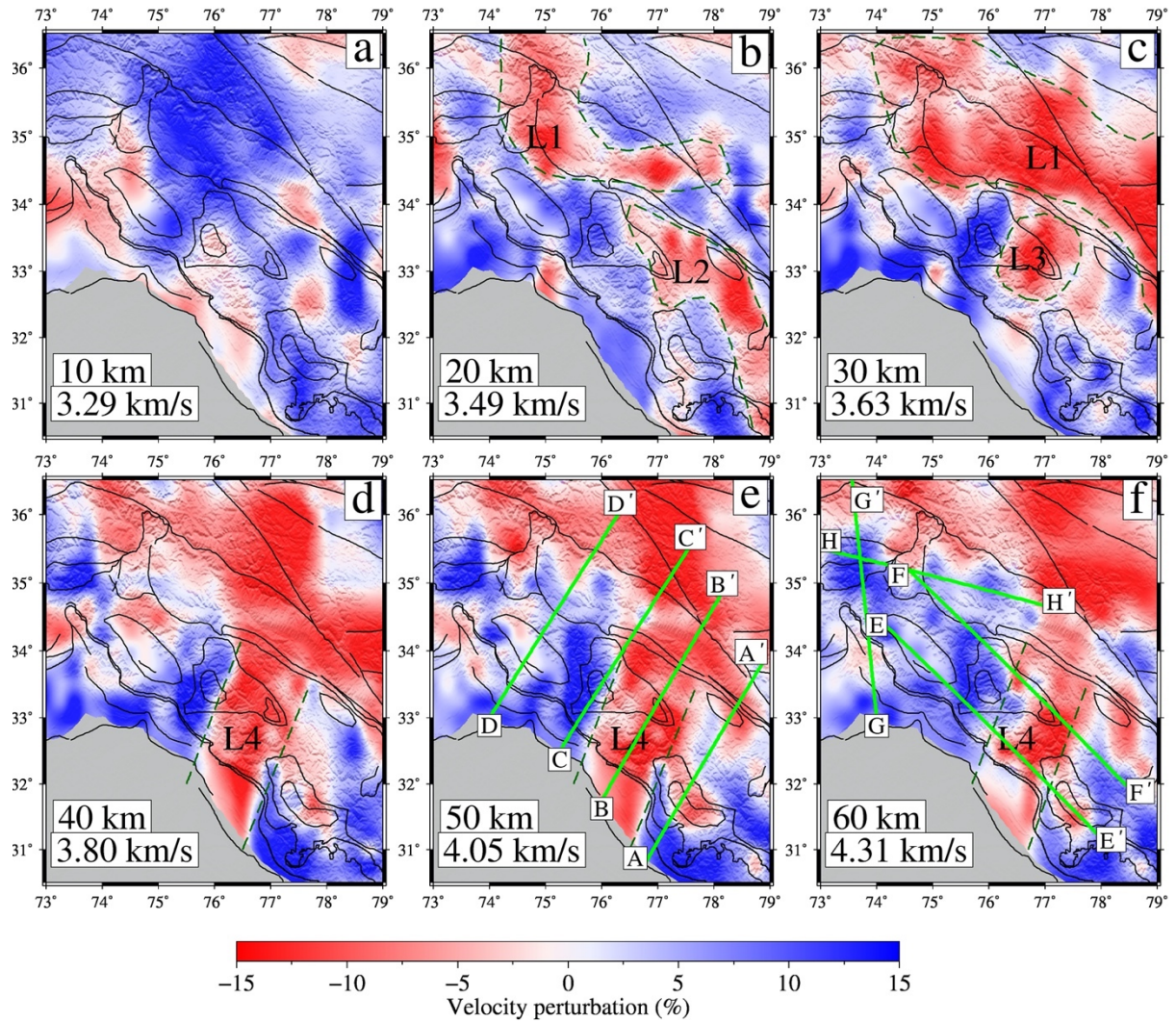
Figure 4.3 *(a-f) Shear velocity maps between 10 to 60 km are plotted as perturbations from the regional mean velocity. L1, L2, L3, and L4 are the mid/lower-crustal low-velocity zones marked by bounding dashed dark green lines. Light green lines are the locations of vertical cross-sections shown in Figures 4.4 and 4.5.*

At the lower crustal level (40-60 km), widespread low velocities in western Tibet, Karakoram, and eastern Ladakh indicate their thicker crust relative to the Himalayan arc. The most notable feature within the Himalayan arc is a near arc normal low-velocity zone (marked as L4) between the Kishtwar and Kullu-Rampur window (~76−77°E). This LVZ, extending beyond 40 km depth, corresponds with lateral changes in surface geology, such as lateral ramp in MCT and MBT, and disruption in the GHS between the Kullu-Rampur and Zanskar crystalline. We interpret the LVZ as probably indicating a major transverse boundary in the underthrusting Indian crust. This feature has not yet been geophysically imaged.

CHAPTER 4

4.4 Velocity sections across NW Himalaya

To understand the detailed crustal structure and associate above mentioned variations in the velocity model, we present the shear wave velocity structure along eight velocity-depth sections (Figures 4.4, 4.5). These include arc normal profiles A−A′ to D−D′, and arc parallel profiles E−E′ to F−F′ covering western Himalaya and Ladakh. Two additional profiles G−G′ to H−H′ investigate the lateral variation of the crustal structure of the Kohistan-Ladakh arc (Profile location is shown in Figure 4.3). We have included available Moho estimates from previous studies primarily based on RF analysis from Rai et al. (2006), Priestley et al. (2019), Mir et al. (2020), and Hazarika et al. (2017). Due to the sparse seismic stations in the western Himalaya and the surrounding region, the assignment of Moho along each profile is not possible. A close inspection of the available Moho depths with our velocity image reveals that Moho largely corresponds to $Vs \sim 4.4$ km/s consistent with Rai et al. (2006). The Main Himalaya Thrust (MHT) is demarcated by $Vs \sim 3.6$ km/s, representing a dry crystalline crust (Christensen & Mooney, 1995).

The velocity profile A−A′ extends from the Kullu-Rampur window in the south to the Tso Morari dome and southwestern Tibet in the north. Rai et al. (2006) and Caldwell et al. (2009) provided crustal structure in the vicinity of the profile. Hazarika et al. (2017) imaged geometry of the MHT along this profile. The MHT geometry marked by $Vs \sim 3.6$ km/s in the velocity profile (A−A′) shows a low-angle north dipping structure from 16-18 km beneath the Sub Himalaya to 20-22 km beneath Lesser and High Himalaya. North of the Kullu-Rampur window, the MHT dips northward gently at 10−16°, where its depth increases to 30−35 km beneath Tethys Himalaya and Tso Morari Dome, and ~45 km beneath southwestern Tibet and farther north. Similar geometry of MHT is mapped by Hazarika et al. (2017). The underthrusting Indian crust has a ~20 km thick high velocity lower crust ($Vs > 4.0$ km/s) above the Moho. The high-velocity layer could be underplated. At the southern edge beneath the Sub Himalaya, the Moho at 50 km dips southward, possibly due to flexure of the Indian crust under the Ganga Basin. There is local variation in Moho depth, such as beneath the Kullu-Rampur window and Higher Himalaya. The Moho depth increases northward, reaching ~60 km beneath the Tethys Himalaya and ~ 70 km beneath the ISZ. The low shear wave velocity (< 3.6 km/s) in the mid/lower crust (20-40 km depth) beneath the Tethys Himalaya at ~ 200 km north of the MFT could potentially indicate metamorphic fluid that escapes from the underthrusted crust and propagates on top of the MHT (Caldwell et al., 2013). The overlying Himalayan wedge above the MHT is

characterized by low velocities (Vs < 3.4 km/s), expected for deformed crustal rocks that are further modified by the presence of partial melt and/ or aqueous fluid. Beneath the Kullu-Rampur window, the velocity contour of 3.4 km/s displays a dome-shaped feature with a thick (at 8-20 km depth) layer of velocity ~ 3.5 km/s above the MHT, possibly representing the Lesser Himalaya Duplexing (LHD) that exposes the Lesser Himalayan rocks on the surface. In the Tethys Himalaya and southwestern Tibet, we identify two low-velocity zones (LVZs) that are locally disconnected. The first one beneath the Tethys Himalaya with the LVZ, up to 20 km depth, may represent MHT fluid (Caldwell et al., 2013) and/or melting due to upper crustal arc-parallel extension (Hintersberger et al., 2010, 2011). The second LVZ could be part of the widespread mid-crustal melt beneath Tibet (Yang et al., 2012). Beneath the Tso Morari Dome and ISZ, we observe a high-velocity upper crust (Vs > 3.6 km/s) up to 20 km depth.

Further west, the profile B−B´ from the Kangra basin in the southern end to the eastern Ladakh batholith in the north through Chamba and Lahul Himalaya, lies in the arc-perpendicular low-velocity zone marked as L4 in Figure 4.3. The velocity structure along this profile is distinct from the other profiles discussed here due to pervasive mid/lower crustal LVZs throughout the length of the profile. We identify two prominent LVZs, one beneath the Ladakh batholith and the other beneath the Gianbul dome and further south. The Gianbul dome is a migmatitic-leucogranitic intrusive complex metamorphosed between 26.6 to 19.8 Ma at a peak partial melting temperature ~ 800°C and depth ~30 km (Robyr et al., 2006). The dome was exhumed by rapid isothermal decompression from 20-30 km depth and formed the volumetrically largest Higher Himalaya Crystalline (HHC) in the Zanskar region. Its formation is distinct from the Central Himalayan Crystalline rocks that extruded laterally southward due to coeval motion on the MCT and STD (Robyr et al., 2006; Searle et al., 2010). The presence of the lowest velocities (Vs ~3.2 km/s) directly beneath the Gianbul dome represents this large-scale melting in the Himalayas. On the other hand, the LVZ beneath the Ladakh batholith may represent crustal melting/aqueous fluid produced due to Ladakh-Baltoro granite melting at ~21 Ma (Rai et al., 2009; Arora et al., 2007). We also observe a nearly flat MHT ~18 km depth with no evidence of a north dipping ramp.

Profiles C−C´ and D−D´ connect the western end of the Zanskar crystalline and Kashmir Himalaya to the Ladakh arc, respectively. In the Kishtwar region (C−C´), a flat-lying MHT at ~20 km depth is mapped between the MFT and ISZ. Similarly, in the

Kashmir Himalaya, the MHT is at 10-12 km depth beneath the MFT and ~16 km beneath the whole width of the Kashmir basin, indicating a very shallow angle or near flat geometry, consistent with previous geophysical studies (Mir et al., 2020; Kaila et al., 1984). Note that the MHT depth is ~ 20 km just north of the ISZ in these two profiles, in contrast with the profile in central Himalaya profiles (A-A′ and others) where MHT is imaged at ~40-45 km depth beneath the ISZ (Caldwell et al., 2013; Schulte-Pelkhum et al., 2005). The mid/lower crust is imaged as a prominent LVZ at 20-40 km depth in Ladakh- Baltoro granite zone. The underthrusting Indian crust has a uniform velocity of ~3.8 km/s with a relatively horizontal Moho at ~58-60 km in the Kashmir Himalaya (Mir et al., 2020). A thick, underplated lower crust underlies the Kishtwar region (Vs > 4.0) between 30 to 50 km depth. Two arc parallel profiles (E−E′ and F−F′) summarize the lateral variation of the crustal structure discussed above using arc perpendicular profiles. We observe the mid/lower crustal LVZ beneath the Chamba and the Gianbul dome marked as L4 in Figure 4.3. The presence of earthquakes characterizes the whole crust of the Himalayan arc. However, clustering of events occurs beneath the Kishtwar region and Kashmir Basin.

The crustal structure beneath the Ladakh-Kohistan arc is presented in profiles G-G′ and H-H′. The profile G−G′ is approximately north-south oriented, showing the transition from the Himalaya to the Kohistan arc. The profile H−H′ illustrates the difference between the Kohistan and Ladakh crust. Precise knowledge of Moho depth from seismic experiments is sparse in the Kohistan-Ladakh region. Crustal thickness varies from 62−70 km beneath the Kohistan arc and Nanga Parbat (Priestley et al., 2019; Hanna et al., 2013), and increases to ~ 75 km in the eastern Ladakh near the Karakoram Fault (Rai et al., 2006). Our most prominent observation beneath the Kohistan arc is a thick (~ 25 km) high-velocity lower crust (Vs > 4.0 km/s after 40 km depth) underlying an upper/mid crust of Vs ~ 3.6−3.7 km/s. The high-velocity lower crust may represent the "density-unstable" lower crust of Kohistan arc root (Jagoutz & Behn, 2013). In the mid-crustal depth, the Nanga Parbat and Ladakh arc is characterized by LVZs (Vs < 3.2 km/s) with gradual eastward thinning of the high-velocity lower crust (~10-15 km beneath eastern Ladakh). We don't observe mid-crustal low velocities in Kohistan.
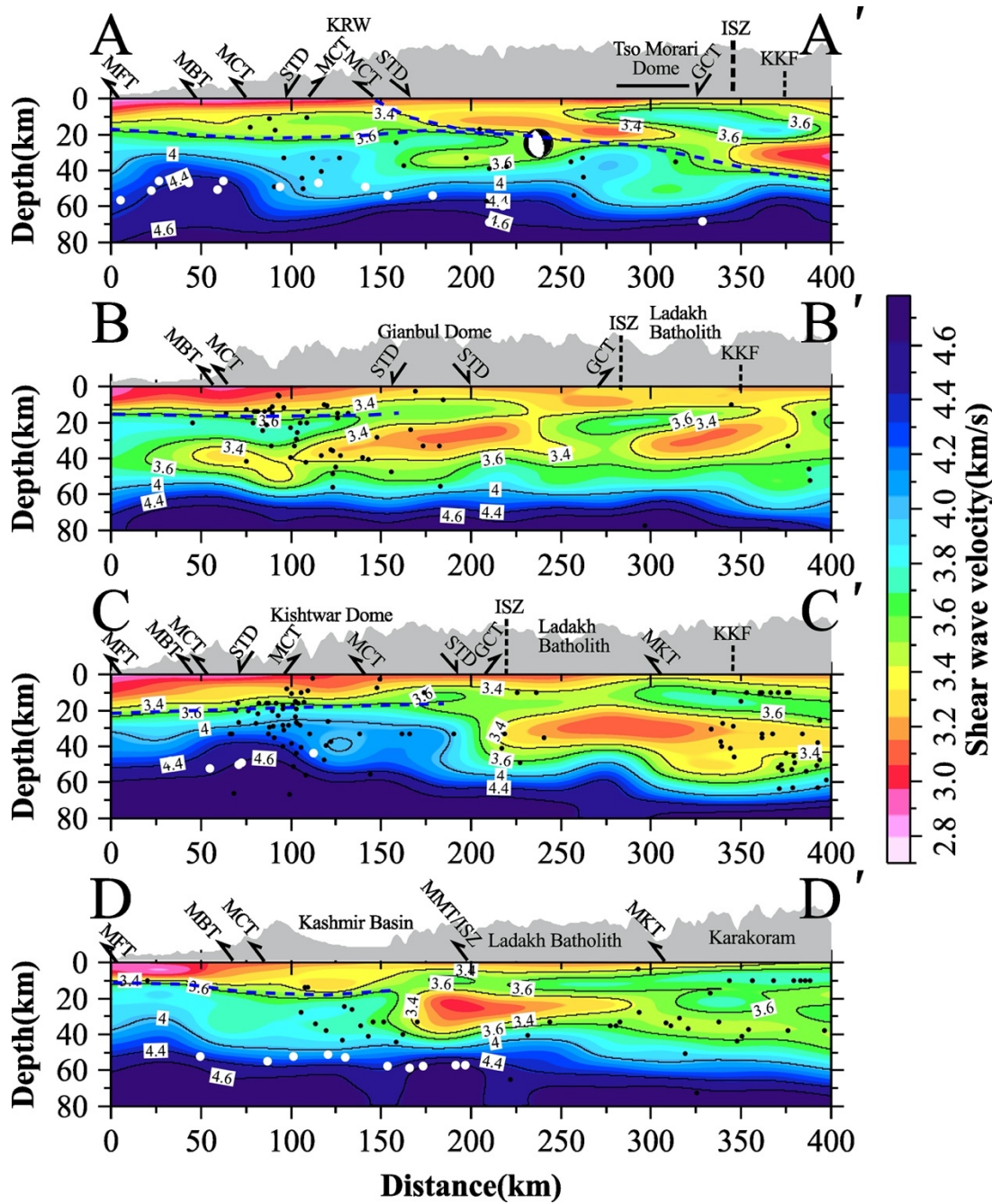
Figure 4.4 *Arc perpendicular velocity-depth sections. The location of each profile (green line) is presented in Figure 4.3. Surface topography with positions of major tectonic blocks and faults are presented at the top of each profile. The color data indicate absolute shear wave velocities for 0-80 km depth. Vs contours at 3.4, 4.0, 4.4, and 4.6 km/s are shown in the black line.*
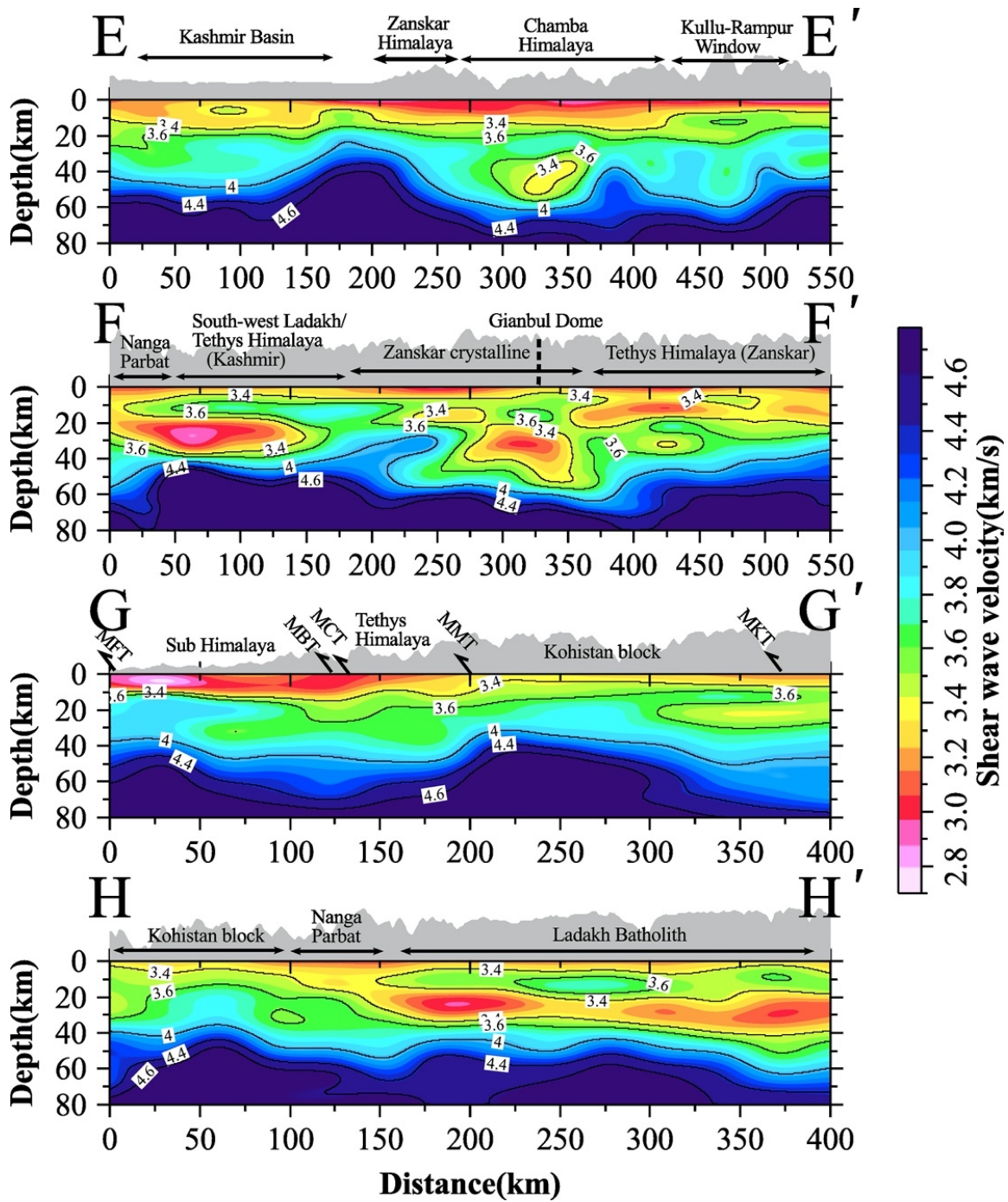
Figure 4.5 *Same as Figure 4.4. Top two profiles are running along the Himalayan arc. Bottom two profiles cover the crustal structure of the Ladakh-Kohistan arc.*

In summary, with the velocity model presented in this study, two primary observations about the crustal structure of the northwestern Himalaya and Ladakh-Kohistan arc are made. The first observation is the presence of the near arc-perpendicular low-velocity anomaly (L4) and the first-order crustal structure essentially in terms of the MHT geometry of the Himalayan arc. The second observation is the high-velocity lower

crust of Kohistan and the variation of the crustal structure under the Kohistan-Ladakh arc. In the following sections, we discuss the broad tectonic implication of these results with a focus on understanding the lateral variation on the crustal structure of the study region that plays a key role in the deformation mechanism of the India-Asia convergence zone.

4.5 Discussion

4.5.1 Segmentation of the MHT across a transverse boundary at ~ 77°E

The along-arc variation of deep crustal structure and its relationship with the surface geology have been used to infer large-scale segmentation of the Himalayan arc (Hetenyi et al., 2016; Dal Zilio et al., 2020; Eugster et al., 2018; Priestley et al., 2019; Arora et al., 2012; Hazarika et al, 2017). Using four arc-perpendicular velocity profiles (Figure 4.4) and shear velocity maps at different depths (Figure 4.3) discussed in the previous sections and combining them with previously published geophysical studies, we observe a noteworthy lateral variation in the geometry of the MHT as imaged by Vs ~3.6 km/s across a nearly arc-perpendicular transverse boundary at ~ 77°E (marked as L4 in Figure 4.3). East of this boundary, the MHT dips gently northward (10−16°) beyond the Greater Himalaya Sequence (GHS) (Profile A−A´, Figure 4.4). Such a north dipping geometry is usually found in the central Himalaya (Figure 4.6), where the depth of the MHT increases from ~20 km beneath the southern boundary of the Tethys Himalaya to ~ 40 km beneath the ISZ (Caldwell et al., 2013; Nábělek et al., 2009; Schulte-Pelkhum et al., 2005; Gao et al., 2016). In addition, this roughly north dipping detachment may contain steep mid to lower crustal ramps (Caldwell et al., 2013; Gao et al., 2016) that facilitate stress localization (Bilham et al., 2017; Stevens & Avouac, 2015), and crustal-scale duplexing (Yin, 2006; Gao et al., 2016; Guo et al., 2017) resulting in the growth of the Himalayan wedge. North of the ISZ, the MHT is almost flat at 45-50 km depth (Gao et al., 2016; Guo et al., 2017). In contrast, along the transverse boundary and further west (Profile B−B´ to D−D´, Figure 4.4), the MHT is a near flat detachment up to 150-200 km north of the MFT. The depth of the MHT is approximately 15-20 km between the MBT, which marks the Himalayan front in the Kashmir and Zanskar region, and the ISZ, which marks the end of the Himalayan arc.
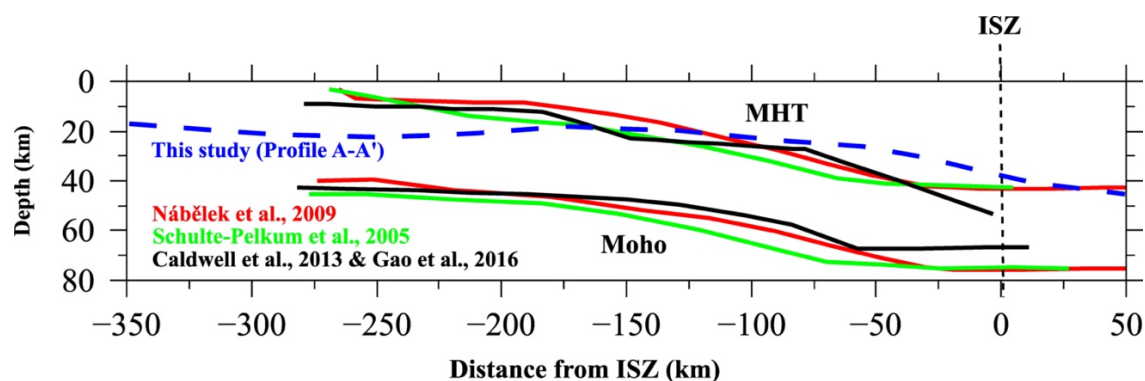
Figure 4.6 *Compilation of MHT geometry in central Himalaya along with Moho depth. The blue dashed line shows the MHT geometry of the profile A−A´. Distance in the horizontal axis is taken with respect to Indus Suture Zone (ISZ).*

Evidence of such a segmentation of the MHT across ~77°E is not yet demonstrated by previous seismic imaging studies (Mir et al., 2020; Priestley et al., 2019). However, lateral changes in the seismicity pattern and the width of the interseismic coupling zone along the length of the Himalayas indicate significant changes in the dip of the MHT across the transverse boundary at ~77°E. The interseismic coupling width changes from 29−78 km in the central Himalaya (77−85°E) to 171−189 km in the western Himalaya (73−77°E) (Bilham et al., 2017; Stevens & Avouac, 2015), which requires the presence of a very shallow dipping or nearly flat MHT west of 77°E (green boundary in Figure 4.7 shows coupling width after Bilham et al., 2017). Arora et al. (2012) discuss the segmentation of the seismicity in the northwestern Himalaya. Moderate and small magnitude events tend to cluster along a band beneath the Higher Himalaya front in the central Himalaya. In contrast, the seismicity becomes widespread and diffuse in the Zanskar and Kashmir Himalaya with relatively less intensity of events in the Kangra-Chamba region (~77°E, Figure 4.7). It is also important to note that the rupture extent of the 1905 Kangra earthquake ends at around 77°E (Figure 4.7). In addition to seismicity, the segmentation is further illustrated by significant changes in the arc-parallel gravity anomaly across 77°E (Hetenyi et al., 2016).

Further evidence of the segmentation across 77°E longitude comes from topographic, exhumational, and structural variability. The central Himalaya (east of 77°E) contains a two-step topography with northward increasing relief. The first step is present at the MFT and the second step (often referred to as "physiographic transition two" or PT$_2$) is at ~ 100 km north of the MFT (essentially tracing the MCT). However, the western Himalaya (west of 77°E) shows one-step topography coinciding with the MBT thrust ramp with discontinuation of the PT$_2$ (Hodges, 2000; Eugster et al., 2018). The PT$_2$ in the central

Himalaya is often considered to be the result of rapid exhumation due to the mid-crustal ramp in the MHT, whereas the exhumation rate decreases west of 77°E (Eugster et al., 2018). A significant lateral ramp in the MBT and MCT occurs across 77°E where the width of the Lesser Himalaya changes from ~100 km in the central Himalaya to < 8 km in the western Himalaya (Yin, 2006).
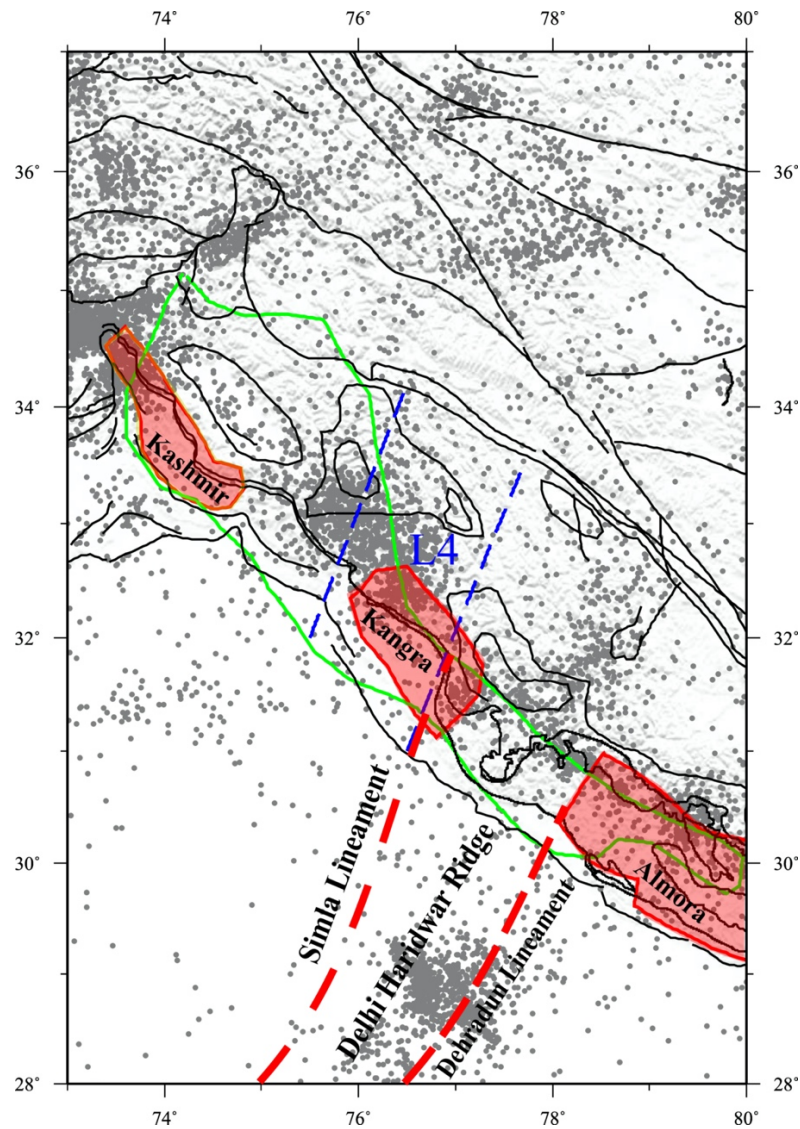
Figure 4.7 *Map showing lateral variability in moderate and small magnitude seismicity (black dots), rupture zones of large magnitude seismicity (red shaded area), interseismic coupling width (green line), imaged transverse anomaly (L4, blue dashed lines), and pre-existing Indian basement faults/lineaments (red dashed lines). Black lines represent major faults and suture zones.*

Combined with our results, the above discussed lateral variability indicates the presence of at least a crust-scale transverse boundary along ~77°E longitude, across which

significant changes are observed right from deep crustal structure (i.e MHT geometry and the resulting flexure of the Indian crust) to surface processes (i.e topography, exhumation, etc.). Note that the velocity structure in the vicinity of this transverse boundary is largely characterized by a crustal-scale low-velocity zone (Figure 4.3) indicating a potential weak boundary. Several mechanisms are proposed to account for this significant along-arc variability in the Himalayas. End member models include westward increasing convergence obliquity between India and Asia (Macedo & Marshak, 1999) and/or changes in sediment influx into the orogenic wedge (Dahlen, 1990) or reactivation of lithospheric scale pre-Himalayan origin transverse faults/lineaments of the Indian peninsula that extend to the northern limit of the Indian lithosphere beneath Tibet (Godin et al., 2019; Godin & Harris, 2014; Hetenyi et al., 2016). Eugster et al. (2018) conclude that convergence obliquity and sediment influx may explain the low exhumation rate in the western Himalaya but are inadequate to account for sharp transition in topography (PT$_2$). As it is clear from our result (Figure 4.3) that the boundary near 77°E could be at least a crustal-scale feature, the role of pre-existing transverse structures (i.e lineaments) of the Indian basement may be a potential mechanism for the observed along-arc variation in the Himalayas. Recent studies in southern Tibet associate lateral variation in the underthrusting Indian lithosphere to slab tears or break-offs that coincide with deep-seated basement faults preserved in the Indian lithosphere (Chen et al., 2015; Li & Song, 2018).

In northwestern Himalaya, the Simla lineament (Figure 4.7) approximately coincides with the western end of the anomaly L4 (Figure 4.3). The lineament forms the western edge of the Delhi-Haridwar ridge (Godin & Harris, 2014). The reactivation of such a lineament as strike-slip faults and subsequent propagation of strain from the down-going plate to the overriding wedge through a weak mid-crustal layer can affect the geometry of the MHT. This subsequently segmented the Himalayan range (Godin & Harris, 2014). The presence of the strong low-velocity zone in the mid/lower crustal depth (anomaly L4) possibly provided the sufficient condition for the deep-seated Simla lineament reactivation that produced lateral ramps in the MBT and MCT across 77°E, and consequently changed the dip of the basal detachment (i.e MHT). The Simla lineament, which also marks the eastern end of the 1905 Kangra earthquake rupture zone, acts as a weak coupling zone between the surrounding segments (Godin & Harris, 2014; Hetenyi et al., 2016). It is highly likely that the imaged transverse boundary near 77°E represents similar segmentation of the Indian lithosphere south of the Himalayan arc. Chun (1986) and Mitra et al. (2011)

observe a significant lateral variation of mid to lower crustal structure beneath the western and eastern Ganga basin. In addition, Saha et al. (2020) imaged segmentation of the Indian lithosphere beneath the Ganga basin at 75°E. Further studies are needed to map inherited basement faults and understand their role in subduction processes in the Himalaya-Tibet region.

4.5.2 Crustal structure of the Kohistan-Ladakh arc

From brief discussions in sections 4.3 and 4.4, it is clear that the Kohistan arc is underlain by a high-velocity lower crust whereas the Ladakh's arc is largely characterized by a mid-crustal LVZ. To further understand the lateral variation in the Kohistan-Ladakh arc's crust and its broad implication, we plot the average 1-D shear wave velocity of Kohistan and Ladakh separately (Figure 4.8). The Kohistan arc is represented as two segments namely the Gilgit complex in the north Kohistan and the combination of Southern Plutonic Complex (SCP) and the Chilas complex in south Kohistan. The average velocity under the Kohistan arc shows a uniform upper and middle crust (< 40 km) with Vs ~3.5 km/s. However, the lower crust (> 40 km) of the southern Kohistan, where arc's lower crustal rocks (mafic to ultra-mafic) are exposed, is characterized by a high-velocity underplated layer (Vs > 4.0 km/s) of thickness ~ 25 km above an average Moho depth of 65 km. In case of the Ladakh arc, the average mid-crustal (20-40 km depth) velocity (Vs < 3.4 km/s) indicate a LVZ with a relatively thin high-velocity lower crust (Vs > 4.0 km/s) at 55-65 km depth.

The observation of a high-velocity lower crust beneath the Kohistan arc is consistent with the previous estimate of a dense lower crust after 40 km depth (Figure 4.8b) derived from laboratory measurements of exposed rocks (Jagoutz & Behn, 2013). The ~25 km thick dense layer indicates ~15 km thick arc root (40-55 km depth) (Jagoutz & Behn, 2013) underlain by ~10 km (55-65 km depth) underplated lower crust of India that underthrusts the Kohistan-Ladakh arc. Such a dense arc root beneath Kohistan arc represents mafic garnet granulite or eclogite lithology that possibly undergoes density sorting and episodic delamination resulting in an overall andesitic nature of modern continental crusts (Jagoutz & Behn, 2013; Jagoutz & Schmidt, 2012). This study provides the first evidence of the above-mentioned dense lower crust of the Kohistan arc using seismic imaging.
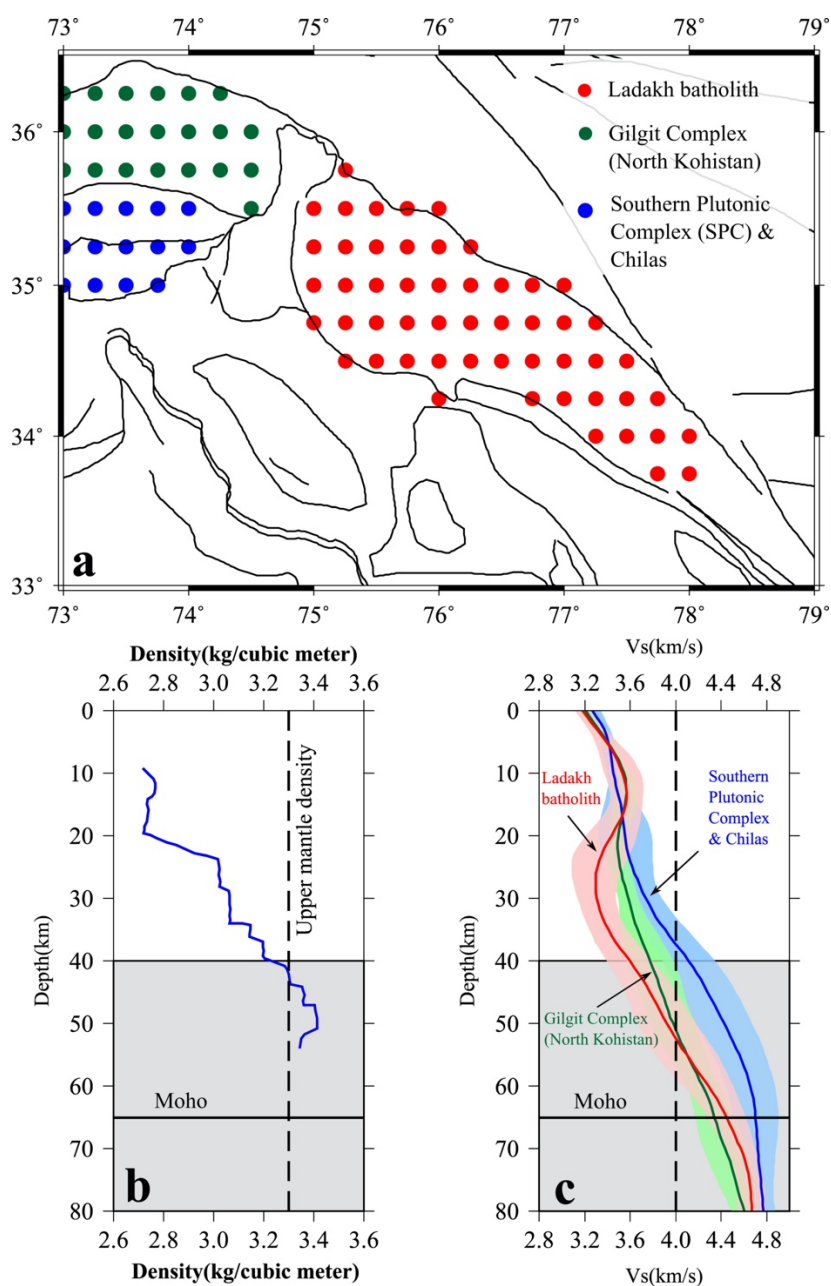
Figure 4.8 *Average 1-D velocity structure of the Kohistan-Ladakh arc. (a) map showing the Kohistan-Ladakh arc. Filled circles represent nodes of this study's velocity model for different lithologic units such as Ladakh batholith (in red), southern Kohistan (blue), and north Kohistan (green). (b) 1-D density plot from (Jagoutz & Behn, 2013) beneath the Kohistan arc. (c) comparison of average 1-D shear velocity model of different segments mentioned in (a).*

The average velocity structure of the Ladakh arc is comparable to southern Tibet (i.e mid-crustal LVZ and ~10-15 km underplated lower crust) indicative of evolutionary linkage. The tectonic processes vary significantly from the east to the west with the Ladakh

arc as a linkage between a typical arc crust in the west (i.e., Kohistan) to the Andean-type arc crust in the east (i.e., southern Tibet). Note that out of the chain of volcanic island arcs all along the India-Asia convergence zone, only Ladakh and Kohistan arc survived. Others possibly got entirely subducted beneath the south and central Tibet (Burg, 2006; Jagoutz & Schmidt, 2012). The distinct geological setting of island-arc preserved orogen in the west and island-arc-subducted orogen in the east requires a significant transfer fault (Burg, 2006). Extension of the Ropar-Manali/Simla lineament (Figure 4.7) further north potentially marks the eastern end of the Ladakh batholith. We speculate that this lineament had a prominent role in explaining such east-west diversity.

4.6 Conclusion

We image an unreported arc normal crustal-scale transverse boundary in the western Himalaya, located between the Kishtwar and Kullu- Rampur window (~77°E), characterized by low-velocity zones (LVZs) (Vs < 3.4 km/s) at the mid to lower crustal depths. In the northern edge, the transverse structure has extremely low velocities (3.2 > Vs < 3.4 km/s) between 20 to 50 km depth beneath the Gianbul dome in the Zanskar Himalaya. The Indian upper crust defining the MHT is mapped as a feature with Vs ~ 3.6 km/s. To the west of this boundary in the Zanskar and Kashmir Himalaya, the Main Himalayan Thrust (MHT) is nearly flat or dips northward at a very low angle. The MHT is at a 15-20 km depth between the Main Frontal Thrust (MFT) and the Indus Suture Zone (ISZ) with no evidence of mid/low crustal ramp. To the east of the transverse boundary in the Himachal Himalaya, the MHT is characterized by crustal-scale ramps dipping gently northward (10-16°) from ~10 km depth below the Lesser Himalaya to ~25 km depth below the Tethys Himalaya to ~40 km below the ISZ. This transverse boundary correlates well with the earlier observed the northward extension of the Ropar-Manali/Simla lineament, a pre-Himalayan lithospheric scale fault of the Indian plate.

Our velocity model reveals a significant lateral variation in the crustal structure below the Kohistan-Ladakh arc. The Kohistan arc shows a uniform upper and middle crust (Vs ~ 3.5 km/s) underlain by a thick (~25 km) high velocity lower crust (Vs > 4.0 km/s). In contrast, the Ladakh arc crust is largely characterized by a mid-crustal LVZ (Vs < 3.4 km/s) between 15 and 40 km depth, and the thick mafic basal layer is absent at greater depths. These results present first-order seismic evidence for lateral variability in the Himalayan arc potentially caused by lithospheric scale transverse faults inherently present in the Indian plate.

CHAPTER 4

CHAPTER 5

Seismic imaging of the Main Himalayan Thrust, Garhwal Himalaya using ambient noise tomography

5.1 Introduction

The largest Himalayan earthquakes are generally accepted to occur due to the episodic release of stress that accumulates with the convergence of India and Tibet. They occur on the Main Himalayan thrust (MHT)- a shallow dipping decollement along which the Indian crust thrusts under Himalaya, and propagate up to the front of the Himalaya where the MHT emerges at the surface (Geller & Kanamori, 1977; Sapkota et al., 2013; Nakata, 1989) as the Himalayan Frontal Thrust (HFT). The MHT dips northward at a low angle in the lower Himalaya and steepens downward onto a mid-crustal ramp beneath the Higher Himalaya before flattening again northward under the Tethys Himalaya and southern Tibet. This mid-crustal ramp could explain the location of the front of the high topography along the MHT and the nucleation of large Himalayan earthquakes (Dal Zillio et al., 2020; Bilham et al., 2017). Recent observations suggest that megathrust earthquake ruptures are generally confined to areas of the plate interface (MHT) that were previously locked (Konca et al., 2008; Moreno et al., 2010; Loveless & Meade, 2011). These earthquakes mostly partially rupture the locked zone. Factors controlling the extent of such partial ruptures are unclear. Possible reasons could be the geometry or heterogeneous frictional properties of the plate interface. In Nepal, Hubbard et al. (2016) proposed that the up-dip edge of the rupture of the 2015 Gorkha earthquake was arrested by a shallow depth ramp along the MHT, a view also supported by quasi-dynamic simulations (Qiu et al., 2016, Sathiakumar & Barbot, 2021). Whether such a small and shallow ramp exists in the Garhwal Himalaya is unknown. Yadav et al. (2019) proposed that the presence of such features is unlikely to be resolved by the GPS measurements of interseismic deformation.

Accurate imaging of MHT along its complete section is critical to understanding fault segmentation, which plays a crucial role in the initiation, propagation, and termination of earthquakes, and estimates the earthquake hazard potential as well as in understanding orogenic processes (Cattin & Avouac, 2000; Wesnousky, 2006; Elliott et al., 2016; Hubbard et al., 2015; Qiu et al., 2016). Despite numerous geophysical experiments in the Himalayas, the accurate mapping of the MHT is still evolving (Stevens & Avouac, 2015), primarily due to the narrow lateral width (< 30 km) and a few kilometers vertical dimension

of the MHT ramp in large part of the central Himalaya (Bilham et al., 2017). Seismological imaging research uses reflection seismic or receiver function (RF) to map the MHT. Both the approaches use impedance contrast as a diagnostic. Particularly with RF time series, the overlying crushed wedge material produces scattering and conversions from the shallow layer that interacts with the response from the deeper layers resulting in complexity. In this chapter, we significantly improve the resolution of the seismic structure of the upper and middle crust and the geometry of MHT beneath the Garhwal Himalaya by modeling ambient noise data recorded on a high-density seismic network that operated between 2005 and 2008 (Figure 5.1).

5.2 Seismotectonics of Garhwal Himalaya and nature of MHT

5.2.1 Geological Background

The Himalayan range formed due to continued subduction of India beneath Eurasia beginning about 55 Ma ago (Powell & Conaghan, 1973; Molnar & Tapponnier, 1975, Yin & Harrison, 2000), is structurally dominated by various thrusts and detachments as a consequence of crustal shortening (see details in Chapter 1). These include the Southern Tibetan Detachment (STD), the Main Central Thrust (MCT), Main Boundary Thrust (MBT), and the Main Frontal Thrust (MFT/HFT). These thrust systems demarcate distinct Himalayan sequences: Tethyan Himalayan Sequence (THS) bounded by the Indus-Zangbo Suture (IZS) in north and STD in the south; Greater Himalayan Sequence (GHS) or High Himalaya (HH) bounded by STD and MCT; Lesser Himalayan Sequence (LHS) or Lower Himalaya (LH) between MCT and MBT; and sub-Himalaya between MBT and MFT (Heim & Gansser 1936; Wadia, 1951) (Figure 5.1). The break in the topographic slope also defines the Lower and Higher Himalayas. There is a progressive younging of thrust systems from MCT (22-18 Ma), MBT (~11 Ma) to HFT (~6 Ma).

The Garhwal Himalaya, geographically located between 77−81°E adjoining Nepal, has served as a platform for classical stratigraphic divisions of the Himalayas (Heim & Gamsser, 1936; Valdiya, 1980, 1988) as described in the previous paragraph and Chapter 1, which is used throughout the arc. It preserves a well-developed duplex in the Lesser Himalaya Sequence (LHS) (Srivastava & Mitra, 1994), representing a stack of thrust faults. The duplex exposed the Higher Himalaya rocks in the Lesser Himalaya as 300 km long Almora klippe. This folding led structural geologists to divide the LHS into two parts i)

outer LHS (Mesoproterozoic unit) north of the south-dipping Tons Thrust (TT), and ii) inner LHS (Neoproterozoic unit) south of the TT (Celerier et al., 2009). The Ramgarh Thrust (RT) is another major thrust fault bounding the southern limit of the Almora klippe.

5.2.2 Nature of MHT and Seismicity in Garhwal Himalaya

Structural reconstructions of MHT in the Garhwal Himalaya suggest a flat-ramp-flat geometry (Srivastava & Mitra, 1994; Mandal et al., 2019) with the ramp (dipping 30−40°) at ∼ 10−17 km depth below the surface expression of the Tons thrust. South of the ramp, the MHT is a flat layer at a depth of ∼ 6−8 km that connects to steeply north dipping Main Frontal thrust at the southern boundary of the Himalaya. The deeper flat portion of the MHT is at ∼ 17−20 km depth at the northern end of the ramp. Using receiver function analysis, Caldwell et al. (2013) imaged the MHT with the negative impedance contrast (dip 2° at ∼ 10 km depth) below the lesser Himalaya while its deeper flat part has positive impedance contrast (dip 4° at ∼ 20 km depth) below the Higher Himalaya. They mapped a gentle mid-crustal ramp with a dip of 10−25° between 10-20 km depth beneath the MCT zone. The MHT is also characterized as a discrete high conductivity layer because of sediment/fluid (Rawat et al., 2014). The high precision location of micro-earthquakes (1 > mag < 5) shows their localization in the vicinity of the mid-crustal ramp (Mahesh et al., 2013) along with another cluster beneath Ramgarh thrust. Recent studies of geodetic measurements indicate a narrow zone of inter-seismic decoupling (< 30 km) in the Garhwal area (Bilham et al., 2017; Stevens & Avouac, 2015). Assuming a constant failure strain in the Himalayas, Bilham et al. (2017) predicted a significant slip deficit in the Garhwal area, which may generate large future earthquakes.

The Garhwal region has not experienced a major earthquake of magnitude > 8.0 in recorded history. It remains speculative as an exceptional segment of the Himalaya collision zone distinguished only by strain releases through small and intermediate magnitude earthquakes such as the 1991 Uttarkashi (M 6.8, 30°45ʹ00ʺ N, 78°51ʹ36ʺ E), the 1999 Chamoli (M 6.3, 30°26ʹ24ʺ N, 79°23ʹ24ʺ E), and the 2005 Chamoli (M 5.3, 30°28ʹ48ʺ N, 79°15' E) suggestive of relatively high ambient stresses in the region (Khattri et al., 1989). The Mw ∼ 6.8 1991 Uttarkashi event initiated along the lower flat of the MHT close to the locked line (Banerjee & Burgmann, 2002), and the rupture extended along the MHT (Cotton et al., 1996) to the south of the crustal ramp. In 1803, an Mw ∼ 8 earthquake occurred ∼ 50 km north of the Uttarkashi earthquake, based on the damage report. This

earthquake ruptured at least a ~200 km-long segment of the MHT (Ambraseys & Douglas, 2004) but did not reach the surface at the front (Kumar et al., 2006). Apart from global observations, serious effort to understand the earthquake genesis in the Garhwal Himalaya started in the 1970s with the deployment of a few portable recorders in the MCT zone (Gaur et al. 1985), followed by the recent deployment of the broadband seismic and magnetotelluric instrument (Ashish et al. 2009; Mahesh et al. 2013; Rawat et al. 2014; Hazarika et al. 2017).
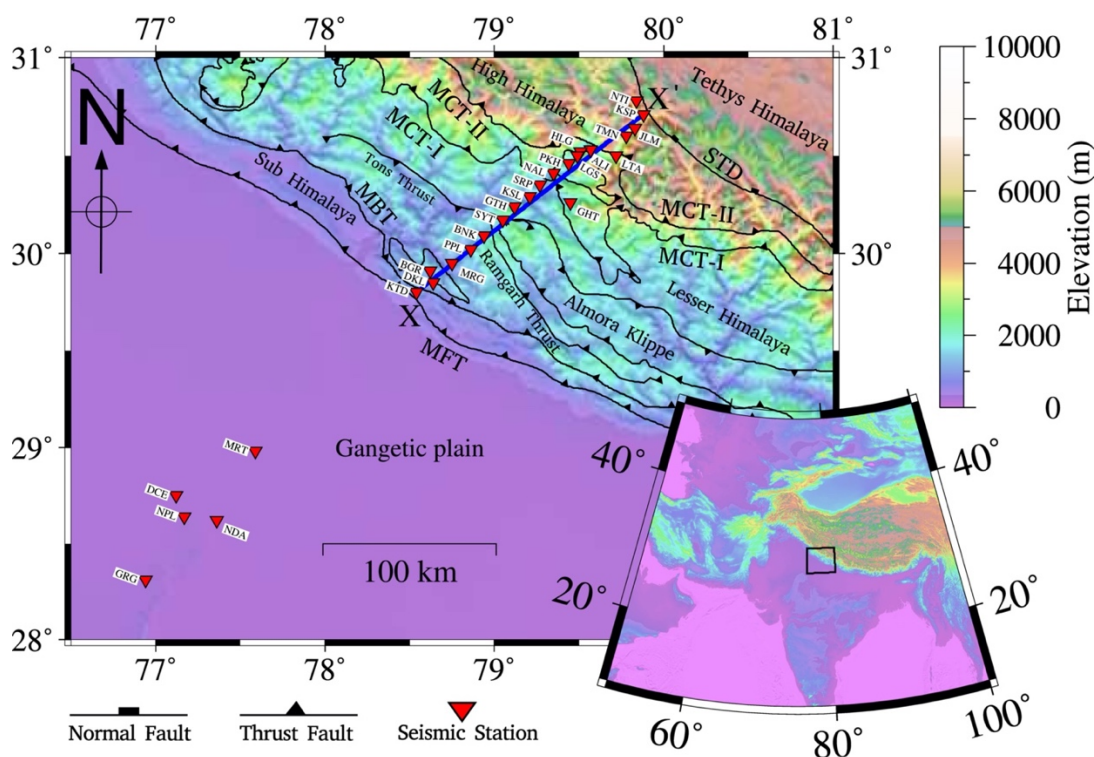
Figure 5.1 *Map of the Garhwal Himalaya showing major tectonic boundaries and faults in black lines. MFT: Main Frontal Thrust, MBT: Main Boundary Thrust, MCT: Main Himalaya Thrust, STD: South Tibetan Detachment. The red inverted triangles represent the seismic stations used in this study. The thick blue line marked by X-X′ is the NE-SW directed profile along which shear wave velocity cross-section is presented in this study. The color data in the map shows elevation from the mean sea level. The black box in the inset image marks the location of the experiment.*

5.3 Data and Method

We used ambient noise waveform data from 26 linearly located broadband seismographs across the Garhwal Himalaya and further south into the Ganga basin that

operated between 2005 and 2008 (Figure 5.1). The average inter-station distance is about 10 km. Data were acquired at 50 sample/s using 120 seconds period Guralp CMG-3T broadband seismometers. Details of the seismic array are presented in Mahesh et al. (2013). The velocity imaging is performed in two steps. Firstly, the inter-station fundamental mode Rayleigh wave phase velocity is computed from ambient noise cross-correlation following Bensen et al. (2007). The inter-station phase velocity dispersion was then converted into equispaced grid point dispersion data using the Fast Marching Surface Tomography (FMST, Rawlinson and Sambridge, 2005) (see Chapter 2 for details). The dispersion data at each node was further inverted in terms of the shear velocity variation with depth following Herrmann (2013).

5.4 Ambient noise analysis and dispersion measurement

As discussed in Chapter 2, imaging the crust and upper mantle structures by extracting inter-station Green's function from ambient noise cross-correlation haVE been an active area of research for the last two decades (Bensen et al., 2007; Yang et al., 2007; Saygin & Kennett, 2010; Shapiro et al., 2005; Sabra et al., 2005). The method improves the vertical and lateral resolution at shorter periods (< 30 sec) than the traditional seismic tomography approach using surface waves from earthquake waveforms. We follow the basic framework of ambient noise processing laid out by Bensen et al. (2007) and Schimmel et al. (2011) to compute inter-station Empirical Green's Function (EGF). The continuous waveform of vertical component seismograms at 50 samples per second was cut to one-day length, followed by correction for instrument response and removal of mean and trend. We filtered the signals from 0.02 Hz to 1 Hz (1 to 50 seconds). The filtered single-day waveforms from different station pairs were cross-correlated using the phase cross-correlation (PCC) method (Schimmel et al., 2011). No explicit temporal and spectral normalization were performed before cross-correlating the signals as the PCC scheme is amplitude unbiased. We combined the negative (acausal) and positive (causal) part of the daily cross-correlations and stacked them using the time-frequency phase-weighted stack (tf-PWS) approach (Schimmel et al., 2011).

Following Bensen et al. (2007), we used the automated Frequency-Time-Analysis (FTAN) method to compute fundamental-mode Rayleigh wave phase velocity dispersion using the stacked cross-correlation (Figure 5.2a). We selected a total of 67 inter-station pairs having phase velocity dispersion from period 6 to 23 seconds that had high SNR ($\geq$

10) and inter-station distance more than equal to twice the wavelengths (λ) (Figure 5.2b). Ray path distribution corresponding to individual time-period of phase velocity is shown in Figure 5.2c. The quality of computed phase velocity dispersion was ascertained by comparing the ambient-noise result of a pair of stations with the two-station method (Figure 5.3). The similarity of the waveforms and phase velocity from the two independent ways strengthens the reliability of this study's dispersion data.
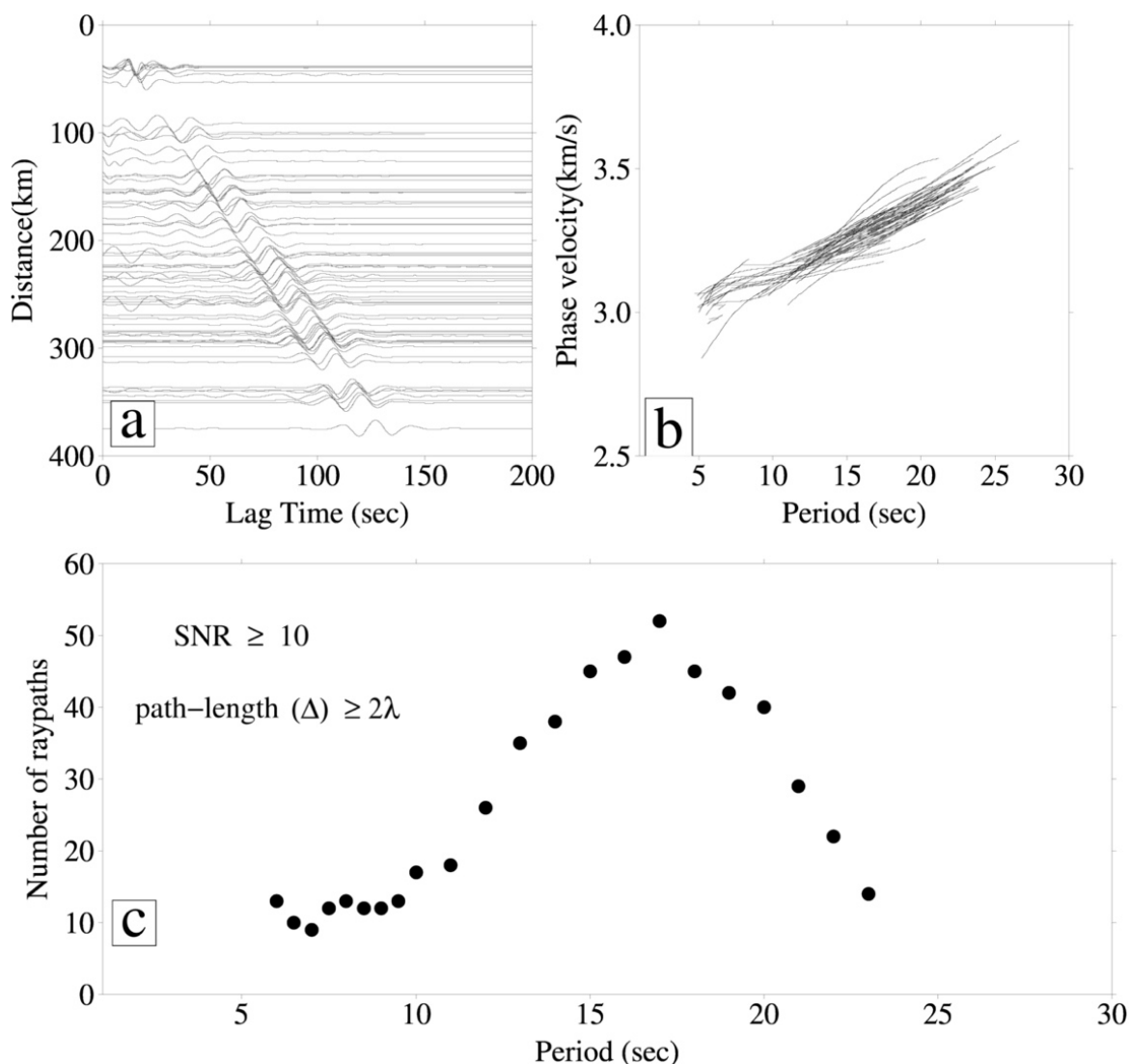
Figure 5.2 *Results of the ambient noise analysis and dispersion measurement. (a) stacked cross-correlations band-passed between 5s to 30 s, plotted against lag-time (sec) for increasing inter-station distances (km). (b) phase-velocity dispersion curves. (c) distribution of the number of inter-station dispersion measurements at different periods satisfying the selection criteria of signal to noise ratio and inter-station path-lengths.* $\lambda = C\tau$, *where C (= 3.5 km/s) is the phase velocity and τ is the period.*
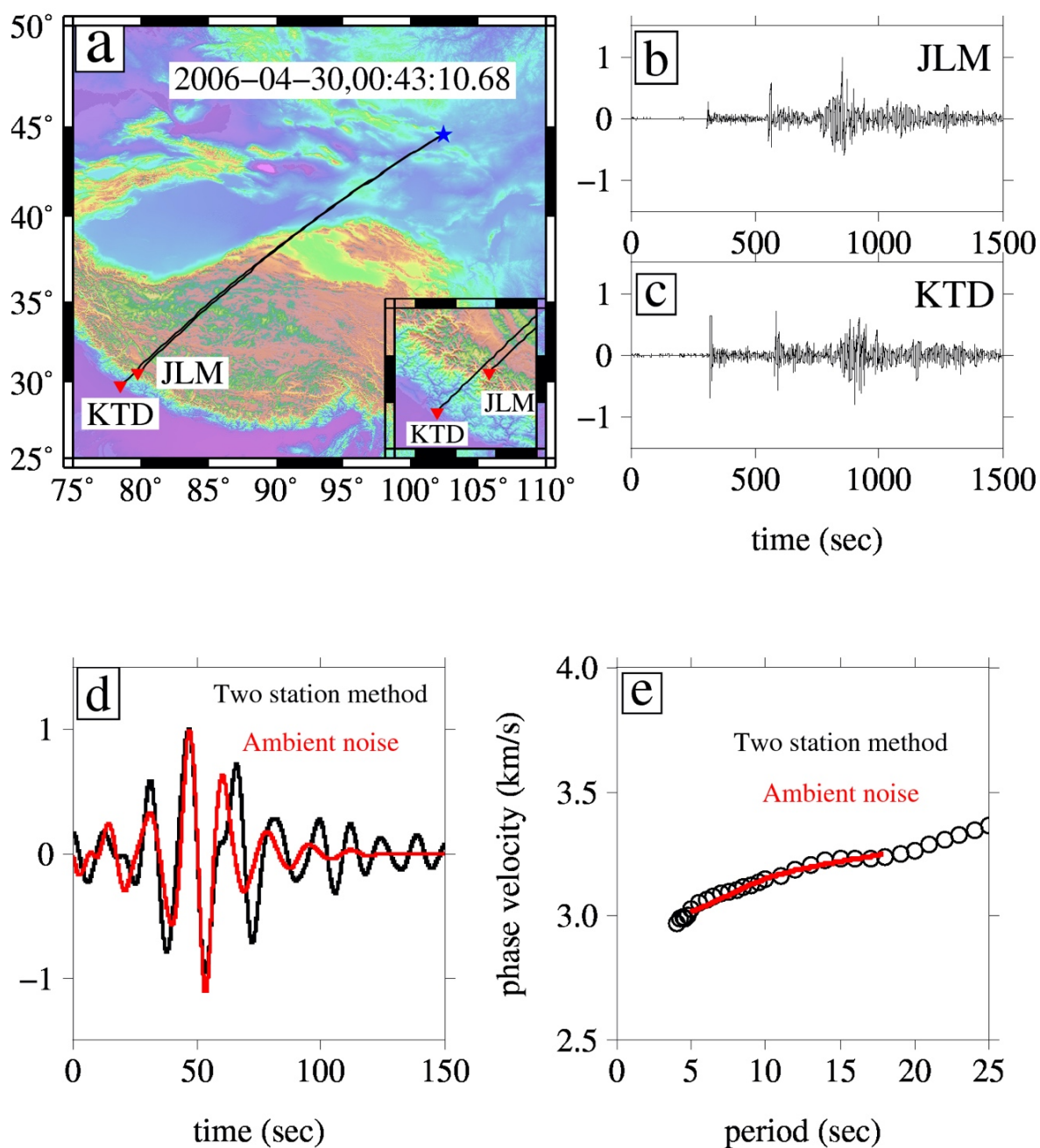
Figure 5.3 *Comparison of ambient noise result with the two-station method. (a) location of two stations (red inverted triangles) used for the two-station method with an event (blue star). (b) event record at these two stations. (c) comparison of ambient noise waveform with that of two station method band-passed between 5s and 30s. (d) comparison of phase velocity obtained by the ambient noise and two-station method.*

5.5 Phase velocity tomography

The Rayleigh wave phase velocities obtained for multiple inter-station paths were inverted in terms of their variation along the path using the iterative linearized inversion- the Fast Marching Surface Tomography (FMST) scheme (Rawlinson & Sambridge, 2005), described in detail in Chapter 2. We used L-curve tests at three representative periods (10, 15, 20 sec) to compute the optimum values of damping (ε) and smoothing (η) parameters, respectively (Figure 5.4a-f) that minimize the trade-off of data residuals with model perturbations and model roughness. The corresponding optimum values are 0.01 and 0.1 for damping and smoothing, respectively.
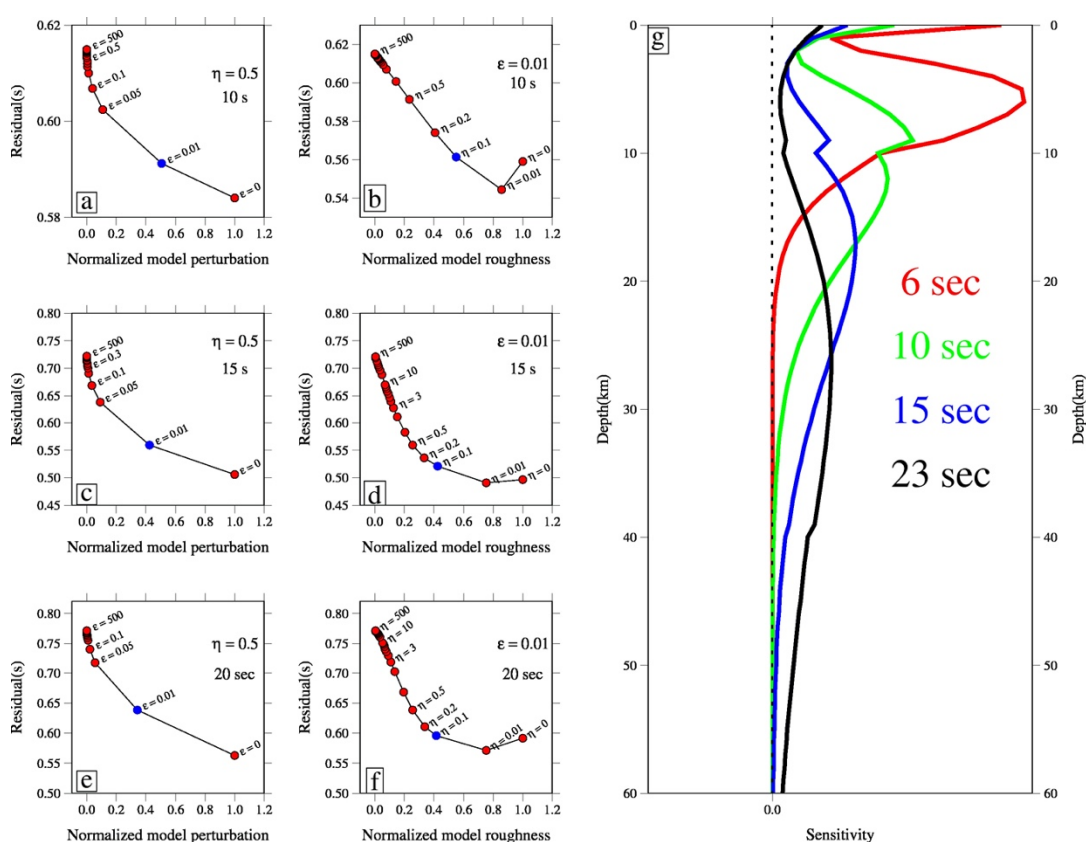
Figure 5.4 *Optimization of regularized parameters for phase velocity tomography. (a-f) L-curve test for damping parameter (ε) in the leftmost panel and smoothing parameter η the middle panel for tomography at different periods. The blue dot represents the selected value used in tomography. (g) Rayleigh wave phase velocity sensitivity curve at different periods.*

A series of checkerboard tests were performed to assess the optimum spatial resolution of the resulting phase velocity map. These tests were performed for the 0.1° and 0.05° grids with alternate positive and negative anomalies (perturbation of 27 % from mean 3 km/s)

separated by 0.1° space between them (Figure 5.5a,b). The inversion could recover an average of 60−80% of the input velocity model for a lateral resolution of ~ 10 km (Figure 5.5c-f,k). At higher periods (> 10-sec period), the phase velocity could be recovered with a horizontal resolution of ~ 5 km (Figure 5.5g-j,l).
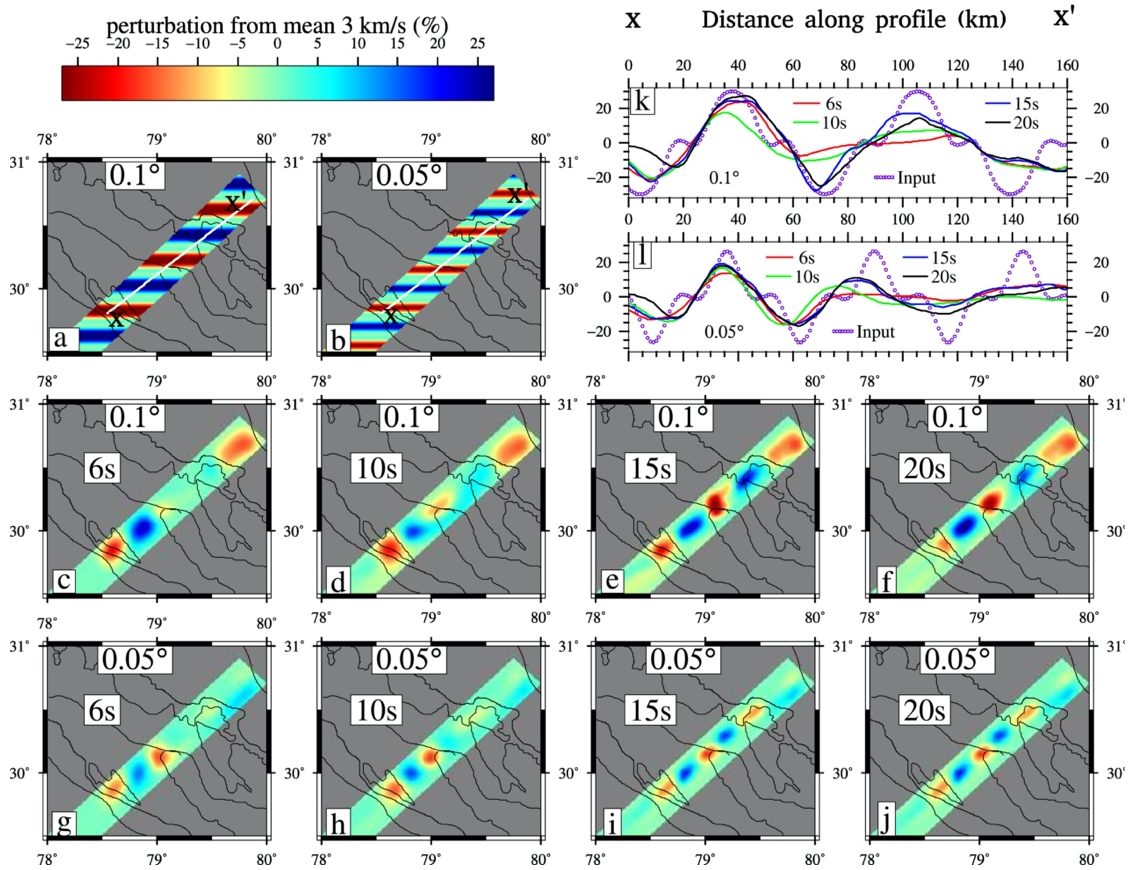
Figure 5.5 *Synthetic checkerboard test to analyze spatial resolution. (a) input model at 0.1° size in latitude. (b) input model at 0.05° size in latitude. Anomalies in both the input models have a maximum perturbation of 27 % from the mean velocity of 3 km/s with 0.1° spacing between them. (c-f) recovered models at different periods corresponding to the input model in (a). (g-j) recovered models at different periods corresponding to the input model in (b). Comparison of input and output model along the profile X-X′ (shown as white line in (a) and (b)) for both the input models are presented in (k) and (l) at the top right corner.*

After optimizing regularization parameters and spatial resolution, we performed the tomographic inversion from period 6 to 23 seconds and generated phase velocity maps at 0.05° × 0.05° grid interval. We used a homogenous phase velocity field derived from the mean phase velocity at each period as a starting reference model with a maximum number

of iteration kept at 50. The phase velocity along the profile X-X′ is presented in Figure 5.6 (top panel), which indicates continuously increasing dispersion with the period. However, its gradient shed light on the presence of upper crustal and mid/lower crustal low-velocity zones (Figure 5.6, bottom panel).
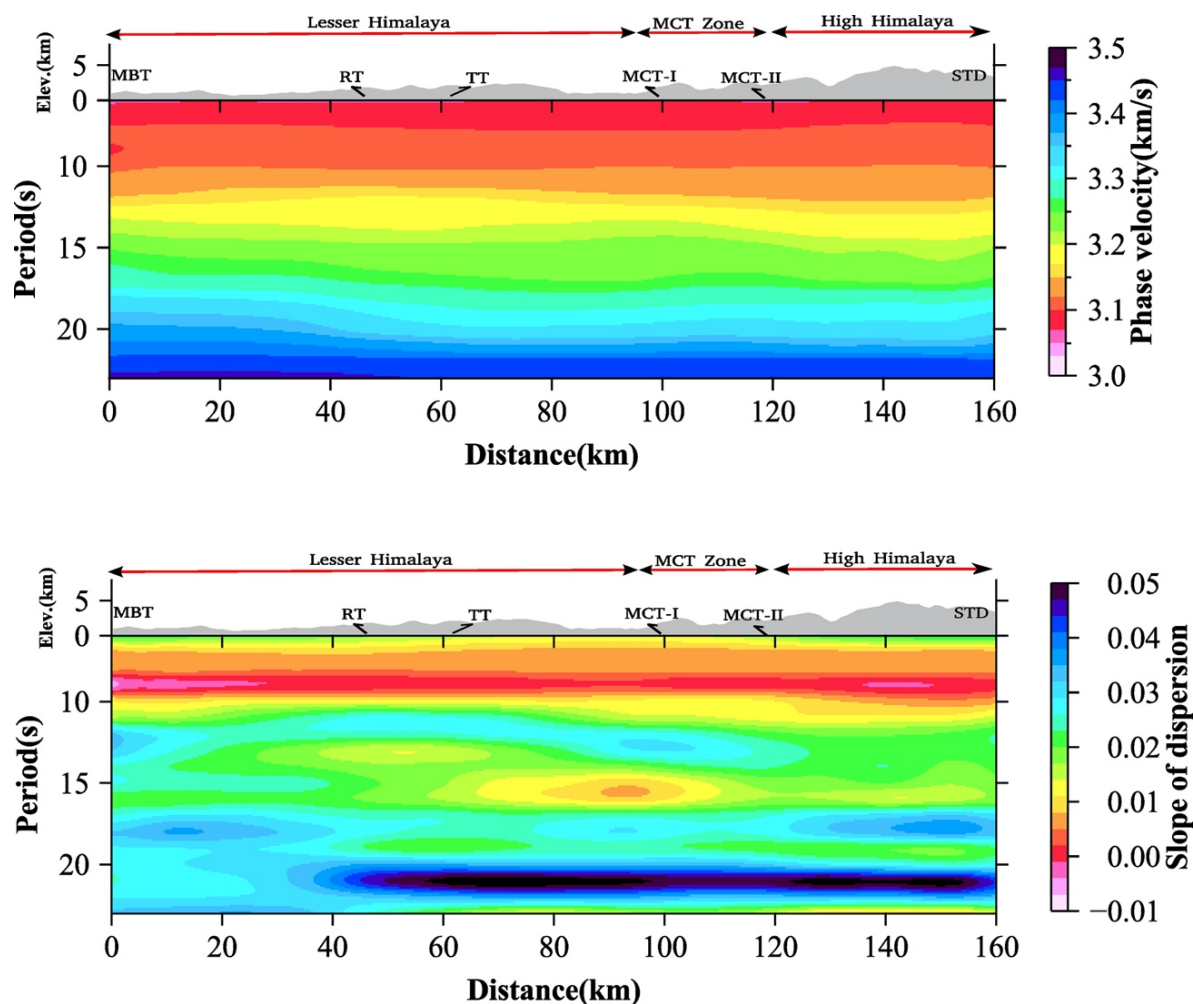
Figure 5.6 *Top panel: Continuous phase velocity along the profile X-X'. Bottom panel: Continuous gradient of phase velocity along the profile X-X'. A decreasing slope indicates waves speed decrease and vice-versa.*

At longer periods (> 18 s), the phase velocity dispersion shows relatively large variability from the average trend as evident from the inter-station dispersion in Figure 5.2b. Possible reasons for this trend include decreasing SNR and increasing area of influence at depth as the period increases. Therefore, we restrict ourselves to upper and mid-crustal structures as the lower-crustal velocities may contain higher uncertainties. With a maximum observed Rayleigh wave phase of 23 seconds, the sensitivity kernel suggests the highest sensitivity to a velocity structure at a depth of 30 km. The data, however, can

image velocity to a depth of ~ 40-45 km (Figure 5.4g). The phase velocity dispersion at the equispaced grid was inverted for the shear wave velocity variation with depth, as discussed in the following section.

5.6 Shear wave velocity structure

We apply an iterative least-square approach using the program *surf96* (Herrmann, 2013) to invert the phase velocity data at each grid-point in terms of the shear wave velocity variation with depth. The method has been extensively used in the inversion of surface wave data (Gilligan et al., 2015; Saha et al., 2020). For the reference model in the inversion, we used the average crustal velocity model of the Garhwal Himalaya determined from joint inversion of earthquake hypocenter and layered earth velocity by Mahesh et al. (2013). The velocity model includes the top 30 km with 2 km thick layers, followed by 5 km thick layers to a depth of 50 km over a half-space. In order to test the sensitivity of different reference models on the inverted model, we performed a synthetic inversion using a multilayered velocity model (Figure 5.7a). Corresponding to this velocity model we computed phase velocity in the period 6-23 s and added random noise for better representation as an experimental phase velocity from earthquake waveform (Figure 5.7b). The noisy phase velocity data were inverted using two reference models: 1) the average model of Mahesh et al. (2013) as discussed above, and 2) a half-space model at 4 km/s (Figure 5.7c). We first compute the damping parameter (Figure 5.7d) and perform the inversion. The inversion result is least sensitive to the initial models' choice as evident from the insignificant difference between inverted models (Figure 5.7e,f). Following this approach, 1-D inversion at each grid node of the phase velocity map of Figure 5.6 was done and subsequently interpolated to produce the shear velocity image along the profile X-X′ (Figure 5.8b, see Figure 5.1 for the profile location).

The crustal shear-velocity structure of the Garhwal Himalaya shows north-south variation consistent with the surface geology (Figure 5.8b). The most prominent feature of the image is the upper crustal low-velocity layer (UCL) with Vs varying between 2.9 km/s and 3.4 km/s in the top 5 to10 km beneath the Lesser-Himalaya that connects to a flat intra-crustal low-velocity layer (LVL) (Vs < 3.4 km/s) between 15 to 25 depth beneath the High-Himalaya. The UCL has a shallow flat base at ~ 5 km depth beneath the MBT, progressively deepening northward to ~ 10−15 km depth and connected through a ramp with a gentle dip of ~ 9°. This ramp extends horizontally from 35 to 65 km distance north

of MBT and underlies the surface trace of the Almora klippe. The low velocity under the Lesser Himalaya is inferred due to underthrusted Ganges sediment and free fluids (Caldwell et al., 2013; Rawat et al., 2014). Beneath the High-Himalaya, we observe two low-velocity layers with an intervening high-velocity one. The shallower one is 5 km thick with Vs ~ 3.0 km/s correlating with the surface exposed leucogranites. The deeper LVL is at 15−25 km depth with Vs of 3.3−3.4 km/s. The intervening high-velocity layer between 5 and 15 km depth has Vs ~3.5−3.7 km/s. Since the two low-velocity layers are disconnected, we suggest that the Himalayan leucogranite is a product of incipient melting and not connected to the mid-crustal LVL (or partial melts) beneath the Tethyan Himalaya and southern Tibet.
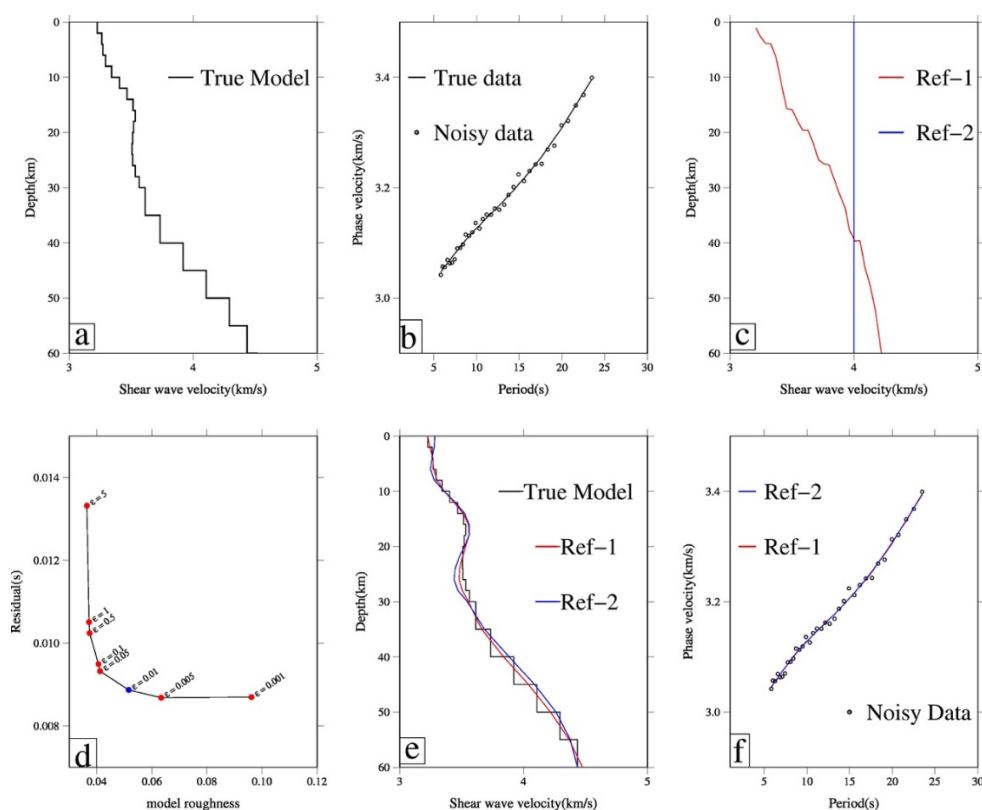
Figure 5.7 *Synthetic 1-D inversion of phase velocity using the program surf96. (a) a multilayered input model of crust. (b) synthetic phase velocity data with and without added random noise. (c) two initial models for the inversion, a homogenous half-space model at four km/s (Ref-1) and smoothed model of Mahesh et al. (2013) (Ref-2), (d) trade-off curve to determine damping parameter. The optimum damping of 0.01 is shown in the blue dot. (e) comparison of the inverted model with the actual input model for two initial velocity models. (f) comparison of fit of the dispersion data for two initial models.*
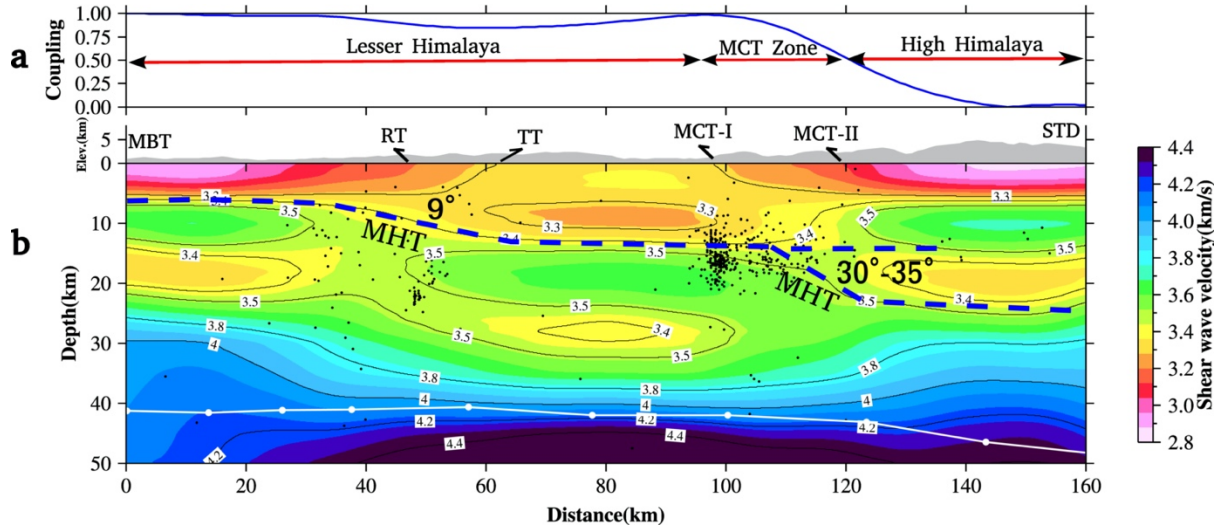
Figure 5.8 *(a) Inter-seismic coupling across the strike of the Garhwal Himalaya based on data from Stevens and Avouac (2015) is plotted along the profile X-X'. (b) shear wave velocity variation with depth along the profile X-X'. The dashed blue line represents the inferred MHT in this study. Black lines are velocity contours. A white line with dots indicates Moho adopted from Caldwell et al. (2013). Major faults are presented on the elevation data plotted in the gray shade above the velocity image. TT: Tons Thrust; RT: Ramgarh Thrust. The location of profile X-X' is shown in Figure 5.1. Black dots represent seismicity from Mahesh et al. (2013). Calculation of ramp angle: Ramp-1 beneath the Almora Klippe- depth changes from 7 km to 12 km in a horizontal distance of 30 km (i.e, $tan^{-1}(5/30) \sim 9°$). Ramp-2 beneath the MCT zone- depth changes from 15 km to 25 km in a horizontal distance of ~15 km (i.e, $tan^{-1}(10/15) \sim 33°$).*

At a deeper depth, we observed two additional low-velocity zones (Vs < 3.4 km/s) beneath the Lesser Himalaya, one between 12 to 20 km depth extending up to 30 km north of the MBT and the other relatively small, at ~ 28 km depth between the Tons and Munsiari (MCT-I) thrusts. These two low-velocity zones could be due to water released during metamorphism and possibly play an important role in nucleating clustered micro-seismicity at mid-crustal depth. Beyond 30 km depth, the velocity increases progressively from 3.8 km/s to ~ 4.2 km/s.

5.7 Geometry of the MHT and shallow crustal structure

To interpret velocity images, we briefly discuss the essential features of shear velocity variation in the crust. The shear wave velocity in the continental crust (upper,

middle, and lower crust) varies from 3.6 to 4.2 km/s considering anhydrous composition (Rudnick & Gao, 2003). It is affected by the temperature and water content. At shallow depth (upper crust) addition of water causes a significant reduction in velocity, while middle and lower crust velocity is less affected. A typical crystalline crust has Vs of 3.6 km/s with a marginal decrease in seismic velocity, possibly due to near-surface fracture and water in it (Christensen & Mooney, 1995). The upper crust Vs of ≤ 3.4 km/s would imply a substantial sediment contribution and partial melt (Diaferia & Cammarano, 2017)

We use the base of the upper crustal low-velocity layer (UCL) beneath the Lesser Himalaya and the intra-crustal low-velocity layer (LVL) beneath the High Himalaya as a diagnostic feature to map the MHT geometry. The inferred MHT is marked by the blue dashed line in Figure 5.8b. This narrow zone is characterized by closely spaced velocity contours of 3.4 km/s and 3.5 km/s. The shear velocities between 3.5 km/s and 3.6 km/s represent the underthrusted Indian crystalline crust, while the overlying crushed rocks forming the Himalayan wedge along with the sediments and fluid-bearing rocks have the shear velocity of 3.4 km/s and less. Caldwell et al. (2013) imaged the MHT at ∼ 10 km depth beneath the Lesser Himalaya and at ∼ 20−25 km depth beneath the Higher Himalaya, which closely matches with the base of the low-velocity zones in our image.

The MTH in the Garhwal Himalaya has two distinct ramps, similar to those in Nepal Himalaya (Hubbard et al., 2016, Qiu et al., 2016, Wang et al., 2017). At the southernmost part in Siwalik Himalaya, the MHT dips at ∼ 2-4° till 40 km north of MBT followed by the first ramp with a gentle dip of ∼ 9° at shallow depth (∼ 7−12 km) beneath the Almora klippe. It connects the southernmost flat portion of the MHT (∼ 5-7 km depth) to the deeper flat part (∼ 12-15 km depth, dipping ∼ 5°) beneath the northern lesser Himalaya. The MHT segment under the Lesser Himalaya is fully locked, also observed in the maximum inter-seismic coupling (Stevens & Avouac, 2015, Dal Zillio et al., 2020). They also report a locally moderate decrease in the coupling (< 0.8) beneath the Almora klippe (Figure 5.8a), coinciding with our inferred ramp below the Ramgarh Thrust. This thrust fault extends parallel to the Himalayan arc from western to central Himalaya and could be a potential stress accumulation zone for future great earthquakes. The proximity of the Tehri dam to the inferred ramp further heightens the earthquake hazard scenario.

Further northward, coupling reduces significantly under the Higher Himalaya with a sharp transition beneath the MCT zone (Figure 5.8a). The transition zone between MCT-I and MCT-II is identified on the velocity image as the second ramp with an angle of ∼ 30−

35° on the MHT (See Figure 5.8's caption for the calculation of ramp angle). Situated ~ 110 km north of the MBT, the ramp is at a depth of ~ 15−25 km beneath the front of the High Himalaya. A comparison of the inferred MHT geometry from this study with previous studies across the Garhwal Himalaya is presented in Figure 5.9. While the overall geometry of the MHT is consistent with Caldwell et al. (2013) and Kanna and Gupta (2020), our estimate of the mid-crustal ramp angle of 30−35° is comparable to that predicted from structural cross-sections of Srivastava and Mitra (1994) and significantly higher than the previous estimate of ~ 16° from the receiver function image of Caldwell et al. (2013).

The ramp's higher dip has important implications for understanding and computation of the width of the interseismic decoupling zone and earthquake occurrence. Great earthquakes along the Himalayas have episodically released strain energy stored in the upper part of the MHT. A decoupling zone separates the fully locked portion of the MHT in the south from the fully unlocked in the north where creep releases energy. The interseismic decoupling zone is dependent on the temperature and its width is dependent on the dip of MHT. At a temperature less than 350°C, the MHT remains locked, and no slip can occur. With the increasing temperature at 450°C, steady creep occurs. With increasing dip of the ramp, the 450° C isotherm is reached at a shorter horizontal distance. Compared to the earlier computed 16° dip of the ramp (Caldwell et al., 2013), the recomputed 30−35° dip would significantly reduce the decoupling zone width to about 33%. The width of the decoupling zone influences the capacity to store elastic energy (given by $0.5 \, V \, E\varepsilon_c^2$, where V is the volume, E is the Young modulus, and ε_c is the critical strain at failure) and hence the amount of slip deficit at the time of rupture. With increasing dip of the thrust, strain is distributed over small volume, and therefore it takes less time to reach the critical failure (Bilham et al. 2017). It remains highly speculative if the frequent occurrence of moderate size earthquakes is linked to the high dip of the MHT ramp and the long absence of large earthquakes in the Kumaon-Garhwal Himalaya.
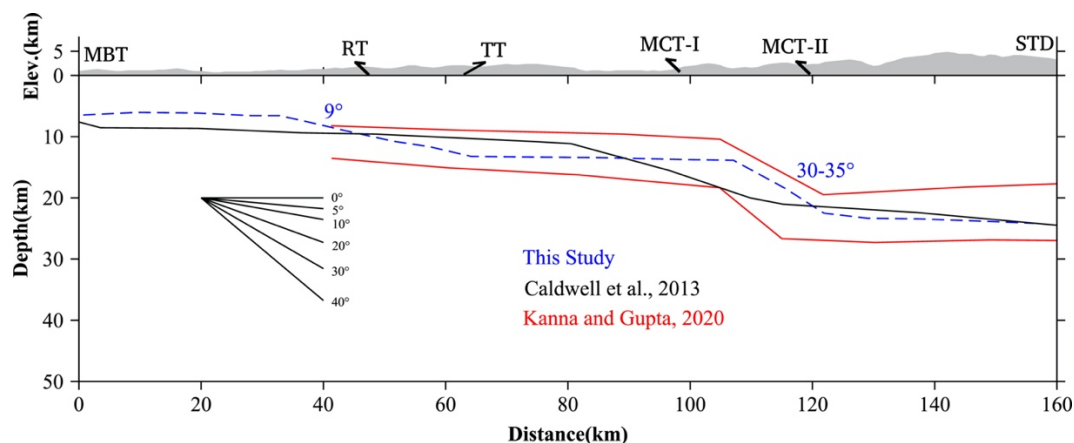
Figure 5.9 *Comparison of this study's MHT geometry with previous studies. The blue dashed line corresponds to this study. The black line and red line represent MHT geometry from Caldwell et al. (2013) and Kanna and Gupta (2020). At the left side of the plot, a reference for ramp angle is provided.*

Since the identification of the MFT and MHT, questions have been raised about how this fault system slips in earthquakes, and whether this slip is surface emergent (Almeida et al., 2018). Seeber and Armbruster (1981) proposed that the MHT extends past the MFT underneath the Gangetic Plain, and that coseismic slip during great earthquakes remains blind. Our result suggests that the décollement at the base of the MBT is 5-7 km deep, dipping at 2-4°. Considering a similar dip that continues southward, the MHT is likely to be ~ 5 km below the surface as proposed earlier (e.g., Lave and Avouac, 2000; Hirschmiller et al., 2014). This is deeper than that imaged at 2 km in Central Nepal (Almedia et al., 2018). We infer the MHT in Garhwal Himalaya extends beyond the MFT into the Ganga basin. In the event of a great Himalayan earthquake (M > 8) in the Garhwal region as suggested by many (Khattri et al., 1989, Bilham et al., 2001, 2017; Wesnuosky, 2020; Ghavri & Jade, 2021), it is possible that coseismic slip remains blind as proposed by Seeber and Armbruster (1981) and poses a serious threat to modern Indian cities in the Gangetic plain.

5.8 Conclusion

Ambient noise analysis of 26 broadband seismic stations in the Garhwal Himalaya provides seismic velocity images of upper and middle crust to a depth of 40 km with a 5−10 km horizontal resolution. The study uses ambient noise tomography to model the velocity structure. The inferred shear wave velocity structure along a NE−SW directed linear profile

crossing all of the Himalayan faults, indicates a hitherto unreported double ramp on the Main Himalayan Thrust. The first ramp is at shallow depth $\sim 7-12$ km (dip $\sim 9°$) below the Tons/ Ramgarh Thrust. The second ramp is imaged beneath the MCT zone at a distance of ~ 110 km north of the MBT at mid-crustal depth ($\sim 15-25$ km), dipping north $\sim 30-35°$. The inferred double ramp geometry in this study highlights the complex segmentation of MHT in the Garhwal Himalaya, which can provide important constraints in simulating earthquake hazard potential and modeling the growth of Himalayan topography. In the Sub Himalaya, below the MFT the decollement is about a depth of 5 km and the MHT extends into the Gangetic plain. The coseismic slip during a great earthquake may, therefore, remains blind posing a serious threat to the cities in the Gangetic plain.

CHAPTER 5

CHAPTER 6

Conclusions

The Himalayas and the Tibetan plateau are colossi among the great mountains of the world. Formed as a consequence of the collision of the Indian subcontinent with Eurasia, the Himalaya-Tibet mountain system for nearly 175 years, has been central to the development of models for the evolution of mountain belts and continents. Construction of its deep structure is critical to the understanding of the engine that drives the orogenesis and helps in solving the most important questions posed by India-Asia collision on quantifying the total amount of crustal shortening across the India plate. We use the dispersion of seismic surface waves generated through the earthquakes and ambient noise from the interaction of the atmosphere-ocean and the solid Earth, to create a 3-D high-resolution seismic wave velocity image of the Earth beneath this region. We focus our study on the western Himalaya-Tibet region that is poorly investigated as compared to the central and the eastern part. The crustal structure of the western Tibet-Pamir-Karakoram and the adjoining western Himalaya-Ladakh region is investigated using a shear wave velocity model with a lateral resolution of 30−50 km to a maximum depth of 100 km. The significant findings are summarized as below:

(1) Moho beneath the Himalayas and south Tibet correlates with a shear wave velocity of 4.4−4.6 km/s, and a reduced velocity of 4.0−4.2 km/s in northern Tibet and Pamir. The Moho depth increase from 50 km in the Himalayas to 80 km in central Tibet below the Bangong Suture. There are marked E-W variations in lower crust complexity in western Tibet between 31−33°N. To the west, beneath Pamir, the Moho is at 70−80 km depth with an extreme of 90 km at 37°N.

(2) Using Moho depth and the nature of high velocity lower crust (Vs > 4.0 km/s), we map the northern limit of the Indian crust that extends further north beyond the Qiangtang block in the western Tibet (77−82°E) than the previously thought boundary in the Lhasa block, continuing till central Pamir.

(3) We do not observe a continuous ductile channel flow in the western Tibet–Himalaya region as proposed for the central and eastern Tibet and Himalaya. Seismic velocity maps suggest laterally discontinuous low-velocity zones (LVZs) (Vs ≤ 3.4 km/s) in the upper and middle crust in Western Tibet. These LVZs generally do not connect to the high Himalaya as expected for a ductile channel flow. In Pamir, the LVZs correlate with the surface distribution of gneiss domes.

(4) The study suggests that the Karakorum Fault is an upper crustal feature. The inference is based on velocity sections across the length of fault that show continuity of mid-crustal low-velocity zones in the depth of 20-40 km without vertical offsets. Further, no significant variation in the underplated lower crustal layers across the fault is observed. Therefore, the fault is inferred as an upper crustal feature and may not play a significant role in crustal shortening.

(5) We present the first seismological evidence for the segmentation of the Main Himalayan Thrust (MHT) across a nearly arc-perpendicular transverse boundary at ~77°E. This transverse boundary is characterized by mid to lower crustal LVZs. To the east of this boundary, the MHT is characterized by a gentle north dipping ramp (10−16°) north of the High Himalayan front. In contrast, along this boundary and further west in Kashmir and Zanskar Himalaya, the MHT is a flat detachment with no evidence of a north dipping ramp. The imaged transverse boundary correlates with the northern extent of the Simla/Ropar-Manali lineament, a pre-Himalayan basement fault of the Indian lithosphere. The presence of the weak mid/lower crust along this boundary may have provided sufficient conditions for the propagation of strain from the down-going plate to the surface after the lineament got reactivated.

(6) The study provides the first seismic evidence of the high-velocity thick lower crustal arc root essentially present beneath the southern part of the Kohistan arc. No evidence of mid-crustal LVZ is observed in the Kohistan arc. However, the velocity model in the Ladakh arc indicates contrasting crustal structure with the presence of large-scale mid-crustal LVZs probably due to the Baltoro granite melting, and no evidence of thick lower crustal arc root.

(7) The ambient noise analysis across the strike of the Garhwal Himalaya using a closely spaced array of stations provides evidence for the complex geometry of the MHT that suggests the presence of double north-dipping ramps. The first, a gentle dipping (~9°) at 7−12 km depth beneath the Almora Klippe in the Lesser Himalaya, and the second, a steeply dipping (~30−35°) at 15−25 km depth beneath the MCT zone at the Higher Himalaya front. In the Sub Himalaya, below the MFT, the decollement is about a depth of 5 km and the MHT probably extends into the Gangetic plain. The coseismic slip during a great earthquake may, therefore, remains blind posing a serious threat to the cities in the Gangetic plain.

APPENDICES

A Measures of deformation

A.1 Strain

Strain is used in analyzing deformation within a continuum. For this, we consider an arbitrary infinitesimal volume element having a length defined by a vector $\overrightarrow{\delta \mathbf{R}}$ with two endpoints P($\mathbf{R}$) and Q($\mathbf{R}$+ $\delta\mathbf{R}$) located at a distance of $\mathbf{R}$ and $\mathbf{R}$+ $\delta\mathbf{R}$, respectively from an origin of a reference frame given in Figure (A1).
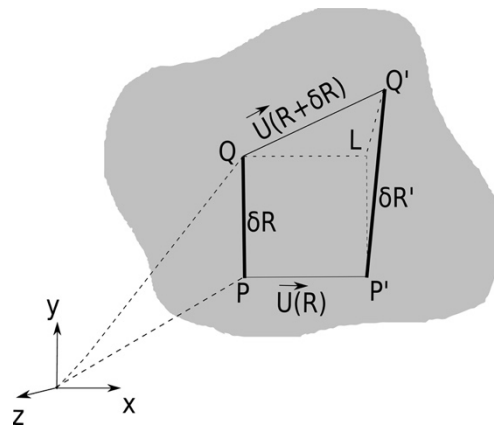
Figure A1. *An arbitrary infinitesimal volume V with a surface S. The frame of reference is denoted by a set of orthogonal axes x, y, and z.*

When subject to deformation, P and Q points will be displaced to new locations, say P' and Q', respectively defining a displaced element $\overrightarrow{\delta \mathbf{R}'}$. $\vec{\mathrm{U}}(\mathbf{R})$ and $\vec{\mathrm{U}}(\mathbf{R} + \delta\mathbf{R})$ represent displacement vectors obtained from PP' and QQ' respectively. We can always construct a parallelogram PQLP' such that PP'=QL=$\vec{\mathrm{U}}(\mathbf{R})$ and PQ=P'L= $\delta\mathbf{R}$. The resultant displacement $(\overrightarrow{\delta \mathbf{R}'} - \overrightarrow{\delta \mathbf{R}})$ is given by the length LQ', which can be written as

$$LQ' = \vec{\mathrm{U}}(\mathbf{R} + \delta\mathbf{R}) - \vec{\mathrm{U}}(\mathbf{R}). \qquad\qquad \text{A1.1}$$

After Taylor series expansion and ignoring the higher-order terms, we get

$$LQ' = \vec{\mathrm{U}}(\mathbf{R}) + J\,\delta\mathbf{R} - \vec{\mathrm{U}}(R) = J\,\delta\mathbf{R}, \qquad\qquad \text{A1.2}$$

$$\mathbf{J}=\begin{bmatrix} \dfrac{\partial U_x}{\partial x} & \dfrac{\partial U_x}{\partial y} & \dfrac{\partial U_x}{\partial z} \\[2mm] \dfrac{\partial U_y}{\partial x} & \dfrac{\partial U_y}{\partial y} & \dfrac{\partial U_y}{\partial z} \\[2mm] \dfrac{\partial U_z}{\partial x} & \dfrac{\partial U_z}{\partial y} & \dfrac{\partial U_z}{\partial z} \end{bmatrix} = \nabla U, \tag{A1.3}$$

where **J** is called the deformation gradient tensor, which can be expressed as sum of symmetric (**e**), anti-symmetric (**Ω**) and trace (**h**) components used to describe a rigid body rotation and deformation:

$$\mathbf{J}= \mathbf{h} + \mathbf{e} + \mathbf{\Omega}, \tag{A1.4}$$

$$\mathbf{h} = \begin{bmatrix} a & 0 & 0 \\ 0 & a & 0 \\ 0 & 0 & a \end{bmatrix},$$

$$\mathbf{a} = \frac{1}{3}\left[\frac{\partial U_x}{\partial x} + \frac{\partial U_y}{\partial y} + \frac{\partial U_z}{\partial z}\right],$$

$$\mathbf{e} = \begin{bmatrix} \dfrac{\partial U_x}{\partial x} - \mathbf{a} & \dfrac{1}{2}\left(\dfrac{\partial U_x}{\partial y} + \dfrac{\partial U_y}{\partial x}\right) & \dfrac{1}{2}\left(\dfrac{\partial U_x}{\partial z} + \dfrac{\partial U_z}{\partial x}\right) \\[3mm] \dfrac{1}{2}\left(\dfrac{\partial U_x}{\partial y} + \dfrac{\partial U_y}{\partial x}\right) & \dfrac{\partial U_y}{\partial y} - \mathbf{a} & \dfrac{1}{2}\left(\dfrac{\partial U_z}{\partial y} + \dfrac{\partial U_y}{\partial z}\right) \\[3mm] \dfrac{1}{2}\left(\dfrac{\partial U_z}{\partial x} + \dfrac{\partial U_x}{\partial z}\right) & \dfrac{1}{2}\left(\dfrac{\partial U_z}{\partial y} + \dfrac{\partial U_y}{\partial z}\right) & \dfrac{\partial U_z}{\partial z} - \mathbf{a} \end{bmatrix}, \tag{A1.5}$$

$$\mathbf{\Omega} = \begin{bmatrix} 0 & \dfrac{1}{2}\left(\dfrac{\partial U_x}{\partial y} - \dfrac{\partial U_y}{\partial x}\right) & \dfrac{1}{2}\left(\dfrac{\partial U_x}{\partial z} - \dfrac{\partial U_z}{\partial x}\right) \\[3mm] -\dfrac{1}{2}\left(\dfrac{\partial U_x}{\partial y} - \dfrac{\partial U_y}{\partial x}\right) & 0 & \dfrac{1}{2}\left(\dfrac{\partial U_y}{\partial z} - \dfrac{\partial U_z}{\partial y}\right) \\[3mm] -\dfrac{1}{2}\left(\dfrac{\partial U_x}{\partial z} - \dfrac{\partial U_z}{\partial x}\right) & -\dfrac{1}{2}\left(\dfrac{\partial U_y}{\partial z} - \dfrac{\partial U_z}{\partial y}\right) & 0 \end{bmatrix}.$$

The trace component (**h**) provides changes in the volume of the infinitesimal element. The initial volume given by $V_i = \partial x \partial y \partial z$ changes to the final volume V_f given by

$$V_f = (\partial x + \partial U_x)(\partial y + \partial U_y)(\partial z + \partial U_z),$$

$$V_f = \partial x \partial y \partial z + \partial U_x \partial y \partial z + \partial U_y \partial x \partial z + \partial U_z \partial x \partial y + \partial U_y \partial U_z \partial x +$$
$$\partial U_x \partial U_z \partial y + \partial U_x \partial U_y \partial z + \partial U_x \partial U_y \partial U_z,$$

Assuming a small deformation where $\partial U_i \partial U_j \to 0$,

$$V_f = \partial x \partial y \partial z + \partial U_X \partial y \partial z + \partial U_y \partial x \partial z + \partial U_z \partial x \partial y, \qquad \text{A1.6}$$

$$V_f - V_i = \partial U_X \partial y \partial z + \partial U_y \partial x \partial z + \partial U_z \partial x \partial y,$$

$$(V_f - V_i)/V_i = (\partial U_X/\partial x) + (\partial U_y/\partial y) + (\partial U_z/\partial z) = \nabla \cdot U.$$

The last equation with the ratio $(V_f - V_i)/V_i$ is called dilatation which is equal to divergence of the displacement U. The dilatation changes volume without altering the shape of the element leading to uniform extension or contraction.

The symmetric component (**e**) with zero trace (**h**) is responsible for the shear deformation of the infinitesimal element, also referred to as the deviatoric strain component, which does not include the hydrostatic strain. The following two-dimensional case describes a pure shear deformation of a square (Figure A2). The deviatoric strain tensor, using indexed notation, is expressed as

$$e_{ij} = \left[\tfrac{1}{2} \{ (\partial U_j/\partial x_i) + (\partial U_i/\partial x_j) \} - h \delta_{ij} \right], \qquad \text{A1.7}$$

where δ is the Kronecker delta function.
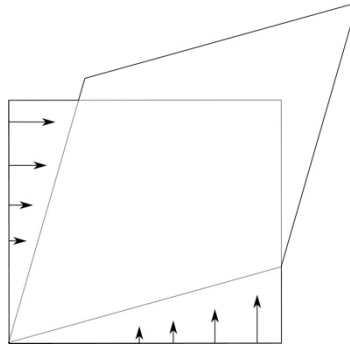
Figure A2. *Pure shear on a two-dimensional object.*

The anti-symmetric component (**Ω**) involves the rigid body rotation of $\delta\mathbf{R}$. In the absence of the dilatation and pure shear (i.e., zero trace and symmetric component), we get

$$LQ' = \Omega\delta\mathbf{R}$$

$$
= \begin{bmatrix}
0 & \frac{1}{2}\left(\frac{\partial U_x}{\partial y} - \frac{\partial U_y}{\partial x}\right) & \frac{1}{2}\left(\frac{\partial U_x}{\partial z} - \frac{\partial U_z}{\partial x}\right) \\
-\frac{1}{2}\left(\frac{\partial U_x}{\partial y} - \frac{\partial U_y}{\partial x}\right) & 0 & \frac{1}{2}\left(\frac{\partial U_y}{\partial z} - \frac{\partial U_z}{\partial y}\right) \\
-\frac{1}{2}\left(\frac{\partial U_x}{\partial z} - \frac{\partial U_z}{\partial x}\right) & -\frac{1}{2}\left(\frac{\partial U_y}{\partial z} - \frac{\partial U_z}{\partial y}\right) & 0
\end{bmatrix}
\begin{bmatrix} \partial x \\ \partial y \\ \partial z \end{bmatrix}
$$

$$
= \left[(0)\partial x + \frac{1}{2}\left(\frac{\partial U_x}{\partial y} - \frac{\partial U_y}{\partial x}\right)\partial y + \frac{1}{2}\left(\frac{\partial U_x}{\partial z} - \frac{\partial U_z}{\partial x}\right)\partial z\right]\hat{\imath} +
$$

$$
\left[-\frac{1}{2}\left(\frac{\partial U_x}{\partial y} - \frac{\partial U_y}{\partial x}\right)\partial x + (0)\partial y + \frac{1}{2}\left(\frac{\partial U_y}{\partial z} - \frac{\partial U_z}{\partial y}\right)\partial z\right]\hat{\jmath} +
$$

$$
\left[-\frac{1}{2}\left(\frac{\partial U_x}{\partial z} - \frac{\partial U_z}{\partial x}\right)\partial x + -\frac{1}{2}\left(\frac{\partial U_y}{\partial z} - \frac{\partial U_z}{\partial y}\right)\partial y + (0)\partial z\right]\hat{\kappa}
$$

$$LQ' = \frac{1}{2}(\nabla \times U) \times \delta\mathbf{R}. \tag{A1.8}$$

A.2 Traction and Stress Tensor components

Traction is a vector that describes force per unit area acting across an internal surface within a continuum. The particles on the one side of the internal surface (S) exert a contact force on the particles of the other side. For a given infinitesimal force ($\delta\mathbf{F}$) acting on an infinitesimal surface ($\delta\mathbf{S}$) with a unit normal $\mathbf{n}$, the traction is in the direction of the applied force due to particles on one side towards which $\mathbf{n}$ points. Hence it is denoted (with two indices) as $\mathbf{T}_l{}^\mathbf{n} = \delta\mathbf{F}/\delta\mathbf{S}$ as $\delta\mathbf{S} \to 0$, where l is the direction of the applied force (Figure A3). For example, in the volume element with six faces (Figure A4a), the traction acting on the shaded surface in the x_1 direction can be written as $\mathbf{T}_1{}^1$. While this notation (i.e., $\mathbf{T}_l{}^\mathbf{n}$) can be used for any arbitrary orientation of surfaces, for cases where a surface is normal to either of the orthogonal axes, the traction ($\mathbf{T}_l{}^\mathbf{n}$) can be represented in terms of stress tensor components with indexed notations as discussed below.

Consider a small tetrahedron (volume $\Delta\mathbf{V}$) with its three faces (Figure A4b) perpendicular to the coordinate axes (x_1, x_2, x_3) and the fourth face with a unit normal $\mathbf{n}$ (with n_1, n_2, n_3 as its direction cosines). Table A1 provides the details of normal vectors and surface areas.

Face	Area	Normal
OAB	∂S_1	$-x_1$

OBC	∂S_2	$-x_2$
OAC	∂S_3	$-x_3$
ABC	∂S	$\vec{n} = n_1 \hat{\imath} + n_2 \hat{\jmath} + n_3 \hat{k}$

Table A1. Details of areas and normal vectors of the tetrahedron in Figure A4b.
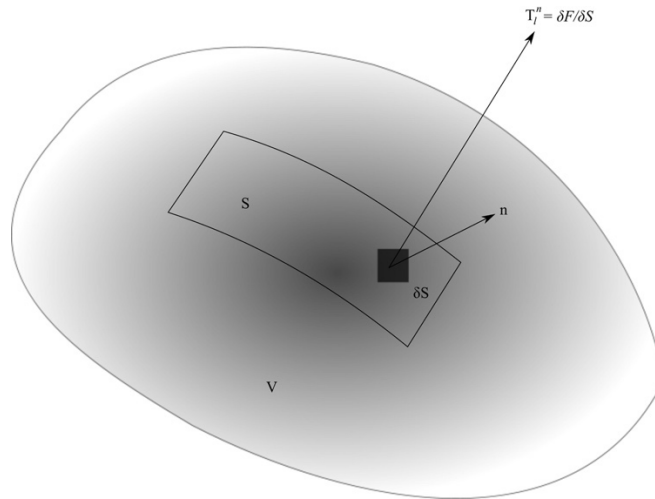
Figure A3. *A volume element V with surface S.*
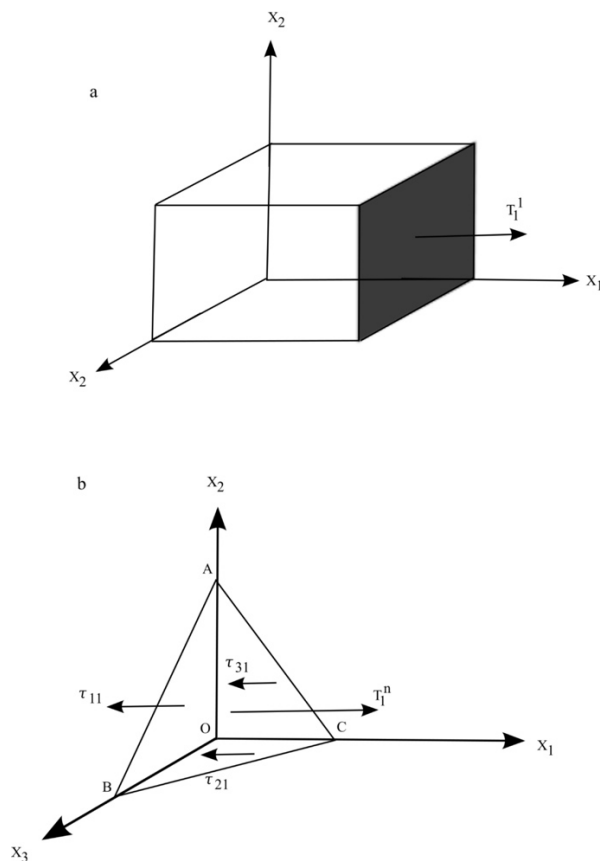
Figure A4. Expression of traction in terms of stress tensor components. (a) A volume element with six faces. (b) A tetrahedron with its three faces perpendicular to orthogonal axes given by x_1, x_2, and x_3.

We write the forces acting on the individual faces in terms of tractions and balance the total forces in x_1 direction

$$-\tau_{11}\,\partial S_1 - \tau_{21}\,\partial S_2 - \tau_{31}\,\partial S_3 + T_1^n\,\partial S + f_1 \Delta V = (\rho \Delta V)a_1, \qquad \text{A1.9}$$

where f_1 and a_1 are the body force per unit volume and acceleration along x_1, respectively. Now taking the volume to be insignificant i.e. $\Delta V \to 0$, the equation A1.9 results into

$$T_1^n\,\partial S = \tau_{11}\,\partial S_1 + \tau_{21}\,\partial S_2 + \tau_{31}\,\partial S_3. \qquad \text{A2.0}$$

The area (∂S_1) can be written in terms of direction cosines of the unit normal **n.** The equation A2.0 is then written as

$$T_1^n\,\partial S = \tau_{11}\,\partial S n_1 + \tau_{21}\,\partial S n_2 + \tau_{31}\,\partial S n_3$$
$$T_1^n = \tau_{11}n_1 + \tau_{21}n_2 + \tau_{31}n_3. \qquad \text{A2.1}$$

Upon writing equation A2.1 for all three orthogonal components, the traction can be expressed as

$$\begin{bmatrix} T_1^n \\ T_2^n \\ T_3^n \end{bmatrix} = \begin{bmatrix} \tau_{11} & \tau_{12} & \tau_{13} \\ \tau_{21} & \tau_{22} & \tau_{23} \\ \tau_{31} & \tau_{32} & \tau_{33} \end{bmatrix} \begin{bmatrix} n_1 \\ n_2 \\ n_3 \end{bmatrix},$$
$$T_i = \tau_{ji}n_j, \qquad \text{A2.2}$$

where the first term on the right-hand side is known as the stress tensor. By equating the rate of change of angular momentum of forces, the symmetricity of the stress tensor can be proved, leading to six independent components. Consider a moment equilibrium of a differential element (with sides $\Delta x_1, \Delta x_2, \Delta x_3$) as in Figure A5. Traction components (e.g., τ_{11}, τ_{22}) that pass through the origin have zero moments. Only shear components are considered for calculating the angular momentum. The moment (M) of all forces with respect to the origin can now be written as

$$\sum M = 0 \qquad \text{A2.3a}$$

$$2\left(\tau_{12}(\Delta x_2 \Delta x_3)\frac{\Delta x_1}{2}\right) - 2\left(\tau_{21}(\Delta x_1 \Delta x_3)\frac{\Delta x_2}{2}\right) = 0 \qquad \text{A2.3b}$$

$$\tau_{12} = \tau_{21}, \text{ or } \tau_{ij} = \tau_{ji} \text{ (stress symmetry)} \qquad \text{A2.3c}$$
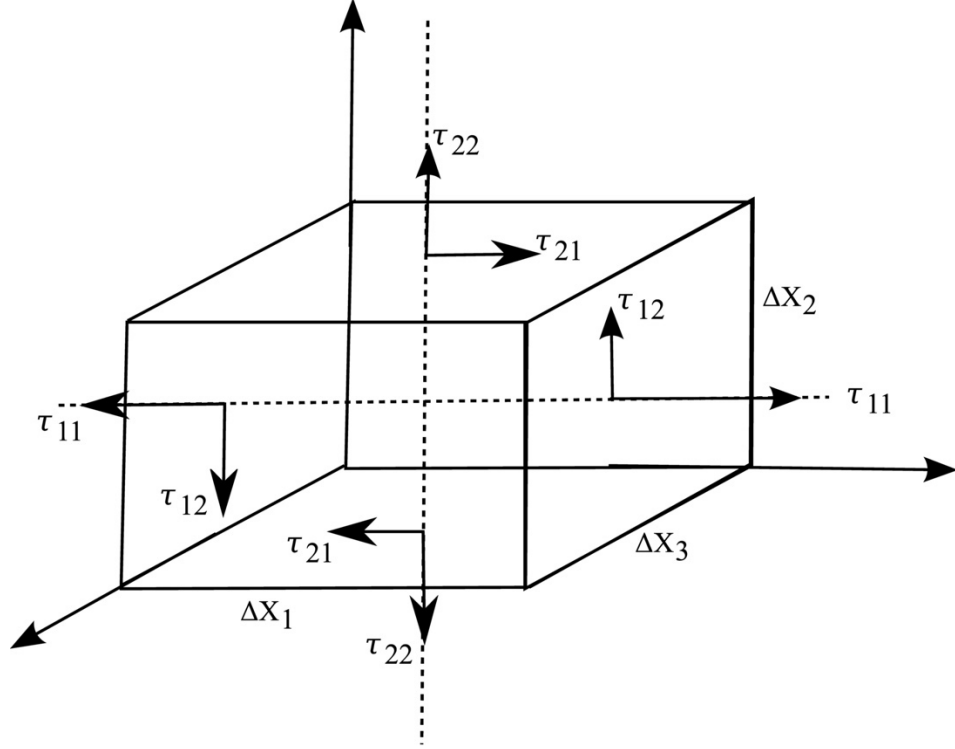
Figure A5. *Conservation of angular momentum. A volume element with six faces. The dashed lines are perpendicular to the axis of rotation.*

      With the definition of traction and stress tensor as discussed above, the acceleration, body force, and traction acting on a particle with an arbitrary volume **V** can be expressed as

$$\frac{\partial}{\partial t}\iiint_v \rho \frac{\partial \mathbf{u}}{\partial t} dV = \iiint_v \mathbf{f} dV + \iint_s \mathbf{T}_l^n dS, \qquad \text{A2.4}$$

where the left-hand side represents the rate of change of momentum in **V,** and the right-hand side represents forces due to external body force (**f**), traction ($\mathbf{T}_l^n$) applied on the surface (**S**) with unit normal **n**. Because the mass is conserved in time, the equation A2.4 can be written as

$$\iiint_v \rho \frac{\partial^2 \mathbf{u}}{\partial t^2} dV = \iiint_v \mathbf{f} dV + \iint_s \mathbf{T}_l^n dS, \qquad \text{A2.5}$$

After substituting the traction as stress tensor and applying Gauss's divergence theorem to the equation A2.5, we get

$$\iiint_v \rho \frac{\partial^2 \mathbf{u}}{\partial t^2} dV = \iiint_v \mathbf{f} dV + \iint_s \tau_{ji} n_j dS, \qquad \text{A2.6}$$

$$\iiint_v \rho \frac{\partial^2 \mathbf{u}}{\partial t^2} dV = \iiint_v \mathbf{f} dV + \iiint_v \tau_{ji,J} dV. \qquad \text{A2.7}$$

For a general volume **V**, the above equation gives the following equation of motion

$$\rho \ddot{\mathbf{u}} = f_i + \tau_{ji,J}. \qquad \text{A2.8}$$

A.3 Stress-Strain relationship and elastic wave equation

The generalized Hooke's law states that the stress tensor is a linear combination of strain tensor components for a linearly elastic body such that

$$\tau_{ij} = C_{ijkl} e_{kl}, \qquad \text{A2.9}$$

where C_{ijkl} is a fourth-order tensor, also called the "elastic constant". Using the symmetry of stress and strain components and the first law of thermodynamics, discussed below, the independent elements of C_{ijkl} are reduced from 81 to 21.

$$C_{ijkl} = C_{jikl}, \text{(stress symmetry)} \qquad \text{A3.0}$$

$$C_{ijkl} = C_{ijlk}, \text{(strain symmetry)} \qquad \text{A3.1}$$

The third symmetry ($C_{ijkl} = C_{klij}$) comes from the first law of thermodynamics, which states that the rate of change of internal energy (kinetic + intrinsic) is equal to the rate of heating and rate of mechanical work done. Hence, we can write the following equation

$$\iiint_v \mathbf{f} \cdot \dot{\mathbf{u}} \, dV + \iint_s \mathbf{T}_l^n \cdot \dot{u} dS + \frac{\partial}{\partial t} \iiint_v Q \, dV = \frac{\partial}{\partial t} \iiint_v \frac{1}{2} \rho \, \ddot{u} dV + \iiint_v \dot{u} \, dV \qquad \text{A3.2}$$

where Q is the heat per unit volume, $\mathcal{U}$ is the internal energy per unit volume. Substituting from equation A2.8 and applying Gauss's divergence theorem to the above equation, we get

$$\dot{\mathcal{U}} = \dot{Q} + \tau_{ij} e_{ij}. \qquad \text{A3.3}$$

Assuming small perturbations, equation A3.3 can be written as

$$dU = dQ + \tau_{ij}de_{ij} = TdS + \tau_{ij}de_{ij}, \qquad \text{A3.4}$$

where T is the absolute temperature, and S is the entropy per unit volume. Considering that U changes under a constant entropy, the equation A3.4 can be expressed as strain-energy relation

$$\tau_{ij} = \left(\frac{dU}{de_{ij}}\right)_S = \left(\frac{dW}{de_{ij}}\right), \qquad \text{A3.5}$$

where W is the strain-energy function. From equations A3.5 and A2.9, we can write

$$\left(\frac{dW}{de_{ij}}\right) = C_{ijkl}e_{kl}, \qquad \text{A3.6}$$

$$\left(\frac{d^2W}{de_{pq}de_{ij}}\right) = \frac{dW}{de_{pq}}C_{ijkl}e_{kl} = C_{ijpq} = \left(\frac{d^2W}{de_{ij}de_{pq}}\right), \qquad \text{A3.7}$$

which further implies $C_{ijkl} = C_{klij}$. Assuming isotropic condition, the elastic constant is further expressed in terms of Lame's constants (λ and μ)

$$C_{ijkl} = \lambda\delta_{ij}\delta_{kl} + \mu(\delta_{ik}\delta_{jl} + \delta_{il}\delta_{jk}). \qquad \text{A3.8}$$

From equations A2.9 and A3.8, each component of the stress field can be written as

$$\tau_{ij} = [\lambda\delta_{ij}\delta_{kl} + \mu(\delta_{ik}\delta_{jl} + \delta_{il}\delta_{jk})]e_{kl}, \qquad \text{A3.9}$$

$$\tau_{ij} = [\lambda\delta_{ij}(e_{x_1x_1} + e_{x_2x_2} + e_{x_3x_3}) + \mu\delta_{ik}\delta_{jl}e_{kl} + \mu\delta_{il}\delta_{jk}e_{kl}, \qquad \text{A4.0}$$

$$\tau_{x_1x_1} = \lambda\theta + 2\mu e_{x_1x_1}$$

$$\tau_{x_2x_2} = \lambda\theta + 2\mu e_{x_2x_2}$$

$$\tau_{x_3x_3} = \lambda\theta + 2\mu e_{x_3x_3}$$

$$\tau_{x_1x_2} = 2\mu e_{x_1x_2} \qquad \text{A4.1}$$

$$\tau_{x_1x_3} = 2\mu e_{x_1x_3}$$

$$\tau_{x_2x_3} = 2\mu e_{x_2x_3}.$$

Above expressions can be generalized as the Hook's law

$$\tau_{ij} = \lambda\theta\delta_{ij} + 2\mu e_{ij}, \qquad \text{A4.2}$$

where $\theta = (e_{x_1x_1} + e_{x_1x_1} + e_{x_1x_1})$. The above equation is valid for perfectly elastic isotropic solid, small deformation, and short time scale conditions. In absence of the body force the equation A2.8 can be written as

$$\nabla \cdot \tau = \rho \frac{d^2 u}{dt^2},$$

$$[\nabla \cdot \tau] = \frac{d}{d_{x_j}} \left[\lambda \theta \delta_{ij} + 2\mu e_{ij} \right]$$

$$= \frac{d}{d_{x_j}} [\lambda \theta] + \mu \frac{d}{d_{x_j}} \left[\frac{du_i}{dx_j} + \frac{du_j}{dx_i} \right] + 2e_{ij} \frac{d\mu}{dx_j}.$$

A4.3

$$= \nabla(\lambda \theta) + \mu \frac{d^2 u_i}{d_{x_j} d_{x_j}} + \mu \left(\frac{d}{d_{x_j}} \left(\frac{du_j}{dx_i} \right) \right) + 2e \cdot \nabla \mu$$

$$\rho \frac{d^2 u}{dt^2} = \nabla(\lambda \theta) + \mu \nabla^2 u + \mu \nabla \theta + 2e \cdot \nabla \mu$$

The last part of the equation A4.3 above is the elastic wave equation which can be further written in terms of displacement as

$$\rho \frac{d^2 u}{dt^2} = \nabla \lambda (\nabla \cdot u) + \nabla \mu \cdot [\nabla u + (\nabla u)^T] + (\lambda + 2\mu)\nabla(\nabla \cdot u) - \mu \nabla \times \nabla \times u \qquad \text{A4.4}$$

A.4 Theorem of Uniqueness

The displacement field u(x, t) is uniquely determined throughout the volume V and surface S given initial conditions:

1) u(x, t_0) and $\dot{u}$ (x, t_0)

2) f (x, t ≥ t_0)

3) T (x, t ≥ t_0) over S_1 ≤ S

4) u (x, t ≥ t_0) over S − S_1

A.5 Theorem of Reciprocity (Betti's Theorem)

For a body force f, boundary condition on S, initial condition at t_o producing a displacement field u(x, t) and a traction T(u, n), and another body force g, boundary condition on S, initial condition at t_o producing a displacement field v(x, t) and a traction T(v, n), where n is normal direction, the following scalar equality holds

$$\iiint_v (\mathbf{f} - \boldsymbol{\rho}\ddot{u}) \cdot v \, dV + \iint_S T(u, n) \cdot v \, dS \qquad \text{A4.5}$$

$$= \iiint_v (g - \rho \ddot{v}) \cdot u \, dV + \iint_S T(v, n) \cdot u \, dS \,.$$

When integrated over time, the above equation can be expressed as following using indexed terms

$$\int_{-\infty}^{\infty} dt \iiint_v \rho(\ddot{u}_i v_i - u_i \ddot{v}_i)\, dV$$

A4.6

$$= \int_{-\infty}^{\infty} dt \iiint_v (v_i f_i - u_i g_i)\, dV$$

$$+ \int_{-\infty}^{\infty} dt \iint_S (v_i T_i^u - u_i T_i^v)\, dS\,.$$

Evaluating the first system u(x, t) at time t and the second system v(x, t) at time $\tau - t$, the left-hand side of the equation A4.6 becomes

$$\int_{-\infty}^{\infty} dt \iiint_v \rho[(\ddot{u}_i(t)v_i(\tau - t) - u_i(t)\ddot{v}_i(\tau - t)]\, dV$$

A4.7

Using causality (i.e., medium at rest until disturbed), the above equation reduces to zero (because $u_i = \dot{u}_i = 0$ and $v_i = \dot{v}_i = 0$ for $t \leq 0$).

$$\int_0^\tau dt \iiint_v \rho[(\ddot{u}_i(t)v_i(\tau - t) - u_i(t)\ddot{v}_i(\tau - t)]\, dV$$

A4.8

$$= \int_0^\tau \rho \frac{d}{dt}[\dot{u}_i(t)v_i(\tau - t) + u_i(t)\dot{v}_i(\tau - t)]dt$$

$$= \rho[\dot{u}_i(\tau)v_i(0) + u_i(0)\dot{v}_i(\tau) - \dot{u}_i(\tau)v_i(0) - u_i(0)\dot{v}_i(\tau)] = 0$$

Hence the right-hand side of the equation A4.6 results into

$$\int_{-\infty}^{\infty} dt \iiint_v (u_i g_i - v_i f_i)dV = \int_{-\infty}^{\infty} dt \iint_S (v_i T_i^u - u_i T_i^v)\, dS,$$

$$\int_{-\infty}^{\infty} dt \iiint_v (u(x,t) \cdot g(x, \tau - t) - v(x, \tau - t) \cdot f(x,t))dV$$

A4.9

$$= \int_{-\infty}^{\infty} dt \iint_S v(x, \tau - t) \cdot T_i^u(x,t) - u(x,t) \cdot T_i^v(x, \tau$$

$$- t))\, dS\,.$$

The last two equations of A4.9 are known as Betti's theorem with causality. It allows representation of the displacement field produced by different body forces and tractions given the causality.

A.6 L-Curve test for group velocity tomography

L-curve tests are performed for optimizing the regularized parameters i.e., damping (ϵ) and smoothing (η) of equation 2.56 (Chapter 2). First, at a fixed value of damping (= 3), the tomographic inversions are performed for a range of smoothing parameters from 0 to 500. A value which minimizes the trade-off between the model roughness and data residuals is chosen for the final tomographic inversion. Figure A6 shows the L-curve test at various periods between 5 and 60 s. A value between 5 and 6 is taken as the optimum smoothing parameter. Now, with this smoothing fixed at 5, another set of tomographic inversions is performed for a range of damping from 0 to 500. Optimum values are between 3 and 4, corresponding to the minimum trade-off between model roughness and data fit (Figure A6).
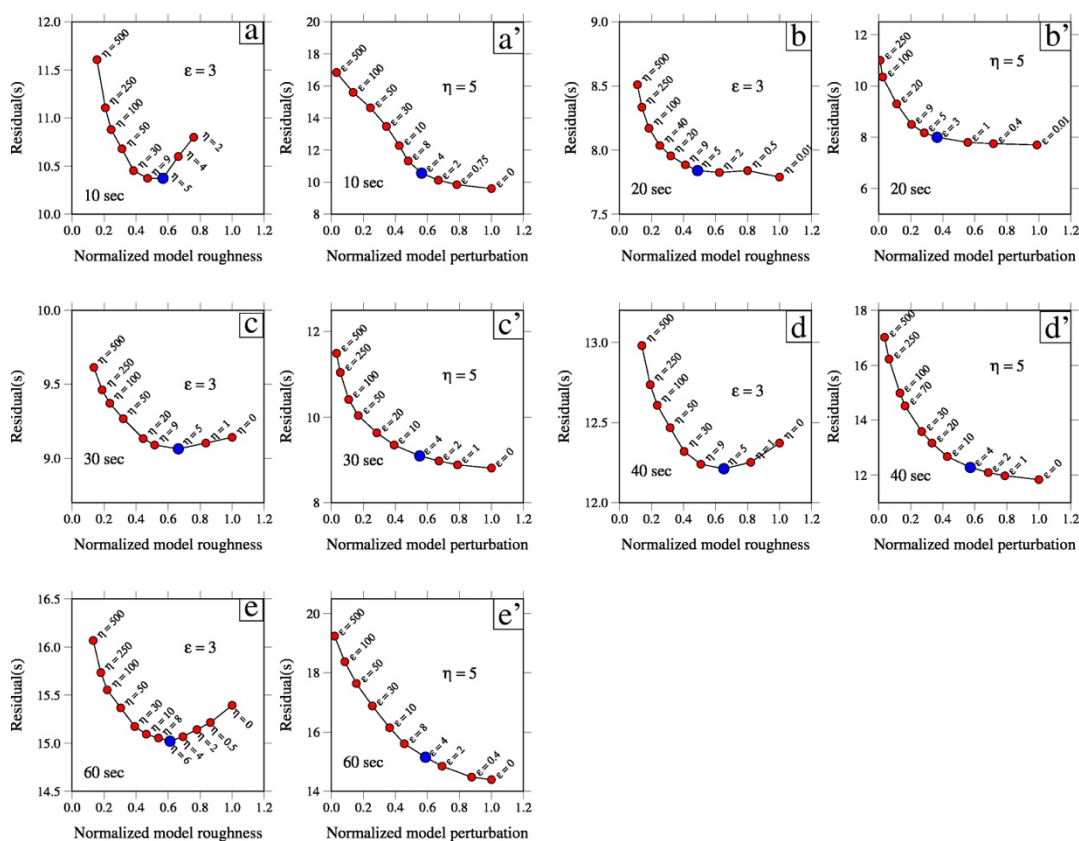
Figure A6. *L-curve test for optimizing damping (ϵ) and smoothing (η) parameter at different period. The optimum values are indicated with blue dots.*

A.7 Test of prior width in the Trans-Dimensional Inversion

Figure A7, presented below, shows a comparison of tomographic models at different prior widths for the 50s period. Figure 3.2 of Chapter 3 presents a similar test for the 40s period. These tests demonstrate that our model is least sensitive to the prior width. However, a suitable prior width is chosen as discussed in Chapter 2 (section 2.7.2).
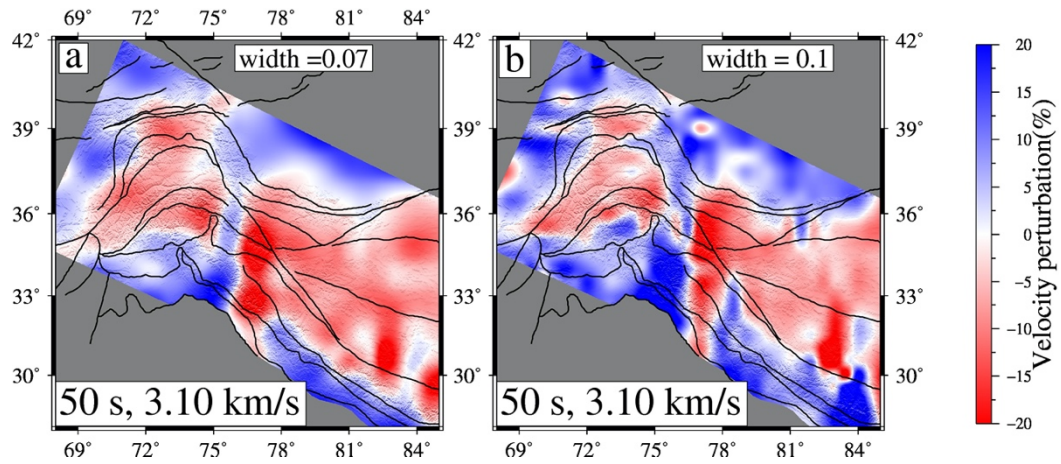
Figure A7. *Effect of prior width on tomographic model at 50 s period at a width of (a) 0.07 and (b) 0.1.*

APPENDICES

REFERENCES

Acevedo, J., Fernández-Viejo, G., Llana-Fúnez, S., López-Fernández, C. and Olona, J., 2019. Ambient noise tomography of the southern sector of the Cantabrian Mountains, NW Spain. *Geophysical Journal International*, *219*(1), pp.479-495.

Acevedo, J., Fernández-Viejo, G., Llana-Fúnez, S., López-Fernández, C. and Olona, J., 2021. Upper-crustal seismic anisotropy in the Cantabrian mountains (north Spain) from shear-wave splitting and ambient noise interferometry analysis. *Seismological Society of America*, *92*(1), pp.421-436.

Acton, C.E., Priestley, K., Gaur, V.K. and Rai, S.S., 2010. Group velocity tomography of the Indo-Eurasian collision zone. *Journal of Geophysical Research: Solid Earth*, *115*(B12).

Acton, C.E., Priestley, K., Mitra, S. and Gaur, V.K., 2011. Crustal structure of the Darjeeling—Sikkim Himalaya and southern Tibet. *Geophysical Journal International*, *184*(2), pp.829-852.

Agius, M.R. and Lebedev, S., 2014. Shear-velocity structure, radial anisotropy and dynamics of the Tibetan crust. *Geophysical Journal International*, *199*(3), pp.1395-1415.

Airy, G.B., 1855. III. On the computation of the effect of the attraction of mountain-masses, as disturbing the apparent astronomical latitude of stations in geodetic surveys. *Philosophical Transactions of the Royal Society of London*, (145), pp.101-104.

Almeida, R.V., Hubbard, J., Liberty, L., Foster, A. and Sapkota, S.N., 2018. Seismic imaging of the Main Frontal Thrust in Nepal reveals a shallow décollement and blind thrusting. *Earth and Planetary Science Letters*, *494*, pp.216-225.

Almqvist, B.S., Burg, J.P., Berger, J. and Burlini, L., 2013. Seismic properties of the Kohistan oceanic arc root: Insights from laboratory measurements and thermodynamic modeling. *Geochemistry, Geophysics, Geosystems*, *14*(6), pp.1819-1841.

Ambraseys, N.N. and Douglas, J., 2004. Magnitude calibration of north Indian earthquakes. *Geophysical Journal International*, *159*(1), pp.165-206.

Argand E., 1924. La tectonique de l' Asie. *Proc. 13th Int. Geol. Congr.,* 7,171–372

REFERENCES

Arita, K., 1983. Origin of the inverted metamorphism of the Lower Himalayas, central Nepal. *Tectonophysics*, *95*(1-2), pp.43-60.

Armijo, R., Tapponnier, P., Mercier, J.L. and Han, T.L., 1986. Quaternary extension in southern Tibet: Field observations and tectonic implications. *Journal of Geophysical Research: Solid Earth*, *91*(B14), pp.13803-13872.

Arora, B.R., Gahalaut, V.K. and Kumar, N., 2012. Structural control on along-strike variation in the seismicity of the northwest Himalaya. *Journal of Asian Earth Sciences*, *57*, pp.15-24.

Arora, B.R., Unsworth, M.J. and Rawat, G., 2007. Deep resistivity structure of the northwest Indian Himalaya and its tectonic implications. *Geophysical Research Letters*, *34*(4).

Ashish, A., Padhi, A., Rai, S.S. and Gupta, S., 2009. Seismological evidence for shallow crustal melt beneath the Garhwal High Himalaya, India: implications for the Himalayan channel flow. *Geophysical Journal International*, *177*(3), pp.1111-1120.

Avouac, J.P. and Tapponnier, P., 1993. Kinematic model of active deformation in central Asia. *Geophysical Research Letters*, *20*(10), pp.895-898.

Avouac, J.P., 2015. From geodetic imaging of seismic and aseismic fault slip to dynamic modeling of the seismic cycle. *Annual Review of Earth and Planetary Sciences*, *43*, pp.233-271.

Bai, D., Unsworth, M.J., Meju, M.A., Ma, X., Teng, J., Kong, X., Sun, Y., Sun, J., Wang, L., Jiang, C. and Zhao, C., 2010. Crustal deformation of the eastern Tibetan plateau revealed by magnetotelluric imaging. *Nature geoscience*, *3*(5), pp.358-362.

Bai, L., Li, G., Khan, N.G., Zhao, J. and Ding, L., 2017. Focal depths and mechanisms of shallow earthquakes in the Himalayan–Tibetan region. *Gondwana Research*, *41*, pp.390-399.

Banerjee, P. and Bürgmann, R., 2002. Convergence across the northwest Himalaya from GPS measurements. *Geophysical Research Letters*, *29*(13), pp.30-1.

Bao, X., Sun, X., Xu, M., Eaton, D.W., Song, X., Wang, L., Ding, Z., Mi, N., Li, H., Yu, D. and Huang, Z., 2015. Two crustal low-velocity channels beneath SE Tibet revealed by joint inversion of Rayleigh wave dispersion and receiver functions. *Earth and Planetary Science Letters*, *415*, pp.16-24.

REFERENCES

Barazangi, M. and Ni, J., 1982. Velocities and propagation characteristics of Pn and Sn beneath the Himalayan arc and Tibetan plateau: Possible evidence for underthrusting of Indian continental lithosphere beneath Tibet. *Geology*, *10*(4), pp.179-185.

Bard, J.P., 1983. Metamorphism of an obducted island arc: example of the Kohistan sequence (Pakistan) in the Himalayan collided range. *Earth and Planetary Science Letters*, *65*(1), pp.133-144.

Bayes, T., 1763. LII. An essay towards solving a problem in the doctrine of chances. By the late Rev. Mr. Bayes, FRS communicated by Mr. Price, in a letter to John Canton, AMFR S. *Philosophical transactions of the Royal Society of London*, (53), pp.370-418.

Beaumont, C., Jamieson, R.A., Nguyen, M.H. and Lee, B., 2001. Himalayan tectonics explained by extrusion of a low-viscosity crustal channel coupled to focused surface denudation. *Nature*, *414*(6865), pp.738-742.

Beaumont, C., Jamieson, R.A., Nguyen, M.H. and Medvedev, S., 2004. Crustal channel flows: 1. Numerical models with applications to the tectonics of the Himalayan-Tibetan orogen. *Journal of Geophysical Research: Solid Earth*, *109*(B6).

Bensen, G.D., Ritzwoller, M.H., Barmin, M.P., Levshin, A.L., Lin, F., Moschetti, M.P., Shapiro, N.M. and Yang, Y., 2007. Processing seismic ambient noise data to obtain reliable broad-band surface wave dispersion measurements. *Geophysical journal international*, *169*(3), pp.1239-1260.

Bettinelli, P., Avouac, J.P., Flouzat, M., Jouanne, F., Bollinger, L., Willis, P. and Chitrakar, G.R., 2006. Plate motion of India and interseismic strain in the Nepal Himalaya from GPS and DORIS measurements. *Journal of Geodesy*, *80*(8), pp.567-589.

Bilham, R., 2001. Slow tilt reversal of the Lesser Himalaya between 1862 and 1992 at 78 E, and bounds to the southeast rupture of the 1905 Kangra earthquake. *Geophysical Journal International*, *144*(3), pp.713-728.

Bilham, R., 2019. Himalayan earthquakes: a review of historical seismicity and early 21st century slip potential. *Geological Society, London, Special Publications*, *483*(1), pp.423-482.

Bilham, R., Mencin, D., Bendick, R. and Bürgmann, R., 2017. Implications for elastic energy storage in the Himalaya from the Gorkha 2015 earthquake and other incomplete ruptures of the Main Himalayan Thrust. *Quaternary International*, *462*, pp.3-21.

REFERENCES

Billington, S., Isacks, B.L. and Barazangi, M., 1977. Spatial distribution and focal mechanisms of mantle earthquakes in the Hindu Kush–Pamir region: A contorted Benioff zone. *Geology*, *5*(11), pp.699-704.

Bodin, T. and Sambridge, M., 2009. Seismic tomography with the reversible jump algorithm. *Geophysical Journal International*, *178*(3), pp.1411-1436.

Bodin, T., Sambridge, M., Rawlinson, N. and Arroucau, P., 2012a. Transdimensional tomography with unknown data noise. *Geophysical Journal International*, *189*(3), pp.1536-1556.

Bodin, T., Sambridge, M., Tkalčić, H., Arroucau, P., Gallagher, K. and Rawlinson, N., 2012b. Transdimensional inversion of receiver functions and surface wave dispersion. *Journal of Geophysical Research: Solid Earth*, *117*(B2).

Bonnefoy-Claudet, S., Cotton, F. and Bard, P.Y., 2006. The nature of noise wavefield and its applications for site effects studies: A literature review. *Earth-Science Reviews*, *79*(3-4), pp.205-227.

Bouilhol, P., Jagoutz, O., Hanchar, J.M. and Dudas, F.O., 2013. Dating the India–Eurasia collision through arc magmatic records. *Earth and Planetary Science Letters*, *366*, pp.163-175.

Brown, E.T., Bendick, R., Bourles, D.L., Gaur, V., Molnar, P., Raisbeck, G.M. and Yiou, F., 2002. Slip rates of the Karakorum fault, Ladakh, India, determined using cosmic ray exposure dating of debris flows and moraines. *Journal of Geophysical Research: Solid Earth*, *107*(B9), pp.ESE-7.

Brown, L.D., Zhao, W., Nelson, K.D., Hauck, M., Alsdorf, D., Ross, A., Cogan, M., Clark, M., Liu, X. and Che, J., 1996. Bright spots, structure, and magmatism in southern Tibet from INDEPTH seismic reflection profiling. *Science*, *274*(5293), pp.1688-1690.

Burchfiel, B.C. and Royden, L.H., 1985. North-south extension within the convergent Himalayan region. *Geology*, *13*(10), pp.679-682.

Burg, J.P., 2006. Two orogenic systems and a transform-transfer fault in the Himalayas: evidence and consequences. *地學前緣*, *13*(4), pp.27-46.

Burg, J.P., 2011. The Asia–Kohistan–India collision: review and discussion. *Arc-continent collision*, pp.279-309.

REFERENCES

Burg, J.P., Brunel, M., Gapais, D., Chen, G.M. and Liu, G.H., 1984. Deformation of leucogranites of the crystalline Main Central Sheet in southern Tibet (China). *Journal of Structural Geology*, *6*(5), pp.535-542.

Burtman, V.S. and Molnar, P.H., 1993. *Geological and geophysical evidence for deep subduction of continental crust beneath the Pamir* (Vol. 281). Geological Society of America.

Caldwell, W.B., Klemperer, S.L., Lawrence, J.F. and Rai, S.S., 2013. Characterizing the Main Himalayan Thrust in the Garhwal Himalaya, India with receiver function CCP stacking. *Earth and Planetary Science Letters*, *367*, pp.15-27.

Caldwell, W.B., Klemperer, S.L., Rai, S.S. and Lawrence, J.F., 2009. Partial melt in the upper-middle crust of the northwest Himalaya revealed by Rayleigh wave dispersion. *Tectonophysics*, *477*(1-2), pp.58-65.

Callen, H.B. and Welton, T.A., 1951. Irreversibility and generalized noise. *Physical Review*, *83*(1), p.34.

Calvert, A.J., 2011. The seismic structure of island arc crust. In *Arc-continent collision* (pp. 87-119). Springer, Berlin, Heidelberg.

Campillo, M. and Paul, A., 2003. Long-range correlations in the diffuse seismic coda. *Science*, *299*(5606), pp.547-549.

Cande, S.C. and Stegman, D.R., 2011. Indian and African plate motions driven by the push force of the Reunion plume head. *Nature*, *475*(7354), pp.47-52.

Cande, S.C., Patriat, P. and Dyment, J., 2010. Motion between the Indian, Antarctic and African plates in the early Cenozoic. *Geophysical Journal International*, *183*(1), pp.127-149.

Capitanio, F.A., Morra, G., Goes, S., Weinberg, R.F. and Moresi, L., 2010. India–Asia convergence driven by the subduction of the Greater Indian continent. *Nature Geoscience*, *3*(2), pp.136-139.

Cattin, R. and Avouac, J.P., 2000. Modeling mountain building and the seismic cycle in the Himalaya of Nepal. *Journal of Geophysical Research: Solid Earth*, *105*(B6), pp.13389-13407.

Célérier, J., Harrison, T.M., Webb, A.A.G. and Yin, A., 2009. The Kumaun and Garwhal Lesser Himalaya, India: Part 1. Structure and stratigraphy. *Geological Society of America Bulletin*, *121*(9-10), pp.1262-1280.

REFERENCES

Chang, C.F. and Cheng, H.L., 1973. Some tectonic features of the Mt. Jolmo Lungma area, southern Tibet, China. *Scientia Sinica*, *16*(2), pp.257-265.

Chatelain, J.L., Roecker, S.W., Hatzfeld, D. and Molnar, P., 1980. Microearthquake seismicity and fault plane solutions in the Hindu Kush region and their tectonic implications. *Journal of Geophysical Research: Solid Earth*, *85*(B3), pp.1365-1387.

Chen, L., Capitanio, F.A., Liu, L. and Gerya, T.V., 2017. Crustal rheology controls on the Tibetan plateau formation during India-Asia convergence. *Nature Communications*, *8*(1), pp.1-8.

Chen, W.P., Martin, M., Tseng, T.L., Nowack, R.L., Hung, S.H. and Huang, B.S., 2010. Shear-wave birefringence and current configuration of converging lithosphere under Tibet. *Earth and Planetary Science Letters*, *295*(1-2), pp.297-304.

Chen, Y., Li, W., Yuan, X., Badal, J. and Teng, J., 2015. Tearing of the Indian lithospheric slab beneath southern Tibet revealed by SKS-wave splitting measurements. *Earth and Planetary Science Letters*, *413*, pp.13-24.

Christensen, N.I. and Mooney, W.D., 1995. Seismic velocity structure and composition of the continental crust: A global view. *Journal of Geophysical Research: Solid Earth*, *100*(B6), pp.9761-9788.

Christensen, N.I., 1996. Poisson's ratio and crustal seismology. *Journal of Geophysical Research: Solid Earth*, *101*(B2), pp.3139-3156.

Chun, K.Y., 1986. Crustal block of the western Ganga basin: a fragment of oceanic affinity?. *Bulletin of the Seismological Society of America*, *76*(6), pp.1687-1698.

Clark, M.K. and Royden, L.H., 2000. Topographic ooze: Building the eastern margin of Tibet by lower crustal flow. *Geology*, *28*(8), pp.703-706.

Clift, P.D., Hannigan, R., Blusztajn, J. and Draut, A.E., 2002. Geochemical evolution of the Dras–Kohistan Arc during collision with Eurasia: evidence from the Ladakh Himalaya, India. *Island Arc*, *11*(4), pp.255-273.

Copley, A., Avouac, J.P. and Royer, J.Y., 2010. India-Asia collision and the Cenozoic slowdown of the Indian plate: Implications for the forces driving plate motions. *Journal of Geophysical Research: Solid Earth*, *115*(B3).

Corfield, R.I. and Searle, M.P., 2000. Crustal shortening estimates across the north Indian continental margin, Ladakh, NW India. *Geological Society, London, Special Publications*, *170*(1), pp.395-410.

REFERENCES

Cotton, F., Campillo, M., Deschamps, A. and Rastogi, B.K., 1996. Rupture history and seismotectonics of the 1991 Uttarkashi, Himalaya earthquake. *Tectonophysics*, *258*(1-4), pp.35-51.

Cox, H., 1973. Spatial correlation in arbitrary noise fields with application to ambient sea noise. *The Journal of the Acoustical Society of America*, *54*(5), pp.1289-1301.

Dahlen, F.A., 1990. Critical taper model of fold-and-thrust belts and accretionary wedges. *Annual Review of Earth and Planetary Sciences*, *18*(1), pp.55-99.

Dal Zilio, L., Jolivet, R. and van Dinther, Y., 2020. Segmentation of the Main Himalayan Thrust illuminated by Bayesian inference of interseismic coupling. *Geophysical Research Letters*, *47*(4), p.e2019GL086424.

Dewey, J.F. and Burke, K.C., 1973. Tibetan, Variscan, and Precambrian basement reactivation: products of continental collision. *The Journal of Geology*, *81*(6), pp.683-692.

Diaferia, G. and Cammarano, F., 2017. Seismic signature of the continental crust: what thermodynamics says. An example from the Italian Peninsula. *Tectonics*, *36*(12), pp.3192-3208.

DiPietro, J.A. and Pogue, K.R., 2004. Tectonostratigraphic subdivisions of the Himalaya: A view from the west. *Tectonics*, *23*(5).

Duvall, T.L., Jeffferies, S.M., Harvey, J.W. and Pomerantz, M.A., 1993. Time–distance helioseismology. *Nature*, *362*(6419), pp.430-432.

Dziewonski, A., Bloch, S. and Landisman, M., 1969. A technique for the analysis of transient seismic signals. *Bulletin of the seismological Society of America*, *59*(1), pp.427-444.

Elliott, J.R., Jolivet, R., González, P.J., Avouac, J.P., Hollingsworth, J., Searle, M.P. and Stevens, V.L., 2016. Himalayan megathrust geometry and relation to topography revealed by the Gorkha earthquake. *Nature Geoscience*, *9*(2), pp.174-180.

England, P. and McKenzie, D., 1982. A thin viscous sheet model for continental deformation. *Geophysical Journal International*, *70*(2), pp.295-321.

Eugster, P., Thiede, R.C., Scherler, D., Stübner, K., Sobel, E.R. and Strecker, M.R., 2018. Segmentation of the Main Himalayan thrust revealed by low-temperature thermochronometry in the Western Indian Himalaya. *Tectonics*, *37*(8), pp.2710-2726.

REFERENCES

Feld, C., Haberland, C., Schurr, B., Sippl, C., Wetzel, H.U., Roessner, S., Ickrath, M., Abdybachaev, U. and Orunbaev, S., 2015. Seismotectonic study of the Fergana Region (Southern Kyrgyzstan): distribution and kinematics of local seismicity. *Earth, Planets and Space*, *67*(1), p.40.

Froment, B., Campillo, M., Roux, P., Gouédard, P., Verdel, A. and Weaver, R.L., 2010. Estimation of the effect of nonisotropically distributed energy on the apparent arrival time in correlations. *Geophysics*, *75*(5), pp.SA85-SA93.

Galvé, A., Jiang, M., Hirn, A., Sapin, M., Laigle, M., De Voogd, B., Gallart, J. and Qian, H., 2006. Explosion seismic P and S velocity and attenuation constraints on the lower crust of the North–Central Tibetan Plateau, and comparison with the Tethyan Himalayas: Implications on composition, mineralogy, temperature, and tectonic evolution. *Tectonophysics*, *412*(3-4), pp.141-157.

Gan, W., Zhang, P., Shen, Z.K., Niu, Z., Wang, M., Wan, Y., Zhou, D. and Cheng, J., 2007. Present-day crustal motion within the Tibetan Plateau inferred from GPS measurements. *Journal of Geophysical Research: Solid Earth*, *112*(B8).

Gansser, A., 1964. Geology of the Himalayas.

Gao, R., Lu, Z., Klemperer, S.L., Wang, H., Dong, S., Li, W. and Li, H., 2016. Crustal-scale duplexing beneath the Yarlung Zangbo suture in the western Himalaya. *Nature Geoscience*, *9*(7), pp.555-560.

Gaur, V.K., Chander, R., Sarkar, I., Khattri, K.N. and Sinvhal, H., 1985. Seismicity and the state of stress from investigations of local earthquakes in the Kumaon Himalaya. *Tectonophysics*, *118*(3-4), pp.243-251.

Geller, R.J. and Kanamori, H., 1977. Magnitudes of great shallow earthquakes from 1904 to 1952. *Bulletin of the Seismological Society of America*, *67*(3), pp.587-598.

Geyer, C.J. and Møller, J., 1994. Simulation procedures and likelihood inference for spatial point processes. *Scandinavian journal of statistics*, pp.359-373.

Ghavri, S. and Jade, S., 2021. Seismic potential of megathrust in the Kumaun-Garhwal region of NW Himalaya: implications from geodetic and seismic strain rates. *International Journal of Earth Sciences*, *110*(4), pp.1439-1452.

Gilligan, A. and Priestley, K., 2018. Lateral variations in the crustal structure of the Indo–Eurasian collision zone. *Geophysical Journal International*, *214*(2), pp.975-989.

REFERENCES

Gilligan, A., Priestley, K.F., Roecker, S.W., Levin, V. and Rai, S.S., 2015. The crustal structure of the western Himalayas and Tibet. *Journal of Geophysical Research: Solid Earth*, *120*(5), pp.3946-3964.

Godin, L. and Harris, L.B., 2014. Tracking basement cross-strike discontinuities in the Indian crust beneath the Himalayan orogen using gravity data–relationship to upper crustal faults. *Geophysical Journal International*, *198*(1), pp.198-215.

Godin, L., La Roche, R.S., Waffle, L. and Harris, L.B., 2019. Influence of inherited Indian basement faults on the evolution of the Himalayan Orogen. *Geological Society, London, Special Publications*, *481*(1), pp.251-276.

Godin, O.A., 2007. Emergence of the acoustic Green's function from thermal noise. *The Journal of the Acoustical Society of America*, *121*(2), pp.EL96-EL102.

Green, P.J., 1995. Reversible jump MCMC computation and Bayesian model determination. Biomeirika, 82: 711-732 Hastings, WK 1970. Monte Carlo sampling methods using Markov chains and their applications. *Biometrika*, *57*, pp.97-109.

Griffin, J.D., Nowack, R.L., Chen, W.P. and Tseng, T.L., 2011. Velocity structure of the Tibetan lithosphere: Constraints from P-wave travel times of regional earthquakes. *Bulletin of the Seismological Society of America*, *101*(4), pp.1938-1947.

Grujic, D., Casey, M., Davidson, C., Hollister, L.S., Kündig, R., Pavlis, T. and Schmid, S., 1996. Ductile extrusion of the Higher Himalayan Crystalline in Bhutan: evidence from quartz microfabrics. *Tectonophysics*, *260*(1-3), pp.21-43.

Grujic, D., Hollister, L.S. and Parrish, R.R., 2002. Himalayan metamorphic sequence as an orogenic channel: insight from Bhutan. *Earth and Planetary Science Letters*, *198*(1-2), pp.177-191.

Guo, X., Li, W., Gao, R., Xu, X., Li, H., Huang, X., Ye, Z., Lu, Z. and Klemperer, S.L., 2017. Nonuniform subduction of the Indian crust beneath the Himalayas. *Scientific Reports*, *7*(1), pp.1-8.

Hable, S., Sigloch, K., Stutzmann, E., Kiselev, S. and Barruol, G., 2019. Tomography of crust and lithosphere in the western Indian Ocean from noise cross-correlations of land and ocean bottom seismometers. *Geophysical Journal International*, *219*(2), pp.924-944.

Hacker, B., Luffi, P., Lutkov, V., Minaev, V., Ratschbacher, L., Plank, T., Ducea, M., Patiño-Douce, A., McWILLIAMS, M.I.C.H.A.E.L. and Metcalf, J.I.M., 2005. Near-

ultrahigh pressure processing of continental crust: Miocene crustal xenoliths from the Pamir. *Journal of Petrology*, *46*(8), pp.1661-1687.

Hacker, B.R., Ratschbacher, L., Rutte, D., Stearns, M.A., Malz, N., Stübner, K., Kylander-Clark, A.R., Pfänder, J.A. and Everson, A., 2017. Building the Pamir-Tibet Plateau—Crustal stacking, extensional collapse, and lateral extrusion in the Pamir: 3. Thermobarometry and petrochronology of deep Asian crust. *Tectonics*, *36*(9), pp.1743-1766.

Hanna, A.C. and Weeraratne, D.S., 2013. Surface wave velocity structure of the western Himalayan syntaxis. *Geophysical Journal International*, *194*(3), pp.1866-1877.

Hansen, P.C., 1992. Analysis of discrete ill-posed problems by means of the L-curve. *SIAM review*, *34*(4), pp.561-580.

Hasselmann, K., 1963. A statistical analysis of the generation of microseisms. *Reviews of Geophysics*, *1*(2), pp.177-210.

Hauck, M.L., Nelson, K.D., Brown, L.D., Zhao, W. and Ross, A.R., 1998. Crustal structure of the Himalayan orogen at~ 90 east longitude from Project INDEPTH deep reflection profiles. *Tectonics*, *17*(4), pp.481-500.

Hawkins, R. and Sambridge, M., 2015. Geophysical imaging using trans-dimensional trees. *Geophysical Journal International*, *203*(2), pp.972-1000.

Hawkins, R., Brodie, R.C. and Sambridge, M., 2018. Trans-dimensional Bayesian inversion of airborne electromagnetic data for 2D conductivity profiles. *Exploration Geophysics*, *49*(2), pp.134-147.

Hazarika, D., Wadhawan, M., Paul, A., Kumar, N. and Borah, K., 2017. Geometry of the Main Himalayan Thrust and Moho beneath Satluj valley, northwest Himalaya: Constraints from receiver function analysis. *Journal of Geophysical Research: Solid Earth*, *122*(4), pp.2929-2945.

He, D., Webb, A.A.G., Larson, K.P. and Schmitt, A.K., 2016. Extrusion vs. duplexing models of Himalayan mountain building 2: The South Tibet detachment at the Dadeldhura klippe. *Tectonophysics*, *667*, pp.87-107.

He, D., Webb, A.A.G., Larson, K.P., Martin, A.J. and Schmitt, A.K., 2015. Extrusion vs. duplexing models of Himalayan mountain building 3: Duplexing dominates from the Oligocene to Present. *International Geology Review*, *57*(1), pp.1-27.

Heim, A. and Gansser, A., 1939. Central Himalaya: Geological observations of Swiss expedition 1936; Reprinted Delhi Hind. *Publ. Co*, *246*.

REFERENCES

Hennino, R., Trégourès, N., Shapiro, N.M., Margerin, L., Campillo, M., Van Tiggelen, B.A. and Weaver, R.L., 2001. Observation of equipartition of seismic waves. *Physical review letters*, *86*(15), p.3447.

Herrmann, R.B., 2013. Computer programs in seismology: An evolving tool for instruction and research. *Seismological Research Letters*, *84*(6), pp.1081-1088.

Hetényi, G., Cattin, R., Berthet, T., Le Moigne, N., Chophel, J., Lechmann, S., Hammer, P., Drukpa, D., Sapkota, S.N., Gautier, S. and Thinley, K., 2016. Segmentation of the Himalayas as revealed by arc-parallel gravity anomalies. *Scientific reports*, *6*(1), pp.1-10.

Hetényi, G., Vergne, J., Bollinger, L. and Cattin, R., 2011. Discontinuous low-velocity zones in southern Tibet question the viability of the channel flow model. *Geological Society, London, Special Publications*, *353*(1), pp.99-108.

Hintersberger, E., R. C. Thiede, and M. R. Strecker 2011, The role of extension during brittle deformation within the NW Indian Himalaya, Tectonics, 30, TC3012, doi:10.1029/2010TC002822.

Hintersberger, E., Thiede, R.C., Strecker, M.R. and Hacker, B.R., 2010. East-west extension in the NW Indian Himalaya. *Bulletin*, *122*(9-10), pp.1499-1515.

Hirschmiller, J., Grujic, D., Bookhagen, B., Coutand, I., Huyghe, P., Mugnier, J.L. and Ojha, T., 2014. What controls the growth of the Himalayan foreland fold-and-thrust belt?. *Geology*, *42*(3), pp.247-250.

Hodges, K.V., 2000. Tectonics of the Himalaya and southern Tibet from two perspectives. *Geological Society of America Bulletin*, *112*(3), pp.324-350.

Hodges, K.V., 2006. A synthesis of the channel flow-extrusion hypothesis as developed for the Himalayan-Tibetan orogenic system. *Geological Society, London, Special Publications*, *268*(1), pp.71-90.

Huang, G.C.D., Roecker, S.W. and Levin, V., 2011. Lower-crustal earthquakes in the West Kunlun range. *Geophysical Research Letters*, *38*(1).

Huang, G.C.D., Wu, F.T., Roecker, S.W. and Sheehan, A.F., 2009. Lithospheric structure of the central Himalaya from 3-D tomographic imaging. *Tectonophysics*, *475*(3-4), pp.524-543.

Hubbard, J., Almeida, R., Foster, A., Sapkota, S.N., Bürgi, P. and Tapponnier, P., 2016. Structural segmentation controlled the 2015 Mw 7.8 Gorkha earthquake rupture in Nepal. *Geology*, *44*(8), pp.639-642.

Ischuk, A., Bendick, R., Rybin, A., Molnar, P., Khan, S.F., Kuzikov, S., Mohadjer, S., Saydullaev, U., Ilyasova, Z., Schelochkov, G. and Zubovich, A.V., 2013. Kinematics of the Pamir and Hindu Kush regions from GPS geodesy. *Journal of geophysical research: solid earth*, *118*(5), pp.2408-2416.

Jade, S., Bhatt, B.C., Yang, Z., Bendick, R., Gaur, V.K., Molnar, P., Anand, M.B. and Kumar, D., 2004. GPS measurements from the Ladakh Himalaya, India: Preliminary tests of plate-like or continuous deformation in Tibet. *Geological Society of America Bulletin*, *116*(11-12), pp.1385-1391.

Jade, S., Mir, R.R., Vivek, C.G., Shrungeshwara, T.S., Parvez, I.A., Chandra, R., Babu, D.S., Gupta, S.V., Rajana, S.S.K. and Gaur, V.K., 2020. Crustal deformation rates in Kashmir valley and adjoining regions from continuous GPS measurements from 2008 to 2019. *Scientific reports*, *10*(1), pp.1-11.

Jade, S., Mukul, M., Gaur, V.K., Kumar, K., Shrungeshwar, T.S., Satyal, G.S., Dumka, R.K., Jagannathan, S., Ananda, M.B., Kumar, P.D. and Banerjee, S., 2014. Contemporary deformation in the Kashmir–Himachal, Garhwal and Kumaon Himalaya: significant insights from 1995–2008 GPS time series. *Journal of Geodesy*, *88*(6), pp.539-557.

Jagoutz, O. and Behn, M.D., 2013. Foundering of lower island-arc crust as an explanation for the origin of the continental Moho. *Nature*, *504*(7478), pp.131-134.

Jagoutz, O. and Kelemen, P.B., 2015. Role of arc processes in the formation of continental crust. *Annual Review of Earth and Planetary Sciences*, *43*, pp.363-404.

Jagoutz, O. and Schmidt, M.W., 2012. The formation and bulk composition of modern juvenile continental crust: The Kohistan arc. *Chemical Geology*, *298*, pp.79-96.

Jagoutz, O., Royden, L., Holt, A.F. and Becker, T.W., 2015. Anomalously fast convergence of India and Eurasia caused by double subduction. *Nature Geoscience*, *8*(6), pp.475-478.

Jia C., 1997. *Tectonic characteristics and petroleum: Tarim Basin, China.* Beijing: Petroleum Industry Press. pp.295

Jones, R.R., Holdsworth, R.E., Hand, M. and Goscombe, B., 2006. Ductile extrusion in continental collision zones: ambiguities in the definition of channel flow and its identification in ancient orogens. *Geological Society, London, Special Publications*, *268*(1), pp.201-219.

REFERENCES

Jouanne, F., Mugnier, J.L., Gamond, J.F., Le Fort, P., Pandey, M.R., Bollinger, L., Flouzat, M. and Avouac, J.P., 2004. Current shortening across the Himalayas of Nepal. *Geophysical Journal International*, *157*(1), pp.1-14.

Kaila, K.L., Tripathi, K.M. and Dixit, M.M., 1984. Crustal structure along Wular Lake-Gulmarg-Naoshera profile across Pir Panjal Range of the Himalayas from deep seismic soundings. *Journal of Geological Society of India (Online archive from Vol 1 to Vol 78)*, *25*(11), pp.706-719.

Kanna, N. and Gupta, S., 2020. Crustal seismic structure beneath the Garhwal Himalaya using regional and teleseismic waveform modelling. *Geophysical Journal International*, *222*(3), pp.2040-2052.

Kanna, N. and Gupta, S., 2021. Seismic crustal shear velocity structure across NW Himalaya and Ladakh-Karakoram using receiver function modelling: Evidence of the Main Himalayan Thrust. *Physics of the Earth and Planetary Interiors*, *311*, p.106642.

Kapp, P. and DeCelles, P.G., 2019. Mesozoic–Cenozoic geological evolution of the Himalayan-Tibetan orogen and working tectonic hypotheses. *American Journal of Science*, *319*(3), pp.159-254.

Kennett, B.L.N., Sambridge, M.S. and Williamson, P.R., 1988. Subspace methods for large inverse problems with multiple parameter classes. *Geophysical Journal International*, *94*(2), pp.237-247.

Kern, H., Popp, T., Gorbatsevich, F., Zharikov, A., Lobanov, K.V. and Smirnov, Y.P., 2001. Pressure and temperature dependence of VP and VS in rocks from the superdeep well and from surface analogues at Kola and the nature of velocity anisotropy. *Tectonophysics*, *338*(2), pp.113-134.

Khan N G, Bai L, Zhao J M, Li G H, Rahman M M, Cheng C, Yang J Y. 2017. Crustal structure beneath Tien Shan orogenic belt and its adjacent regions from multi-scale seismic data. Science China Earth Sciences, 60: 1769–1782, doi: 10.1007/s11430-017-9068-0.

Khan, S.D., Walker, D.J., Hall, S.A., Burke, K.C., Shah, M.T. and Stockli, L., 2009. Did the Kohistan-Ladakh island arc collide first with India?. *Geological Society of America Bulletin*, *121*(3-4), pp.366-384.

REFERENCES

Khattri, K.N., Chander, R., Gaur, V.K. and Sarkar, I., 1989. New seismological results on the tectonics of the Garhwal Himalaya. *Proceedings of the Indian Academy of Sciences-Earth and Planetary Sciences*, *98*(1), pp.91-109.

Klemperer, S.L., 2006. Crustal flow in Tibet: geophysical evidence for the physical state of Tibetan lithosphere, and inferred patterns of active flow. *Geological Society, London, Special Publications*, *268*(1), pp.39-70.

Klemperer, S.L., Kennedy, B.M., Sastry, S.R., Makovsky, Y., Harinarayana, T. and Leech, M.L., 2013. Mantle fluids in the Karakoram fault: Helium isotope evidence. *Earth and Planetary Science Letters*, *366*, pp.59-70.

Konca, A.O., Avouac, J.P., Sladen, A., Meltzner, A.J., Sieh, K., Fang, P., Li, Z., Galetzka, J., Genrich, J., Chlieh, M. and Natawidjaja, D.H., 2008. Partial rupture of a locked patch of the Sumatra megathrust during the 2007 earthquake sequence. *Nature*, *456*(7222), pp.631-635.

Kubo, R., 1966. The fluctuation-dissipation theorem. *Reports on progress in physics*, *29*(1), p.255.

Kufner, S.K., Schurr, B., Haberland, C., Zhang, Y., Saul, J., Ischuk, A. and Oimahmadov, I., 2017. Zooming into the Hindu Kush slab break-off: A rare glimpse on the terminal stage of subduction. *Earth and Planetary Science Letters*, *461*, pp.127-140.

Kufner, S.K., Schurr, B., Sippl, C., Yuan, X., Ratschbacher, L., Ischuk, A., Murodkulov, S., Schneider, F., Mechie, J. and Tilmann, F., 2016. Deep India meets deep Asia: Lithospheric indentation, delamination and break-off under Pamir and Hindu Kush (Central Asia). *Earth and Planetary Science Letters*, *435*, pp.171-184.

Kumar, N., Aoudia, A., Guidarelli, M., Babu, V.G., Hazarika, D. and Yadav, D.K., 2019. Delineation of lithosphere structure and characterization of the Moho geometry under the Himalaya–Karakoram–Tibet collision zone using surface-wave tomography. *Geological Society, London, Special Publications*, *481*(1), pp.19-40.

Kumar, P., Yuan, X., Kumar, M.R., Kind, R., Li, X. and Chadha, R.K., 2007. The rapid drift of the Indian tectonic plate. *Nature*, *449*(7164), pp.894-897.

Kumar, S., Wesnousky, S.G., Rockwell, T.K., Briggs, R.W., Thakur, V.C. and Jayangondaperumal, R., 2006. Paleoseismic evidence of great surface rupture earthquakes along the Indian Himalaya. *Journal of Geophysical Research: Solid Earth*, *111*(B3).

REFERENCES

Lavé, J. and Avouac, J.P., 2000. Active folding of fluvial terraces across the Siwaliks Hills, Himalayas of central Nepal. *Journal of Geophysical Research: Solid Earth*, *105*(B3), pp.5735-5770.

Law, R.D., Searle, M.P. and Simpson, R.L., 2004. Strain, deformation temperatures and vorticity of flow at the top of the Greater Himalayan Slab, Everest Massif, Tibet. *Journal of the Geological Society*, *161*(2), pp.305-320.

Le Pichon, X., Fournier, M. and Jolivet, L., 1992. Kinematics, topography, shortening, and extrusion in the India-Eurasia collision. *Tectonics*, *11*(6), pp.1085-1098.

Lebedev, S., Adam, J.M.C. and Meier, T., 2013. Mapping the Moho with seismic surface waves: a review, resolution analysis, and recommended inversion strategies. *Tectonophysics*, *609*, pp.377-394.

Leech, M.L., 2008. Does the Karakoram fault interrupt mid-crustal channel flow in the western Himalaya?. *Earth and Planetary Science Letters*, *276*(3-4), pp.314-322.

LeFort, P., 1975. Himalayas-collided range-present knowledge of continental arc: American Journal of Science, v.

Levshin, A.L. and Ritzwoller, M.H., 2001. Automated detection, extraction, and measurement of regional surface waves. In *Monitoring the comprehensive nuclear-test-ban treaty: Surface waves* (pp. 1531-1545). Birkhäuser, Basel.

Levshin, A.L., Pisarenko, V.F. and Pogrebinsky, G.A., 1972. On a frequency-time analysis of oscillations. In *Annales de geophysique* (Vol. 28, No. 2, pp. 211-218). Centre National de la Recherche Scientifique.

Li, C., Yao, H., Fang, H., Huang, X., Wan, K., Zhang, H. and Wang, K., 2016. 3D near-surface shear-wave velocity structure from ambient-noise tomography and borehole data in the Hefei urban area, China. *Seismological Research Letters*, *87*(4), pp.882-892.

Li, J. and Song, X., 2018. Tearing of Indian mantle lithosphere from high-resolution seismic images and its implications for lithosphere coupling in southern Tibet. *Proceedings of the National Academy of Sciences*, *115*(33), pp.8296-8300.

Li, W., Chen, Y., Yuan, X., Schurr, B., Mechie, J., Oimahmadov, I. and Fu, B., 2018. Continental lithospheric subduction and intermediate-depth seismicity: Constraints from S-wave velocity structures in the Pamir and Hindu Kush. *Earth and Planetary Science Letters*, *482*, pp.478-489.

REFERENCES

LITVINOVSKY, B.A., STEELE, I.M. and WICKHAM, S.M., 2000. Silicic magma formation in overthickened crust: melting of charnockite and leucogranite at 15, 20 and 25 kbar. *Journal of Petrology*, *41*(5), pp.717-737.

Lobkis, O.I. and Weaver, R.L., 2001. On the emergence of the Green's function in the correlations of a diffuse field. *The Journal of the Acoustical Society of America*, *110*(6), pp.3011-3017.

Longuet-Higgins, M.S., 1950. A theory of the origin of microseisms. *Philosophical Transactions of the Royal Society of London. Series A, Mathematical and Physical Sciences*, *243*(857), pp.1-35.

Loveless, J.P. and Meade, B.J., 2011. Spatial correlation of interseismic coupling and coseismic rupture extent of the 2011 Mw= 9.0 Tohoku-oki earthquake. *Geophysical Research Letters*, *38*(17).

Luo, Y., Yang, Y., Xu, Y., Xu, H., Zhao, K. and Wang, K., 2015. On the limitations of interstation distances in ambient noise tomography. *Geophysical Journal International*, *201*(2), pp.652-661.

Lyon-Caen, H. and Molnar, P., 1985. Gravity anomalies, flexure of the Indian plate, and the structure, support and evolution of the Himalaya and Ganga Basin. *Tectonics*, *4*(6), pp.513-538.

Macedo, J. and Marshak, S., 1999. Controls on the geometry of fold-thrust belt salients. *Geological Society of America Bulletin*, *111*(12), pp.1808-1822.

Maceira, M. and Ammon, C.J., 2009. Joint inversion of surface wave velocity and gravity observations and its application to central Asian basins shear velocity structure. *Journal of Geophysical Research: Solid Earth*, *114*(B2).

Mahesh, P., Rai, S.S., Sivaram, K., Paul, A., Gupta, S., Sarma, R. and Gaur, V.K., 2013. One-dimensional reference velocity model and precise locations of earthquake hypocenters in the Kumaon–Garhwal himalaya. *Bulletin of the Seismological Society of America*, *103*(1), pp.328-339.

Makovsky, Y. and Klemperer, S.L., 1999. Measuring the seismic properties of Tibetan bright spots: Evidence for free aqueous fluids in the Tibetan middle crust. *Journal of Geophysical Research: Solid Earth*, *104*(B5), pp.10795-10825.

Makovsky, Y., Klemperer, S.L., Huang, L., Lu, D. and Project INDEPTH Team, 1996. Structural elements of the southern Tethyan Himalaya crust from wide-angle seismic data. *Tectonics*, *15*(5), pp.997-1005.

REFERENCES

Malinverno, A. and Briggs, V.A., 2004. Expanded uncertainty quantification in inverse problems: Hierarchical Bayes and empirical Bayes. *Geophysics*, *69*(4), pp.1005-1016.

Mandal, S., Robinson, D.M., Kohn, M.J., Khanal, S. and Das, O., 2019. Examining the tectono-stratigraphic architecture, structural geometry, and kinematic evolution of the Himalayan fold-thrust belt, Kumaun, northwest India. *Lithosphere*, *11*(4), pp.414-435.

Mattauer, M., 1986. Intracontinental subduction, crust-mantle décollement and crustal-stacking wedge in the Himalayas and other collision belts. *Geological Society, London, Special Publications*, *19*(1), pp.37-50.

Mechie, J., Yuan, X., Schurr, B., Schneider, F., Sippl, C., Ratschbacher, L., Minaev, V., Gadoev, M., Oimahmadov, I., Abdybachaev, U. and Moldobekov, B., 2012. Crustal and uppermost mantle velocity structure along a profile across the Pamir and southern Tien Shan as derived from project TIPAGE wide-angle seismic data. *Geophysical Journal International*, *188*(2), pp.385-407.

Mir, R.R., Parvez, I.A., Gaur, V.K., Chandra, R. and Romshoo, S.A., 2017. Crustal structure beneath the Kashmir Basin adjoining the western Himalayan syntaxis. *Bulletin of the Seismological Society of America*, *107*(5), pp.2443-2458.

Mitra, S., Kainkaryam, S.M., Padhi, A., Rai, S.S. and Bhattacharya, S.N., 2011. The Himalayan foreland basin crust and upper mantle. *Physics of the Earth and Planetary Interiors*, *184*(1-2), pp.34-40.

Mohadjer, S., Bendick, R., Ischuk, A., Kuzikov, S., Kostuk, A., Saydullaev, U., Lodi, S., Kakar, D.M., Wasy, A., Khan, M.A. and Molnar, P., 2010. Partitioning of India-Eurasia convergence in the Pamir-Hindu Kush from GPS measurements. *Geophysical Research Letters*, *37*(4).

Molnar, P. and Lyon-Caen, H., 1989. Fault plane solutions of earthquakes and active tectonics of the Tibetan Plateau and its margins. *Geophysical Journal International*, *99*(1), pp.123-153.

Molnar, P. and Stock, J.M., 2009. Slowing of India's convergence with Eurasia since 20 Ma and its implications for Tibetan mantle dynamics. *Tectonics*, *28*(3).

Molnar, P. and Tapponnier, P., 1975. Cenozoic tectonics of Asia: effects of a continental collision. *science*, *189*(4201), pp.419-426.

REFERENCES

Molnar, P. and Tapponnier, P., 1978. Active tectonics of Tibet. *Journal of Geophysical Research: Solid Earth*, *83*(B11), pp.5361-5375.

Molnar, P., 1988. Continental tectonics in the aftermath of plate tectonics. *Nature*, *335*(6186), pp.131-137.

Molnar, P., England, P. and Martinod, J., 1993. Mantle dynamics, uplift of the Tibetan Plateau, and the Indian monsoon. *Reviews of Geophysics*, *31*(4), pp.357-396.

Monsalve, G., Sheehan, A., Rowe, C. and Rajaure, S., 2008. Seismic structure of the crust and the upper mantle beneath the Himalayas: Evidence for eclogitization of lower crustal rocks in the Indian Plate. *Journal of Geophysical Research: Solid Earth*, *113*(B8).

Moreno, M., Rosenau, M. and Oncken, O., 2010. Maule earthquake slip correlates with pre-seismic locking of Andean subduction zone. *Nature*, *467*(7312), pp.198-202.

Murodov, D., Zhao, J., Xu, Q., Liu, H. and Pei, S., 2018. Complex N–S variations in Moho depth and V p/V s ratio beneath the western Tibetan Plateau as revealed by receiver function analysis. *Geophysical Journal International*, *214*(2), pp.895-906.

Murphy, M.A. and Copeland, P., 2005. Transtensional deformation in the central Himalaya and its role in accommodating growth of the Himalayan orogen. *Tectonics*, *24*(4).

Murphy, M.A. and Yin, A., 2003. Structural evolution and sequence of thrusting in the Tethyan fold-thrust belt and Indus-Yalu suture zone, southwest Tibet. *Geological Society of America Bulletin*, *115*(1), pp.21-34.

Murphy, M.A., Sanchez, V. and Taylor, M.H., 2010. Syncollisional extension along the India–Asia suture zone, south-central Tibet: Implications for crustal deformation of Tibet. *Earth and Planetary Science Letters*, *290*(3-4), pp.233-243.

Nábělek, J., Hetényi, G., Vergne, J., Sapkota, S., Kafle, B., Jiang, M., Su, H., Chen, J. and Huang, B.S., 2009. Underplating in the Himalaya-Tibet collision zone revealed by the Hi-CLIMB experiment. *Science*, *325*(5946), pp.1371-1374.

Nakata, T., 1989. Active faults of the Himalaya of India and Nepal. *Tectonics of the Western Himalayas*, *232*, pp.243-264.

Nawa, K., Suda, N., Fukao, Y., Sato, T., Aoyama, Y. and Shibuya, K., 1998. Incessant excitation of the Earth's free oscillations. *Earth, planets and space*, *50*(1), pp.3-8.

Nelson, K.D., Zhao, W., Brown, L.D., Kuo, J., Che, J., Liu, X., Klemperer, S.L., Makovsky, Y., Meissner, R.J.J.M., Mechie, J. and Kind, R., 1996. Partially molten middle crust

beneath southern Tibet: synthesis of project INDEPTH results. *science*, *274*(5293), pp.1684-1688.

Ni, J. and Barazangi, M., 1984. Seismotectonics of the Himalayan collision zone: Geometry of the underthrusting Indian plate beneath the Himalaya. *Journal of Geophysical Research: Solid Earth*, *89*(B2), pp.1147-1163.

Nowack, R.L., Chen, W.P. and Tseng, T.L., 2010. Application of Gaussian-beam migration to multiscale imaging of the lithosphere beneath the Hi-CLIMB array in Tibet. *Bulletin of the Seismological Society of America*, *100*(4), pp.1743-1754.

O'Brien, P.J., 2019. Eclogites and other high-pressure rocks in the Himalaya: a review. *Geological Society, London, Special Publications*, *483*(1), pp.183-213.

Oreshin, S., Kiselev, S., Vinnik, L., Prakasam, K.S., Rai, S.S., Makeyeva, L. and Savvin, Y., 2008. Crust and mantle beneath western Himalaya, Ladakh and western Tibet from integrated seismic data. *Earth and Planetary Science Letters*, *271*(1-4), pp.75-87.

Owens, T.J. and Zandt, G., 1997. Implications of crustal property variations for models of Tibetan plateau evolution. *Nature*, *387*(6628), pp.37-43.

Pandey, M.R., Tandukar, R.P., Avouac, J.P., Vergne, J. and Heritier, T., 1999. Seismotectonics of the Nepal Himalaya from a local seismic network. *Journal of Asian Earth Sciences*, *17*(5-6), pp.703-712.

Pasyanos, M.E., 2005. A variable resolution surface wave dispersion study of Eurasia, North Africa, and surrounding regions. *Journal of Geophysical Research: Solid Earth*, *110*(B12).

Patriat, P. and Achache, J., 1984. India–Eurasia collision chronology has implications for crustal shortening and driving mechanism of plates. *Nature*, *311*(5987), pp.615-621.

Pavlis, G.L. and Das, S., 2000. The Pamir-Hindu Kush seismic zone as a strain marker for flow in the upper mantle. *Tectonics*, *19*(1), pp.103-115.

Pegler, G. and Das, S., 1998. An enhanced image of the Pamir–Hindu Kush seismic zone from relocated earthquake hypocentres. *Geophysical Journal International*, *134*(2), pp.573-595.

Pei, S., Sun, Y. and Toksöz, M.N., 2011. Tomographic Pn and Sn velocity beneath the continental collision zone from Alps to Himalaya. *Journal of Geophysical Research: Solid Earth*, *116*(B10).

REFERENCES

Pilia, S., Jackson, J., Hawkins, R., Kaviani, A. and Ali, M.Y., 2020. The southern Zagros collisional orogen: new insights from transdimensional-trees inversion of seismic noise.

Powell, C.M. and Conaghan, P.J., 1973. Plate tectonics and the Himalayas. *Earth and Planetary Science Letters*, *20*(1), pp.1-12.

Prasad, B.R., Klemperer, S.L., Rao, V.V., Tewari, H.C. and Khare, P., 2011. Crustal structure beneath the Sub-Himalayan fold–thrust belt, Kangra recess, northwest India, from seismic reflection profiling: Implications for Late Paleoproterozoic orogenesis and modern earthquake hazard. *Earth and Planetary Science Letters*, *308*(1-2), pp.218-228.

Pratt, J.H., 1859. XXIX. On the deflection of the plumb-line in India, caused by the attraction of the Himmalaya mountains and of the elevated regions beyond; and its modification by the compensating effect of a deficiency of matter below the mountain mass. *Philosophical Transactions of the Royal Society of London*, (149), pp.745-778.

Priestley, K., Ho, T. and Mitra, S., 2019. The crustal structure of the Himalaya: A synthesis. *Geological Society, London, Special Publications*, *483*(1), pp.483-516.

Priestley, K., Jackson, J. and McKenzie, D., 2008. Lithospheric structure and deep earthquakes beneath India, the Himalaya and southern Tibet. *Geophysical Journal International*, *172*(1), pp.345-362.

Qiu, Q., Hill, E.M., Barbot, S., Hubbard, J., Feng, W., Lindsey, E.O., Feng, L., Dai, K., Samsonov, S.V. and Tapponnier, P., 2016. The mechanism of partial rupture of a locked megathrust: The role of fault morphology. *Geology*, *44*(10), pp.875-878.

Rai, S.S., Padhi, A. and Sarma, P.R., 2009. High crustal seismic attenuation in Ladakh–Karakoram. *Bulletin of the Seismological Society of America*, *99*(1), pp.407-415.

Rai, S.S., Priestley, K., Gaur, V.K., Mitra, S., Singh, M.P. and Searle, M., 2006. Configuration of the Indian Moho beneath the NW Himalaya and Ladakh. *Geophysical Research Letters*, *33*(15).

Rawat, G., Arora, B.R. and Gupta, P.K., 2014. Electrical resistivity cross-section across the Garhwal Himalaya: Proxy to fluid-seismicity linkage. *Tectonophysics*, *637*, pp.68-79.

Rawlinson, N. and Sambridge, M., 2003. Seismic traveltime tomography of the crust and lithosphere. *Advances in geophysics*, *46*, pp.81-199.

REFERENCES

Rawlinson, N. and Sambridge, M., 2004. Wave front evolution in strongly heterogeneous layered media using the fast marching method. *Geophysical Journal International*, *156*(3), pp.631-647.

Rawlinson, N. and Sambridge, M., 2005. The fast marching method: an effective tool for tomographic imaging and tracking multiple phases in complex layered media. *Exploration Geophysics*, *36*(4), pp.341-350.

Rawlinson, N., Pozgay, S. and Fishwick, S., 2010. Seismic tomography: a window into deep Earth. *Physics of the Earth and Planetary Interiors*, *178*(3-4), pp.101-135.

Rawlinson, N., Spakman, W., 2016. On the use of sensitivity tests in seismic tomography. Geophysical Journal International 205, 1221 -1243.

Razi, A.S., Levin, V., Roecker, S.W. and Huang, G.C.D., 2014. Crustal and uppermost mantle structure beneath western Tibet using seismic traveltime tomography. *Geochemistry, Geophysics, Geosystems*, *15*(2), pp.434-452.

Reuber, I., 1986. Geometry of accretion and oceanic thrusting of the Spongtang Ophiolite, Ladakh-Himalaya. *Nature*, *321*(6070), pp.592-596.

Rhie, J. and Romanowicz, B., 2004. Excitation of Earth's continuous free oscillations by atmosphere–ocean–seafloor coupling. *Nature*, *431*(7008), pp.552-556.

Rickett, J.E. and Claerbout, J.F., 2000. Calculation of the sun's acoustic impulse response by multi-dimensional spectral factorization. In *Helioseismic Diagnostics of Solar Convection and Activity* (pp. 203-210). Springer, Dordrecht.

Rippe, D. and Unsworth, M., 2010. Quantifying crustal flow in Tibet with magnetotelluric data. *Physics of the Earth and Planetary Interiors*, *179*(3-4), pp.107-121.

Ritzwoller, M.H., Lin, F.C. and Shen, W., 2011. Ambient noise tomography with a large seismic array. *Comptes Rendus Geoscience*, *343*(8-9), pp.558-570.

Robyr, M., Hacker, B.R. and Mattinson, J.M., 2006. Doming in compressional orogenic settings: New geochronological constraints from the NW Himalaya. *Tectonics*, *25*(2).

Roecker, S.W., 1982. Velocity structure of the Pamir-Hindu Kush region: Possible evidence of subducted crust. *Journal of Geophysical Research: Solid Earth*, *87*(B2), pp.945-959.

Rolland, Y., Pecher, A. and Picard, C., 2000. Middle Cretaceous back-arc formation and arc evolution along the Asian margin: the Shyok Suture Zone in northern Ladakh (NW Himalaya). *Tectonophysics*, *325*(1-2), pp.145-173.

REFERENCES

Rosalia, S., Cummins, P., Widiyantoro, S., Yudistira, T., Nugraha, A.D. and Hawkins, R., 2020. Group velocity maps using subspace and transdimensional inversions: ambient noise tomography in the western part of Java, Indonesia. *Geophysical Journal International*, *220*(2), pp.1260-1274.

Roux, P., Song, H.C. and Kuperman, W.A., 2003. Time-reversal using ambient noise as a probe source. *The Journal of the Acoustical Society of America*, *113*(4), pp.2218-2218.

Rudnick, R.L. and Fountain, D.M., 1995. Nature and composition of the continental crust: a lower crustal perspective. *Reviews of geophysics*, *33*(3), pp.267-309.

Rudnick, R.L., 1995. Making continental crust. *Nature*, *378*(6557), pp.571-578.

Rudnick, R.L., Gao, S., Holland, H.D. and Turekian, K.K., 2003. Composition of the continental crust. *The crust*, *3*, pp.1-64.

Rutte, D., Ratschbacher, L., Schneider, S., Stübner, K., Stearns, M.A., Gulzar, M.A. and Hacker, B.R., 2017. Building the Pamir-Tibetan Plateau—Crustal stacking, extensional collapse, and lateral extrusion in the Central Pamir: 1. Geometry and kinematics. *Tectonics*, *36*(3), pp.342-384.

Sabra, K.G., Gerstoft, P., Roux, P., Kuperman, W.A. and Fehler, M.C., 2005. Extracting time-domain Green's function estimates from ambient seismic noise. *Geophysical Research Letters*, *32*(3).

Saha, G.K., Prakasam, K.S. and Rai, S.S., 2020. Diversity in the peninsular Indian lithosphere revealed from ambient noise and earthquake tomography. *Physics of the Earth and Planetary Interiors*, *306*, p.106523.

Saito, M. and Doornbos, D.J., 1988. Seismological algorithms: Computational methods and computer programs.

Salomón, J., Pastén, C., Ruiz, S., Leyton, F., Sáez, M. and Rauld, R., 2021. Shear wave velocity model of the Abanico Formation underlying the Santiago City metropolitan area, Chile, using ambient seismic noise tomography. *Geophysical Journal International*, *225*(2), pp.1222-1235.

Sapin, M. and Hirn, A., 1997. Seismic structure and evidence for eclogitization during the Himalayan convergence. *Tectonophysics*, *273*(1-2), pp.1-16.

Sapkota, S.N., Bollinger, L., Klinger, Y., Tapponnier, P., Gaudemer, Y. and Tiwari, D., 2013. Primary surface ruptures of the great Himalayan earthquakes in 1934 and 1255. *Nature Geoscience*, *6*(1), pp.71-76.

REFERENCES

Sass, P., Ritter, O., Ratschbacher, L., Tympel, J., Matiukov, V.E., Rybin, A.K. and Batalev, V.Y., 2014. Resistivity structure underneath the Pamir and southern Tian Shan. *Geophysical Journal International*, *198*(1), pp.564-579.

Sathiakumar, S. and Barbot, S., 2021. The stop-start control of seismicity by fault bends along the Main Himalayan Thrust. *Communications Earth & Environment*, *2*(1), pp.1-11.

Saygin, E. and Kennett, B.L., 2010. Ambient seismic noise tomography of Australian continent. *Tectonophysics*, *481*(1-4), pp.116-125.

Scaillet, B., Holtz, F., Pichavant, M. and Schmidt, M., 1996. Viscosity of Himalayan leucogranites: Implications for mechanisms of granitic magma ascent. *Journal of Geophysical Research: Solid Earth*, *101*(B12), pp.27691-27699.

Scales, J.A. and Snieder, R., 1998. What is noise?. *Geophysics*, *63*(4), pp.1122-1124.

Schelling, D. and Arita, K., 1991. Thrust tectonics, crustal shortening, and the structure of the far-eastern Nepal Himalaya. *Tectonics*, *10*(5), pp.851-862.

Schettino, A. and Scotese, C.R., 2005. Apparent polar wander paths for the major continents (200 Ma to the present day): a palaeomagnetic reference frame for global plate tectonic reconstructions. *Geophysical Journal International*, *163*(2), pp.727-759.

Schiffman, C., Bali, B.S., Szeliga, W. and Bilham, R., 2013. Seismic slip deficit in the Kashmir Himalaya from GPS observations. *Geophysical Research Letters*, *40*(21), pp.5642-5645.

Schimmel, M. and Gallart, J., 2007. Frequency-dependent phase coherence for noise suppression in seismic array data. *Journal of Geophysical Research: Solid Earth*, *112*(B4).

Schimmel, M. and Paulssen, H., 1997. Noise reduction and detection of weak, coherent signals through phase-weighted stacks. *Geophysical Journal International*, *130*(2), pp.497-505.

Schimmel, M., 1999. Phase cross-correlations: Design, comparisons, and applications. *Bulletin of the Seismological Society of America*, *89*(5), pp.1366-1378.

Schimmel, M., Stutzmann, E. and Gallart, J., 2011. Using instantaneous phase coherence for signal extraction from ambient noise data at a local to a global scale. *Geophysical Journal International*, *184*(1), pp.494-506.

Schneider, F.M., Yuan, X., Schurr, B., Mechie, J., Sippl, C., Haberland, C., Minaev, V., Oimahmadov, I., Gadoev, M., Radjabov, N. and Abdybachaev, U., 2013. Seismic

imaging of subducting continental lower crust beneath the Pamir. *Earth and Planetary Science Letters*, *375*, pp.101-112.

Schneider, F.M., Yuan, X., Schurr, B., Mechie, J., Sippl, C., Kufner, S.K., Ratschbacher, L., Tilmann, F., Oimahmadov, I., Gadoev, M. and Minaev, V., 2019. The crust in the Pamir: Insights from receiver functions. *Journal of Geophysical Research: Solid Earth*, *124*(8), pp.9313-9331.

Schulte-Pelkum, V., K. H. Mahan, W. Shen, and J. C. Stachnik (2017), The distribution and composition of highvelocity lower crust across the continental U.S.: Comparison of seismic and xenolith data and implications for lithospheric dynamics and history, Tectonics, 36, 1455–1496, doi: 10.1002/ 2017TC004480.

Schulte-Pelkum, V., Monsalve, G., Sheehan, A., Pandey, M.R., Sapkota, S., Bilham, R. and Wu, F., 2005. Imaging the Indian subcontinent beneath the Himalaya. *Nature*, *435*(7046), pp.1222-1225.

Schurr, B., Ratschbacher, L., Sippl, C., Gloaguen, R., Yuan, X. and Mechie, J., 2014. Seismotectonics of the Pamir. *Tectonics*, *33*(8), pp.1501-1518.

Schwab, M., Ratschbacher, L., Siebel, W., McWilliams, M., Minaev, V., Lutkov, V., Chen, F., Stanek, K., Nelson, B., Frisch, W. and Wooden, J.L., 2004. Assembly of the Pamirs: Age and origin of magmatic belts from the southern Tien Shan to the southern Pamirs and their relation to Tibet. *Tectonics*, *23*(4).

Searle, M.P. and Hacker, B.R., 2019. Structural and metamorphic evolution of the Karakoram and Pamir following India–Kohistan–Asia collision. *Geological Society, London, Special Publications*, *483*(1), pp.555-582.

Searle, M.P., 2015. 6.11 Mountain Building, Tectonic Evolution, Rheology, and Crustal Flow in the Himalaya, Karakoram, and Tibet.

Searle, M.P., Cottle, J.M., Streule, M.J. and Waters, D.J., 2010. Crustal melt granites and migmatites along the Himalaya: melt source, segregation, transport and granite emplacement mechanisms. *Transactions of the Royal Society of Edinburgh*, *100*, pp.219-233.

Searle, M.P., Elliott, J.R., Phillips, R.J. and Chung, S.L., 2011. Crustal–lithospheric structure and continental extrusion of Tibet. *Journal of the Geological Society*, *168*(3), pp.633-672.

REFERENCES

Seeber, L., Armbruster, J.G. and Quittmeyer, R.C., 1981. Seismicity and continental subduction in the Himalayan arc. *Zagros Hindu Kush Himalaya Geodynamic Evolution*, *3*, pp.215-242.

Sengör, A.C. and Natal'In, B.A., 1996. Turkic-type orogeny and its role in the making of the continental crust. *Annual Review of Earth and Planetary Sciences*, *24*(1), pp.263-337.

Sethian, J.A. and Popovici, A.M., 1999. 3-D traveltime computation using the fast marching method. *Geophysics*, *64*(2), pp.516-523.

Sethian, J.A., 1996. A fast marching level set method for monotonically advancing fronts. *Proceedings of the National Academy of Sciences*, *93*(4), pp.1591-1595.

Shapiro, N.M. and Campillo, M., 2004. Emergence of broadband Rayleigh waves from correlations of the ambient seismic noise. *Geophysical Research Letters*, *31*(7).

Shapiro, N.M., Campillo, M., Stehly, L. and Ritzwoller, M.H., 2005. High-resolution surface-wave tomography from ambient seismic noise. *Science*, *307*(5715), pp.1615-1618.

Shapiro, N.M., Ritzwoller, M.H., Molnar, P. and Levin, V., 2004. Thinning and flow of Tibetan crust constrained by seismic anisotropy. *Science*, *305*(5681), pp.233-236.

Sharma, R.P. and Virdi, N.S., 1982. Tectonic evolution of Simla and Kumaon Himalaya, based on Landsat-I multispectral imagery and aerial photo-interpretation. *Miscellaneous publication-Geological survey of India*, pp.115-132.

Shen, W., Ritzwoller, M.H., Kang, D., Kim, Y., Lin, F.C., Ning, J., Wang, W., Zheng, Y. and Zhou, L., 2016. A seismic reference model for the crust and uppermost mantle beneath China from surface wave dispersion. *Geophysical Journal International*, *206*(2), pp.954-979.

Sippl, C., Schurr, B., Yuan, X., Mechie, J., Schneider, F.M., Gadoev, M., Orunbaev, S., Oimahmadov, I., Haberland, C., Abdybachaev, U. and Minaev, V., 2013. Geometry of the Pamir-Hindu Kush intermediate-depth earthquake zone from local seismic data. *Journal of Geophysical Research: Solid Earth*, *118*(4), pp.1438-1457.

Solon, K.D., Jones, A.G., Nelson, K.D., Unsworth, M.J., Kidd, W.F., Wei, W., Tan, H., Jin, S., Deng, M., Booker, J.R. and Li, S., 2005. Structure of the crust in the vicinity of the Banggong-Nujiang suture in central Tibet from INDEPTH magnetotelluric data. *Journal of Geophysical Research: Solid Earth*, *110*(B10).

REFERENCES

Srivastava, P. and Mitra, G., 1994. Thrust geometries and deep structure of the outer and lesser Himalaya, Kumaon and Garhwal (India): Implications for evolution of the Himalayan fold-and-thrust belt. *Tectonics*, *13*(1), pp.89-109.

Stevens, V.L. and Avouac, J.P., 2015. Interseismic coupling on the main Himalayan thrust. *Geophysical Research Letters*, *42*(14), pp.5828-5837.

Styron, R.H., Taylor, M.H. and Murphy, M.A., 2011. Oblique convergence, arc-parallel extension, and the role of strike-slip faulting in the High Himalaya. *Geosphere*, *7*(2), pp.582-596.

Tahirkheli, R.K., 1979. Geology of Kohistan and adjoining Eurasian and Indo-Pakistan continents, Pakistan. *Geol. Bull. Univ. Peshawar*, *11*(1), pp.1-30.

Takei, Y., 2000. Acoustic properties of partially molten media studied on a simple binary system with a controllable dihedral angle. *Journal of Geophysical Research: Solid Earth*, *105*(B7), pp.16665-16682.

Taylor, M. and Yin, A., 2009. Active structures of the Himalayan-Tibetan orogen and their relationships to earthquake distribution, contemporary strain field, and Cenozoic volcanism. *Geosphere*, *5*(3), pp.199-214.

Thakur, V.C., Jayangondaperumal, R. and Joevivek, V., 2019. Seismotectonics of central and NW Himalaya: plate boundary–wedge thrust earthquakes in thin-and thick-skinned tectonic framework. *Geological Society, London, Special Publications*, *481*(1), pp.41-63.

Thiede, R.C., Arrowsmith, J.R., Bookhagen, B., McWilliams, M., Sobel, E.R. and Strecker, M.R., 2006. Dome formation and extension in the Tethyan Himalaya, Leo Pargil, northwest India. *Geological Society of America Bulletin*, *118*(5-6), pp.635-650.

Treloar, P.J., O'Brien, P.J., Parrish, R.R. and Khan, M.A., 2003. Exhumation of early Tertiary, coesite-bearing eclogites from the Pakistan Himalaya. *Journal of the Geological Society*, *160*(3), pp.367-376.

Treloar, P.J., Rex, D.C., Guise, P.G., Coward, M.P., Searle, M.P., Windley, B.F., Petterson, M.G., Jan, M.Q. and Luff, I.W., 1989. K-Ar and Ar-Ar geochronology of the Himalayan collision in NW Pakistan: Constraints on the timing of suturing, deformation, metamorphism and uplift. *Tectonics*, *8*(4), pp.881-909.

Tseng, T.L., Chen, W.P. and Nowack, R.L., 2009. Northward thinning of Tibetan crust revealed by virtual seismic profiles. *Geophysical Research Letters*, *36*(24).

REFERENCES

Unsworth, M., Wenbo, W., Jones, A.G., Li, S., Bedrosian, P., Booker, J., Sheng, J., Ming, D. and Handong, T., 2004. Crustal and upper mantle structure of northern Tibet imaged with magnetotelluric data. *Journal of Geophysical Research: Solid Earth*, *109*(B2).

Unsworth, M.J., Jones, A.G., Wei, W., Marquis, G., Gokarn, S.G. and Spratt, J.E., 2005. Crustal rheology of the Himalaya and Southern Tibet inferred from magnetotelluric data. *Nature*, *438*(7064), pp.78-81.

Valdiya, K.S., 1980. Geology of the Kumaon Lesser Himalaya. Wadia Institute of Himalaya, Dehra Dun, India, 291 pp.

Valdiya, K.S., 1988. Tectonics and evolution of the central sector of the Himalaya. *Philosophical Transactions of the Royal Society of London. Series A, Mathematical and Physical Sciences*, *326*(1589), pp.151-175.

Van Hinsbergen, D.J., Lippert, P.C., Dupont-Nivet, G., McQuarrie, N., Doubrovine, P.V., Spakman, W. and Torsvik, T.H., 2012. Greater India Basin hypothesis and a two-stage Cenozoic collision between India and Asia. *Proceedings of the National Academy of Sciences*, *109*(20), pp.7659-7664.

Van Hinsbergen, D.J., Steinberger, B., Doubrovine, P.V. and Gassmöller, R., 2011. Acceleration and deceleration of India-Asia convergence since the Cretaceous: Roles of mantle plumes and continental collision. *Journal of Geophysical Research: Solid Earth*, *116*(B6).

Van Tiggelen, B.A., 2003. Green function retrieval and time reversal in a disordered world. *Physical review letters*, *91*(24), p.243904.

Ventosa, S., Schimmel, M. and Stutzmann, E., 2019. Towards the processing of large data volumes with phase cross-correlation. *Seismological Research Letters*, *90*(4), pp.1663-1669.

Virdi, N.S., 1979. On the geodynamic significance of mega-lineaments in the Outer and Lesser regions of western Himalaya.

Wadia, D.N., 1951. Plio-Pleistocene boundary in NW India. *Int. Geol. Congr. London (1948)*, *18*, pp.43-48.

Wang, Q., Hawkesworth, C.J., Wyman, D., Chung, S.L., Wu, F.Y., Li, X.H., Li, Z.X., Gou, G.N., Zhang, X.Z., Tang, G.J. and Dan, W., 2016. Pliocene-Quaternary crustal melting in central and northern Tibet and insights into crustal flow. *Nature Communications*, *7*(1), pp.1-11.

REFERENCES

Wang, X., Wei, S. and Wu, W., 2017. Double-ramp on the Main Himalayan Thrust revealed by broadband waveform modeling of the 2015 Gorkha earthquake sequence. *Earth and Planetary Science Letters*, *473*, pp.83-93.

Wapenaar, K., 2004. Retrieving the elastodynamic Green's function of an arbitrary inhomogeneous medium by cross correlation. *Physical review letters*, *93*(25), p.254301.

Weaver, R.L. and Lobkis, O.I., 2001. Ultrasonics without a source: Thermal fluctuation correlations at MHz frequencies. *Physical Review Letters*, *87*(13), p.134301.

Wesnousky, S.G., 2006. Predicting the endpoints of earthquake ruptures. *Nature*, *444*(7117), pp.358-360.

Wessel, P., Luis, J.F., Uieda, L., Scharroo, R., Wobbe, F., Smith, W.H.F. and Tian, D., 2019. The generic mapping tools version 6. *Geochemistry, Geophysics, Geosystems*, *20*(11), pp.5556-5564.

Westaway, R., 1995. Crustal volume balance during the India-Eurasia collision and altitude of the Tibetan Plateau: A working hypothesis. *Journal of Geophysical Research: Solid Earth*, *100*(B8), pp.15173-15192.

White, L.T. and Lister, G.S., 2012. The collision of India with Asia. *Journal of Geodynamics*, *56*, pp.7-17.

Wittlinger, G., Farra, V., Hetényi, G., Vergne, J. and Nábělek, J., 2009. Seismic velocities in Southern Tibet lower crust: a receiver function approach for eclogite detection. *Geophysical Journal International*, *177*(3), pp.1037-1049.

Wittlinger, G., Vergne, J., Tapponnier, P., Farra, V., Poupinet, G., Jiang, M., Su, H., Herquel, G. and Paul, A., 2004. Teleseismic imaging of subducting lithosphere and Moho offsets beneath western Tibet. *Earth and Planetary Science Letters*, *221*(1-4), pp.117-130.

Xu, Q., Zhao, J., Yuan, X., Liu, H. and Pei, S., 2017. Detailed configuration of the underthrusting Indian lithosphere beneath western Tibet revealed by receiver function images. *Journal of Geophysical Research: Solid Earth*, *122*(10), pp.8257-8269.

Xu, Z.J., Song, X. and Zhu, L., 2013. Crustal and uppermost mantle S velocity structure under Hi-CLIMB seismic array in central Tibetan Plateau from joint inversion of surface wave dispersion and receiver function data. *Tectonophysics*, *584*, pp.209-220.

REFERENCES

Yadav, R.K., Gahalaut, V.K., Bansal, A.K., Sati, S.P., Catherine, J., Gautam, P., Kumar, K. and Rana, N., 2019. Strong seismic coupling underneath garhwal–kumaun region, NW Himalaya, India. *Earth and Planetary Science Letters*, *506*, pp.8-14.

Yang, Y. and Ritzwoller, M.H., 2008. Characteristics of ambient seismic noise as a source for surface wave tomography. *Geochemistry, Geophysics, Geosystems*, *9*(2).

Yang, Y., Ritzwoller, M.H., Levshin, A.L. and Shapiro, N.M., 2007. Ambient noise Rayleigh wave tomography across Europe. *Geophysical Journal International*, *168*(1), pp.259-274.

Yang, Y., Ritzwoller, M.H., Zheng, Y., Shen, W., Levshin, A.L. and Xie, Z., 2012. A synoptic view of the distribution and connectivity of the mid-crustal low velocity zone beneath Tibet. *Journal of Geophysical Research: Solid Earth*, *117*(B4).

Yang, Y., Zheng, Y., Chen, J., Zhou, S., Celyan, S., Sandvol, E., Tilmann, F., Priestley, K., Hearn, T.M., Ni, J.F. and Brown, L.D., 2010. Rayleigh wave phase velocity maps of Tibet and the surrounding regions from ambient seismic noise tomography. *Geochemistry, Geophysics, Geosystems*, *11*(8).

Yao, H. and Van Der Hilst, R.D., 2009. Analysis of ambient noise energy distribution and phase velocity bias in ambient noise tomography, with application to SE Tibet. *Geophysical Journal International*, *179*(2), pp.1113-1132.

Yin, A. and Harrison, T.M., 2000. Geologic evolution of the Himalayan-Tibetan orogen. *Annual Review of Earth and Planetary Sciences*, *28*(1), pp.211-280.

Yin, A., 2000. Mode of Cenozoic east-west extension in Tibet suggesting a common origin of rifts in Asia during the Indo-Asian collision. *Journal of Geophysical Research: Solid Earth*, *105*(B9), pp.21745-21759.

Yin, A., 2006. Cenozoic tectonic evolution of the Himalayan orogen as constrained by along-strike variation of structural geometry, exhumation history, and foreland sedimentation. *Earth-Science Reviews*, *76*(1-2), pp.1-131.

Yu, H., Webb, A.A.G. and He, D., 2015. Extrusion vs. duplexing models of Himalayan mountain building 1: Discovery of the Pabbar thrust confirms duplex-dominated growth of the northwestern Indian Himalaya since Mid-Miocene. *Tectonics*, *34*(2), pp.313-333.

Yuan, H. and Bodin, T., 2018. A probabilistic shear wave velocity model of the crust in the central West Australian Craton constrained by transdimensional inversion of ambient noise dispersion. *Tectonics*, *37*(7), pp.1994-2012.

REFERENCES

Zeng, X., Lancelle, C., Thurber, C., Fratta, D., Wang, H., Lord, N., Chalari, A. and Clarke, A., 2017. Properties of noise cross-correlation functions obtained from a distributed acoustic sensing array at Garner Valley, California. *Bulletin of the Seismological Society of America*, *107*(2), pp.603-610.

Zhang, Z., Wang, Y., Houseman, G.A., Xu, T., Wu, Z., Yuan, X., Chen, Y., Tian, X., Bai, Z. and Teng, J., 2014. The Moho beneath western Tibet: Shear zones and eclogitization in the lower crust. *Earth and Planetary Science Letters*, *408*, pp.370-377.

Zhao, J., Yuan, X., Liu, H., Kumar, P., Pei, S., Kind, R., Zhang, Z., Teng, J., Ding, L., Gao, X. and Xu, Q., 2010. The boundary between the Indian and Asian tectonic plates below Tibet. *Proceedings of the National Academy of Sciences*, *107*(25), pp.11229-11233.

Zhao, W., Kumar, P., Mechie, J., Kind, R., Meissner, R., Wu, Z., Shi, D., Su, H., Xue, G., Karplus, M. and Tilmann, F., 2011. Tibetan plate overriding the Asian plate in central and northern Tibet. *Nature geoscience*, *4*(12), pp.870-873.

Zhao, W., Nelson, K.D., Che, J., Quo, J., Lu, D., Wu, C. and Liu, X., 1993. Deep seismic reflection evidence for continental underthrusting beneath southern Tibet. *Nature*, *366*(6455), pp.557-559.

Zhu, L. and Helmberger, D.V., 1998. Moho offset across the northern margin of the Tibetan Plateau. *Science*, *281*(5380), pp.1170-1172.